ANALYSIS OF STABILITY, WAVEFORM INVARIANCE, AND NON-RECIPROCITY IN NONLINEAR PERIODIC STRUCTURES

A Dissertation
Presented to
The Academic Faculty

by

Matthew David Fronk

In Partial Fulfillment
of the Requirements for the Degree
Doctor of Philosophy in the
George W. Woodruff School of Mechanical Engineering

Georgia Institute of Technology
May 2020

ANALYSIS OF STABILITY, WAVEFORM INVARIANCE, AND NON-RECIPROCITY IN NONLINEAR PERIODIC STRUCTURES

Approved by:

Dr. Michael Leamy, Advisor
School of Mechanical Engineering
Georgia Institute of Technology

Dr. Massimo Ruzzene
School of Mechanical Engineering
University of Colorado Boulder

Dr. Aldo Ferri
School of Mechanical Engineering
Georgia Institute of Technology

Dr. Martin Maldovan
School of Chemical and Biomolecular Engineering
Georgia Institute of Technology

Dr. Karim Sabra
School of Mechanical Engineering
Georgia Institute of Technology

Date Approved: April 07, 2020

To Dad

ACKNOWLEDGEMENTS

This thesis did not arise from myself alone. I have profound gratitude for the various people who made this work possible. Words can never fully capture the impact you all have had on my life yet here I describe the ways you have shaped me during such formative years.

Firstly, I am grateful for my research advisor Dr. Michael Leamy. He welcomed me into his laboratory group and provided me with complex, stimulating research topics upon which I could work. He challenged me to do honest, high-quality work and strive for excellence. Furthermore, he worked hard alongside me to publish various journal articles and provided numerous opportunities to present my research at conferences—both national and international. I am also deeply thankful for his personal investment in me. Dr. Leamy played a pivotal role in preparing, guiding, and inspiring me to pursue an academic position, which I am now blessed to have at the Department of Physics in the United States Naval Academy. I should also mention that despite the demands of research, he often reiterated to me the importance of personal health and balance, two areas of life that are unfortunately easy to "trade-in" for professional success. Lastly, Dr. Leamy made a marked effort to support me during times of loss and personal hardship.

I would also like to thank the members of my reading committee, Dr. Aldo Ferri, Dr. Karim Sabra, Dr. Martin Maldovan, and Dr. Massimo Ruzzene. The investment of their time and attention towards reviewing my work is highly appreciated, and their positive criticism improved the quality of my research.

Various faculty and staff at Georgia Tech provided resources and technical support as I conducted my doctoral research. I would like to specifically thank Dr. Karim Sabra and Dr. Alper Erturk for permitting me to use some of their experimental equipment. Additionally, Louis Boulanger and Scott Elliot among other staff at the Montgomery Machining Mall provided excellent service with their fabrication of experimental components and technical guidance for experimental design. Other support came from Kyle French and Andrew Keller at the Electronics Lab and countless student volunteers at the Invention Studio. I would also like to thank Dr. Muhammad Salman, professor of mechanical engineering at Kennesaw State University, for his assistance in designing, fabricating, testing, and analyzing my experimental studies.

My labmates were a constant source of support, understanding, and knowledge during my graduate school years. The early influence of Dr. Jason Kulpe was impactful in showing me what it takes to succeed-in—and enjoy—gradate school. Douglas Cox, Oscar Peña, Saeid Loghavi, Noah Schaich, and Christian Free were outstanding Master's Students who I could rely-upon to lift my spirits. I witnessed as a fellow doctoral student nearly the entire Ph.D. studies of Dr. Justin Wilbanks and Dr. Amir Darabi, so we have a special bond from many shared experiences. My travels and interactions with labmate Yingdan Wu have also been memorable. Ph.D. students who recently joined Dr. Leamy's lab—Lezheng Fang, Emily Kliewer, and Sai Kuchibhatla—have become my good friends. I am also thankful for my interactions and relationships with an array of post-docs and visiting scholars from around the world such as Dr. Pawel Packo, Dr. Priscilla Brandão Silva, Dr. Rafal Radecki, Jiansong Li, Alex Alyukov, among others.

Living-out my Catholic faith is important to me and I am thankful for the community at the Georgia Tech Catholic Center for providing a place of worship, friendship, and spiritual growth during these critical years. I will always value the spiritual guidance of many chaplains, most especially Fr. Joshua Allen.

Lastly, I would like to thank my family for their inexhaustible love and kindness over these years. My mom has understood and listened to me through periods of challenge and celebrated with me during moments of triumph. My siblings, Aly, Mary, and Stewart each lifted me up in their own unique ways and have been a constant reminder of the joys of family life. I am also grateful for my dad, who I love and miss, for all he did to raise me and provide for me in the years leading-up to my graduate studies. It is my prayer that he can see this accomplishment as a testament of his influential fatherhood, and I dedicate this work to him.

TABLE OF CONTENTS

LIST OF TABLES

LIST OF FIGURES

SUMMARY

Wave propagation in periodic structures and metamaterials has attracted the interest of the engineering community due to the presence of bandgaps, or forbidden frequency ranges of propagation, which have inspired devices to include filters, diodes, switches, and waveguides. Geometric and material nonlinearities present in periodic structures result in propagation features (*e.g.* direction, cut-off/cut-on frequencies, group velocity) dependent on wave amplitude, thereby providing an additional means to manipulate wave propagation. This work explores waveform invariance, stability, and non-reciprocity as enabled by nonlinear periodic structures. One-dimensional and two-dimensional discrete lattices are considered. Waveform invariance, in which a multi-harmonic solution persists without dispersing for all space and time, and plane wave stability, in which high amplitude waves undergo significant distortion of their spectral content, are informed by perturbation analysis of the lattices' equations of motion. Extensions of the invariant plane wave solutions include special fundamental frequencies that avoid higher-harmonic generation and a slow-scale energy modulation between internally-resonant wave propagation modes. Non-reciprocity exploits a preferred energy transfer that occurs from large to small scales, coupled by strongly nonlinear restoring forces, to create a periodic lattice with highly asymmetrical wave propagation. Theoretical findings are validated with numerical simulations and experimental testing and may apply to damage detection, data encryption, and shock and vibration mitigation.

CHAPTER 1. INTRODUCTION

1.1 Overview

This research investigates stability, waveform invariance, and non-reciprocity in nonlinear periodic structures and metamaterials. Spatially-repeating patterns of material properties, geometry, and/or boundary conditions characterize periodic media, or lattices, which possess inherent filtering and wave-guiding properties. The consideration of stiffness nonlinearities in periodic structures enables amplitude to further tune these unique wave propagation features. For a nonlinear lattice, the acoustic band diagram which relates frequency to wavenumber and identifies bandgaps that prohibit wave propagation, evolves with wave amplitude allowing the bandgap size and location to be adjusted *in-situ*. Yet questions remain regarding the nature and capabilities of wave propagation in nonlinear lattices, giving rise to the aforementioned investigation of stability, waveform invariance, and non-reciprocity.

Little attention has been given to the stability of plane-wave propagation in nonlinear periodic structures. Under what conditions do plane waves retain—or lose—stability? Clearly, phenomena such as amplitude-dependent filtering are desired to occur stably. The potential of instabilities of plane waves in mechanical lattices has been largely unexplored and would provide design parameters to avoid or novel behavior to exploit. Furthermore, it is well-known that a single-frequency propagating in nonlinear media generates higher-harmonics. A single harmonic forcing applied to a nonlinear medium results-in a wave that undergoes significant changes to its spectral composition, which has been used successfully for nondestructive damage evaluation, for example. However, are plane waves

in nonlinear media limited to a spatially and temporally variable frequency content? Do nonlinear lattices possess a preferred distribution of spectral energy for invariant plane-wave propagation? Lastly, linear, time invariant materials are bound by reciprocity: sources and receivers will transmit and measure the same amount of energy should their locations exchange. Nonlinearity, therefore, provides the potential to break this symmetry and does not require any active system components or external bias. Can a nonlinear lattice be designed to passively break reciprocity?

This work explores waveform invariance, stability, and non-reciprocity in nonlinear periodic media, demonstrating their existence and proposing their significance. The rest of this chapter is organized as follows: Section 1.2 provides a background of the characteristics of wave propagation in linear and nonlinear lattices. Prior work relevant to and motivational for the study of invariance, stability, and non-reciprocity is contained in Section 1.3, 1.4, and 1.5, respectively. Section 1.6 summarizes the main contributions of this work to the engineering and physics communities. Lastly, Section 1.7 details the structure for the remaining chapters.

1.2 Wave Propagation in Linear and Nonlinear Periodic Media

1.2.1 Linear Periodic Media

Periodic media consists of spatially-repeating patterns of material properties, geometry, and/or boundary conditions. They arise naturally in civil, automotive, and aerospace applications to maintain structural integrity of components such as aircraft wings and bridges, as depicted in Figure 1-1a and Figure 1-1b, respectively. It is beneficial, therefore, for engineers to understand, predict, and control the effects of dynamic loads on

these periodic arrangements after such structural components are assembled. However, it is also advantageous to design periodicity into a system because of its interaction with and handling of dynamic loads, *e.g.* waves and vibrations. It is well known that periodically-spaced elastic components effectively function as mechanical filters, blocking ranges of frequency from propagating [1]. This property sparks several intriguing applications such as the Surface Acoustic Wave (SAW) filter, pictured in Figure 1-1c, in which an electromagnetic signal is transduced into a surface acoustic wave, filtered mechanically by periodically-spaced fingers, and then re-converted into an electromagnetic signal [2]. The SAW filtration process has been introduced in cell phone technology as a method to preserve battery life.

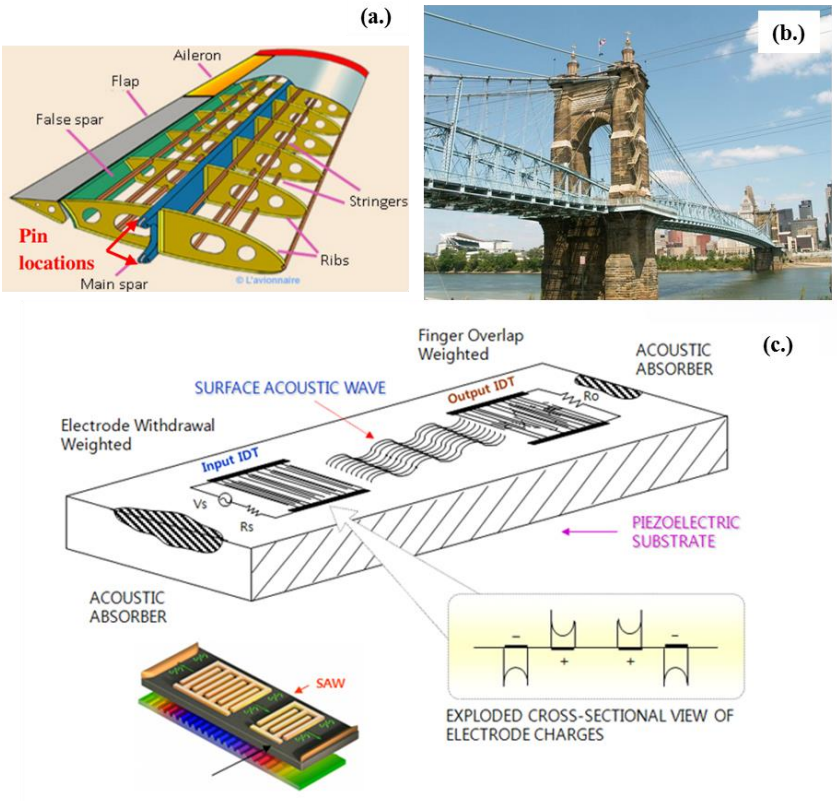

Figure 1-1. Engineering examples of periodic structures. Periodicity arises naturally from the structural supports in bridges (a.) and aircraft components (b.). Periodicity

can also be intentionally designed into systems, such as the Surface Acoustic Wave filter (c.). Images sources are [3-5].

Key to understanding the filtering property of periodic media is the band diagram, or band structure, which relates frequency to wavenumber much like an electronic band diagram relates energy to wavenumber. Figure 1-2a displays a sample two-dimensional periodic plate system whereby the geometry of the periodicity dictates the lattice directions and hence the Irreducible Brillouin Zone illustrated in Figure 1-2b. For its band structure in Figure 1-2c, note that there are ranges of frequency that are permitted, termed passbands, and those that are forbidden, termed bandgaps. Bandgap formation can be understood by realizing that the band structure itself must be periodic for a periodic system and that interference patterns between reflected and transmitted waves at each unit cell will undergo complete cancellation at certain frequency ranges. Other methods of bandgap formation include local resonance [6] and inertial amplification [7]. The Bloch Wave Expansion [8] expedites the process for obtaining band structures by posing an eigenvalue problem for a single unit cell that identifies all possible wave propagation modes and consequently relates the eigen-frequency to a propagation constant (which relates to wavenumber) at each mode.

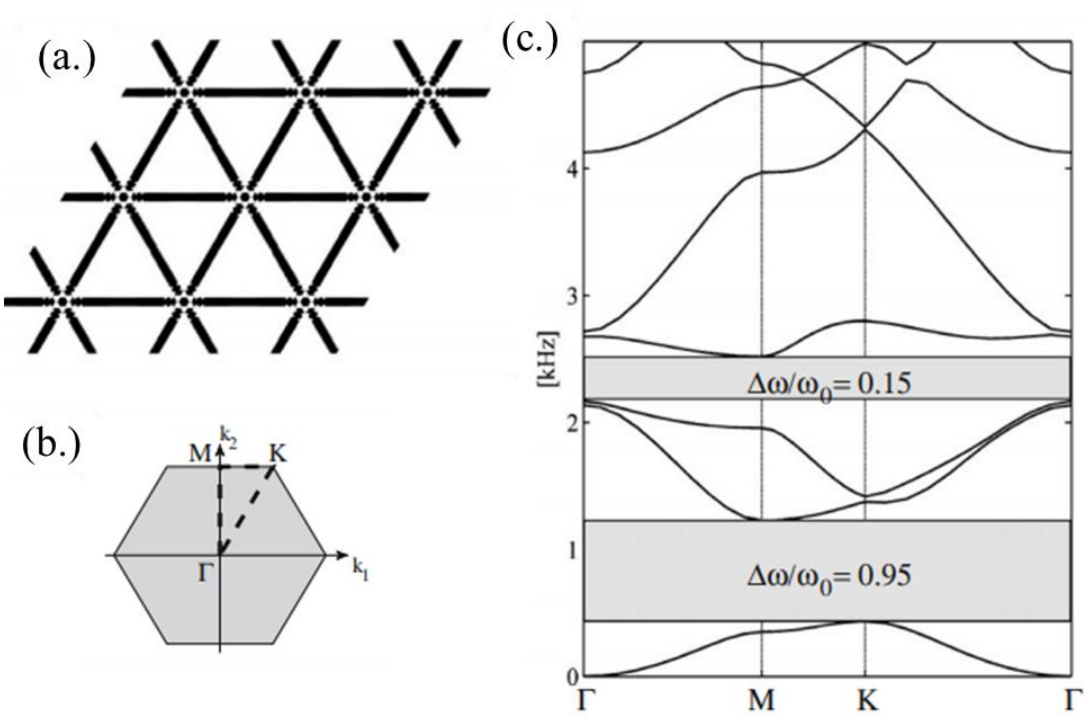

Figure 1-2. 2-D elastic periodic structure (a.) geometry of the plate structure (b.) irreducible Brillouin zone for propagation constant definition (c.) band structure identifying passbands and bandgaps [9].

1.2.2 Nonlinear Periodic Media

Nonlinear stiffness interactions, whether the result of geometry or a material's constitutive law, enables rich physics for wave propagation in periodic media unseen by its linear counterpart, such as amplitude-dependent behavior and the coupling of wave propagation modes. A seminal study in the field of wave propagation in nonlinear periodic media was conducted in 1955 by the scientists Fermi, Pasta, Ulam, and Tsingou at Los Alamos National Laboratories [10]. Hypothesizing that a chain of many particles coupled with weakly nonlinear restoring forces would exhibit ergodicity, the team carried-out numerical integration of the chain's equation of motion assigning energy to its fundamental (linear) vibration mode as the initial condition. The numerical results astonishingly

produced behavior opposite to the expected ergodicity: there was recurrence to the simulation's initial conditions. Energy periodically exchanged between modes instead of distributing across all modes (*i.e.*, equipartition). Such result sparked many subsequent findings in the same lattice, such as the perturbation theories proposed by Kolmogorov, Arnold, and Moser [11-13], the integrable dynamics of the lattice's continuous limit [14], and even chaotic behavior [15].

Several advancements to the analysis of wave propagation in nonlinear periodic structures have been made over recent years. Vakakis and King characterized the amplitude-dependent propagation and attenuation zones in monocoupled nonlinear lattices [16]. Chakraborty and Mallik derived expressions governing the bandgap shifts as a function of wave amplitude in infinite and finite monatomic chains [17]. Ganesh and Gonella investigated modal-mixing of nonlinear lattices whereby higher branches of a lattice's band structure activate under excitation at lower branches [18]. They enriched their finding of modal mixing by extending their perturbation framework to combine the effects of second harmonic generation from quadratic nonlinearity and bandgap shifting from cubic nonlinearity [19]. Dubus *et al.* studied a linear monatomic chain linearly coupled to a second, nonlinear monatomic chain [20]. Strong energy transfer occurs between the chains at critical wavenumbers. Manktelow [21] and Narisetti [22] presented a multiple scales framework for uncovering closed-form expressions governing amplitude-dependent dispersion shifts in nonlinear periodic media. In two-dimensional lattices, the extension of such perturbation framework reveals that wave amplitude can adjust the cut-off frequency for a given wave propagation direction [23].

1.3 Invariant Waveforms

Dispersive media tends to separate multi-frequency signals since, by definition, wave speed varies with frequency. Such phenomena poses challenges for coherent signal processing over long spatial and temporal scales such as SONAR detection in shallow water [24]. By virtue of their periodicity, lattices are inherently dispersive and therefore the same challenges arise. Nonlinearity offers the potential to enable invariant wave propagation, which by contrast, maintains a given spectral distribution over the course of wave propagation, exuding the signature of a d 'Alembert travelling wave solution. Various classes of invariant waveforms have been uncovered in nonlinear dispersive media.

A soliton is a well-known invariant waveform characterized by its pulse-like distribution of wave energy—or compact support—that retains its shape over the course of propagation and after collision with another soliton. Such solutions occur due to a balance between softening-type dispersion and hardening-type nonlinearity at prescribed amplitudes and wave speeds. Solitons were originally observed in water [25] and have since been found in fiber-optic cables [26, 27], granular media [28, 29], and weakly nonlinear lattices [30, 31]. A common approach to their identification is to substitute a general wave solution of permanent form into the governing equations and impose the solution's boundedness, or compact support, yielding a relationship between the soliton's amplitude and velocity [14, 32, 33].

Variants of the soliton have been studied and exhibit differences between the spatiotemporal character of the pulse. The main attribute of the breather, for instance, is its modulating envelope [34, 35] which describes molecular-level phenomena such as dipole oscillations in a 1-D condensate [36]. The existence of breathers in micro-resonators has been recently discovered [37]. Kink, or topological, solitons possess an arctangent

distribution [38, 39] and have been observed in mechanical systems such as chains of rotating pendula [40, 41]. Additionally, dark solitons comprise localized "dips" superposed on a propagating wave background [42-44] and their existence in shear lattices with nonlinear foundations was recently revealed [45].

Another invariant waveform is the so-called cnoidal wave, which in contrast to the soliton "pulse" is a periodic solution characterized by a long wavelength, flat troughs, and sharp crests. Figure 1-3 presents cnoidal waves captured by U.S. Army Bombers flying over Panama in 1933 [46]. Like solitons, cnoidal waves were originally discovered in water in which the dispersion inherent to low amplitude shallow water waves balances with amplitude-dependent phase velocity to manifest as a wave of permanent form. These periodic solutions are expressed in terms of elliptic functions and satisfy—in closed form—the Korteweg de Vries (KdV) partial differential equation [33, 47, 48]. Recently, Friesecke and Mikikits-Leitner [20] demonstrated that the nonlinear interaction of particles in a discrete chain uncover, in the continuum limit, continuous partial differential equations, such as the KdV equation and thus cnoidal waves. In a similar study, Gaison *et al*. [21] applied homogenization techniques to the long wavelength limit of a nonlinear monatomic lattice with periodic material properties and uncovered solutions that approximately satisfy a KdV equation.

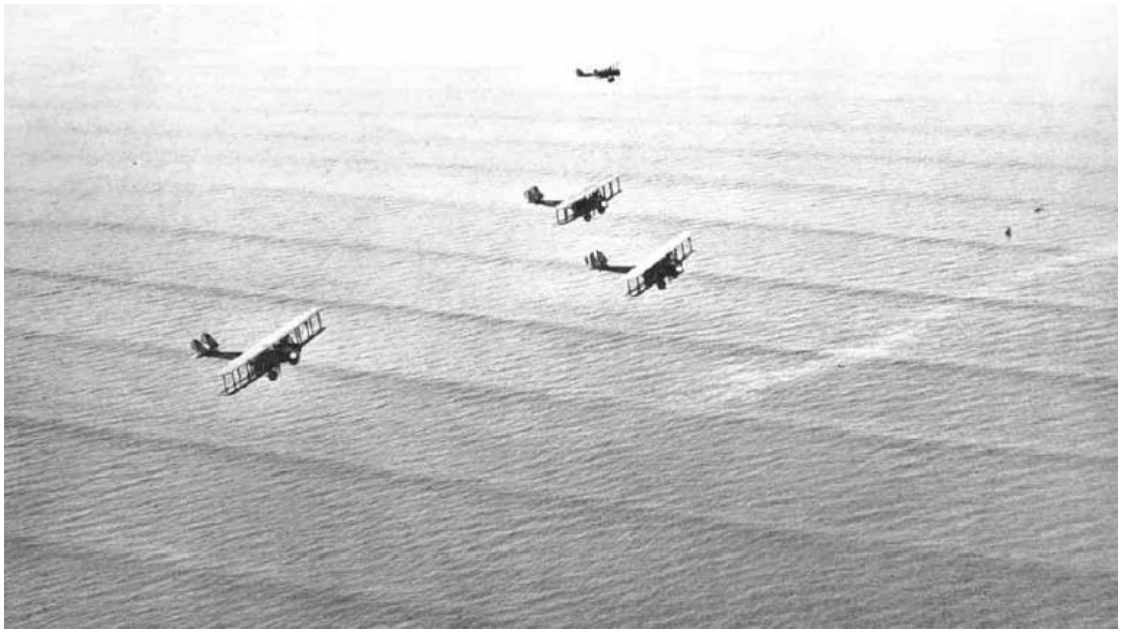

Figure 1-3. Cnoidal waves observed by U.S. bombers over the Panama coast [46]

1.4 Stability

The stability of waves in elastic and acoustic nonlinear media has received varying degrees attention, depending upon the waveform and type of media. In [49], Newton and Keller present a strategy for determining the stability of plane waves in continuous media governed by a general class of nonlinear partial differential equations. Their perturbation framework introduces a general plane wave solution at higher orders and subsequently derives the conditions for the existence of real or imaginary frequencies signaling stability or instability, respectively. The stability of invariant plane waves in water has been considered extensively. For example, the leading terms of a Stoke's wave possesses fundamental and second harmonic plane waves that theoretically should travel invariantly. To assess such a wave's stability, a low frequency envelope is introduced and conditions for its modulation or unbounded growth are investigated, leading to the celebrated Benjamin-Feir [50, 51] and Benjamin-Feir-Lighthill [52-54] criteria. The so-called

modulation instability, or growth of sidebands from a carrier wave, disintegrates plane waves in nonlinear media presuming certain resonant-like conditions are met between the sideband frequencies and its primary carrier wave.

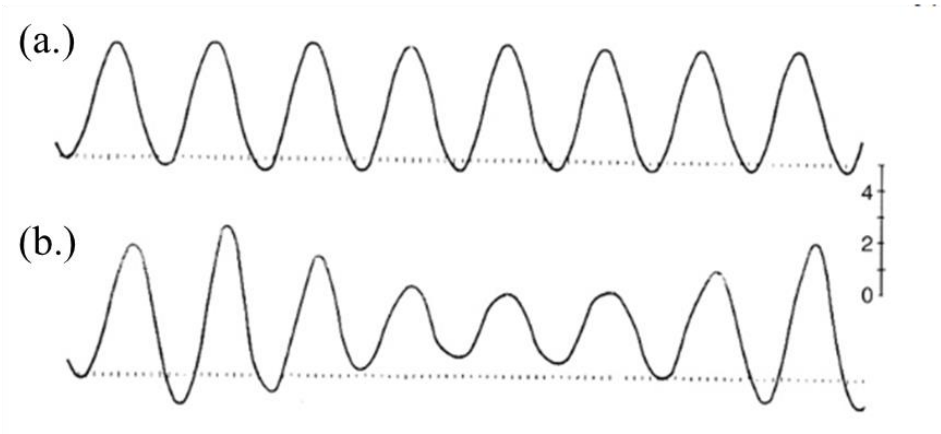

Figure 1-4. Instability of a water wave experimentally captured in a water tank in which a wave maker oscillates at 0.85 Hz [54]. Note the higher-harmonics characteristic to the signal recorded at 60 m from the source (a.) whereas the disintegration of the multi-harmonic wave is recorded at 120 m from the source (b.).

Other studies have considered waveform stability in nonlinear periodic media yet have considered solutions other than plane waves. Bickham *et al*. [55] studied the stability of localized modes in a monoatomic chain with quadratic and cubic force interactions. Numerical simulations introduced local static distortions into chains. Instabilities of the localized vibration modes began to arise in simulations in which the cubic anharmonicity increased to the point where the lowest possible plane wave frequency was reached. Further increases in the cubic anharmonicity led to behavior reminiscent of a triatomic molecule, until further increases created instabilities yet again. Friesecke and Pego [56] identified exponential growth in amplitude of waves in discrete lattices by applying Floquet theory and analyzing evolution equations. In [57], Flach and Gorbach uncovered a threshold for tangent bifurcations in discrete breathers. Huang and Hu [58] investigated the stability of

diatomic lattices using a quasi-discreteness approach. They derived evolution equations and fixed points for acoustic and optical modes and identified the presence of asymmetrical gap solitons. Gorbach and Johansson [59] presented findings on the linear stability of discrete gap breathers in a 1-D diatomic chain with harmonic intersite potential and nonlinear external potential. Six types of instabilities were identified, which took on either oscillatory or non-oscillatory forms. An "inversion of stability" regime was found characterized by practically radiationless mobility. For nonlinear periodic structures, very little efforts have been directed towards understanding the stability of plane waves.

Instabilities in metamaterials are often studied in terms of non-convex curvature in the media's potential energy landscape [60]. Unit cells comprising bi-stable elements inherently possess unstable fixed points and exhibit "snap-through" behavior [61-64], supporting the propagation of transition waves [65, 66] and asymmetrical wave transmission [67].

1.5 Non-Reciprocity

Reciprocity is a property of linear time invariant media in which a source transmits energy to a receiver and the same energy transmission will occur should the source and receiver exchange positions. It has mathematical analogs in heat and electricity carrying media, and is widely used in linear modal testing to obtain frequency response functions as well as for transducer calibration. Recent research efforts have explored methods of breaking this symmetry, with a practical opportunity of designing "one-way" devices that permit propagation of elastic or acoustic waves in one direction but block it in the reverse

direction. Such behavior is termed *non-reciprocity* and it has been achieved using both active and passive approaches.

Many studies have reported non-reciprocity in systems with odd-symmetric external biases, or some active external force that biases the direction of energy transmission. Such external biases range from magnetic fields in electrical systems [68] to circulating fluid flow in acoustic systems [69, 70] to moving, zero-index acoustic meta-materials [71]. Additional active methods of breaking reciprocity include space/time modulation of material properties which has received increasing intention in recent years. By periodically varying density and Young's modulus, Trainiti and Ruzzene [72] reported large disparities in opposite directions of band diagrams, from which the optimal modulation speed for maximizing nonreciprocity was derived. In [73], harmonic spatiotemporal modulation of density and modulus in periodic laminates produces asymmetric propagation for supersonic and subsonic modulation speeds. In the scale-separated homogenization limit, the Willis stress-velocity momentum-strain coupling tensor provides a direct measurement of the non-reciprocity. A comprehensive dispersion analysis of modulating material properties in two-dimensional phononic crystals is provided in [74]. Alternatively, the geometric properties of acoustic cavities can also be modulated [75]. Photon-phonon conversion [76], activation/deactivation of periodically spaced electrodes [77], and magnetically active elastic materials [78] are other recent efforts of breaking reciprocity through modulation of a medium's properties.

Considerably less attention has been given to systems that passively break reciprocity—particularly within the acoustics and vibrations community. Liang *et al.* [79, 80] developed an acoustic rectifier by coupling a linear superlattice to a nonlinear medium and exploiting

the bandgaps of the superlattice and the higher harmonic generation of the nonlinear medium to induce nearly one-way wave propagation. A similar study was carried-out by Luo *et al.* [81] in which linear and nonlinear lattices with identical masses were joined at an interface. A shift in the acoustic branch but not in the optical branch occurred, enabling a bias in propagation direction at sufficiently high amplitudes. Boechler *et al.* [82] experimentally observed acoustic rectification by similar means in a granular chain with a point defect. In these studies, the location of the interface or the defect relative to the source of excitation limits the application of the designs for sound and vibration isolation. The strategies in [79, 80, 82] requires the "upconverting" of the wave at its fundamental frequency to higher harmonics, thus not retaining all signal information at the fundamental operating frequency. In another study [67], reciprocity was broken in a periodic structure by activating a supratransmission instability. Dispersion analysis of the nonreciprocal wave propagation was reported.

1.6 Main Results

This work reveals several novel aspects of wave propagation in nonlinear periodic media. These findings introduce rich new behavior and analysis techniques, building-upon prior work that predicted and validated amplitude-dependent dispersion characteristics of nonlinear lattices and metamaterials. The primary contributions of this work include:

- A higher-order perturbation analysis is detailed that predicts the stability of and invariant spectral content for plane waves in an arbitrary nonlinear one-dimensional and two-dimensional lattice systems.

- Multi-harmonic plane waves are derived that retain their spectral energy distribution across space and time. Such finding is remarkable due to the dispersive nature of lattices. It enables a continuous distribution of plane wave energy to propagate unaltered, potentially useful for the detection strategies of SONAR systems, for example.
- At special frequencies, these invariant waveforms consist of solely its fundamental term, thus circumventing the production of higher-harmonic frequency content across space and time.
- Furthermore, internal resonances in nonlinear lattices exhibits a unique form of waveform invariance in which two internally resonant wave propagation modes exchange energy in a closed-periodic orbit of their phase space for all space and time.
- Plane wave stability is established whereby certain amplitude ranges and, counterintuitively, directions of nonlinear lattices exhibit variable degrees of stability for plane wave propagation. Such findings may inspire wave-based mechanical encryption techniques.
- A lattice incorporating nonlinearity, asymmetry, and internal hierarchy is demonstrated to passively break reciprocity for broadband (impulsive) excitation. This media is entirely passive, not relying upon an external source of energy to bias the wave propagation direction.

1.7 Organization of the Work

This dissertation is organized as follows: Chapter 2 presents a higher-order perturbation analysis of one-dimensional (1-D) weakly nonlinear lattices, revealing amplitude-dependent stability and multi-harmonic content associated with waveform invariance. Chapter 3 extends the higher-order perturbation analysis to two-dimensional (2-D) shear lattices. In addition to the amplitude-dependence observed in 1-D chains, waveform invariance and stability surprisingly take-on angular-dependence in lattices with symmetric stiffness terms. Chapters 4 and 5 describe two special classes of waveform invariance. In Chapter 4, a slow scale energy exchange between two internally-resonant wave propagation modes is captured by reformulating the multiple scales analysis. In Chapter 5, multiple scales predicts specific frequencies at which invariant plane waves comprise only their fundamental term, thereby suggesting an aversion to higher-harmonic generation at these select frequencies. Experimental validation of amplitude-dependent dispersion shifting and waveform stability is outlined in Chapter 6. Chapter 7 overviews non-reciprocity as enabled by lattices with strong nonlinearity, asymmetry, and internal hierarchy. Lastly, Chapter 8 summarizes the contributions of the present work and proposes exciting avenues for follow-on studies.

CHAPTER 2. AMPLITUDE-DEPENDENT STABILITY AND WAVEFORM INVARIANCE IN ONE-DIMENSIONAL NONLINEAR PERIODIC STRUCTURES

2.1 Overview

This chapter develops a higher-order multiple scales procedure that reveals amplitude-dependent stability and waveform invariance of plane waves in one-dimensional (1-D) nonlinear periodic structures. Prior studies of such systems derived amplitude-dependent band diagrams through a 1st-order perturbation analysis [21, 22]. Furthermore, the consideration of stability and waveform invariance have been centered-around spatially localized solutions such as the soliton [58, 83, 84] and breather [57, 59, 85, 86]. By contrast, this work examines plane waves of infinite temporal and spatial extent in weakly nonlinear monatomic and diatomic chains. A local fixed-point analysis describes an amplitude-dependent transition from stable to unstable plane wave propagation. Additionally, multi-harmonic invariant plane waves are identified that maintain their spectral distribution over the course of propagation. Such features are made manifest through a higher-order multiple scales framework: a 1st-order analysis is not sufficient for capturing this behavior.

The chapter is organized as follows. Section 2.2 describes the example systems considered in this work: weakly nonlinear monatomic and diatomic chains. Nonlinearity arises from the inclusion of small quadratic and cubic stiffness terms. Section 2.3 and 2.4 present a higher-order multiple scales analysis of the monatomic and diatomic systems, respectively. The results are key for predicting waveform invariance and stability. Section 2.5

summarizes the approach to conducting numerical simulations of the lattice equations of motion which is used to validate the multiple scales findings. While not the principal goal of this work, Section 2.6 documents higher-order dispersion shifts, confirming the negligible role of quadratic stiffness in bandgap shifting. Section 2.7 studies the stability of plane waves, beginning with a local fixed point analysis of the multiple scales evolution equations and supporting the predictions with numerical simulations. Section 2.8 reveals and numerically validates waveform invariance as predicted by the higher-order perturbation analysis. Lastly, conclusions are drawn in Section 2.9.

2.2 System Description: 1-D Chains

This section introduces the two systems studied herein, namely nonlinear monatomic and diatomic chains, defining their equations of motion to which the asymptotic analyses are applied and presenting schematics for ease of system visualization. For the monatomic chain, the smallest repeatable subsystem, or unit cell, consists of a single mass and its connecting springs and dampers, as presented in Figure 2-1.

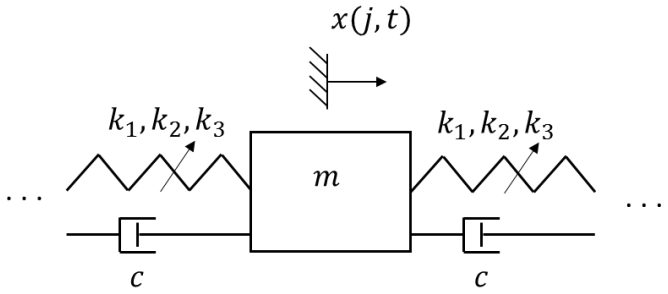

Figure 2-1. Schematic of the unit cell for the monatomic chain.

A force balance on the j^{th} mass yields its equation of motion

$$m\ddot{x}_j + k_1(2x_j - x_{j+1} - x_{j-1}) - \varepsilon k_2(x_{j+1} - x_j)^2 + \varepsilon k_2(x_{j-1} - x_j)^2$$

$$-\varepsilon k_3\left(x_{j+1}-x_j\right)^3-\varepsilon k_3\left(x_{j-1}-x_j\right)^3+\varepsilon c\left(2\dot{x}_j-\dot{x}_{j+1}-\dot{x}_{j-1}\right)=0 \quad (2.1)$$

where $x_j = x(j,t)$ denotes the displacement from equilibrium of the j^{th} mass, m its mass, k_1, k_2, and k_3 the linear, quadratic, and cubic stiffnesses, respectively, and c denotes the linear damping coefficient. Time derivatives of x_j—$\dot{x}_j$ and $\ddot{x}_j$—denote the velocity and acceleration of the j^{th} mass, respectively. The parameter ε is assumed to be small and introduced herein as a bookkeeping device.

By contrast, the unit cell of the diatomic chain, depicted in Figure 2-2, contains two masses coupled with identical springs and dampers.

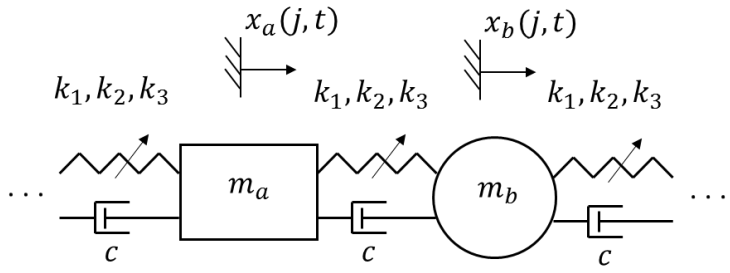

Figure 2-2. Schematic of the unit cell for the diatomic chain.

Summing the forces on each degree of freedom in the j^{th} unit cell leads to its equation of motion

$$M\underline{\ddot{x}}_j+\sum_{l=j-1}^{j+1}K_l\underline{x}_l+\sum_{l=j-1}^{j+1}\varepsilon C_l\underline{\dot{x}}-\varepsilon\underline{f}_{quadratic}-\varepsilon\underline{f}_{cubic}=\underline{0} \quad (2.2)$$

where

$$\underline{x}_j = \begin{bmatrix} x_a(j,t) \\ x_b(j,t) \end{bmatrix} \tag{2.3}$$

$$M = \begin{pmatrix} m_a & 0 \\ 0 & m_b \end{pmatrix} \tag{2.4}$$

$$K_{j-1} = \begin{pmatrix} 0 & -k_1 \\ 0 & 0 \end{pmatrix}, K_j = \begin{pmatrix} 2k_1 & -k_1 \\ -k_1 & 2k_1 \end{pmatrix}, K_{j+1} = \begin{pmatrix} 0 & 0 \\ -k_1 & 0 \end{pmatrix} \tag{2.5}$$

$$C_{j-1} = \begin{pmatrix} 0 & -c \\ 0 & 0 \end{pmatrix}, C_j = \begin{pmatrix} 2c & -c \\ -c & 2c \end{pmatrix}, C_{j+1} = \begin{pmatrix} 0 & 0 \\ -c & 0 \end{pmatrix} \tag{2.6}$$

$$\underline{f}_{quadratic} = \begin{bmatrix} -k_2\big(x_b(j-1,t) - x_a(j,t)\big)^2 + k_2\big(x_b(j,t) - x_a(j,t)\big)^2 \\ -k_2(x_a(j,t) - x_b(j,t))^2 + k_2\big(x_a(j+1,t) - x_b(j,t)\big)^2 \end{bmatrix} \tag{2.7}$$

$$\underline{f}_{cubic} = \begin{bmatrix} k_3\big(x_b(j-1,t) - x_a(j,t)\big)^3 + k_3\big(x_b(j,t) - x_a(j,t)\big)^3 \\ k_3\big(x_a(j,t) - x_b(j,t)\big)^3 + k_3\big(x_a(j+1,t) - x_b(j,t)\big)^3 \end{bmatrix} \tag{2.8}$$

It is noted here that the presence of linear and small cubic and quadratic force displacement relationships describes many systems whose nonlinear interactions are expanded in a Taylor series.

2.3 Higher-Order Multiple Scales Analysis: Monatomic Chain

In this section, a higher-order method of multiple scales (MMS) is developed for the monatomic chain presented in Section 2, extending the analysis through the 2nd-order to capture harmonic content and time evolution of amplitude and phase. It is shown in Section 5.3 that inclusion of these higher-order features increases the invariance of the cnoidal-like wave. Higher-order results also facilitate the stability and dispersion analyses, providing insight to behavior not evident at solely the 1st-order.

Multiple time scales are assumed to exist such that

$$T_0 = t, T_1 = \varepsilon t, T_2 = \varepsilon^2 t, \dots, T_n = \varepsilon^n t \tag{2.9}$$

where t denotes the original time scale and T_n represents the n^{th} time scale. Since $\varepsilon \ll 1$, each time scale advances more slowly than its predecessor. Introducing these times scales plays an important role in detecting amplitude-dependent dispersion shifts since phase change at each slow time scale can be interpreted as dispersion corrections.

In accordance with these time scales, differentiation with respect to time contains multiple orders,

$$(\dot{\ }) = D_0(\ ) + \varepsilon D_1(\ ) + \varepsilon^2 D_2(\ ) + \cdots + \varepsilon^n D_n(\ ), \tag{2.10}$$

where $D_n(\ )$ denotes an operator defined to represent differentiation with respect to T_n.

It follows that

$$(\ddot{\ }) = \left(D_0(\ ) + \varepsilon D_1(\ ) + \varepsilon^2 D_2(\ ) + \cdots + \varepsilon^n D_n(\ )\right)^2$$

$$= D_0^2(\ ) + 2\varepsilon D_0 D_1(\ ) + \varepsilon^2 D_1^2(\ ) + 2\varepsilon^2 D_0 D_2(\ ) + O(\varepsilon^3) \tag{2.11}$$

The MMS seeks a series expansion of the solution of the form

$$x_j = x_j^{(0)} + \varepsilon x_j^{(1)} + \varepsilon^2 x_j^{(2)} + \cdots + \varepsilon^n x_j^{(n)} \tag{2.12}$$

where $x_j^{(n)}$ denotes the n^{th} order solution. Thus, the asymptotic solution is expanded about a known 0[th]-order solution $x_j^{(0)}$. Substituting Eqs. (2.10), (2.11), and (2.12) into Eq. (2.1) and collecting matching orders of ε yields $n + 1$ equations. The first 3 are presented here,

ε^0: $$mD_0^2 x_j^{(0)} + k_1\left(2x_j^{(0)} - x_{j+1}^{(0)} - x_{j-1}^{(0)}\right) = 0 \tag{2.13}$$

ε^1: $$mD_0^2 x_j^{(1)} + k_1\left(2x_j^{(1)} - x_{j+1}^{(1)} - x_{j-1}^{(1)}\right) = -2mD_0 D_1 x_j^{(0)}$$

$$-cD_0\left(2x_j^{(0)} - x_{j+1}^{(0)} - x_{j-1}^{(0)}\right) + k_2\left(x_{j+1}^{(0)} - x_j^{(0)}\right)^2 - k_2\left(x_{j-1}^{(0)} - x_j^{(0)}\right)^2$$

$$+k_3\left(x_{j+1}^{(0)}-x_j^{(0)}\right)^3+k_3\left(x_{j-1}^{(0)}-x_j^{(0)}\right)^3 \tag{2.14}$$

$$\varepsilon^2\colon\ mD_0^2x_j^{(2)}+k_1\left(2x_j^{(2)}-x_{j+1}^{(2)}-x_{j-1}^{(2)}\right)=-2mD_0D_2x_j^{(0)}-mD_1^2x_j^{(0)}-2mD_0D_1x_j^{(1)}-$$
$$cD_1\left(2x_j^{(0)}-x_{j+1}^{(0)}-x_{j-1}^{(0)}\right)-cD_0\left(2x_j^{(1)}-x_{j+1}^{(1)}-x_{j-1}^{(1)}\right)+$$
$$f_{quadratic}\left(x_{j-1},x_j,x_{j+1}\right)+f_{cubic}\left(x_{j-1},x_j,x_{j-1}\right) \tag{2.15}$$

where

$$f_{quadratic}\left(x_{j-1},x_j,x_{j+1}\right)=-2k_2x_{j-1}^{(0)}x_{j-1}^{(1)}+2k_2x_{j-1}^{(0)}x_j^{(1)}+2k_2x_{j-1}^{(1)}x_j^{(0)}-$$
$$2k_2x_{j+1}^{(1)}x_j^{(0)}-2k_2x_{j+1}^{(0)}x_j^{(1)}+2k_2x_{j+1}^{(0)}x_{j+1}^{(1)} \tag{2.16}$$

$$f_{cubic}\left(x_{j-1},x_j,x_{j+1}\right)=3k_3{x_{j-1}^{(0)}}^2x_{j-1}^{(1)}-3k_3x_{j-1}^{(0)}{x_j^{(1)}}^2-6k_3x_{j-1}^{(0)}x_{j-1}^{(1)}x_j^{(0)}+$$
$$6k_3x_{(j-1)}^{(0)}x_j^{(0)}x_j^{(1)}+3k_3x_{j-1}^{(1)}{x_j^{(0)}}^2-6k_3{x_j^{(0)}}^2x_j^{(1)}+3k_3x_{j+1}^{(1)}{x_j^{(0)}}^2+$$
$$6k_3x_{j+1}^{(0)}x_j^{(0)}x_j^{(1)}-6k_3x_{j+1}^{(0)}x_{j+1}^{(1)}x_j^{(0)}-3k_3{x_{j+1}^{(0)}}^2x_j^{(1)}+3k_3{x_{j+1}^{(0)}}^2x_{j+1}^{(1)} \tag{2.17}$$

Note that the left-hand sides of Eq. (2.13) through (2.15) are similar; *i.e.*, the linear kernels of the collected equations take the same form. Also note that each order is effectively forced by the solution obtained from the previous order.

By examination of Eq. (2.13), it is apparent that $x_j^{(0)}$ takes the form of a Bloch wave since its governing equation is linear with periodic coefficients,

$$x_j^{(0)}=\frac{1}{2}Ae^{i\omega_0T_0}e^{-i\mu j}+c.c. \tag{2.18}$$

where A denotes the wave's amplitude, ω_0 and μ the wave's fundamental temporal and spatial frequencies, respectively, and $c.c.$ denotes the complex conjugate of all preceding terms.

Since A is generally a complex quantity, it is useful to express it in polar form

$$A = \alpha e^{i\beta} \tag{2.19}$$

where $\alpha = \alpha(T_1, T_2, \dots, T_n)$ and $\beta = \beta(T_1, T_2, \dots, T_n)$ are real quantities. Wave amplitude is a critical parameter as it determines the strength of the nonlinearities and consequently the amount of dispersion shifting and the relevancy of the MMS results.

The 0th-order dispersion relationship follows from the Bloch solution form in Eq. (2.18) and the governing equation in Eq. (2.13)

$$\omega_0 = \sqrt{\frac{2k_1}{m}(1 - \cos\mu)} \tag{2.20}$$

This relationship, which stems from the linear, undamped chain ($\varepsilon = 0$), shifts for waves at different amplitudes in the presence of nonlinearities.

With $x_j^{(0)}$ known, $x_j^{(1)}$ is found by updating Eq. (2.14) with Eq. (2.18). Secular terms, *i.e.* those that contain $e^{i\omega_0 T_0} e^{-i\mu j}$, or its complex conjugate, induce resonant responses and thus cause the series solution to become non-uniform over the time scales of interest. Consequently, they are set to zero:

$$\begin{aligned} 0 = k_3\alpha^3\left(\frac{3}{4}\cos 2\mu - 3\cos\mu + \frac{9}{4}\right) + ci\omega_0\alpha(1 - \cos\mu) \\ + im\omega_0 D_1\alpha - m\omega_0\alpha D_1\beta \end{aligned} \tag{2.21}$$

which, after separating real and imaginary parts and setting to zero, restricts the evolution of α and β with respect to T_1

$$D_1\alpha = -\gamma\alpha \tag{2.22}$$

$$D_1\beta = \delta\alpha^2 \tag{2.23}$$

where

$$\gamma = \frac{c}{m}(1 - \cos\mu) \tag{2.24}$$

$$\delta = \frac{3k_3}{4m\omega_0}(\cos 2\mu - 4\cos\mu + 3) \tag{2.25}$$

Eqs. (2.22) and (2.23) represent evolution equations describing the dynamics of the wave on a slower time scale. Phase evolution governs dispersion shifts whereas amplitude evolution affects wave stability as will be presented in Sections 5.1 and 5.2.1, respectively.

With secular terms removed, Eq. (2.14) reduces to a linear, 1st-order ODE with constant coefficients and harmonic forcing at $2\omega_0$ and $3\omega_0$. The homogeneous solution is ignored since it contains no information than that already given by $x_j^{(0)}$, so a particular solution is sought of the form

$$x_j^{(1)} = \frac{1}{2}B_1 e^{2i\omega_0 T_0} e^{-2i\mu j} + \frac{1}{2}C_1 e^{3i\omega_0 T_0} e^{-3i\mu j} + c.c. \tag{2.26}$$

where $B_1$and C_1 can be found using the method of undetermined coefficients

$$B_1 = \frac{ik_2A^2(\sin 2\mu - 2\sin\mu)}{4m\omega_0^2 + 2k_1\cos 2\mu - 2k_1} = b_1A^2 \tag{2.27}$$

$$C_1 = \frac{k_3A^3(3\cos 2\mu - \cos 3\mu - 3\cos\mu + 1)}{18m\omega_0^2 + 4k_1\cos 3\mu - 4k_1} = c_1A^3 \tag{2.28}$$

The amplitudes in Eq. (2.27) and (2.28) describe the amount of 2nd and 3rd harmonic content that make-up the 1st-order plane wave solution.

Turning attention to the 2nd-order problem, Eq. (2.15), with known solutions for $x_j^{(0)}$ and $x_j^{(1)}$, the same procedure is carried out. Removal of secular terms now determines the evolution of α and β with respect to T_2

$$D_2\alpha = \frac{\gamma\delta}{\omega_0}\,\alpha^3 \tag{2.29}$$

$$D_2\beta = \mathrm{X}\alpha^4 + \Upsilon\alpha^2 + \mathrm{Z} \tag{2.30}$$

where

$$\mathrm{X} = -\frac{1}{4m\omega_0}\left(k_3c_1(9\cos\mu - 9\cos 2\mu + 3\cos 3\mu - 3) + 2\delta^2 m\right) \tag{2.31}$$

$$\Upsilon = -\frac{k_2b_1}{im\omega_0}(2\sin\mu - \sin 2\mu) \tag{2.32}$$

$$\mathrm{Z} = -\frac{\gamma^2}{2\omega_0} \tag{2.33}$$

The particular solution for $x_j^{(2)}$ takes the form

$$x_j^{(2)} = \frac{1}{2}B_2e^{2i\omega_0T_0}e^{-2i\mu j} + \frac{1}{2}C_2e^{3i\omega_0T_0}e^{-3i\mu j} + \frac{1}{2}E_2e^{4i\omega_0T_0}e^{-4i\mu j} + \frac{1}{2}F_2e^{5i\omega_0T_0}e^{-5i\mu j} + c.c. \tag{2.34}$$

where

$$B_2 = b_{21}\alpha^4e^{2i\beta} + b_{22}\alpha^2e^{2i\beta} \tag{2.35}$$

$$C_2 = c_{21}\alpha^5e^{3i\beta} + c_{22}\alpha^3e^{3i\beta} \tag{2.36}$$

$$E_2 = e_2A^4 \tag{2.37}$$

$$F_2 = f_2A^5 \tag{2.38}$$

and

$$b_{21} = \frac{1}{2e^{i\mu}\left(4m\omega_0^2e^{2i\mu} + k_1e^{4i\mu} - 2k_1e^{2i\mu} + k_1\right)}\left(3k_3b_1e^{6i\mu} - 2k_2c_1e^{6i\mu} - 6k_3b_1e^{5i\mu} + 2k_2c_1e^{5i\mu} - 16mb_1\omega_0\delta e^{3i\mu} - 3k_3b_1e^{4i\mu} + 2k_2c_1e^{4i\mu} + 12k_3b_1e^{3i\mu} - 3k_3b_1e^{2i\mu} - 2k_2c_1e^{2i\mu} - 6k_3b_1e^{i\mu} - 2k_2c_1e^{i\mu} + 3k_3b_1 + 2k_2c_1\right) \tag{2.39}$$

$$b_{22} = \frac{4icb_1\omega_0(1-\cos 2\mu) - 8ib_1\gamma m\omega_0}{4\left(m\omega_0^2 + k_1\cos^2\mu - k_1\right)} \tag{2.40}$$

$$c_{21} = -\frac{3}{2\left(k_1e^{6i\mu} + 9m\omega_0^2e^{3i\mu} - 2k_1e^{3i\mu} + k_1\right)}c_1\left(-16k_3e^{3i\mu}\cos^4\mu + 2k_3e^{6i\mu} - k_3e^{5i\mu} + 16k_3e^{3i\mu}\cos^2\mu + 12e^{3i\mu}\delta m\omega_0 + 2k_3e^{4i\mu} - 6k_3e^{3i\mu} + 2k_3e^{2i\mu} - k_3e^{i\mu} + 2k_3\right) \tag{2.41}$$

$$c_{22} = -\frac{36i\gamma c_1m\omega_0 + icc_1\omega_0(12\cos 3\mu - 12) + ib_1k_2(-4\sin 3\mu + 4\sin 2\mu + 4\sin\mu)}{2\left(9m\omega_0^2 + 2k_1\cos 3\mu - 2k_1\right)} \tag{2.42}$$

$$e_2 = -\frac{b_1k_3(12\cos\mu + 6\cos 4\mu - 12\cos 3\mu - 6) + ic_1k_2(8\sin\mu - 8\sin 4\mu + 8\sin 3\mu)}{8\left(8m\omega_0^2 + k_1\cos 4\mu - k_1\right)} \tag{2.43}$$

$$f_2 = \frac{c_1k_3(3\cos 2\mu - 6\cos\mu + 6\cos 4\mu - 3\cos 5\mu - 3\cos 3\mu + 3)}{50m\omega_0^2 + 4k_1\cos 5\mu - 4k_1} \tag{2.44}$$

These amplitudes build upon the higher harmonic content introduced at the 1st-order to describe more completely the multi-harmonic solutions that exist in this nonlinear media. As will be discussed in Section 5.3, this higher-order solution, when added to the 1st and 0th-order solutions, propagates more invariantly, *i.e.* with less growth and decay in its spectral content.

After substituting the results from Eqs. (2.18), (2.26), and (2.34) into Eq. (2.12), the solution for x_j is now known up to $O(\varepsilon^3)$.

2.4 Higher-Order Multiple Scales Analysis: Diatomic Chain

Next, the MMS is developed for the diatomic chain. As with the monatomic chain, higher-order results reveal the magnitudes of the spatially and temporally invariant harmonics induced by the quadratic and cubic nonlinearities as well as amplitude and phase evolution equations utilized in the stability and dispersion shift analyses. It is again assumed that there are multiple time scales at which the system evolves and a series expansion of the solution is assumed

$$\underline{x}_j = \underline{x}_j^{(0)} + \varepsilon \underline{x}_j^{(1)} + \varepsilon^2 \underline{x}_j^{(2)} + \cdots + \varepsilon^n \underline{x}_j^{(n)} \tag{2.45}$$

where $\underline{x}_j^{(n)}$ denotes the n^{th} order solution vector

$$\underline{x}_j^{(n)} = \begin{bmatrix} x_a^{(n)}(j,t) \\ x_b^{(n)}(j,t) \end{bmatrix} \tag{2.46}$$

Collecting matching orders of ε in Eq. (2.2) yields $n+1$ vector equations. The first 2 are presented here

ε^0: $$M D_0^2 \underline{x}_j^{(0)} + \sum_{l=j-1}^{j+1} K_l \underline{x}_l^{(0)} = \underline{0} \tag{2.47}$$

ε^1:
$$MD_0^2\underline{x}_j^{(1)} + \sum_{j-1,j,j+1} K_l\underline{x}_l^{(1)} = -2MD_0D_1\underline{x}_j^{(0)} + \underline{f}_{damping,1} + \underline{f}_{quadratic,1} + \underline{f}_{cubic,1} \quad (2.48)$$

$$\underline{f}_{damping,1} = \begin{bmatrix} cD_0\left(x_b^{(0)}(j,t) - x_a^{(0)}(j,t)\right) + cD_0(x_b^{(0)}(j-1,t) - x_a^{(0)}(j,t)) \\ cD_0(x_a^{(0)}(j+1,t) - x_b^{(0)}(j,t)) + cD_0(x_a^{(0)}(j,t) - x_b^{(0)}(j,t)) \end{bmatrix} \quad (2.49)$$

$$\underline{f}_{quadratic,1} = \begin{bmatrix} k_2\left(x_b^{(0)}(j,t) - x_a^{(0)}(j,t)\right)^2 - k_2\left(x_b^{(0)}(j-1,t) - x_a^{(0)}(j,t)\right)^2 \\ k_2\left(x_a^{(0)}(j+1,t) - x_b^{(0)}(j,t)\right)^2 - k_2\left(x_a^{(0)}(j,t) - x_b^{(0)}(j,t)\right)^2 \end{bmatrix} \quad (2.50)$$

$$\underline{f}_{cubic,1} = \begin{bmatrix} k_3\left(x_b^{(0)}(j,t) - x_a^{(0)}(j,t)\right)^3 + k_3\left(x_b^{(0)}(j-1,t) - x_a^{(0)}(j,t)\right)^3 \\ k_3\left(x_a^{(0)}(j+1,t) - x_b^{(0)}(j,t)\right)^3 + k_3\left(x_a^{(0)}(j,t) - x_b^{(0)}(j,t)\right)^3 \end{bmatrix} \quad (2.51)$$

By inspection of Eq. (2.47), the 0th-order solution takes the Bloch form

$$\underline{x}_j^{(0)} = \frac{1}{2}A\,\underline{\phi}e^{i\omega_0 T_0}e^{-i\mu j} + c.c. \quad (2.52)$$

where A denotes the complex amplitude and $\underline{\phi}$ a wave mode shape.

Substituting Eq. (2.52) into Eq. (2.47) leads to an eigenvalue problem for two wave modes and their dispersion relationship $\omega_0(\mu)$. There are two independent solutions, corresponding to the acoustic and optical branches

$$\underline{\phi_{ac}} = \begin{bmatrix} \frac{(1+e^{i\mu})m_b}{m_b - m_a + \sqrt{m_a^2 + m_b^2 + 2m_a m_b\cos\mu}} \\ 1 \end{bmatrix} \quad (2.53)$$

$$\underline{\phi_{opt}} = \begin{bmatrix} 1 \\ \frac{m_a - m_b + \sqrt{m_a^2 + m_b^2 + 2m_a m_b\cos\mu}}{-(1+e^{i\mu})m_b} \end{bmatrix} \quad (2.54)$$

$$\omega_{0,ac} = \sqrt{\frac{k_1(m_b+m_a)}{m_a m_b} - \frac{k_1}{2}\sqrt{\frac{4m_b^2+4m_a^2+8m_a m_b\cos\mu}{m_a^2 m_b^2}}} \quad (2.55)$$

$$\omega_{0,opt} = \sqrt{\frac{k_1(m_b+m_a)}{m_a m_b} + \frac{k_1}{2}\sqrt{\frac{4m_b^2+4m_a^2+8m_a m_b\cos\mu}{m_a^2 m_b^2}}} \quad (2.56)$$

As with the monatomic chain, these 0^{th}-order dispersion relationships completely characterize the linear, undamped chain ($\varepsilon = 0$). Higher-order results add amplitude-dependent corrections to this relationship due to the nonlinearities.

It is worth noting that at $\mu = \pi$ when $m_b > m_a$, the optical mode shape simplifies from an indeterminate form to $\begin{bmatrix}1\\0\end{bmatrix}$ through application of L'Hopital's rule.

The known form of $\underline{x}_j^{(0)}$ is then substituted into Eq. (2.48). Projecting the secular terms against the Hermitian conjugate of the corresponding mode shape leads to evolution expressions for $D_1\alpha$ and $D_1\beta$

$$D_1\alpha = -\gamma_d\alpha \tag{2.57}$$

$$D_1\beta = \delta_d\alpha^2 \tag{2.58}$$

where

$$\gamma_d = \gamma_d\left(\mu, c, \underline{\phi_a}, m_a, m_b\right) \tag{2.59}$$

$$\delta_d = \delta_d\left(\mu, k_3, \underline{\phi_a}, \underline{\phi_b}, m_a, m_b, \omega_0\right) \tag{2.60}$$

The functional dependence only is provided although complete expressions can be found in a straight-forward manner using a symbolic manipulator. Such dependence is significant because of arguments made about the influence of different chain parameters on dispersion shifts and stability in Sections 5.1 and 5.3, respectively.

A particular solution for $\underline{x}_j^{(1)}$ can be found using the form

$$\underline{x}_j^{(1)} = \frac{1}{2}\underline{B_1}e^{2i\omega_0 T_0}e^{-2i\mu j} + \frac{1}{2}\underline{C_1}e^{3i\omega_0 T_0}e^{-3i\mu j} + c.c. \tag{2.61}$$

where the vectors $\underline{B_1}$ and $\underline{C_1}$ are found using the method of undetermined coefficients.

$$\underline{B_1} = \begin{bmatrix} b_{1,a}A^2 \\ b_{1,b}A^2 \end{bmatrix} \tag{2.62}$$

$$\underline{C_1} = \begin{bmatrix} c_{1,a}A^3 \\ c_{1,b}A^3 \end{bmatrix} \tag{2.63}$$

where

$$b_{1,a} = b_{1,a}\left(\mu, m_a, m_b, k_1, k_2, \underline{\phi_a}, \underline{\phi_b}, \omega_0\right) \tag{2.64}$$

$$b_{1,b} = b_{1,b}\left(\mu, m_a, m_b, k_1, k_2, \underline{\phi_a}, \underline{\phi_b}, \omega_0\right) \tag{2.65}$$

$$c_{1,a} = c_{1,a}\left(\mu, m_a, m_b, k_1, k_3, \underline{\phi_a}, \underline{\phi_b}, \omega_0\right) \tag{2.66}$$

$$c_{1,b} = c_{1,b}\left(\mu, m_a, m_b, k_1, k_3, \underline{\phi_a}, \underline{\phi_b}, \omega_0\right) \tag{2.67}$$

These amplitudes detail how much 2nd and 3rd harmonics arise due to the quadratic and cubic nonlinearities, respectively, and will be shown to make up an invariant waveform.

Note that this solution may not exist very close to μ values associated with internal resonance – *i.e.*, where $(2\omega_0, 2\mu)$ or $(3\omega_0, 3\mu)$ satisfy the 0th-order dispersion relationship in Eq. (2.55) or (2.56), inducing a resonant response. For these cases, the particular solution becomes unbounded and must be removed using an additional (*e.g.*, detuning) parameter as is discussed in Chapter 4.

Reapplying the procedure on the 2nd-order yields evolution equations for α and β of the following form

$$D_2\alpha = D_2\alpha\left(\alpha, \mu, m_a, m_b, k_2, k_3, c, \gamma_d, \delta_d, \underline{\phi_a}, b_{1,a}, b_{1,b}, c_{1,a}, c_{1,b}, \omega_0\right) \tag{2.68}$$

$$D_2\beta = D_2\beta\left(\alpha, \mu, m_a, m_b, k_2, k_3, c, \gamma_d, \delta_d, \underline{\phi_a}, b_{1,a}, b_{1,b}, c_{1,a}, c_{1,b}, \omega_0\right) \tag{2.69}$$

The second-order particular solution then takes the form

$$\underline{x}_j^{(2)} = \frac{1}{2}\underline{B_2}e^{2i\omega_0 T_0}e^{-2i\mu j} + \frac{1}{2}\underline{C_2}e^{3i\omega_0 T_0}e^{-3i\mu j} + \frac{1}{2}\underline{E_2}e^{4i\omega_0 T_0}e^{-4i\mu j}$$

$$+\frac{1}{2}\underline{F_2}e^{5i\omega_0 T_0}e^{-5i\mu j} + c.c \tag{2.70}$$

where the vectors $\underline{B_2}$, $\underline{C_2}$, $\underline{E_2}$, and $\underline{F_2}$ can be found using the method of undetermined coefficients.

As with the monatomic chain, 2nd-order analysis adds to the spectral content at the 2nd and 3rd harmonics and introduces new spectral content at the 4th and 5th harmonics further defining the multi-harmonic invariant wave.

It is noted here that the diatomic results can recover the monatomic results by setting $m_a = m_b = m$ and replacing μ with $\mu/2$.

2.5 Numerical Simulations

This section briefly presents the procedure for numerically injecting perturbation-based waveforms into numerical simulations of Eqs. (2.1) and (2.2), forming the foundation to the numerical results presented in the remaining sections. They rely on initial conditions associated with the multiple scales solutions, assigning the order of terms at which to truncate the multi-harmonic wave solution. In doing so, this procedure allows for measurement of the validity of the MMS solutions since waveforms existing in the medium should persist after they are initially set, as detailed in Section 5.3. This section also introduces dimensionless parameters that combine the effects of nonlinear stiffness and

wave amplitude into convenient expressions useful for simulating chains and interpreting results.

Displacement and velocity initial conditions required to numerically integrate Eqs. (2.1) and (2.2) are found using the series solutions in Eqs. (2.12) and (2.45), respectively. Thus, $x(j,0) = x_j\big|_{t=0}$ and $\dot{x}(j,0) = \frac{d}{dt}\left(x_j\right)\Big|_{t=0}$ where $x_j\big|_{t=0}$ is truncated to a desired order n and $\frac{d}{dt}(\quad)$ must correspond to the *total time derivative* defined in Eq. (2.10), truncated at the same order n.

By carrying the expansions out and truncating, 1st and 2nd-order initial conditions can be determined. To emulate an infinite domain, the number of unit cells N should be sufficiently large—generally on the order of 1800 to 2000—such that $\mu N \gg 1$. Within this domain, analysis of a chain's behavior remains at a central region—usually the middle 800 to 1000 unit cells—such that reflection from the boundaries does not propagate to the region within the time scale of the simulation. In these studies, either fixed-fixed or free-free boundary conditions are used.

A given simulation is characterized by the following dimensionless parameters introduced here:

$$\tau = \omega_0 t, \Pi_1 = \frac{\varepsilon c \omega_0}{k_1}, \Pi_2 = \frac{\varepsilon k_2 \alpha_0}{k_1}, \Pi_3 = \frac{\varepsilon k_3 \alpha_0^2}{k_1}, \Pi_4 = \frac{m_b}{m_a} \tag{2.71}$$

where $\Pi_1, \Pi_2,$ and Π_3 can be interpreted as relative strengths of the damping, quadratic nonlinearity, and cubic nonlinearity, respectively, and Π_4, a mass ratio, applies only to the diatomic chain. The parameters Π_2 and Π_3 are particularly useful since they combine the effects of the nonlinear stiffness and wave amplitude into single parameters, both of which

affect the magnitude of dispersion shifts. Note, however, that Π_2 and Π_3 are proportional to—not exact measurements of—the strength of the quadratic and cubic nonlinearities, respectively. That is to say, these parameters are not an exact ratio of spring forces because α_0 is the 0^{th}-order wave amplitude and not necessarily the spring stretch, $x_{j+1} - x_j$. Thus, $\Pi_2, \Pi_3 < 0.1$ are *conservative bounds* on the MMS applicability (weak nonlinearity assumption). In general, the parameters in Eq. (2.71) facilitate parameter definition as outlined in the following procedure outline.

These steps were carried out for each simulation:

- Specify Π_1, Π_2, and Π_3 values. Set m and k_1 equal to 1, without loss of generality. For diatomic simulations, prescribe m_a, m_b values (based on a desired Π_4 value) as well as a branch of excitation (acoustic or optical).
- Specify a propagation constant μ restricted to the 1st Irreducible Brillouin Zone. A corresponding ω_0 value can then be assigned to it according to Eqs. (2.20), (2.55), or (2.56). Note that this is not guaranteed to be the ensuing temporal frequency of the chain but merely a parameter used to evaluate initial conditions. For diatomic simulations, $\underline{\phi_{ac}}$ or $\underline{\phi_{opt}}$ can now be evaluated, depending on the branch of excitation that was selected.
- Set k_3 equal to 1 (hardening) or -1 (softening) and then solve for $c, k_2,$ and α_0 values which satisfy the desired Π_1, Π_2, and Π_3 values, respectively.
- Define the number of unit cells to emulate an infinite system (Usually $N = 1800$ or 2000 such that $\mu N \gg 1$)

- Assign an initial displacement and velocity distribution to the chain according to Eqs. (2.12) or (2.45) evaluated at time $t = 0$ and truncated at a specified order n ($n = 0,1,$ or 2). The ε parameter is chosen to be small (*e.g.*, $\varepsilon = 0.1$).
- Set two boundary conditions. For each end, use either fixed—zero displacement—or free—zero force.
- Simulate the equations of motion by numerically integrating Eqs. (2.1) or (2.2) using Matlab's ODE45 routine.
- For analyzing the results, study only a fixed middle portion of the chain (*e.g.* the middle 800 to 1000 unit cells) such that boundary effects can be ignored. Visually inspect the results to make sure that boundary effects have not propagated into this central region during the time range of interest.

2.6 Dispersion Shifts

This section details amplitude-dependent dispersion shifts arising from both cubic and quadratic nonlinearities, a finding useful for device design [22]. It will be shown that the MMS analysis uncovers dispersion shifts to the 0^{th}-order ($\varepsilon = 0$, linear undamped) relationship. The measurement of these predicted shifts in numerical simulations affirms the validity of the MMS results at the 1^{st} and 2^{nd}-orders and demonstrates that quadratic nonlinearities govern shifts at higher-orders only, *i.e.* an effect not captured by a 1^{st}-order analysis.

At the 0^{th} order, the temporal frequency ω_0 relates to the spatial frequency μ through dispersion relationships represented by Eqs. (2.20), (2.55), and (2.56). Figure 2-3 displays

these 0^{th}-order expressions for the monatomic and diatomic chains. Note that the monatomic chain has a cutoff for $\omega_0 > 2\sqrt{\frac{k_1}{m}}$, and the diatomic chain exhibits a bandgap.

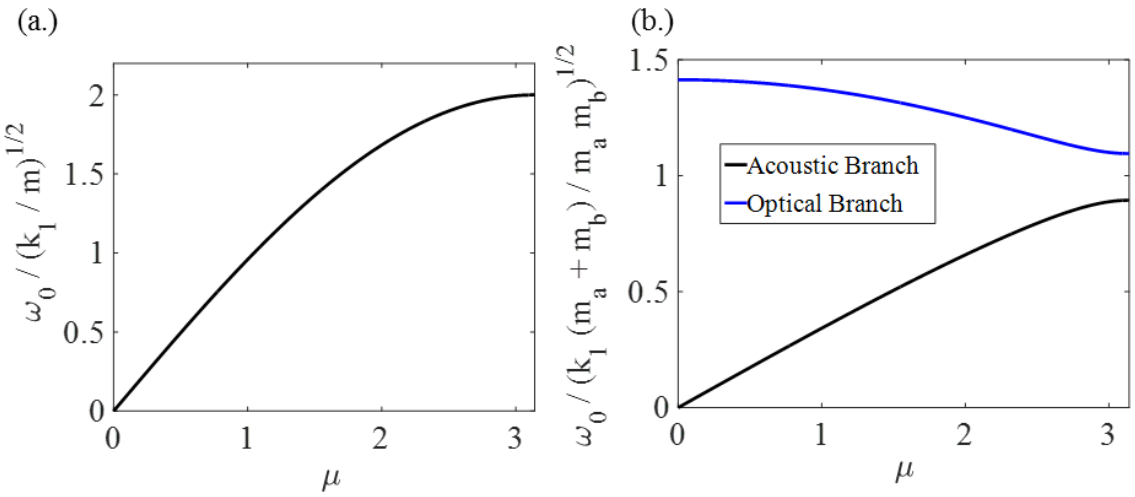

Figure 2-3. 0^{th}-order dispersion relationship for the monatomic (a.) and diatomic (b.) chains.

Closed-form, amplitude-dependent dispersion shifts will now be derived from the MMS results. For undamped chains, $D_1\alpha = D_2\alpha = 0$. Thus, the wave amplitude is constant ($\alpha = \alpha_0$). For the monatomic chain, the evolution equations for phase, Eqs. (2.23) and (2.30), reduce to

$$D_1\beta = \delta\alpha_0^2, \quad c = 0 \tag{2.72}$$

$$D_2\beta = \mathrm{X}\alpha_0^4 + \Upsilon\alpha_0^2 + \mathrm{Z}, \quad c = 0 \tag{2.73}$$

Similar expressions result for the diatomic chain by replacing δ in Eq. (2.72) with δ_d from Eq. (2.60), and replacing the left side of Eq. (2.73) with the expression in Eq. (2.69) evaluated at $\alpha = \alpha_0$.

Reconstituting the phase expression using $D_1\beta$ and $D_2\beta$ in Eq. (2.10), and returning to the original time scale, leads to the wave's temporal phase behavior

$$\dot{\beta} = \varepsilon D_1\beta + \varepsilon^2 D_2\beta = \varepsilon\delta\alpha_0^2 + \varepsilon^2(\mathrm{X}\alpha_0^4 + \Upsilon\alpha_0^2 + \mathrm{Z}) \tag{2.74}$$

for the monatomic chain; a similar expression occurs for the diatomic chain.

Since $D_1\beta$ and $D_2\beta$ do not explicitly depend on time, they can be interpreted as corrections to the frequency at their respective order, yielding 1st and 2nd-order-accurate corrections

$$\omega_{O(\varepsilon^1)} = \omega_0 + \varepsilon D_1\beta \tag{2.75}$$

$$\omega_{O(\varepsilon^2)} = \omega_0 + \varepsilon D_1\beta + \varepsilon^2 D_2\beta \tag{2.76}$$

Inspection of Eqs. (2.72)-(2.73) and (2.75)-(2.76) shows that the quadratic nonlinearity does not shift the frequency until the 2nd-order correction is included, implying a small influence as compared to the cubic nonlinearity, which appears at both the 1st and 2nd-orders. For positive coefficients k_2 and k_3, the shifts further increase the frequency (for a given μ) with increasing wave amplitude α_0.

For both monatomic and diatomic chains, numerical studies of undamped systems confirm the theoretical shifts as documented in Figure 2-4. For different μ values prescribed in simulation initial conditions, the 1st and 2nd-order MMS-predicted temporal frequencies are compared to the measured dominant temporal frequency of a central unit cell in the chain. Recall that assigning a μ value does not guarantee the ensuing temporal frequency but rather is used to define all initial parameters. Thus, the simulations given 1st and 2nd-order initial conditions ($n = 1, 2$) were measured to have dominant temporal frequencies close to the 1st and 2nd-order perturbation corrections ($\omega_{O(\varepsilon^1)}$, $\omega_{O(\varepsilon^2)}$), respectively. Theoretical

expressions for the 0^{th}-order, un-shifted temporal frequency, ω_0 (Eqs. (2.20)—monatomic, Eqs. (2.55) and (2.56)—diatomic) are also plotted as references to visualize the shifts that occur. For each simulation, the dominant temporal frequency is computed by taking an FFT of the time history of a central mass in the chain. To collect accurate data, temporal sampling frequencies are many integer multiple times higher than the expected shifted frequency, *e.g.* $f_{sampling} = 600\ {}^{\omega_{O(\varepsilon^1)}}/_{2\pi}$ or $f_{sampling} = 600\ {}^{\omega_{O(\varepsilon^2)}}/_{2\pi}$.

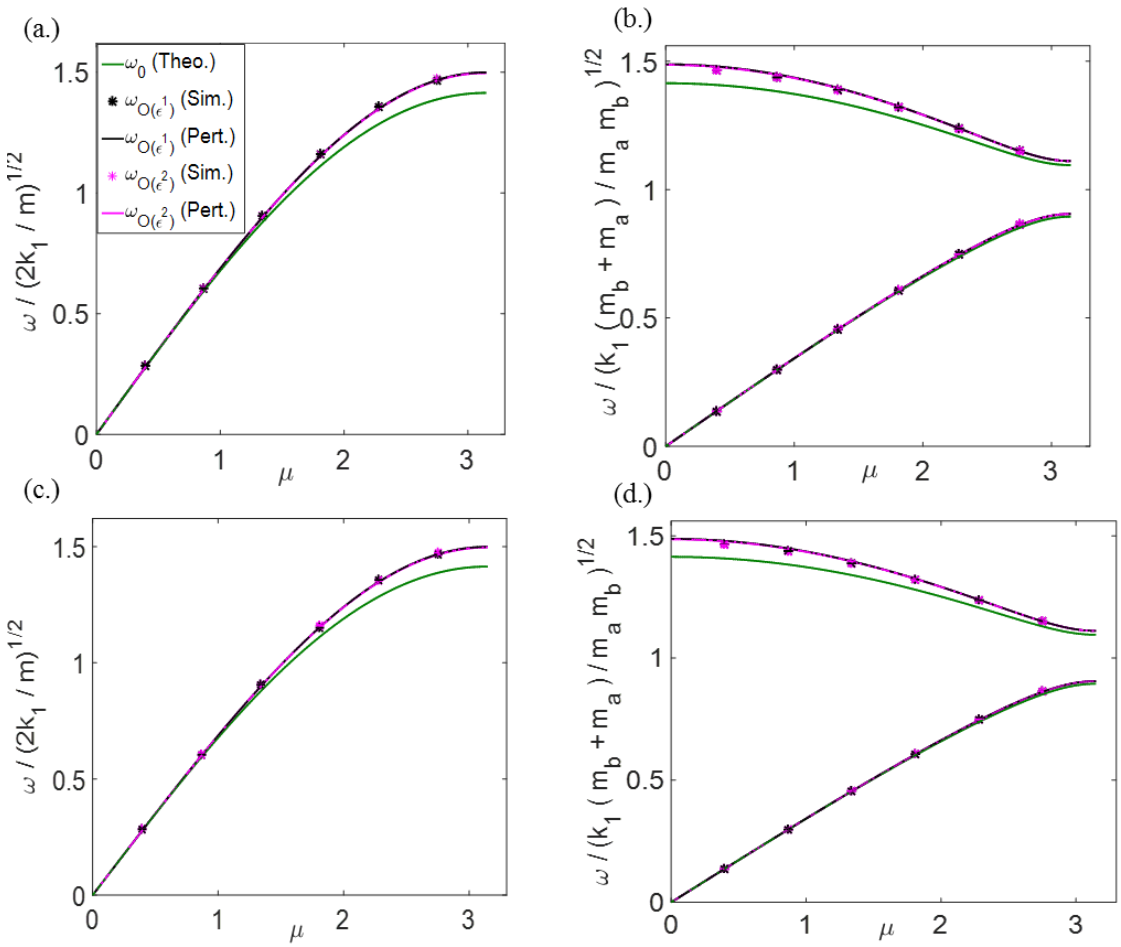

Figure 2-4. 1st and 2nd-order dispersion shifts in the monatomic and diatomic chains. Monatomic: $\Pi_1 = 0, \Pi_2 = 0.04$ (a), $\Pi_2 = 0$ (b), $\Pi_3 = 0.04$, Diatomic: $\Pi_1 = 0, \Pi_2 = 0.04$ (c), $\Pi_2 = 0$ (d), $\Pi_3 = 0.04, \Pi_4 = 1.5$.

Inspection of the bottom two subplots in Figure 2-4 reveals that k_2 bears little to no effect on the 1st-order dispersion correction. As Π_2 changes from 0.04 to 0, which corresponds to no quadratic nonlinearity present, the 1st-order perturbation and simulation results change by an average amount of 0.043%. For lightly damped chains $D_1\alpha, D_2\alpha \neq 0$, corrections can be interpreted as instantaneous dispersion shifts since the amplitude decays slowly.

2.7 Stability Considerations

The stability of wave propagation is of primary concern for designing devices informed by these discrete systems. Herein, instability is defined as any qualitative shift from the multi-harmonic plane wave solution predicted by the MMS. Thus, it is important to characterize the types of instabilities that take place in these systems and the conditions at which they occur. An analytical stability analysis is first presented to see if the evolution equations for amplitude reveal any information on stability loss. Informed by this analysis, numerical studies are carried out to determine the onset of instabilities.

2.7.1 Local Stability Analysis

Because it is a critical parameter that determines the strength of the nonlinearities in the system, amplitude is chosen to be analyzed to assess the stability of the wave. It will be shown that the 1st-order results reveal only a damping induced decay of amplitude (stable solution) whereas the inclusion of 2nd-order results reveal a possible growth in amplitude (unstable solution). Though it is outside the conservative bounds of the MMS solution, the unstable solution provides a foundation to the numerical stability studies presented in Section 5.2.2.

Applying Eq. (2.10) to wave amplitude α and recalling that $D_0\alpha = 0$ leads to its reconstituted evolution equation,

$$\dot{\alpha} = \varepsilon D_1\alpha + \varepsilon^2 D_2\alpha \tag{2.77}$$

which suggests the existence of fixed points, or α^* such that $\dot{\alpha} = 0$. These fixed points are found from

$$\dot{\alpha}|_{\alpha^*} = 0 \tag{2.78}$$

A local stability analysis can then be performed near each fixed point by introducing small perturbations from α^*. The result of doing so is that the stability of each fixed points depends on the sign of λ arising from

$$\frac{d}{d\alpha}\dot{\alpha}|_{\alpha^*} \equiv \lambda \tag{2.79}$$

where $\lambda > 0$ yields an unstable fixed point, $\lambda < 0$ a stable fixed point, and $\lambda = 0$ is neutrally stable. Thus, the fixed points for the monatomic chain can be readily found by substituting in the values from Eqs. (2.22) and (2.29) into Eqs. (2.77) and (2.78)

$$\alpha^* = 0, \pm\sqrt{\frac{\omega_0}{\varepsilon\delta}} \tag{2.80}$$

The fixed point $\alpha^* = \pm\sqrt{\frac{\omega_0}{\varepsilon\delta}}$ exists only when $\delta > 0$ (cubic hardening) since α is assumed to be strictly real. Application of Eq. (2.79) yields

$$\lambda|_{\alpha^*=0} = -\varepsilon\gamma \tag{2.81}$$

$$\lambda|_{\alpha^*=\pm\sqrt{\frac{\omega_0}{\varepsilon\delta}}} = 2\varepsilon\gamma \tag{2.82}$$

The fixed point $\alpha^* = 0$ is of the highest relevancy since (1) amplitudes near it are small-enough to satisfy the conservative weakly nonlinear ansatz, $\Pi_2, \Pi_3 < 0.1$; (2) this is the fixed point to which asymptotically-predicted plane waves will be attracted to in the presence of damping, therefore its stability establishes plane wave stability of interest herein. Since, $\lambda|_{\alpha^*=0} < 0$ for damped chains ($c > 0$), the fixed point $\alpha^* = 0$ is stable. Note that $\alpha^* = 0$ is the only fixed point informed by a 1st-order analysis as $\alpha^* = \pm\sqrt{\frac{\omega_0}{\varepsilon\delta}}$ originates from 2nd-order terms. Also note that the presence of damping enables the

stability of the fixed points to be classified: undamped chains yield $\lambda|_{\alpha^*=0} = \lambda|_{\alpha^*=\pm\sqrt{\frac{\omega_0}{\varepsilon\delta}}} = 0$, which is neutrally stable.

By similar arguments, since Eq. (2.82) is positive for damped chains ($c > 0$), the fixed point $\alpha^* = \pm\sqrt{\frac{\omega_0}{\varepsilon\delta}}$ is unstable. However, closer inspection of this fixed point reveals that it is at a large-enough amplitude that its accuracy cannot be expected. After substituting Eqs. (2.20) and (2.25) into the expression for α^*, a critical Π_3 value results dependent on only μ,

$$\Pi_{3,crit} = \frac{\varepsilon k_3 {\alpha^*}^2}{k_1} = \frac{8(1-\cos\mu)}{3(\cos 2\mu - 4\cos\mu + 3)} \tag{2.83}$$

Examining Eq. (2.83), the lowest value of $\Pi_{3,crit}$ in the first Brillouin zone, $0 \leq \mu \leq \pi$, is approximately 0.66, which is beyond the conservative weak nonlinearity ansatz used for MMS analysis. However, as evident in results presented in Section 5.2.2, the existence of such a fixed point is likely since large-amplitude plane waves are observed to grow unboundedly in numerical simulations.

The stability of the monatomic chain is summarized in Figure 2-5. As indicated, only initial wave amplitude, and not initial phase, determines the basins of attraction.

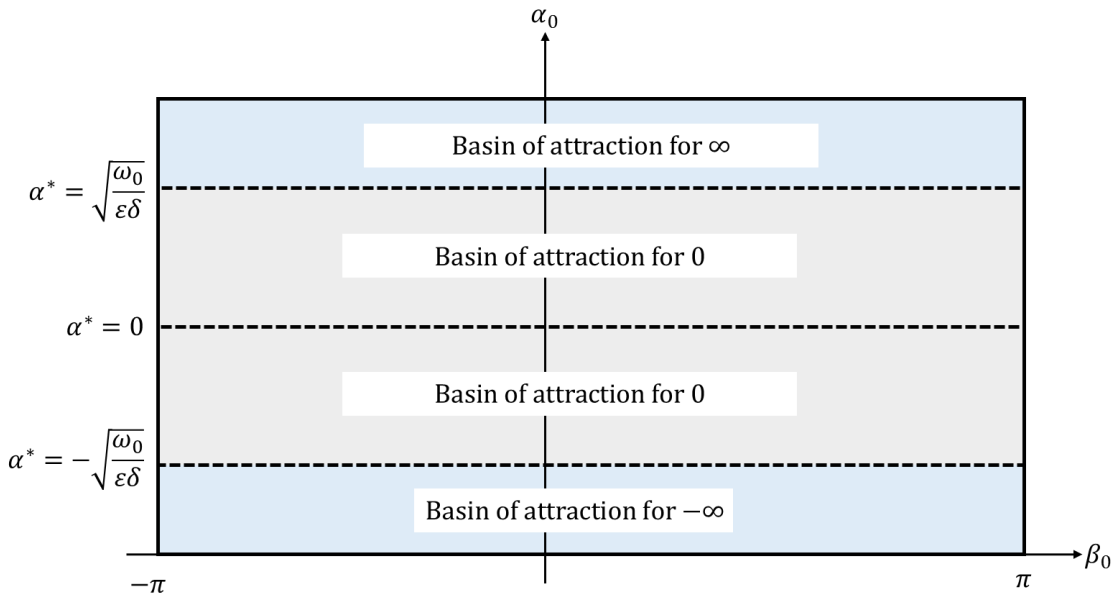

Figure 2-5. Fixed points and basins of attractions for the monatomic chain.

Stability of the diatomic chain can also be studied analytically. Its reconstituted evolution equation for α can be written as

$$\dot{\alpha} = P_1\alpha^5 + P_2\alpha^3 + P_3\alpha \tag{2.84}$$

where P_1, P_2, P_3 denote constants known from Eqs. (2.57) and (2.68). Fixed-points can be solved for by setting $\dot{\alpha} = 0$. Thus, a given system admits at most five fixed points; however, because α is assumed to be real, imaginary fixed points are ignored. Inspection of Eq. (2.84) indicates that

$$\alpha^* = 0, \pm\left[-\frac{P_2}{P_1} \pm \frac{1}{2}\sqrt{\frac{P_2^2}{P_1^2} - \frac{4P_3}{P_1}}\right]^{\frac{1}{2}} \tag{2.85}$$

where it is again emphasized that α^* must be strictly real. The stability of a given fixed point can be studied by examining the sign of each value of λ,

$$\lambda = 5P_1\alpha^{*4} + 3P_2\alpha^{*2} + P_3 \tag{2.86}$$

Results are similar to the monatomic chain. For $\alpha^* \neq 0$, many values of λ can be computed using the P_1, P_2, and P_3 values associated with a prescribed set of Π_1, Π_2, Π_3, and Π_4 values and branch. The fixed point $\alpha^* = 0$ is always stable for $c > 0$. Other fixed points are unstable but have corresponding Π_2 and Π_3 values never simultaneously less than 0.1. Therefore, they are of large-enough amplitude to not be of interest to plane waves predicted herein.

2.7.2 Numerical Stability Studies

This section details numerical studies that investigate stability beyond the applicable range of the MMS. It also confirms the general trends predicted by the local stability analysis, which is that at low amplitudes, multi-harmonic plane waves are stable, and at high amplitudes (or, equivalently, large nonlinearities) the plane wave solutions predicted may lose stability. Note that such a conclusion cannot be drawn from only 1st-order information. These studies quantify the stability of the predicted waveforms over a wide range of Π_2 and Π_3 values for a given value of Π_1 and, if diatomic, Π_4. Simulations begin with the initial conditions corresponding to the series solutions in Eqs. (2.12) and (2.45) for the monatomic and diatomic chain, respectively. An unstable response is defined to be any deviation from the nature of the plane wave propagation predicted by the perturbation analysis. Thus, such studies aim to identify the stability limits of the MMS-predicted multi-harmonic solutions. Although different types of instability are observed, it is not the primary concern of this work to explore further the ensuing solutions.

One such type of instability that occurred in numerical simulations is characterized by a spreading of the wave's spectral content. Chains with large Π_3 values exhibit this behavior.

The spectral content of these waves initially contains integer multiples of ω_0 and μ, but following longer simulation times, the plane wave nature of the response breaks down into an assortment of incommensurate frequencies. Figure 2-6 depicts this phenomenon.

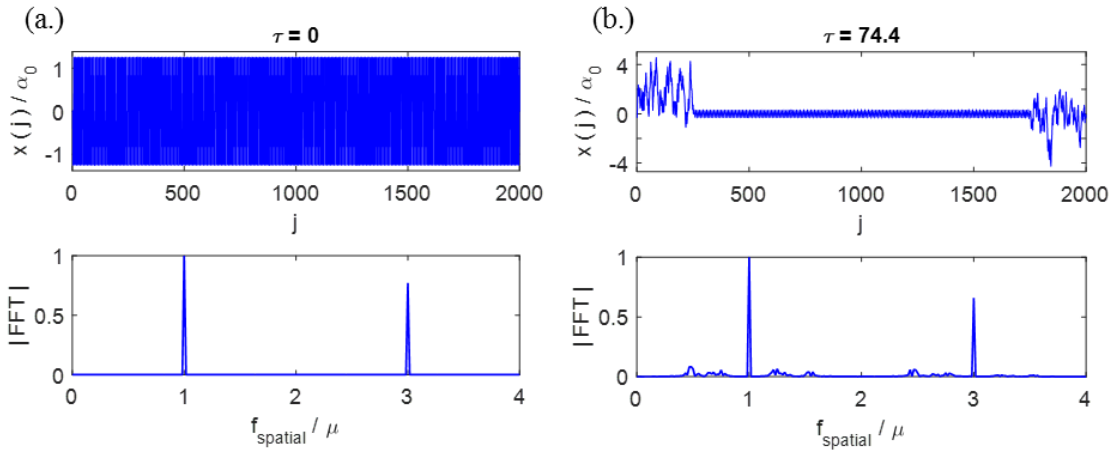

Figure 2-6. An example chain exhibiting a breakdown in spectral content. The initial plane wave (a.) is unstable such that at a later time (b.) its spectral content spreads across incommensurate frequencies: $\Pi_1 = 0.01, \Pi_2 = 0, \Pi_3 = 3.7$, 2nd-order IC's .

The other type of instability observed in simulations is characterized by an unbounded growth in the wave's amplitude. Chains with large positive or large negative Π_2 values, as well as chains with large negative Π_3 values, exhibit this behavior. The initial amplitude is unstable such that, as time progresses, the wave propagates with increasingly larger amplitudes. Notes that this is similar to the exponential growth in amplitude instability presented in [49]. Figure 2-7 depicts this phenomenon. It is noted that all oscillations cease when the amplitude starts to grow.

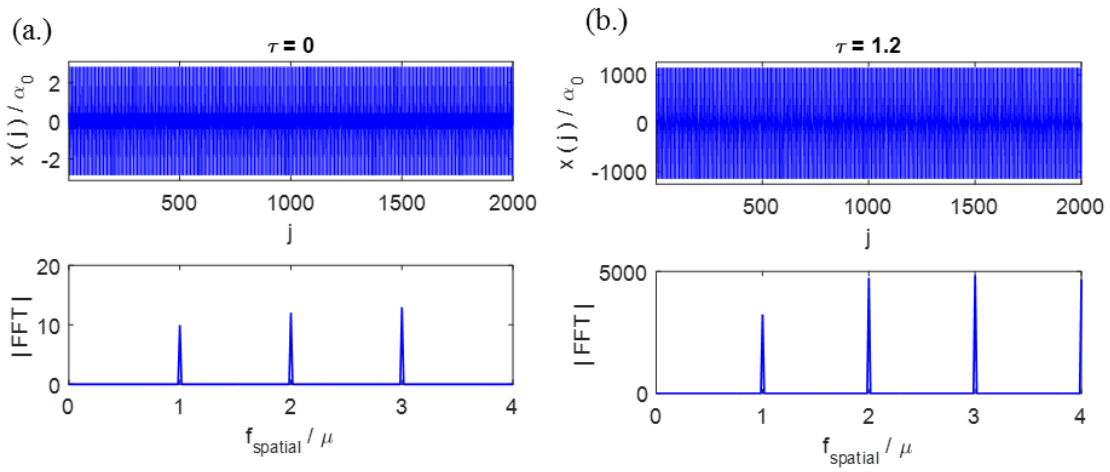

Figure 2-7. An example chain exhibiting a growth in amplitude. The initial plane wave (a.) is unstable such that at a later time (b.) there is an unbounded growth in amplitude: $\boldsymbol{\Pi_1 = 0.01, \Pi_2 = 1, \Pi_3 = 0}$, 2nd-order IC's.

For automating instability detection in simulated results, criteria are developed which determine when one of the two types occur, thus signifying a loss of stability, or deviation from the multi-harmonic plane wave solution. When either one of the two instability types occur, the parameter set is considered "unstable", without distinguishing exactly which type of instability developed. Thus, an instability occurs when a set number of peaks in a spatial FFT exceeds a certain fraction of the maximum peak at that instant or when the instantaneous amplitude grows to a certain multiple of the simulation's original amplitude. A time limit is prescribed for simulations: if an instability does not arise within the prescribed time, or $\tau = 12(2\pi)$ for these simulations, the parameter set is considered stable. For the diatomic chain, instability criteria are applied to x_a and x_b separately.

Figure 2-8 presents the stability results for the monatomic chain as a function of Π_2 and Π_3. The parameters $\Pi_{2,crit}$ and $\Pi_{3,crit}$ are the values of Π_2 and Π_3, accurate to the nearest tenth, at which an unstable response is first observed when the other nonlinear Π-value is set to zero (*i.e.*, $\Pi_{2,crit}$ occurs when $\Pi_3 = 0$ and $\Pi_{3,crit}$ occurs when $\Pi_2 = 0$). Each plot

verifies the local stability analysis; namely, that plane waves characterized by small values of $\Pi_2/\Pi_{2,crit}$ and $\Pi_3/\Pi_{3,crit}$ are stable. Figure 2-9 presents similar stability results for the diatomic chain applied to x_a. Plots for the stability study of x_b depict similar trends and are given in Appendix A.

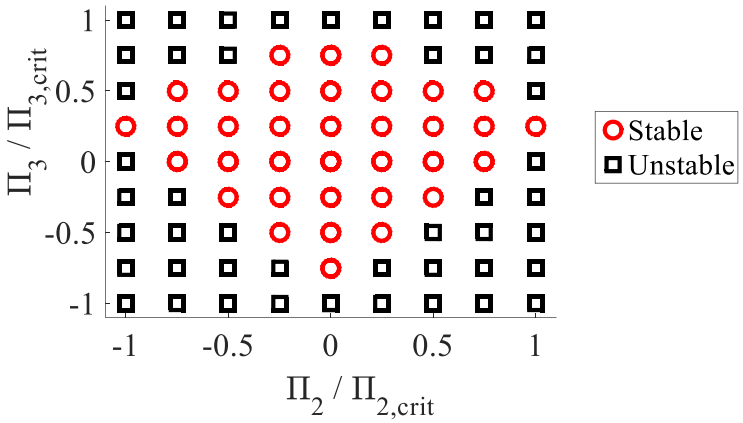

Figure 2-8. Monatomic Chain Stability Study: 2nd-order IC's, $\Pi_1 = 0.01, \mu = \frac{\pi}{4}$.

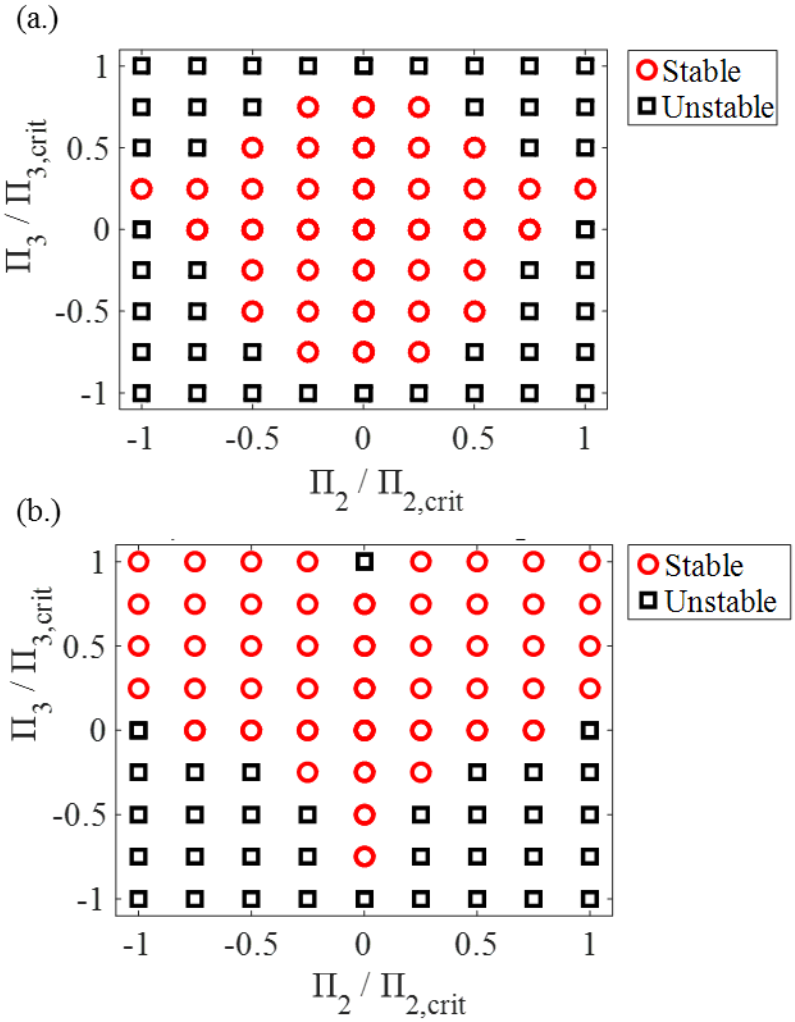

Figure 2-9. Diatomic Chain Stability Study: x_a, 2nd-order IC's, $\Pi_1 = 0.01, \Pi_4 = 1.5, \mu = \frac{\pi}{4}$, Acoustic (a.), Optical (b.).

For some chains simulated using free-free boundary conditions, a DC harmonic appears that causes the two masses in each unit cell to separate by a constant amount, in addition to their expected oscillation. The location of the center of mass remains unchanged, as expected to satisfy conservation of momentum. However, since the magnitude of this separation is generally small for the parameters being studied, such responses are considered stable.

It is also worth noting that loss of stability through the development of incommensurate frequencies takes-on a non-stationary nature as observed in numerical simulations. For example, if computing the spatial frequency content of a fixed region in space, unstable plane waves can feature different sets of incommensurate frequencies at different instances in time. This subtle behavior accentuates the unstable character of these waveforms but is not of primary interest to distinguishing between the preservation or loss of stability.

Although the amplitudes at which point stability is lost in the numerical simulations do not align with the nonzero fixed points predicted by multiple scales approach, the results of these numerical studies qualitatively confirm the findings. Wave amplitudes below a critical value decay over time towards zero due to the presence of damping. Above this critical amplitude value, the wave will become unstable by either growing unboundedly or decomposing its original multi-harmonic content into incommensurate frequencies.

2.8 Waveform Invariance

This section describes how higher-order MMS results converge to an invariant waveform, a finding that offers new insight for predicting and modeling the wave propagation in these weakly nonlinear discrete systems and further validation of the MMS approach. In the absence of damping, the presented perturbation approach does not distinguish between any two points in space, nor any two points in time. Thus, in the limit as the asymptotic expansions are taken to higher orders, and assuming convergent vis-à-vis divergent behavior, it can be hypothesized that the waveforms should propagate for all space and time without change – *i.e.*, they should be an invariant form akin to cnoidal waves studied in other contexts. It is worth noting that such an argument does not rely on a continuum approximation as in other studies [87-89]. Note that this is a very different perspective taken from other works carrying-out perturbation approaches in wave propagation problems ([90, 91]), which more conventionally analyze higher harmonic *generation* and/or the closely-related concept of phonon *generation* and *lifetimes*.

To test the invariant hypothesis, numerical integration of Eqs. (2.1) and (2.2) is carried out using the procedure presented in Section 4. Thus, plane waves corresponding to the asymptotic expansions in Eq. (2.12) and (2.45) truncated at different orders are injected into the simulated chains. During simulation, the spatial harmonic content of the waves, is quantified using FFTs at different instances in time to track the generation (or loss) of the initially prescribed harmonic content. As mentioned in Section 4, to emulate an infinite chain, analysis was restricted to a central region of the chain so that boundary effects could be ignored. According to the hypothesis, waves incorporating higher-order terms should exhibit measurably less variation, and hence propagate more invariantly. Only $\Pi_3 > 0$ chains were sampled since it was found while conducting the numerical stability studies in

Section 5.2.2 that negative Π_3 values become unstable at much lower magnitudes than positive ones.

For monatomic chains, a parameter that measures the spatial variance of a simulated waveform is proposed as

$$\sigma_p^{(n)} \equiv \frac{1}{L}\sum_{l=1}^{L}\left|1 - a_{l,p}\right| \tag{2.87}$$

where $a_{l,p}$ denotes the amplitude of the p^{th} harmonic at the l^{th} instant in time normalized by its initially prescribed value, L the number of time instances that make up the numerical solution, and n denotes the order of perturbation terms retained in Eq. (2.12). Since $\sigma_p^{(n)}$ measures variance, lower values of $\sigma_p^{(n)}$ indicate more invariant waveforms, and thus it is expected (if the hypothesis holds) that $\sigma_p^{(n)}$ decreases as n increases. Figure 2-10 verifies the expected reduction in variance for monatomic chains given 2nd versus 1st-order initial conditions – all values of (Π_2, Π_3) simulated experience decreases in variance. Because Figure 2-10 plots the normalized *reduction* in variance—$\sigma_p^{(1)} - \sigma_p^{(2)}/\sigma_{p,max}^{(1)}$ $(p = 2,3)$—a value of 1.0 indicates elimination of all variance using 2nd-order initial conditions, while a value of 0.0 indicates no variance reduction.

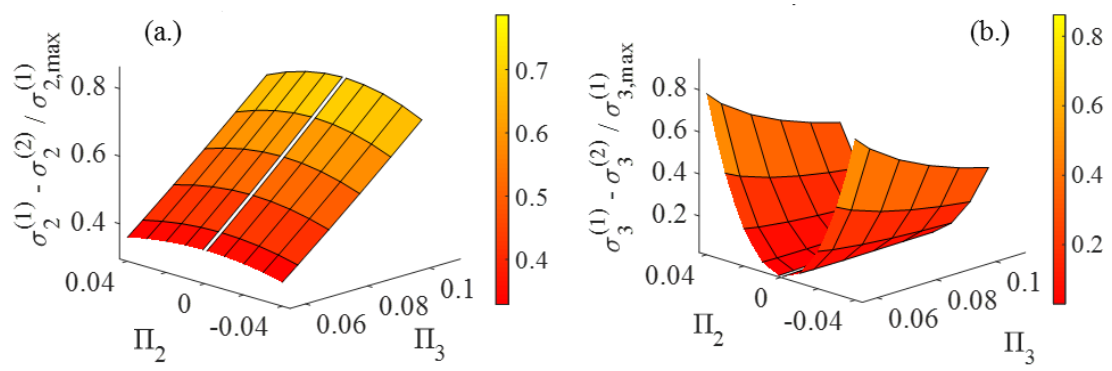

Figure 2-10. Reduction of variance of the 2nd (a.) and 3rd harmonics (b.), monatomic chain, $\boldsymbol{\mu = \frac{\pi}{4}, \Pi_1 = 0}$.

For diatomic chains, the variance parameter specializes to each degree of freedom: $\sigma_{p,a}^{(n)}$ and $\sigma_{p,b}^{(n)}$ for x_a and x_b, respectively. Similar numerical simulations are carried out and the 2nd and 3rd spatial harmonics are tracked over time for waves on the acoustic and optical branches. Figure 2-11 presents the variance results for x_a; Appendix A provides results for x_b. The trend in variance reduction is again present.

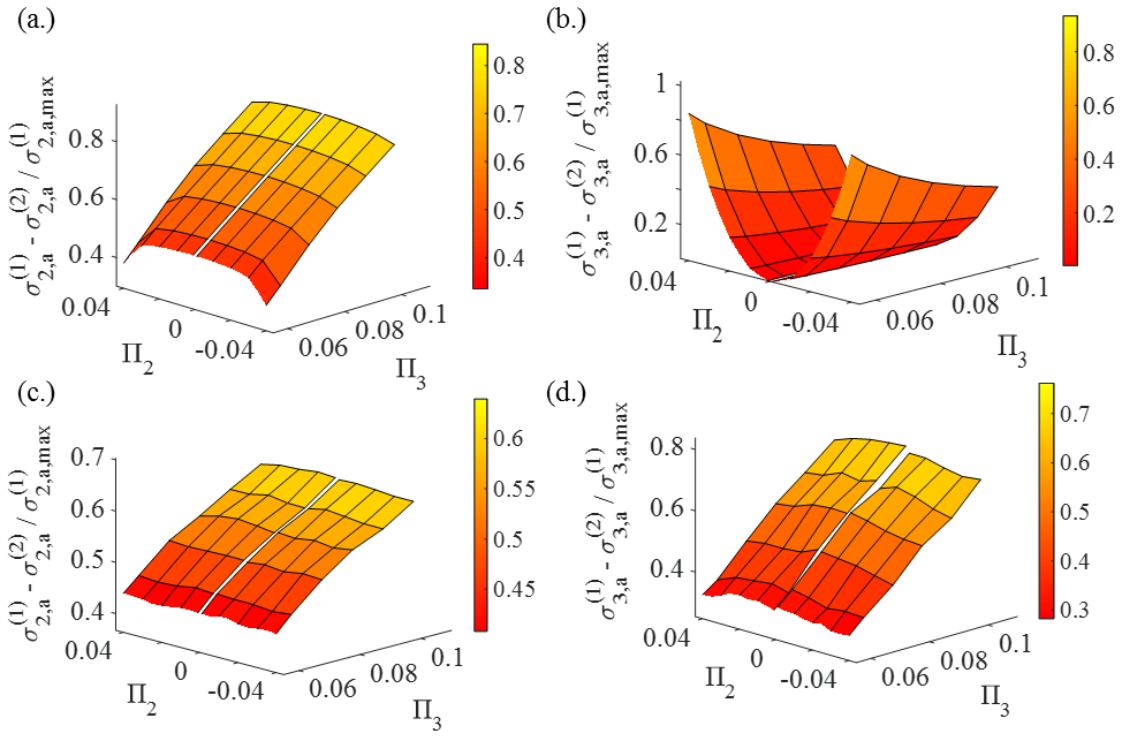

Figure 2-11. Reduction of variance in x_a of the diatomic chain: 2nd harmonic acoustic branch (a.), 3rd harmonic acoustic branch (b.), 2nd harmonic optical branch (c.), 3rd harmonic optical branch (d.). For (a.)-(d.), $\Pi_4 = 2, \mu = \frac{\pi}{4}, \Pi_1 = 0$.

Figure 2-10 and Figure 2-11 also show that an increase in the magnitude of Π_2 leads to a large variance reduction in the 3rd harmonic, and conversely, an increase in Π_3 leads to a large variance reduction of the 2nd harmonic. This counter-intuitive crossing effect can be understood by close examination of the 2nd-order results in Eqs. (2.39) - (2.42) for the monatomic chain (the same argument can be made for the diatomic chain). There, k_2 influences the particular solution governing the 3rd harmonic, and k_3 influences the particular solution governing the 2nd harmonic. Note that, the 1st-order solution does not contain such a crossing effect and thus injected waveforms based solely on it will not be sufficient for preventing an exchange of energy between different harmonics. In contrast, because the presence of the crossing terms in 2nd-order injected waves keeps spectral

energy where it is initially assigned, the crossing effect becomes necessary for increasing invariance. This is yet another example of the richness in system behavior uncovered by higher-order perturbation analysis.

2.9 Concluding Remarks

A higher-order multiple scales analysis demonstrates that plane waves in weakly nonlinear chains possess amplitude-dependent stability and invariant multi-harmonic solutions. Nontrivial fixed points identify that sufficiently high amplitude wave propagation is unstable as opposed to low amplitude wave propagation which is inherently stable (for media with weak dissipation) or neutrally stable (for lossless media). Higher-order multiple scales also predicts multi-harmonic plane wave solutions that retain their spectral distribution over the course of wave propagation, circumventing dispersion. Both findings of stability and waveform invariance are validated through direct numerical simulation of the lattice equations of motion.

CHAPTER 3. AMPLITUDE AND DIRECTION-DEPENDENT STABILITY AND WAVEFORM INVARIANCE IN TWO-DIMENSIONAL NONLINEAR PERIODIC STRUCTURES

3.1 Overview

Informed by the findings of stability and invariance in 1-D periodic systems, this chapter extends the higher-order perturbation analysis to two-dimensional (2-D) weakly nonlinear lattices. In addition to affirming their amplitude-dependence, such results reveal direction-dependence in both the stability characteristics and invariant solutions. Counterintuitively, this directional behavior manifests in lattices with symmetrical stiffness terms. The new findings of direction-dependence of stability and waveform invariance have implications for mechanical data encryption and damage detection which are briefly discussed.

Compared to their one-dimensional counterpart, two-dimensional periodic structures filter directions in addition to frequencies of propagation. Langley *et al.* demonstrated the relationship between the presence of caustics and spatial "dead-regions" in an infinite 2-D periodic system [92, 93]. Laude *et al.* [94] and Kulpe *et al.* [95, 96] studied plane waves incident on 2-D and 3-D periodic systems, uncovering direction-dependent "deaf Bloch modes," which are antisymmetric with respect to a symmetry axis of the periodic crystal. Phani *et al.* conducted an extensive analysis of various 2-D topologies confirming the direction-dependent spatial filtering capabilities in triangular, hexagonal, and square honeycomb as well as Kagomé lattices [97]. Other studies reported directional bandgaps in auxetic [98] and chiral lattices [99] in addition to plates with truss-like cores [100]. Picó

et al. experimentally validated angular-bandgaps in a sonic crystal (methacrylate scatterers in air) [101]. For tuning the band-gap size in 2-D structures, prior studies have highlighted filling fraction [102], material properties [103], depth-to-pitch ratio [104], and inclusion orientation [105] as critical design parameters. Specifically, Kuang *et al.* noted that band-gap size will increase if the rotation of the inclusion increases the maximally-achievable filling-factor [106]. The consideration of weak stiffness nonlinearity in 2-D lattices causes amplitude-dependency to develop in the beaming frequencies, thereby enabling amplitude to control wave propagation direction [23].

This chapter is organized as follows. Section 3.2 describes the example systems considered, 2-D monatomic and diatomic lattices with weak quadratic and cubic stiffness terms. Section 3.3 presents a higher-order multiple scales analysis of a generic 2-D lattice, and later specializes the analysis to the two example systems. Section 3.4 describes the strategy and analysis tools for numerical simulations of the lattice equations of motion. Section 3.5 reports directional waveform invariance: for a given wave propagation direction, a unique distribution of harmonic content leads to a waveform that propagates with little to no variation in its spectral composition. Directionality of variance reduction in numerical simulations aligns well with the direction-dependence of perturbation-based multi-harmonic coefficients. Section 3.6 presents a local fixed-point analysis, with accompanying numerical verification, revealing that stability also depends on wave propagation direction. Lattice directions are inherently less stable than inclined directions for systems with symmetrical stiffness terms and at frequencies unassociated with beaming. Section 3.7 proposes two technological applications of the directional stability and Section 3.8 offers some concluding remarks.

3.2 System Description: 2-D Lattices

Figure 3-1 displays the nine nearest neighbors in a generic two-dimensional periodic structure. Lattice vectors $\mathbf{a_1}$ and $\mathbf{a_2}$ describe the periodicity of the system. The coordinate pair (j,k) contains the unit cell indices along each of the two $\mathbf{a_1}$ and $\mathbf{a_2}$ directions. A global right-handed coordinate system is established by the $\hat{\mathbf{x}}$ and $\hat{\mathbf{y}}$ unit vectors. Reciprocal lattice vectors $\mathbf{b_1}$ and $\mathbf{b_2}$ are orthonormal with respect to the lattice vectors such that $\mathbf{b_u} \cdot \mathbf{a_v} = \delta_{uv}$ where δ_{mn} represents the Kronecker delta for integers m and n.

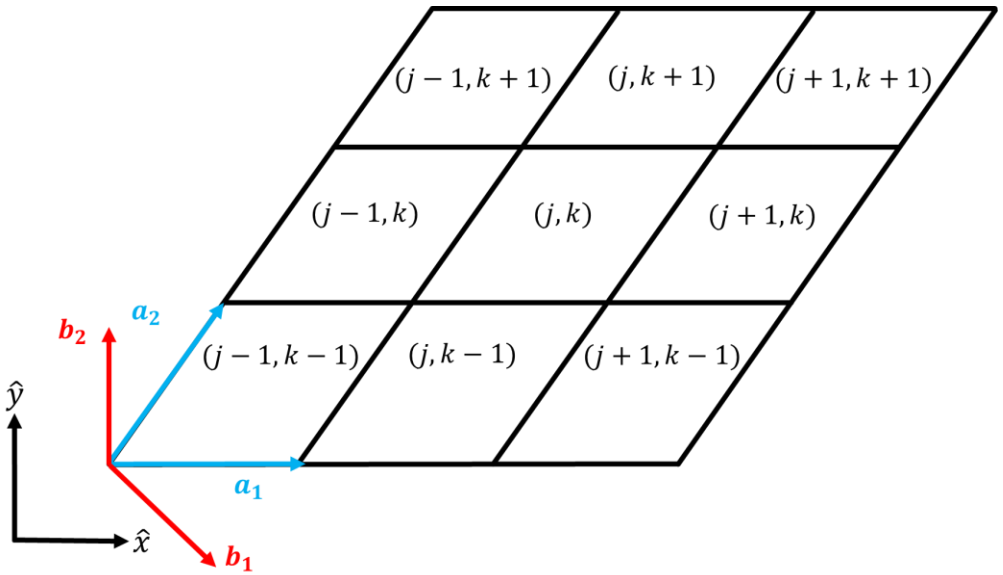

Figure 3-1. Nine nearest neighbors of a general two-dimensional lattice.

In general, the equation of motion governing the unit cell at (j,k) is

$$\mathbf{M}\ddot{\mathbf{z}}_{j,k} + \sum_{p,q=-1}^{+1}\left[\varepsilon\mathbf{C}^{(p,q)}\dot{\mathbf{z}}_{j+p,k+q} + \mathbf{K}^{(p,q)}\mathbf{z}_{j+p,k+q} + \varepsilon\mathbf{f}_{\mathbf{NL}}\left(\mathbf{z}_{j+p,k+q}\right)\right] = \mathbf{0}, \quad \mathrm{j,k} = -\infty \ldots \infty \tag{3.1}$$

where $\mathbf{z}_{j,k}, \dot{\mathbf{z}}_{j,k}, \ddot{\mathbf{z}}_{j,k}$ denote the vectors of out-of-plane displacements, velocities, and accelerations of all masses within the unit cell at (j,k), $\mathbf{M}$ denotes the mass matrix, and

$\mathbf{C}^{(p,q)}, \mathbf{K}^{(p,q)}$ denote the damping, and stiffness matrices, respectively. The small parameter ε is employed as a bookkeeping device. All forces from nonlinear stiffness terms are grouped into the $\mathbf{f_{NL}}$ vector.

3.3 Higher-Order Multiple Scales Analysis

Since the lattices are weakly nonlinear, the Method of Multiple Scales (MMS) can readily be carried-out on Eq. (3.1). Time scales of successively slower evolution are defined as

$$T_0 = t, T_1 = \varepsilon t, \dots, T_n = \varepsilon^n t \tag{3.2}$$

Accordingly, time derivatives can be written as

$$\left(\dot{\ }\right) = \mathrm{D}_0(\ \ ) + \varepsilon \mathrm{D}_1(\ \ ) + \cdots + \varepsilon^n \mathrm{D}_n(\ \ ) \tag{3.3}$$

and

$$\begin{aligned}\left(\ddot{\ }\right) = \mathrm{D}_0^2(\ \ ) + 2\varepsilon \mathrm{D}_0\mathrm{D}_1(\ \ ) + \varepsilon^2 \mathrm{D}_1^2(\ \ ) + \\ 2\varepsilon^2 \mathrm{D}_0\mathrm{D}_2(\ \ ) + \mathrm{O}(\varepsilon^3)\end{aligned} \tag{3.4}$$

where $\mathrm{D}_n(\ \ )$ denotes differentiation with respect to T_n. Additionally, a series solution is introduced

$$\mathbf{z}_{\mathrm{j,k}} = \mathbf{z}_{j,k}^{(0)} + \varepsilon \mathbf{z}_{j,k}^{(1)} + \cdots + \varepsilon^n \mathbf{z}_{j,k}^{(n)} \tag{3.5}$$

Collecting matching orders of ε yields each ordered equation. The first three are listed here

$$\varepsilon^0\colon\ \mathrm{D}_0^2 \mathbf{M}\mathbf{z}_{j,k}^{(0)} + \sum_{p,q=-1}^{+1}\left[\mathbf{K}^{(p,q)}\mathbf{z}_{j+p,k+q}^{(0)}\right] = \mathbf{0} \tag{3.6}$$

$$\varepsilon^1\colon\ \mathrm{D}_0^2 \mathbf{M}\mathbf{z}_{j,k}^{(1)} \sum_{p,q=-1}^{+1}\left[\mathbf{K}^{(p,q)}\mathbf{z}_{j+p,k+q}^{(1)}\right] = -2\mathrm{D}_0\mathrm{D}_1 \mathbf{M}\mathbf{z}_{j,k}^{(0)} -$$

$$\sum_{p,q=-1}^{+1}\left[\mathrm{D}_0\mathbf{C}^{(p,q)}\mathbf{z}_{j+p,k+q}^{(0)}+\mathbf{f}_{\mathbf{NL}}\left(\mathbf{z}_{j+p,k+q}^{(0)}\right)\right]+\mathrm{c.c.} \tag{3.7}$$

$$\varepsilon^2\colon\ \mathrm{D}_0^2\mathbf{M}\mathbf{z}_{j,k}^{(2)}\sum_{p,q=-1}^{+1}\left[\mathbf{K}^{(p,q)}\mathbf{z}_{j+p,k+q}^{(2)}\right]=-(2\mathrm{D}_0\mathrm{D}_2+\mathrm{D}_1^2)\mathbf{M}\mathbf{z}_{j,k}^{(0)}-$$

$$\sum_{p,q=-1}^{+1}\left[\mathrm{D}_0\mathbf{C}^{(p,q)}\mathbf{z}_{j+p,k+q}^{(1)}+\mathrm{D}_1\mathbf{C}^{(p,q)}\mathbf{z}_{j+p,k+q}^{(0)}+\mathbf{f}_{\mathbf{NL}}^{(2)}\left(\mathbf{z}_{j+p,k+q}^{(0)},\mathbf{z}_{j+p,k+q}^{(1)}\right)\right]+\mathrm{c.c.} \tag{3.8}$$

where $\mathbf{f}_{\mathbf{NL}}^{(2)}\left(\mathbf{z}_{j+p,k+q}^{(0)},\mathbf{z}_{j+p,k+q}^{(1)}\right)$ contains all the $\mathrm{O}(\varepsilon^2)$ terms from the nonlinear force vector.

Eq. (3.6) possesses a Bloch wave as its solution

$$\mathbf{z}_{j,k}^{(0)}=\tfrac{1}{2}\boldsymbol{\phi}A\mathrm{e}^{\mathrm{i}\omega_0T_0}\mathrm{e}^{-\mathrm{i}\mu_1 j}\mathrm{e}^{-\mathrm{i}\mu_2 k}+\mathrm{c.c.} \tag{3.9}$$

where A denotes the complex wave amplitude, ω_0 the fundamental temporal frequency, $\boldsymbol{\phi}$ a vector of mode shapes for the unit cell, and c. c. denotes the complex conjugate of all preceding terms. It is convenient to represent the wavenumber vector $\boldsymbol{\mu}$ in terms of the reciprocal lattice basis vectors $\boldsymbol{\mu}=\mu_1\mathbf{b_1}+\mu_2\mathbf{b_2}$ such that $\boldsymbol{\mu}\cdot(j\mathbf{a_1}+k\mathbf{a_2})=\mu_1 j+\mu_2 k$.

Additionally, the wave's amplitude $A(T_1,T_2,\dots,T_n)$ can be written in polar form

$$A=\alpha\mathrm{e}^{\mathrm{i}\beta} \tag{3.10}$$

where $\alpha=\alpha(T_1,T_2,\dots T_n)$ and $\beta=\beta(T_1,T_2,\dots,T_n)$ denote real quantities. Substitution of the Bloch waveform into the 0^{th}-order governing equation yields a linear dispersion relationship: $\omega_0=\omega_0(\mu_1,\mu_2)$ and corresponding wave mode shapes $\boldsymbol{\phi}$. In general, a unit cell with N degrees of freedom will have N distinct dispersion curves.

Updating Eq. (3.7) with the 0^{th}-order results yields inhomogeneous terms in two distinct forms: secular terms at $\mathrm{e}^{\mathrm{i}(\omega_0T_0-\mu_1 j-\mu_2 k)}+\mathrm{c.c.}$ and nonsecular terms at $\mathrm{e}^{\mathrm{i}h(\omega_0T_0-\mu_1 j-\mu_2 k)}+\mathrm{c.c.}, h\neq 1$. For the series solution to converge, all secular terms must be identically zero. To facilitate this process, the damping and nonlinear vectors on the right-hand side can be combined and represented by the summation of their Fourier components $\sum_{l=0}^{\infty}\mathbf{f}_l^{(1)}e^{il(\omega_0T_0-\mu_1 j-\mu_2 k)}$. Converting the solution to modal coordinates $\mathbf{z}_{j,k}^{(n)}=\boldsymbol{\Phi}\boldsymbol{u}_{j,k}^{(n)}$,

where $\boldsymbol{\Phi} = [\boldsymbol{\phi_1}, \boldsymbol{\phi_2}, \ldots, \boldsymbol{\phi_N}]$, diagonalizes the left hand side of Eq. (3.7) after pre-multiplying by $\boldsymbol{\phi}_\sigma^{\mathbf{H}}$, the Hermitian transpose of mode σ.

$$m_\sigma \mathrm{D}_0^2 u_{j,k}^{(1)} + k_\sigma u_{j,k}^{(1)} = -2\mathrm{i} m_\sigma \omega_0 \mathrm{D}_1 \left(\alpha e^{\mathrm{i}\beta}\right) e^{\mathrm{i}(\omega_0 T_0 - \mu_1 j - \mu_2 k)} + \boldsymbol{\phi}_\sigma^{\mathbf{H}} \sum_{l=0}^{\infty} \mathbf{f}_l^{(1)} e^{\mathrm{i}l(\omega_0 T_0 - \mu_1 j - \mu_2 k)} + \mathrm{c.c.} \tag{3.11}$$

where m_σ and k_σ denote the modal mass and wavenumber-reduced stiffness values for mode σ and $u_{j,k}$ is the modal coordinate governing mode σ.

Secular terms can readily be eliminated by imposing

$$-2\mathrm{i} m_\sigma \omega_0 (\mathrm{D}_1 \alpha + \mathrm{i}\alpha \mathrm{D}_1 \beta) e^{\mathrm{i}\beta} = \boldsymbol{\phi}_\sigma^{\mathrm{H}} \mathbf{f}_1^{(1)} \tag{3.12}$$

whereupon dividing Eq. (3.12) into its real and imaginary parts yields a coupled set of 1st-order evolution equations for α and β. Prior studies have demonstrated that $\mathrm{D}_1\beta$ leads to amplitude-dependent shifts to the 0th-order dispersion curve [21, 23]. The remaining nonsecular terms produce a particular solution at higher-harmonics of the 0th-order solution

$$u_{j,k}^{(1)} = \sum_{h=0}^{\infty} a_h^{(1)} \mathrm{e}^{\mathrm{i}h(\omega_0 T_0 - \mu_1 j - \mu_2 k)} + \mathrm{c.c.} \tag{3.13}$$

where $h \neq 1$. By grouping like terms, unknown coefficients can be solved for

$$a_h^{(1)} = \frac{\boldsymbol{\phi}_\sigma^{\mathrm{T}} \mathbf{f}_h^{(1)}}{-(h\omega_0)^2 m_\sigma + k_\sigma} \tag{3.14}$$

Analysis at the 2nd-order follows a similar procedure. Upon updating the 2nd-order equation and reverting to modal coordinates gives

$$m_\sigma \mathrm{D}_0^2 u_{j,k}^{(2)} + k_\sigma u_{j,k}^{(2)} = -m_\sigma (\mathrm{D}_1^2 + 2\mathrm{i}\omega_0 \mathrm{D}_2) \left(\alpha \mathrm{e}^{\mathrm{i}\beta}\right) \mathrm{e}^{\mathrm{i}(\omega_0 T_0 - \mu_1 j - \mu_2 k)} + \boldsymbol{\phi}_\sigma^{\mathrm{H}} \sum_{l=0}^{\infty} \mathbf{f}_l^{(2)} \mathrm{e}^{\mathrm{i}l(\omega_0 T_0 - \mu_1 j - \mu_2 k)} + \mathrm{c.c.} \tag{3.15}$$

where $\mathbf{f}_l^{(2)}$ is the l^{th} Fourier coefficient for the 2nd-order damping and nonlinear inhomogeneous terms. Removal of secular terms determines $\mathrm{D}_2\alpha$ and $\mathrm{D}_2\beta$ by satisfying

$$-m_\sigma(\mathrm{D}_1^2 + 2\mathrm{i}\omega_0\mathrm{D}_2)\left(\alpha \mathrm{e}^{\mathrm{i}\beta}\right) = \boldsymbol{\phi}_\sigma^{\mathrm{H}}\mathbf{f}_1^{(2)} \tag{3.16}$$

The remaining nonsecular terms yield a particular solution of the form

$$u_{j,k}^{(2)} = \sum_{h=0}^{\infty} a_h^{(2)} \mathrm{e}^{\mathrm{i}h(\omega_0 T_0 - \mu_1 j - \mu_2 k)} + \text{c. c.} \tag{3.17}$$

where

$$a_h^{(2)} = \frac{\boldsymbol{\phi}_\sigma^{\mathrm{H}}\mathbf{f}_h^{(2)}}{-(h\omega_0)^2 m_\sigma + k_\sigma} \tag{3.18}$$

The extension to still higher-orders develops increasingly complicated expressions but follows the same process: removal of secular terms by determining new evolution equations followed by obtaining particular solutions from each harmonic of the non-secular terms. As will be discussed in Section 3.5, the summation of all particular solutions from Eqs. (3.13) and (3.17) produces an invariant waveform: *i.e.,* multi-harmonic plane waves that propagate with no alteration to their spectral content. Additionally, Section 3.6 reconstitutes the evolution equations for α to provide information about the stability of plane waves.

3.3.1 Monatomic Lattice

An example system considered next is a 2-D monatomic shear lattice. Figure 3-2 depicts a unit cell in which a single mass extends in the x- and y-directions such that $\mathbf{a_1} = a_1\hat{\mathbf{x}}$ and $\mathbf{a_2} = a_2\hat{\mathbf{y}}$ where a_1 and a_2 denote lattice constants. Each mass couples to its four nearest neighbors via a linear spring, linear damper, and quadratic and cubic nonlinear springs. The Γ-X-M circuit defines the Irreducible Brillouin Zone.

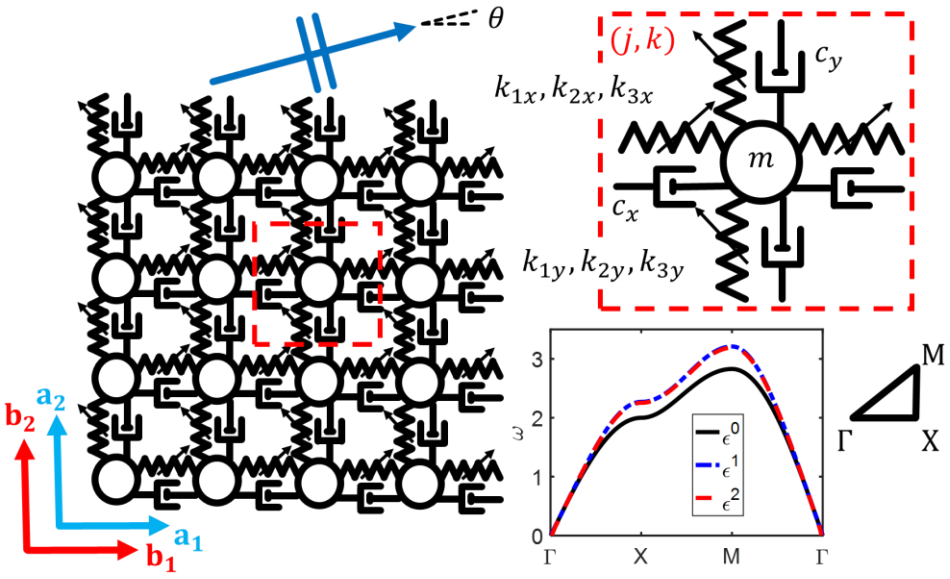

Figure 3-2. Unit cell of the 2-D monatomic lattice with its associated nonlinear dispersion curves. $\boldsymbol{\alpha = 0.3, m = 1, k_{1x} = 1, k_{2x} = 0.1, k_{3x} = 1, c_x = 0, k_{1y} = 1, k_{2y} = 0.1, k_{3y} = 1, c_y = 0, a_1 = 1, a_2 = 1.}$

Thus, by the formulation in Eq. (3.1), the following definitions apply

$$\mathbf{z}_{j,k} = z_{j,k} \tag{3.19}$$

$$\mathbf{M} = m \tag{3.20}$$

$$\mathbf{K}^{(0,0)} = 2\left(k_{1x} + k_{1y}\right) \tag{3.21}$$

$$\mathbf{K}^{(p,q)} = 0 \; \forall p = \pm 1, q = \pm 1 \tag{3.22}$$

$$\mathbf{K}^{(p,q)} = -k_{1x} \; \forall p = \pm 1, q = 0 \tag{3.23}$$

$$\mathbf{K}^{(p,q)} = -k_{1y} \; \forall p = 0, q = \pm 1 \tag{3.24}$$

$$\mathbf{f_{NL}} = k_{2x}\left(z_{j,k} - z_{j+p,k}\right)^2 + k_{2y}\left(z_{j,k} - z_{j,k+q}\right)^2 + k_{3x}\left(z_{j,k} - z_{j+p,k}\right)^3 + k_{3y}\left(z_{j,k} - z_{j,k+q}\right)^3, \forall\, p = \pm 1, q = \pm 1 \tag{3.25}$$

Since the damping matrix $\mathbf{C}^{(p,q)}$ follows the same pattern as the stiffness matrix $\mathbf{K}^{(p,q)}$, it is omitted from these definitions for brevity.

Application of the multiple scales procedure generates equations at each order of ε. The equation at ε^0 is

$$m\mathrm{D}_0^2 z_{j,k}^{(0)} + k_{1x}\left(z_{j,k}^{(0)} - z_{j-1,k}^{(0)} - z_{j+1,k}^{(0)}\right) + k_{1y}\left(z_{j,k}^{(0)} - z_{j,k-1}^{(0)} - z_{j,k+1}^{(0)}\right) = 0 \tag{3.26}$$

which admits the scalar Bloch-Wave

$$z_{j,k}^{(0)} = \frac{1}{2} A \mathrm{e}^{\mathrm{i}(\omega_0 T_0 - \mu_1 j - \mu_2 k)} + \mathrm{c.c.} \tag{3.27}$$

The associated dispersion relationship has only a single branch

$$\omega_0 = \sqrt{\frac{2k_{1x}}{m}(1 - \cos\mu_1) + \frac{2k_{1y}}{m}(1 - \cos\mu_2)} \tag{3.28}$$

Figure 3-2 displays this dispersion curve evaluated along the lattice's Irreducible Brillouin Zone. After substituting the solution in Eq. (3.27) to the ε^1 equations, secular terms must be removed. This procedure yields 1st-order evolution equations governing α and β

$$\mathrm{D}_1\alpha = -\gamma\alpha \tag{3.29}$$

$$\mathrm{D}_1\beta = \delta\alpha^2 \tag{3.30}$$

where

$$\gamma = \frac{c_x}{m}(1 - \cos\mu_1) + \frac{c_y}{m}(1 - \cos\mu_2) \tag{3.31}$$

and

$$\begin{aligned}\delta = {} & \frac{3}{2}\frac{k_{3x}\cos^2\mu_1}{m\omega_0} + \frac{3}{2}\frac{k_{3x}}{m\omega_0} - 3\frac{k_{3x}\cos\mu_1}{m\omega_0} \\ & + \frac{3}{2}\frac{k_{3y}\cos^2\mu_2}{m\omega_0} + \frac{3}{2}\frac{k_{3y}}{m\omega_0} - 3\frac{k_{3y}\cos\mu_2}{m\omega_0}\end{aligned} \tag{3.32}$$

Non-secular terms in the ε^1 equations at $\mathrm{e}^{2\mathrm{i}\omega_0 T_0}\mathrm{e}^{-2\mathrm{i}\mu_1 j}\mathrm{e}^{-2\mathrm{i}\mu_2 k}$ and $\mathrm{e}^{3\mathrm{i}\omega_0 T_0}\mathrm{e}^{-3\mathrm{i}\mu_1 j}e^{-3\mathrm{i}\mu_2 k}$ generate particular solutions at the same frequencies. Thus, the particular solution to Eq. (3.14) reduces to

$$z_{j,k}^{(1)} = \frac{1}{2} B_1 \mathrm{e}^{2\mathrm{i}(\omega_0 T_0 - \mu_1 j - \mu_2 k)} + \frac{1}{2} C_1 \mathrm{e}^{3\mathrm{i}(\omega_0 T_0 - \mu_1 j - \mu_2 k)} + \mathrm{c.c.} \tag{3.33}$$

where

$$B_1 = \frac{k_{2x}A^2}{m[2\omega_0(\mu_1,\mu_2)]^2 - [\omega_0(2\mu_1,2\mu_2)]^2}(-\cos 2\mu_1 + 2\cos\mu_1 - 1)$$

$$+\frac{k_{2y}A^2}{m[2\omega_0(\mu_1,\mu_2)]^2-[\omega_0(2\mu_1,2\mu_2)]^2}(-\cos 2\mu_2 + 2\cos\mu_2 - 1) \quad (3.34)$$

$$C_1 = \frac{k_{3x}A^3}{m[3\omega_0(\mu_1,\mu_2)]^2-[\omega_0(3\mu_1,3\mu_2)]^2}\left(-\frac{1}{2}\cos 3\mu_1 + \frac{3}{2}\cos 2\mu_1 - \frac{3}{2}\cos\mu_1 + \frac{1}{2}\right)$$

$$+\frac{k_{3y}A^3}{m[3\omega_0(\mu_1,\mu_2)]^2-[\omega_0(3\mu_1,3\mu_2)]^2}\left(-\frac{1}{2}\cos 3\mu_2 + \frac{3}{2}\cos 2\mu_2 - \frac{3}{2}\cos\mu_2 + \frac{1}{2}\right) \quad (3.35)$$

As the frequency approaches zero, the numerators and denominators in Eq. (3.34) and (3.35) tend to zero. Application of L'Hospital's rule reveals that $\lim_{\mu_1,\mu_2\to 0} B_1$ is unbounded (due to an internal resonance in which the quadratic nonlinearity produces a DC term) whereas $\lim_{\mu_1,\mu_2\to 0} C_1$ is bounded (since the cubic nonlinearity does not produce a DC term). Chapter 4 treats this isolated internal resonance through proper introduction of a detuning parameter.

Updating the ε^2 equations with results from the prior orders produces both secular and non-secular terms. Removal of secular terms provides the following 2nd-order evolution equations

$$\mathrm{D}_2\alpha = \xi\alpha^3 \quad (3.36)$$

$$\mathrm{D}_2\beta = \mathrm{X}\alpha^4 + \Upsilon\alpha^2 + \mathrm{Z} \quad (3.37)$$

where

$$\xi = \frac{\gamma\delta}{\omega_0} \quad (3.38)$$

$$\mathrm{X} = \frac{k_{3x}c_1}{m\omega_0}\left(-3\cos^3\mu_1 + \frac{9}{2}\cos^2\mu_1 - \frac{3}{2}\right)$$

$$+\frac{k_{3y}c_1}{m\omega_0}\left(-3\cos^3\mu_2 + \frac{9}{2}\cos^2\mu_2 - \frac{3}{2}\right) - \frac{\delta^2}{2\omega_0} \quad (3.39)$$

$$\Upsilon = \frac{2k_{2x}b_1}{m\omega_0}(\cos^2\mu_1 - 1) + \frac{2k_{2y}b_1}{m\omega_0}(\cos^2\mu_2 - 1) \quad (3.40)$$

$$\mathrm{Z} = \frac{\gamma c_x}{m\omega_0}(1-\cos\mu_1) + \frac{\gamma c_y}{m\omega_0}(1-\cos\mu_2) + \frac{\gamma^2}{2\omega_0} \tag{3.41}$$

and $b_1 = {B_1}/{A^2}$ and $c_1 = {C_1}/{A^3}$. The particular solution builds-upon the second and third harmonics introduced at the 1st-order and adds fourth and fifth harmonic terms.

$$\begin{aligned} z_{j,k}^{(2)} = {} & \frac{1}{2}B_2 \mathrm{e}^{2\mathrm{i}(\omega_0 T_0 - \mu_1 j - \mu_2 k)} \\ & + \frac{1}{2}C_2 \mathrm{e}^{3\mathrm{i}(\omega_0 T_0 - \mu_1 j - \mu_2 k)} \\ & + \frac{1}{2}E_2 \mathrm{e}^{4\mathrm{i}(\omega_0 T_0 - \mu_1 j - \mu_2 k)} \\ & + \frac{1}{2}F_2 \mathrm{e}^{5\mathrm{i}(\omega_0 T_0 - \mu_1 j - \mu_2 k)} + \mathrm{c.c.} \end{aligned} \tag{3.42}$$

where the coefficients $B_2, C_2, E_2,$ and F_2 can be expressed in terms of the lattice parameters.

Amplitude-dependent dispersion corrections directly follow from the evolution equations for phase, *i.e.*, $\omega = \omega_0 + \varepsilon \mathrm{D}_1\beta + \varepsilon^2 \mathrm{D}_2\beta + \cdots + \varepsilon^n \mathrm{D}_\mathrm{n}\beta$. Figure 3-2 plots the 0th order (linear) as well as 1st and 2nd-order corrected dispersion curves for the 2-D monatomic lattice. Similar to the results of the 1-D monatomic chain in Section 2.6, quadratic stiffnesses do not appear in the dispersion corrections until the 2nd order.

3.3.2 Diatomic Lattice

Figure 3-3 depicts the second example system studied herein: the 2-D diatomic lattice. Alternating masses (m_a, m_b) extend in the x and y directions such that $\mathbf{a_1} = a_1\hat{\mathbf{x}}$ and $\mathbf{a_2} = \frac{a_2}{\sqrt{2}}(\hat{\mathbf{x}} + \hat{\mathbf{y}})$ where again a_1 and a_2 denote lattice constants and Γ-X-M defines the Irreducible Brillouin Zone.

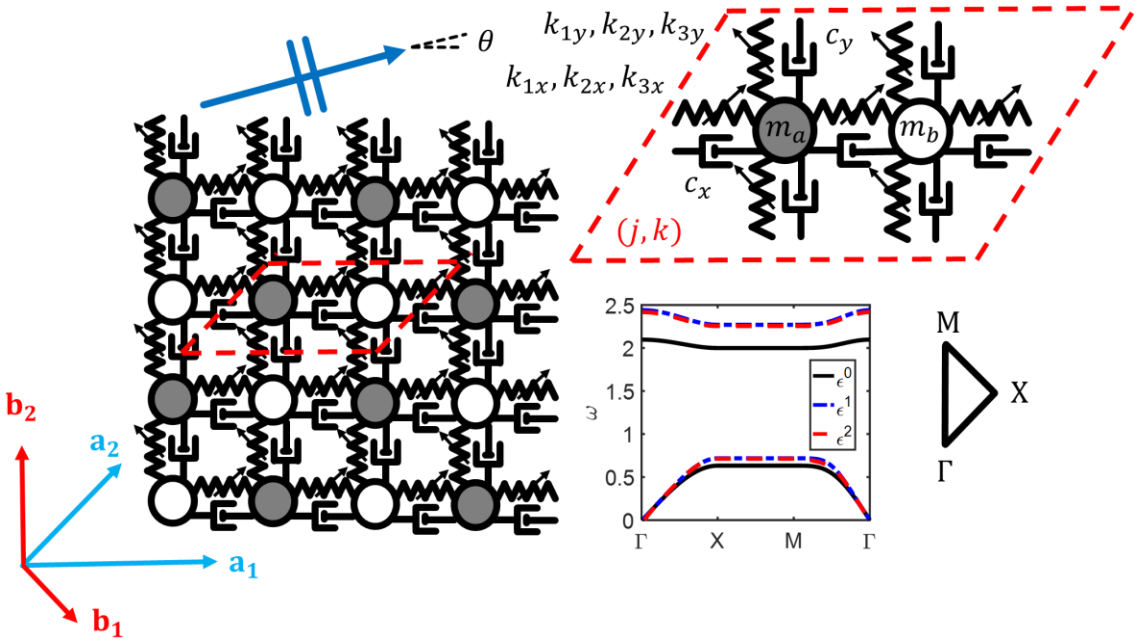

Figure 3-3. Unit cell of the 2-D diatomic lattice with associated nonlinear dispersion curves: $\boldsymbol{\alpha = 0.6, m_a = 1, m_b = 10, k_{1x} = 1, k_{2x} = 0.1, k_{3x} = 1, c_x = 0, k_{1y} = 1, k_{2y} = 0.1, k_{3y} = 1, c_y = 0, a_1 = 1, a_2 = \frac{1}{\sqrt{2}}}$.

Since there are two degrees of freedom per unit cell, the formulation in Eq. (3.1) results in

$$\mathbf{z_{j,k}} = \begin{bmatrix} z_{a\,j,k} \\ z_{b\,j,k} \end{bmatrix} \tag{3.43}$$

$$\mathbf{M} = \begin{bmatrix} m_a & 0 \\ 0 & m_b \end{bmatrix} \tag{3.44}$$

$$\mathbf{K}^{(0,0)} = \begin{bmatrix} 2(k_{1x} + k_{1y}) & -k_{1x} \\ -k_{1x} & 2(k_{1x} + k_{1y}) \end{bmatrix} \tag{3.45}$$

$$\mathbf{K}^{(p,q)} = \begin{bmatrix} 0 & 0 \\ 0 & 0 \end{bmatrix} \forall (p,q) = [(1,1),(-1,-1)] \tag{3.46}$$

$$\mathbf{K}^{(p,q)} = \begin{bmatrix} 0 & -k_{1y} \\ 0 & 0 \end{bmatrix} \forall (p,q) = [(-1,1),(0,-1)] \tag{3.47}$$

$$\mathbf{K}^{(p,q)} = \begin{bmatrix} 0 & 0 \\ -k_{1y} & 0 \end{bmatrix} \forall (p,q) = [(0,1),(1,-1)] \tag{3.48}$$

$$\mathbf{f}_{\mathrm{NL}}(1) = k_{2x}\left(z_{a_{0,0}} - z_{b_{0,0}}\right)^2 + k_{2x}\left(z_{a_{0,0}} - z_{b_{-1,0}}\right)^2$$
$$+k_{2y}\left(z_{a_{0,0}} - z_{b_{-1,1}}\right)^2 + k_{2y}\left(z_{a_{0,0}} - z_{b_{0,-1}}\right)^2$$
$$+k_{3x}\left(z_{a_{0,0}} - z_{b_{0,0}}\right)^3 + k_{3x}\left(z_{a_{0,0}} - z_{b_{-1,0}}\right)^3$$

$$+k_{3y}\left(z_{a_{0,0}}-z_{b_{-1,1}}\right)^3+k_{3y}\left(z_{a_{0,0}}-z_{b_{0,-1}}\right)^3 \tag{3.49}$$

$$\begin{aligned}\mathbf{f}_{\mathrm{NL}}(2)=&\,k_{2x}\left(z_{b_{0,0}}-z_{a_{0,0}}\right)^2+k_{2x}\left(z_{b_{0,0}}-z_{a_{1,0}}\right)^2\\&+k_{2y}\left(z_{b_{0,0}}-z_{a_{0,1}}\right)^2+k_{2y}\left(z_{b_{0,0}}-z_{a_{1,-1}}\right)^2\\&+k_{3x}\left(z_{b_{0,0}}-z_{a_{0,0}}\right)^3+k_{3x}\left(z_{b_{0,0}}-z_{a_{1,0}}\right)^3\\&+k_{3y}\left(z_{b_{0,0}}-z_{a_{0,1}}\right)^3+k_{3y}\left(z_{b_{0,0}}-z_{a_{1,-1}}\right)^3\end{aligned} \tag{3.50}$$

As with the monatomic lattice, the damping matrix $\mathbf{C}^{(p,q)}$ follows the same pattern as the stiffness matrix $\mathbf{K}^{(p,q)}$.

The 0th-order equation yields a Bloch wave with two dispersion branches and wave mode shapes

$$\begin{aligned}\omega_0^2=\frac{1}{m_a m_b}\Big(&k_{1x}m_a+k_{1x}m_b+k_{1y}m_a+k_{1y}m_b\pm\big(4\sin\mu_1\cos\mu_2\sin\mu_2\,k_{1y}^2m_am_b-\\&4\cos\mu_1\sin^2\mu_2\,k_{1y}^2m_am_b+4\sin\mu_1\sin\mu_2\,k_{1x}k_{1y}m_am_b+\\&4\cos\mu_1\cos\mu_2\,k_{1x}k_{1y}m_am_b+2\cos\mu_1\,k_{1x}^2m_a^2m_b+2\cos\mu_1\,k_{1y}^2m_am_b+\\&4\cos\mu_2\,k_{1x}k_{1y}m_am_b+k_{1x}^2m_a^2+k_{1x}^2m_b^2+2k_{1x}k_{1y}m_a^2-4k_{1x}k_{1y}m_am_b+\\&2k_{1x}k_{1y}m_b^2+k_{1y}^2m_a^2+k_{1y}^2m_b^2\big)^{1/2}\Big)\end{aligned} \tag{3.51}$$

$$\begin{aligned}\phi_a=\;&k_{1x}\left(-\tfrac{1}{2}-\tfrac{1}{2}\cos\mu_1-\tfrac{1}{2}\mathrm{i}\sin\mu_1\right)+k_{1y}\left(-\tfrac{1}{2}\cos\mu_1\cos\mu_2+\tfrac{1}{2}\mathrm{i}\cos\mu_1\sin\mu_2-\right.\\&\left.\tfrac{1}{2}\mathrm{i}\sin\mu_1\cos\mu_2-\tfrac{1}{2}\sin\mu_1\sin\mu_2-\tfrac{1}{2}\cos\mu_2-\tfrac{1}{2}\mathrm{i}\sin\mu_2\right)\end{aligned} \tag{3.52}$$

$$\phi_b=\;-\tfrac{1}{2}m_a\omega_0^2+k_{1x}+k_{1y} \tag{3.53}$$

where the "-" is taken for the acoustic branch and "+" for the optical branch and $\boldsymbol{\phi}=\begin{bmatrix}\phi_a\\ \phi_b\end{bmatrix}$.

Figure 3-3 plots the 0th-order dispersion curve for this system. Higher frequency modes correspond to the optical branch whereas lower frequency modes correspond to the acoustic branch.

Expressions for the ε^1 and ε^2 orders of the Multiple Scales analysis are not easily reproduced; however, it is noted that they follow the same functional form as those in Eqs. (3.29) through (3.42) for the monatomic lattice. Thus, the 1st-order results appear as

$$\mathrm{D}_1\alpha = -\gamma\alpha \tag{3.54}$$

$$\mathrm{D}_1\beta = \delta\alpha^2 \tag{3.55}$$

$$\boldsymbol{z}_{j,k}^{(1)} = \frac{1}{2}\mathbf{B}_1 e^{2\mathrm{i}(\omega_0 T_0 - \mu_1 j - \mu_2 k)} + \frac{1}{2}\mathbf{C}_1 e^{3\mathrm{i}(\omega_0 T_0 - \mu_1 j - \mu_2 k)} + \text{c. c.} \tag{3.56}$$

where $\mathbf{B_1} = \begin{bmatrix} B_{1a} \\ B_{1b} \end{bmatrix}$ and $\mathbf{C_1} = \begin{bmatrix} C_{1a} \\ C_{1b} \end{bmatrix}$. The 2nd-order results appear as

$$\mathrm{D}_2\alpha = \xi\alpha^3 \tag{3.57}$$

$$\mathrm{D}_2\beta = \mathrm{X}\alpha^4 + \Upsilon\alpha^2 + \mathrm{Z} \tag{3.58}$$

$$\begin{aligned} \mathbf{z}_{j,k}^{(2)} = {} & \frac{1}{2}\mathbf{B}_2 \mathrm{e}^{2\mathrm{i}(\omega_0 T_0 - \mu_1 j - \mu_2 k)} \\ & + \frac{1}{2}\mathbf{C}_2 \mathrm{e}^{3\mathrm{i}(\omega_0 T_0 - \mu_1 j - i\mu_2 k)} \\ & + \frac{1}{2}\mathbf{E}_2 \mathrm{e}^{4\mathrm{i}(\omega_0 T_0 - \mu_1 j - \mu_2 k)} \\ & + \frac{1}{2}\mathbf{F}_2 \mathrm{e}^{5\mathrm{i}(\omega_0 T_0 - \mu_1 j - \mu_2 k)} + \text{c. c.} \end{aligned} \tag{3.59}$$

where $\mathbf{B_2} = \begin{bmatrix} B_{2a} \\ B_{2b} \end{bmatrix}$ and $\mathbf{C_2} = \begin{bmatrix} C_{2a} \\ C_{2b} \end{bmatrix}$.

Figure 3-3 displays the 0th, 1st, and 2nd-order dispersion curves for the 2-D diatomic lattice. Note that in small wavenumber ranges around a few isolated points, internal resonances (*i.e.*, large 2nd-order particular solutions) can occur for some lattices where wavenumber combinations satisfy $n\omega_0(\mu_1, \mu_2) - \omega_0(n\mu_1, n\mu_2) = 0$ for $n = 2,3$. Treatment of such cases is the subject of Chapter 4.

3.4 Numerical Simulations

Direct numerical integration of the equations of motion for the monatomic lattice in Eqs. (3.19-3.25) and diatomic lattice in Eqs. (3.43-3.50) was conducted using MATLAB's ode45 solver. Large lattices (~300 x 300 unit cells) were simulated, and linear viscous dampers with coefficients that increase towards the edges of the structure were added to mitigate reflections. Plane waves were introduced into the medium by employing one of two methods: the first method harmonically displaces a single mass in the lattice's center, which produces a wave that spreads radially outwards in all directions with decreasing amplitude. The second method inputs initial conditions (*i.e.*, displacements and velocities) corresponding to the series solution in Eq. (3.5) truncated to a given order. This latter technique injects perturbation solutions into the lattice to determine whether or not such solutions persist over time. Specific orientations can be prescribed for plane-wave initial conditions by imposing $\tan\theta = \mu_y/\mu_x$ where $\mu_x = \boldsymbol{\mu} \cdot \hat{\mathbf{x}}$ and $\mu_y = \boldsymbol{\mu} \cdot \hat{\mathbf{y}}$ and θ is measured counterclockwise relative to the $\hat{\mathbf{x}}$-direction as illustrated in Figure 3-2 and Figure 3-3.

Essential to the investigation of waveform invariance and stability is the determination of the lattice's spectral content. A Fast Fourier Transform (FFT) is computed for either spatial or temporal signals. By collecting the displacements of a line of masses at a snapshot in time, $z(\mathbf{R}, t^*)$, a spatial FFT can be obtained $z(\mathbf{R}, t^*) \rightarrow Z(\Lambda, t^*)$. Alternatively, the time history of a single mass in space, $z(j^*, k^*, t)$, can be transformed $z(j^*, k^*, t) \rightarrow Z(j^*, k^*, \Omega)$.

Using this framework, a variance parameter $\sigma_{p,n}$ is calculated by comparing the spectral growth and decay of a given spatial harmonic amplitude over time for a line of masses along a unit direction $\hat{\mathbf{r}}$.

$$\sigma_{p,n} = \frac{1}{A_{p,n}} \sqrt{\frac{1}{L+1} \sum_{l=0}^{L} \left(Z^{(n)}(p(\boldsymbol{\mu} \cdot \hat{\mathbf{r}}), l\Delta t) - A_{p,n} \right)^2} \tag{3.60}$$

where

$$A_{p,n} = \frac{1}{L+1} \sum_{l=0}^{L} Z^{(n)}(p(\boldsymbol{\mu} \cdot \hat{\mathbf{r}}), l\Delta t) \tag{3.61}$$

and $Z^{(n)}(p(\boldsymbol{\mu} \cdot \hat{\mathbf{r}}), l\Delta t)$ denotes the amplitude of the p^{th} harmonic of $\boldsymbol{\mu}$ projected onto the desired direction $\hat{\mathbf{r}}$, after l cycles of duration Δt for simulations given initial conditions retaining terms up to the n^{th} order . The $\sigma_{p,n}$ parameter can be interpreted as the root-mean-square average of the temporal variation in the lattice's spatial harmonic content along a given direction centered about and normalized by its mean value. Additionally, the change in variance $\Delta\sigma_{p,n}$ can be computed as

$$\Delta\sigma_{p,n} = \sigma_{p,n} - \sigma_{p,0} \tag{3.62}$$

which measures the amount of variance reduction derived from including higher-order terms in the lattice's initial conditions relative to the variance of the 0^{th}-order solution.

For monitoring stability, the energy E_t within a frequency band Ω_1 to Ω_2 can be determined

$$E_t = \int_{\Omega_1}^{\Omega_2} \left| Z^{(n)}(j^*, k^*, \Omega) \right|^2 \mathrm{d}\Omega \tag{3.63}$$

Using Eq. (3.63), stability can be assessed by monitoring the amount energy concentrated within a fundamental frequency and its associated harmonics. Accordingly, $E_{t,\delta}$ can be introduced

$$E_{t,\delta} = 1 - \frac{1}{E_{t,\text{total}}} \sum_{n=1}^{5} \left[\int_{l\omega-\Delta_t}^{l\omega+\Delta_t} \left| Z^{(n)}(j^*, k^*, \Omega) \right|^2 \mathrm{d}\Omega \right] \tag{3.64}$$

where $E_{t,\text{total}}$ denotes the total spectral energy of the unit cell and $2\Delta_t$ denotes a small bandwidth centered about the n^{th} harmonic of the forcing frequency ω. The spatial analogue to Eq. (63) is

$$E_s = \int_{\Lambda_1}^{\Lambda_2} \left| Z^{(n)}(\Lambda, t^*) \right|^2 \mathrm{d}\Lambda \tag{3.65}$$

where $Z^{(n)}(\Lambda, t^*)$ is the complex Fourier coefficient at the spatial frequency Λ for a group of masses along the $\hat{\mathbf{r}}$-direction. For plane-wave initial conditions, instability was defined to occur when a significant fraction of E_s fell outside of integer multiples of $\boldsymbol{\mu} \cdot \hat{\mathbf{r}}$

$$E_{s,\delta} = 1 - \frac{1}{E_{\text{s,total}}} \sum_{l=1}^{5} \left[\int_{l(\boldsymbol{\mu}\cdot\hat{\mathbf{r}})-\Delta_s}^{l(\boldsymbol{\mu}\cdot\hat{\mathbf{r}})+\Delta_s} \left| Z^{(n)}(\Lambda, t^*) \right|^2 \mathrm{d}\Lambda \right] \tag{3.66}$$

where $E_{\text{s,total}}$ denotes the total energy of the line of masses and $2\Delta_s$ denotes a small bandwidth centered about $\boldsymbol{\mu} \cdot \hat{\mathbf{r}}$. Thus, large values of $E_{s,\delta}$ signify a substantial presence of incommensurate frequencies in the spatial distribution of masses in the lattice.

3.5 Directional Waveform Invariance

Inspection of Eqs. (3.13) and (3.17) indicate that these nonlinear lattices admit multi-harmonic solutions that propagate for all space and time. Higher-harmonic amplitudes are added at each order of the perturbation analysis in addition to building-upon the harmonic amplitudes introduced at prior orders. Thus, the series solution in Eq. (3.5) is expected to converge to a multi-harmonic waveform that propagates *invariantly*; in other words, these solutions describe waves whose spectral amplitudes interact in such a way so as to eliminate the development and exchange of energy between higher-harmonics. Because the solutions possess integer multiples of both the spatial and temporal frequencies, these waveforms travel at a single phase velocity and spectral content should not modulate across

either space or time. Note that higher-harmonic generation [107] and inter-harmonic energy exchange [108] are well-documented phenomena for waves in nonlinear media. Clearly, knowledge of invariant waveforms could impact communications applications in which information at a carrier frequency must be transmitted through nonlinear media with as little loss or distortion as possible.

In symmetrical lattices, these solutions might reasonably be expected to propagate identically for any given orientation, particularly at sufficiently low frequencies wherein beaming does not occur. However, Figure 3-4 displays the multi-harmonic amplitudes governing the second and third harmonics in the monatomic lattice evaluated as a function of the plane wave's angle. Note the considerable variation for most frequencies and wavenumbers. It is therefore expected that waves generate and exchange spectral content at different rates along different angles, and hypothesized to be more pronounced variation for directions in which the multi-harmonic amplitudes are larger due to the greater deficit of the invariant amplitudes in the 0^{th}-order solution.

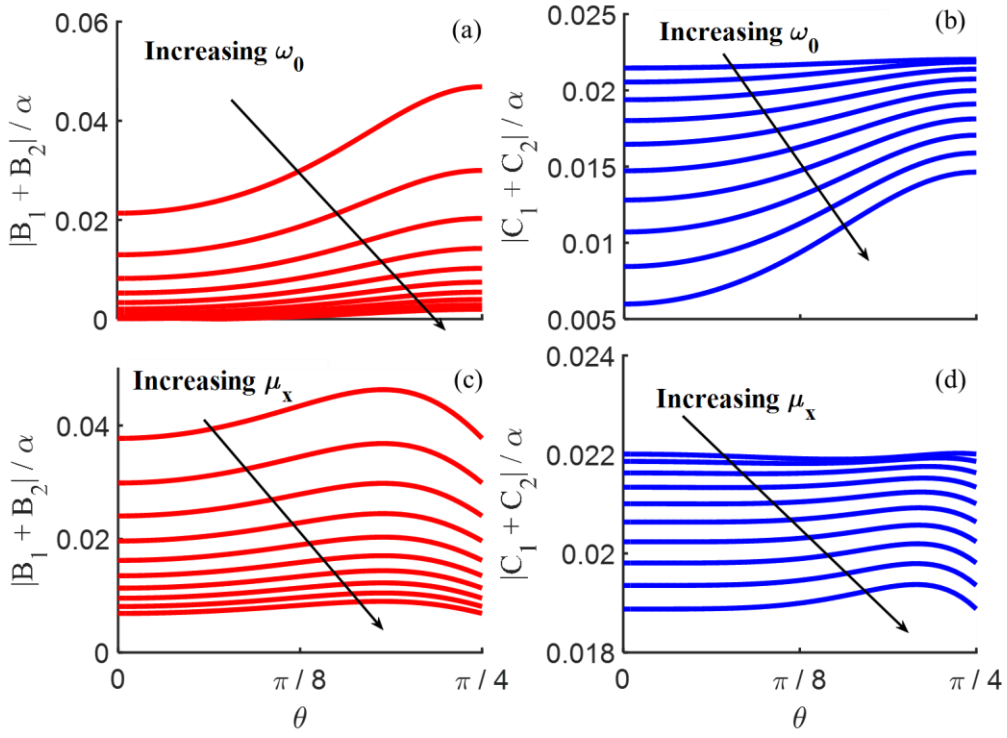

Figure 3-4. Perturbation-based multi-harmonic content evaluated as a function of plane-wave angle in the monatomic lattice. Coefficients are computed with constant ω_0 (a,b) or μ_x (c,d): $\alpha = 0.4, m = 1, k_{1x} = 1, k_{2x} = 0.01, k_{3x} = 1, c_x = 0, k_{1y} = 1, k_{2y} = 0.01, k_{3y} = 1, c_y = 0, a_1 = 1, a_2 = 1$.

This hypothesis was tested and validated in numerical simulations for both the monatomic and diatomic lattices. Using the plane-wave initial conditions described in Section 3.4, the series solution in Eq. (3.5) was truncated at the ε^0 and ε^2 orders and applied as initial conditions for the solver for different angles θ. The metrics in Eqs. (3.60) through (3.62) were applied with $\hat{\mathbf{r}} = \hat{\mathbf{x}}$ such that $\boldsymbol{\mu} \cdot \hat{\mathbf{r}} = \mu_x$. Figure 3-5 presents the numerically-determined variance reduction in the monatomic lattice for the second and third harmonics evaluated as a function of the plane wave's angle. For these simulations, μ_x remained fixed as the plane-wave angle varied to ensure higher-harmonics did not exceed the Nyquist frequency determined by the FFT's frequency spectrum. The trend of direction-dependent

variance reduction closely follows that of the higher-harmonic solution amplitudes, consistent with the aforementioned hypothesis.

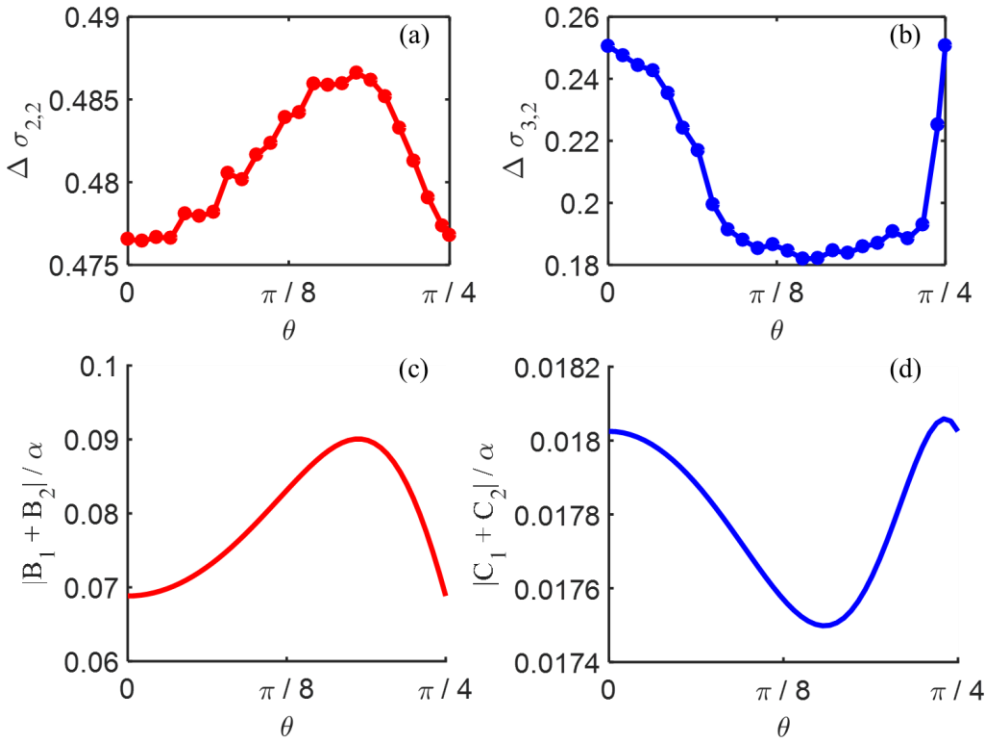

Figure 3-5. Waveform invariance in the monatomic lattice: numerical reduction in variance (a,b) compared to perturbation coefficients governing the 2nd and 3rd harmonics (c,d): $\boldsymbol{\mu_x = \frac{\pi}{4}, \alpha = 0.4, m = 1, k_{1x} = 1, k_{2x} = 0.1, k_{3x} = 1, c_x = 0, k_{1y} = 1, k_{2y} = 0.1, k_{3y} = 1, c_y = 0, a_1 = 1, a_2 = 1.}$

In a similar manner, variance in the diatomic lattice was numerically investigated. Figure 3-6 and Figure 3-7 depict the direction dependence of the perturbation-based multi-harmonic solution amplitudes in the diatomic lattice. The same hypothesis was proposed: greater variance reduction should be measured in directions in which the multi-harmonic content is larger.

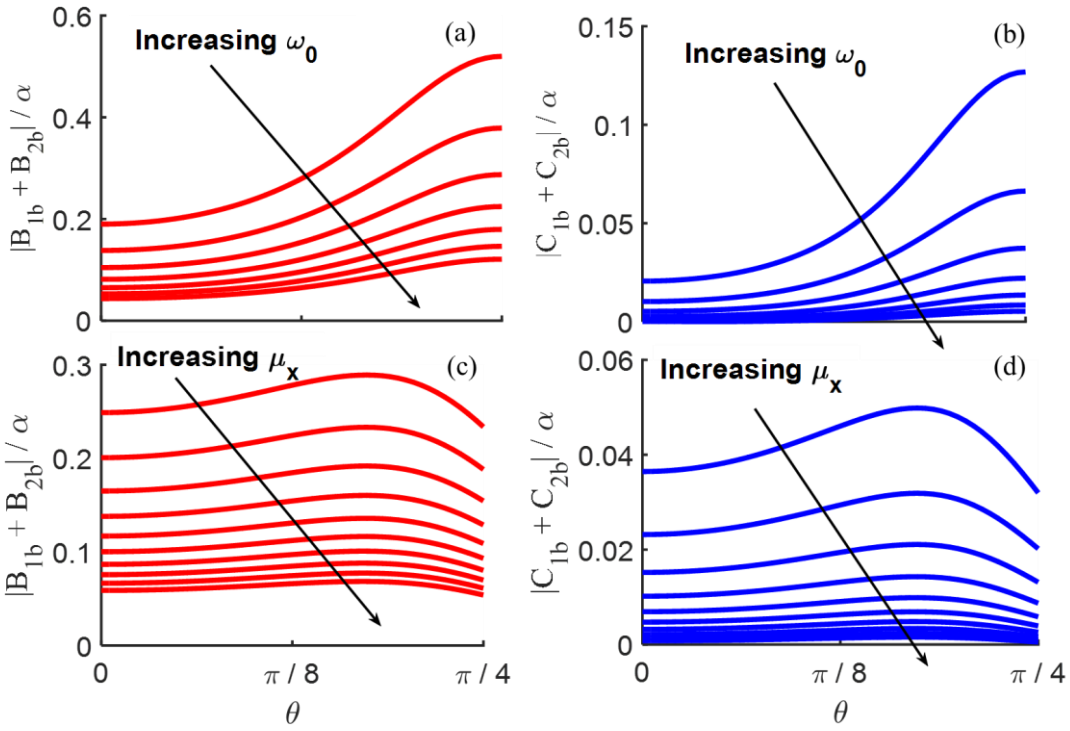

Figure 3-6. Perturbation-based multi-harmonic content evaluated as a function of plane-wave angle in the diatomic lattice for m_b masses. Coefficients are computed with constant ω_0 (a,b) or μ_x (c,d): $\alpha = 0.1, m_a = 1, m_b = 1.5, k_{1x} = 1, k_{2x} = 0.1, k_{3x} = 1, c_x = 0, k_{1y} = 1, k_{2y} = 0.1, k_{3y} = 1, c_y = 0, a_1 = 1, a_2 = \frac{1}{\sqrt{2}}$.

The variance parameter can be applied to either degree of freedom: $\sigma_{p,n,a}$ and $\sigma_{p,n,b}$ for m_b and m_b masses, respectively. Figure 3-7 presents the numerical computation of variance reduction in the diatomic lattice compared to the multi-harmonic amplitudes evaluated at the same μ_x values. The trend of direction-dependent variance reduction again closely follows that of the multi-harmonic coefficients.

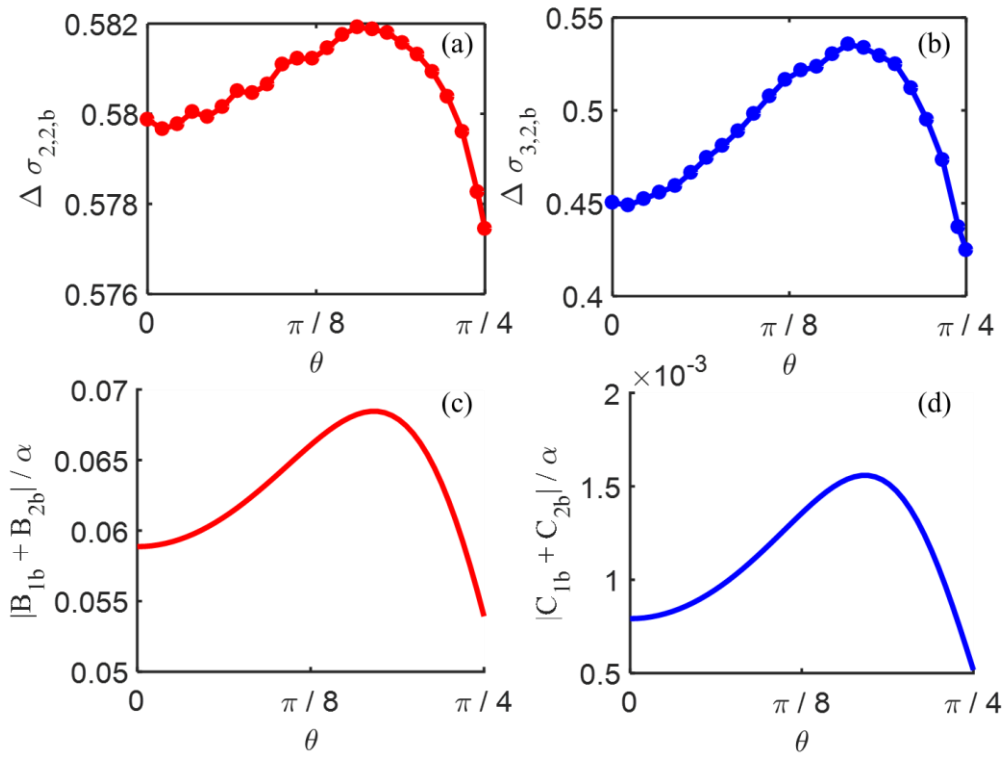

Figure 3-7. Waveform invariance in the acoustic branch of the diatomic lattice. Numerical variance reduction (a,b) are compared to magnitude of perturbation

coefficients (c,d): $\boldsymbol{\mu_x = \frac{\pi}{4}, \alpha = 0.1, m_a = 1, m_b = 1.5, k_{1x} = 1, k_{2x} = 0.1, k_{3x} = 1, c_x = 0, k_{1y} = 1, k_{2y} = 0.1\ , k_{3y} = 1, c_y = 0, a_1 = 1, a_2 = \frac{1}{\sqrt{2}}}$.

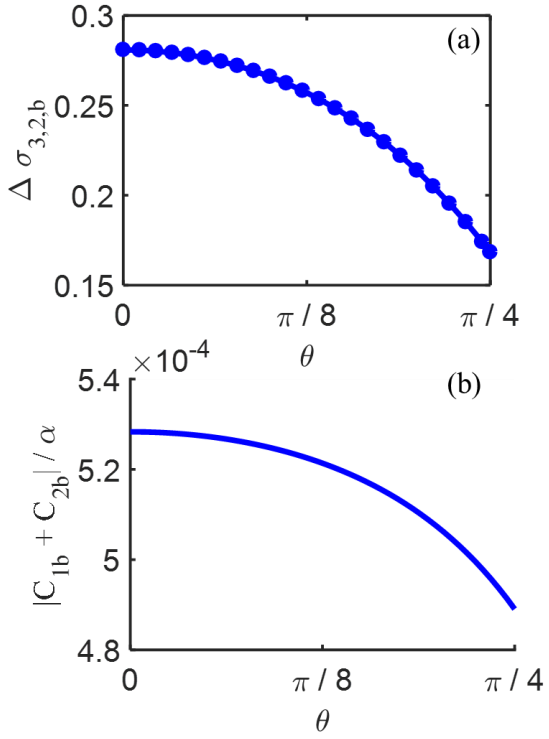

Figure 3-8. Waveform invariance in the optical branch of the diatomic lattice. Numerical variance reduction (a) are compared to magnitude of perturbation coefficients (b): $\boldsymbol{\mu_x = \frac{\pi}{6}, \alpha = 0.1, m_a = 1, m_b = 1.5, k_{1x} = 1, k_{2x} = 0.1, k_{3x} = 1, c_x = 0, k_{1y} = 1, k_{2y} = 0.1\ , k_{3y} = 1, c_y = 0, a_1 = 1, a_2 = \frac{1}{\sqrt{2}}}$.

For both the monatomic lattice and acoustic branch of the diatomic lattice, the variance reduction in the third harmonic exhibits much stronger angular dependence than that in the second harmonic. For the acoustic branch of the diatomic lattice, this aligns well with the weaker angular relationship of the second harmonic amplitude compared to that of the third, but not so for the monatomic lattice. It is possible there exists a connection between nonlinear the normal modes [109] of a finite lattice and the waveform invariance in infinite lattices reported in this work. The approach to numerically verifying waveform invariance

considered herein motivates this possible connection: when a structure is excited precisely according to a modal solution, it continues to vibrate at that isolated mode.

3.6 Directional Stability

While Eqs. (3.9), (3.13), and (3.17) define plane-wave solutions for the lattice, they do not provide *a-priori* indication of their stability. Amplitude can be expected to play a critical role in the stability of the wave propagation solutions reported in this work. Low-amplitude waveforms simulated in Section 3.5, for example, continued to propagate for many cycles. For sufficiently large amplitudes, however, nonlinear interactions become more dominant and plane-wave propagation may break-down. Less intuitive is the influence of propagation *direction* on stability, especially for a symmetrical lattice. Waves travelling in one direction may reasonably be expected to propagate with the same stability as any another direction.

Reconstituting the 0^{th}-order amplitude to the original time scale yields the time variation of the wave amplitude

$$\dot{\alpha} = \varepsilon \mathrm{D}_1 \alpha + \varepsilon^2 \mathrm{D}_2 \alpha \tag{3.67}$$

Denoting fixed point solutions as α^*, the stability of each fixed point is assessed through a local analysis by computing its associated λ value

$$\lambda \equiv \frac{\mathrm{d}}{\mathrm{d}\alpha} \dot{\alpha}|_{\alpha^*} \tag{3.68}$$

where $\lambda > 0$ implies instability, $\lambda < 0$ stability, and $\lambda = 0$ neutral stability. For both the monatomic and diatomic lattices, two distinct fixed points arise

$$\alpha^* = 0, \sqrt{\frac{\omega_0}{\varepsilon\delta}} \tag{3.69}$$

Whether analysis is truncated at the 1st or 2nd order, the stable fixed point $\alpha^* = 0$ exists for all the lattices considered. Such a solution indicates that small amplitude waves decay due to damping. Higher-order (*i.e.*, $O(\varepsilon^2)$) terms in the reconstituted amplitude equation reveal unstable non-zero fixed points ($\alpha^*_{\mathrm{NZ}} = \sqrt{\frac{\omega_0}{\varepsilon\delta}}$). Thus, waves with initial amplitudes in the neighborhood of α^*_{NZ} propagate unstably whereas those with low amplitudes (*i.e.*, sufficiently close to $\alpha^* = 0$) stably decay due to dissipation in the lattice. This finding highlights the significance of higher-order perturbation analysis: 1st-order expressions alone give no indication of instability in these lattices.

While not immediately apparent when examining the MMS results, the unstable fixed points in symmetric lattices exhibit strong angular dependence. Using expressions for the monatomic lattice (the diatomic lattice gives similar results), Figure 3-9 plots basins of attraction for plane waves along different angles, θ, and initial amplitudes, α_0. Waves with α_0 values above the threshold marked by the black line propagate in an unstable manner whereas waves with α_0 values below this threshold propagate in a stable manner. Note that, while symmetric parameters are used, there is still the indication of *directional stability* in the system: stability increases as the angle increases since higher threshold α_0 values imply greater stability. The black line is computed from the local stability analysis while the colored points are found from numerically integrating Eq. (3.67) and identifying, based on either a subsequent increase or decrease in amplitude, the stability or instability, respectively, of the wave. Again, direction dependence appears in the stability. It is clear that for some amplitudes, *e.g.* $\alpha_0 = 1.5$, the wave propagates in a stable manner along the

45 degree direction, but in an unstable manner along the 0 degree direction. In fact, it is apparent that $\theta = 0^o$ (the lattice direction) is the least stable angle, and stability increases as plane waves depart from this orientation.

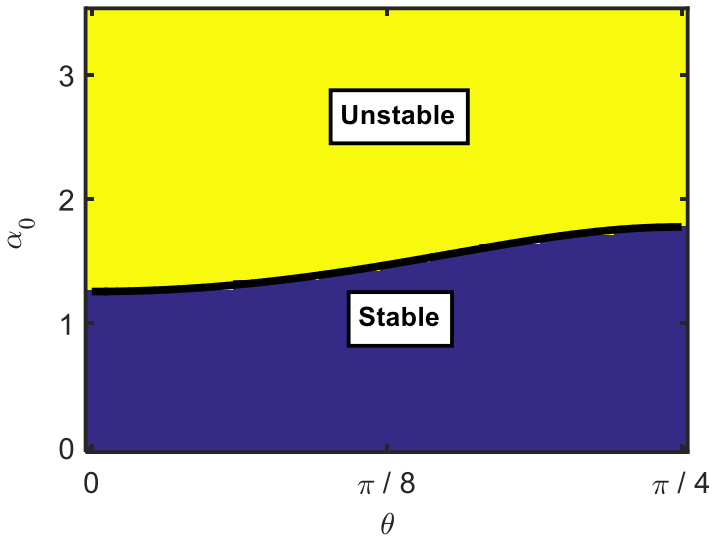

Figure 3-9. Basins of attraction for the 2-D monatomic lattice as predicted by the perturbation results: $\boldsymbol{m = 1, k_{1x} = 1, k_{1y} = 1, k_{2x} = 1, k_{2y} = 1, k_{3x} = 1, k_{3y} = 1, c_x = 0.1, c_y = 0.1, \omega_0 = 1.3, a_1 = 1, a_2 = 1.}$

Similar to the findings in Section 2.7.1, the fixed points from the local stability analysis cannot be expected to accurately predict the true threshold for instability in this system or the exact angular-dependence of the fixed points. This conclusion stems from the weak nonlinearity assumption intrinsic to the perturbation analysis: the fixed points indicating a loss of stability are large enough to violate this assumption. Defining the dimensionless strength of the cubic nonlinearity as $\Pi_3 = \varepsilon k_{3x} {\alpha^*_{\mathrm{NZ}}}^2 / k_{1x}$, the fixed point that gives the weakest nonlinearity is $\Pi_{3,\min} = 0.667$, well above the conservative limit of 0.1. Nonetheless, numerical simulations were performed to investigate if the perturbation

analysis informs the nature of stability in these lattices—specifically its direction-dependence.

Figure 3-10 presents the results of applying a high-amplitude harmonic displacement to the central mass of a symmetric monatomic lattice. The parameter $E_{t,\delta}$ from Eq. (3.64) is computed and displayed at each point in the 20 x 20 unit cell region around the center. Black lines represent displacement contours. For a wave that propagates nearly uniformly outward (*i.e.* no beaming, as is known to occur at high frequencies) spectral content differs drastically along different angles far away from the source. The FFT's at two separate locations reveal that propagation along the $\hat{\boldsymbol{x}}$-direction breaks down from its original fundamental frequency into incommensurate frequencies, signaling a loss of stability. The 45-degree direction, on the other hand, retains nearly all the spectral content from the harmonic point forcing. Thus, the lattice direction exhibits less stability than the 45-degree direction.

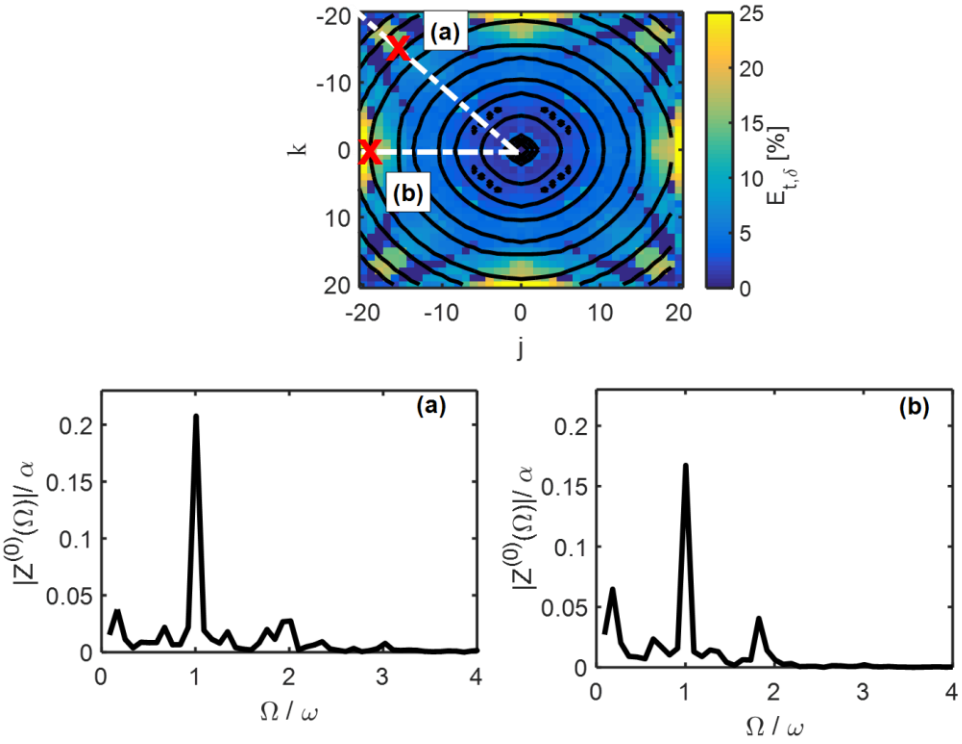

Figure 3-10. Point forcing of a monatomic lattice at its center. Stable spectral content at $\boldsymbol{\theta = 0^o}$ (a.) is compared to unstable spectral content at $\boldsymbol{\theta = 45^o}$ (b.): $\boldsymbol{m = 1, k_{1x} = 1, k_{1y} = 1, k_{2x} = 0, k_{2y} = 0, k_{3x} = 1, k_{3y} = 1, c_x = 0, c_y = 0, \omega = 1.3, \alpha = 2.7, a_1 = 1, a_2 = 1}$.

Such direction-dependence occurs also in simulations given plane-wave initial conditions. Considering again the monatomic lattice, high amplitude plane-wave initial conditions are injected in Figure 3-11, producing either propagation along the lattice direction or 45 degree direction. Only 0th order terms are retained such that the development of many frequencies over time is expected. Stable propagation should generate harmonics of the fundamental frequency whereas unstable propagation should break-down into incommensurate frequency content as the waveform injected into it cannot persist over time. Indeed, visual comparison of the displacements and corresponding spatial frequency content for both cases clearly delineates the stable propagation along the 45 degree

direction and unstable propagation along the lattice direction, in agreement with both the MMS results and harmonic point forcing simulation in Figure 3-12.

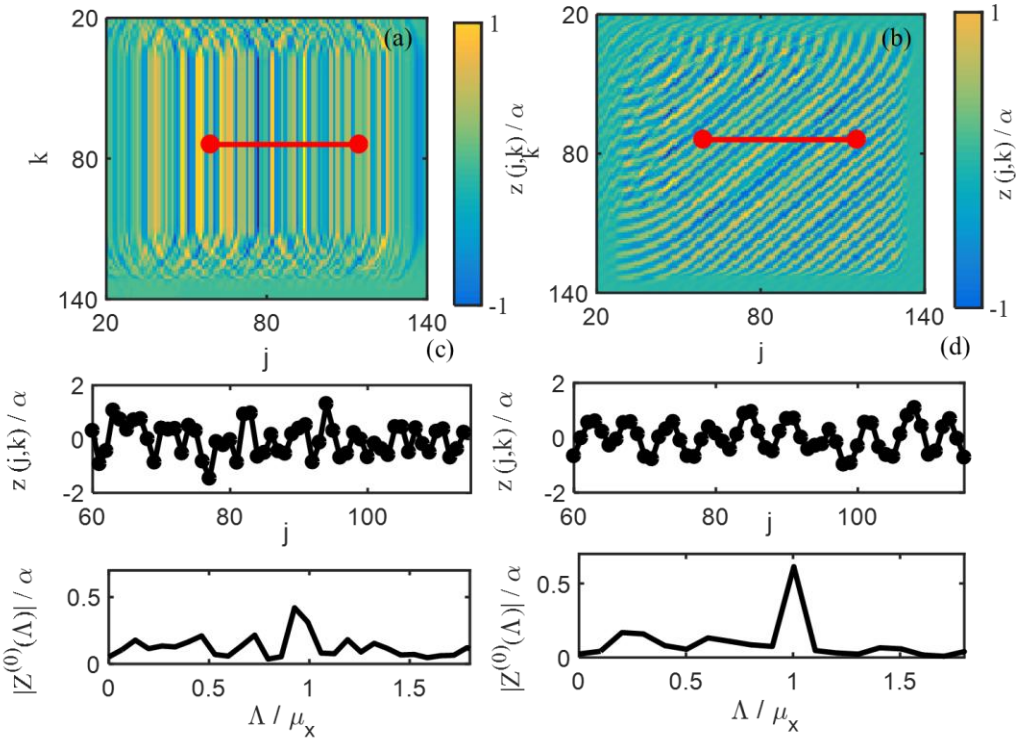

Figure 3-11. Plane-wave initial conditions in a monatomic lattice at high amplitudes for $\theta = 0^o$ (a.) as compared to $\theta = 45^o$ (b.). Red lines denote the group of masses at which the spatial FFT's (bottom) were computed: $m = 1, k_{1x} = 1, k_{1y} = 1, k_{2x} = 0, k_{2y} = 0, k_{3x} = 1, k_{3y} = 1, c_x = 0, c_y = 0, \omega_0 = 1.5, \alpha = 1.5, a_1 = 1, a_2 = 1.$

To determine numerically the stability of various directions, the angle θ and amplitude α were varied in multiple simulations and the amount of incommensurate energy in the lattice $E_{s,\delta}$ was recorded after 4 cycles of the 0[th]-order temporal frequency ω_0. The direction $\hat{\mathbf{r}}$ was selected to be $\hat{\mathbf{x}}$ such that $\boldsymbol{\mu} \cdot \hat{\mathbf{r}} = \mu_x$. Figure 3-12 through Figure 3-14 present the results for the monatomic and diatomic lattices as compared to the analytical fixed points α^* evaluated as a function of wave orientation θ at different frequencies ω_0. Numerical

results capture the perturbation trends: greater stability occurs as θ departs from 0 as well as when ω_0 decreases.

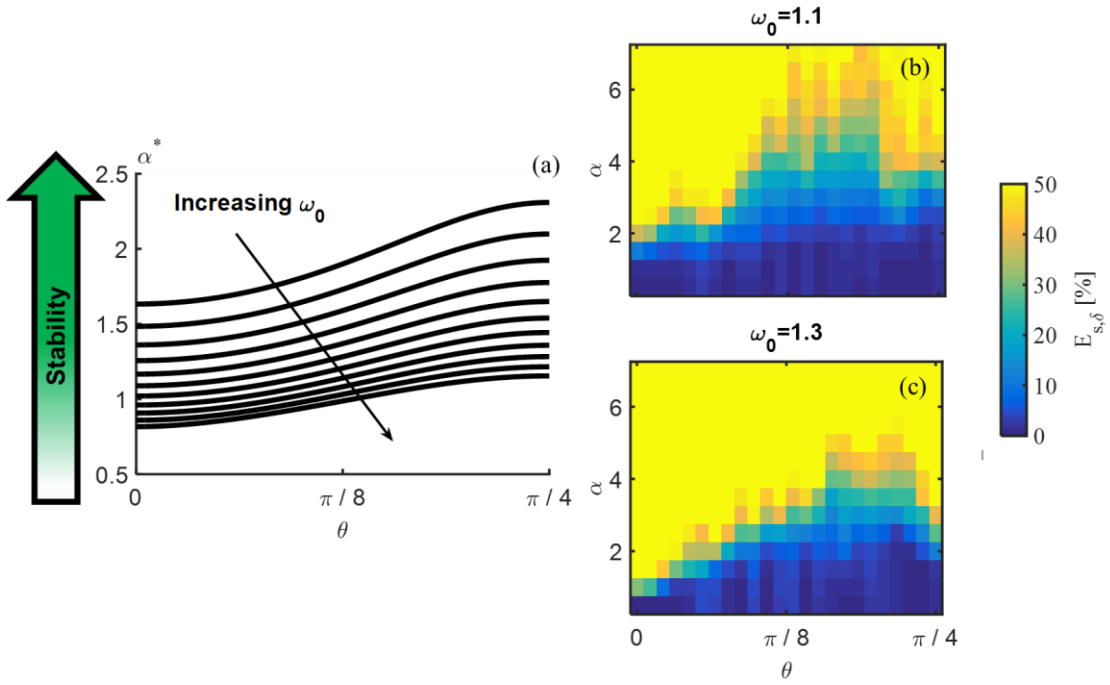

Figure 3-12. Unstable fixed points in the monatomic lattice evaluated as a function of propagation angle, exhibiting more stability as the angle departs from $\theta = 0$. Perturbation results (a) are compared to numerical results (b,c), demonstrating

similar trends as θ and ω_0 are independently varied: $m = 1, k_{1x} = 1, k_{1y} = 1, k_{2x} = 0, k_{2y} = 0, k_{3x} = 1, k_{3y} = 1, c_x = 0.1, c_y = 0.1, a_1 = 1, a_2 = 1$.

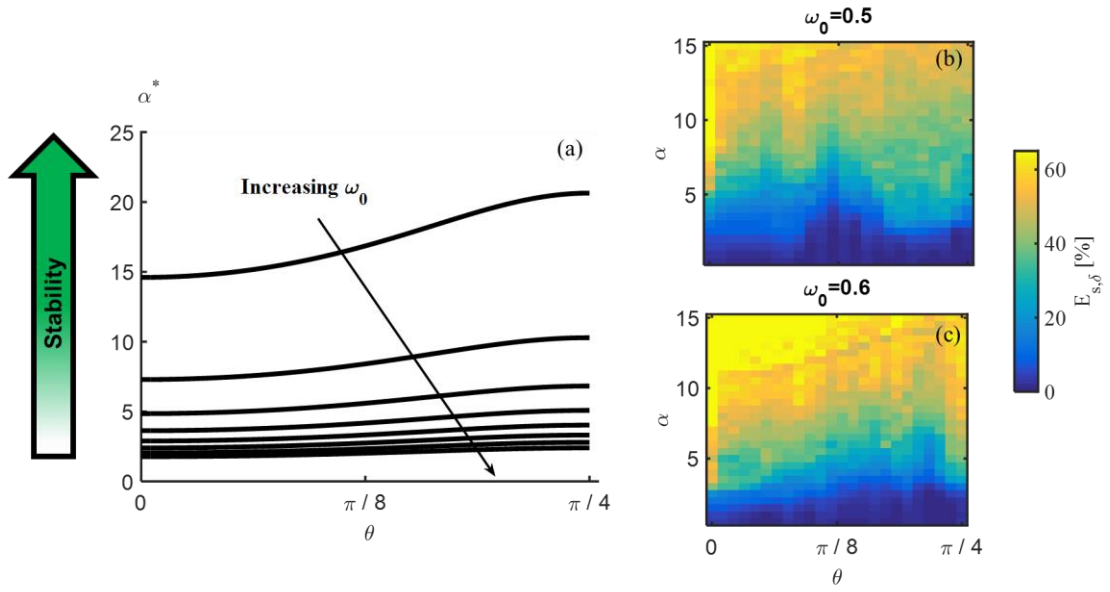

Figure 3-13. Unstable fixed points in the acoustic branch of the diatomic lattice evaluated as a function of propagation angle. Numerical results (a) capture the same trends in the angle and frequency dependence as the perturbation results (b,c): $m = 1, k_{1x} = 1, k_{1y} = 1, k_{2x} = 0, k_{2y} = 0, k_{3x} = 1, k_{3y} = 1, c_x = 0.1, c_y = 0.1, a_1 = 1, a_2 = \frac{1}{\sqrt{2}}$.

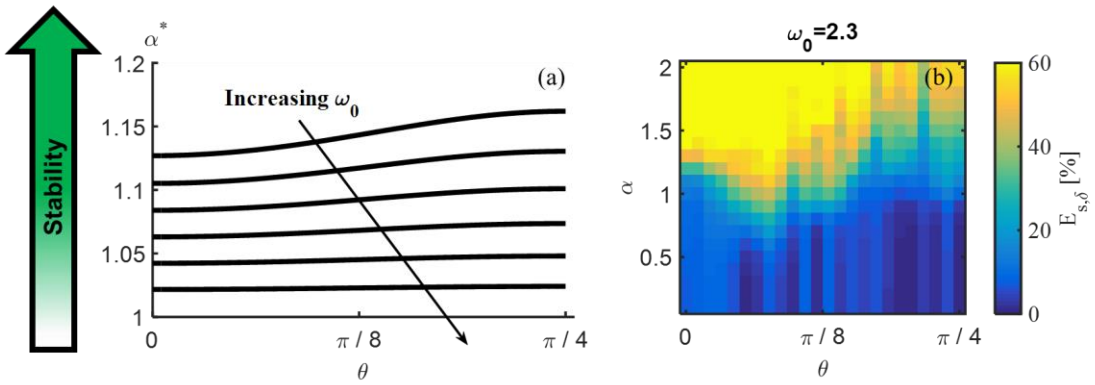

Figure 3-14. Unstable fixed points in the optical branch of the diatomic lattice evaluated as a function of propagation angle. Perturbation results (a) qualitatively

agree with numerical simulations (b): $m = 1, k_{1x} = 1, k_{1y} = 1, k_{2x} = 0, k_{2y} = 0, k_{3x} = 1, k_{3y} = 1, c_x = 0.1, c_y = 0.1, a_1 = 1, a_2 = \frac{1}{\sqrt{2}}$.

As was observed in simulations of the 1-D chain, unstable plane waves in the 2-D lattice can exhibit a non-stationary nature. Comparing snapshots of an unstable plane wave's spatial frequency content at different time instances has demonstrated that an unstable plane wave develops time-varying incommensurate frequency content.

The direction-dependence of the multi-harmonic coefficients (at fixed ω_0) resembles that of the plane-wave stability (also at fixed ω_0). Plane waves oriented along the lattice direction undergo relatively more variation in their spectral content after the inclusion of higher-order terms from the series solution than inclined directions. The same directions were found to destabilize (by breaking-down into incommensurate frequencies) at relatively low amplitudes of the 0th order solution. It is not surprising that directions that exchange more energy between spectral amplitudes when given a single harmonic have less stability because the generation of incommensurate frequency content implies a high degree of energy conversion. In other words, spectral energy appears to be naturally "more mobile" along the lattice direction, requiring more terms to become invariant and possessing a greater tendency towards instability.

3.7 Potential Applications

Directional stability may inspire new technology and devices. Two concepts are presented in this section. The first, pictured in Figure 3-15, proposes a new method for spatially encrypting data, in which the phasing between transducers produces a stable plane wave only when the correct passcode is entered. Otherwise, an unstable wave generates

incommensurate frequencies and information stored at the fundamental frequency is corrupted.

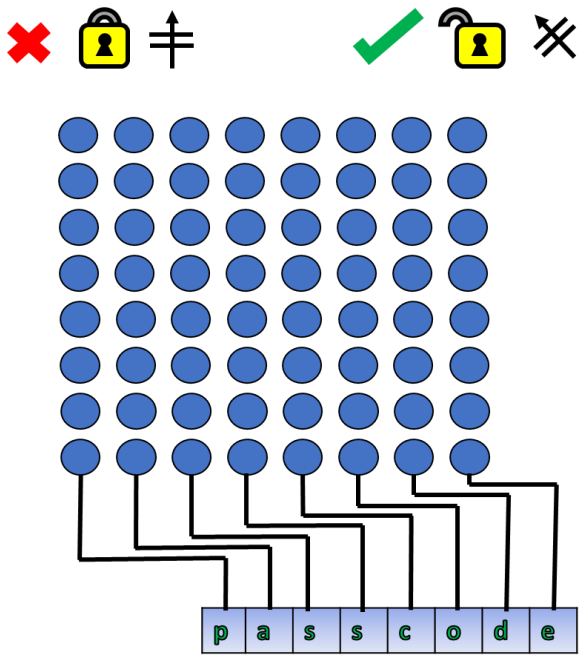

Figure 3-15. Encryption of information by setting the phasing between transducers to generate stable plane waves only when the correct passcode is entered.

Additionally, orientation of cracks in structures such as bridges, buildings, and aircraft could be identified in a novel, low power manner. Figure 3-16 depicts a transducer array mounted on a structure with a crack. Signals from the transducers reveal if the crack is oriented closer to 45^o or 0^o by simply examining the presence or absence of incommensurate frequencies. Information about crack orientation may be critical for assessing the threat cracks pose to the structure. Such application would function best in locations sufficiently removed from boundaries and impedance changes.

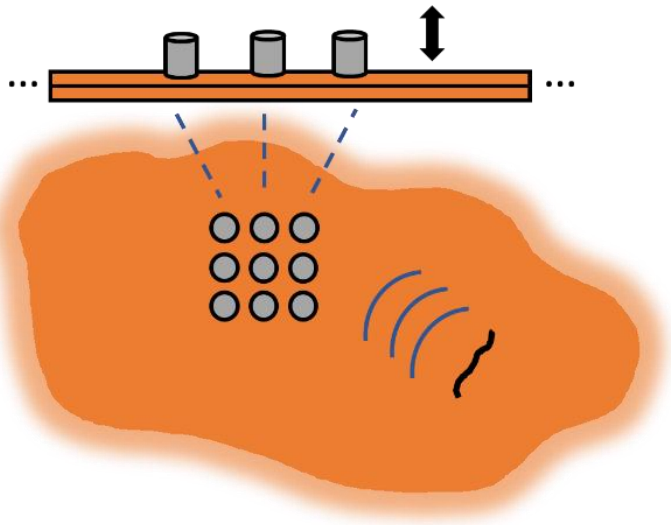

Figure 3-16. Orientation of cracks can be detected by examining the presence (or absence) of incommensurate frequencies in a transducer array.

3.8 Concluding Remarks

Higher-order multiple scales analysis uncovered directional invariant waveforms and plane-wave stability in two-dimensional nonlinear periodic lattices. Lattices admit multi-harmonic plane waves that propagate with little re-distribution of their spectral content, in contrast to waves in nonlinear media that generate and exchange energy with higher-harmonics. Such solutions exhibit directional-dependence which is confirmed by numerical simulations. These waveforms could inform technology that transmits and receives signals over long distances and times. Additionally, plane-wave stability is assessed by a local analysis including higher-order terms. Directions are shown to have varying stability in symmetrical lattices, a counterintuitive finding unexplored by prior studies. Numerical simulations capture this behavior, following the patterns of the direction-dependent basins of attraction predicted by perturbation. Devices are proposed that exploit directional stability for data encryption and damage detection.

CHAPTER 4. INTERNALLY-RESONANT WAVE ENERGY EXCHANGE IN WEAKLY NONLINEAR LATTICES AND METAMATERIALS

4.1 Overview

This chapter presents a multiple-scales analysis approach capable of capturing internally-resonant wave interactions in weakly nonlinear lattices and metamaterials. Example systems considered include a diatomic chain and a locally-resonant metamaterial-type lattice. At a number of regions in the band structure, both the frequency and wavenumber of one nonlinear plane wave may relate to another in a near-commensurate manner (such as in a 2:1 or 3:1 ratio) resulting in an internal resonance mechanism. As shown herein, nonlinear interactions in the lattice couple these waves and enable an energy exchange to occur. Near such internal resonances, previously-derived higher-order dispersion corrections for single plane wave propagation may break down, leading to singularities in the predicted nonlinear dispersion relationships. Using the presented multiple-scales approach and the two example systems, this chapter examines internal resonance occurring (i) within the same branch and (ii) between different branches of the band structure, resolving the aforementioned singularity issue while capturing the energy exchange.

Little attention has been given to internally-resonant wave interactions in nonlinear media. Considering commensurate wave-wave interaction of bulk waves in continuous solids with cubic nonlinearities, Rushchitsky *et al.* employed the method of slowly varying amplitude to derive spatial evolution equations for the amplitude exchange and energy conservation

laws for the interacting waves [110, 111]. Manktelow *et al.* investigated wave-wave interactions in a nonlinear monatomic lattice, with the aim of controlling the frequency shift of a primary wave in the presence of a secondary wave, each occupying a unique space on the lattice's band structure [112]. A special case in which the two waves possess commensurate frequency content (in the long wavelength limit) was examined, and their slow-scale energy exchange was remarked upon but was not of primary interest for their dispersion analysis. In [108, 113], a series of studies focused-on the harmonic excitation of a pre-compressed granular chain in the regime of weak quadratic stiffness with an extension to continuous layered systems in [114]. Using a perturbation expansion, the spatiotemporal higher-harmonic generation was derived, notably possessing a periodic amplitude exchange between the fundamental and second harmonic for the case of propagative driving frequencies. Panigrahi *et al.* explored internal resonances in the long wavelength limit of monatomic lattices with quadratic stiffness nonlinearities [115]. A multiple scales-derived phase portrait, aided by a local stability analysis, revealed transitions from oscillatory to emergent evolution of the interacting wave amplitudes which was validated qualitatively in numerical simulations.

This chapter is organized as follows. Section 4.2 describes the example lattices considered herein, namely a diatomic chain and locally-resonant metamaterial system. Section 4.3 details a multiple scales analysis of internally-resonant wave energy exchange in weakly nonlinear lattices, with the specific aim of capturing the energy exchange between propagating modes related in a 2:1 or 3:1 manner. In Section 4.4, a local stability analysis of the evolution equations reveals the fixed points of the dynamical systems. Of interest are those associated with neutrally stable temporal modulation of energy between the plane

waves. Section 4.5 compares results from direct numerical simulation of the lattice equations of motion to the perturbation predictions of the energy exchange. Good agreement is documented in the frequency and amplitude of the energy exchange. Section 4.6 conducts a dispersion analysis for internally-resonant plane waves, developing expressions that are valid for frequencies in which previous higher-order perturbation analyses for a single plane wave break down. Conclusions are drawn in Section 4.7.

4.2 System Description

Figure 4-1 displays a prototypical, weakly nonlinear layered system whose governing equations may admit internally-resonant waves. Such a system can model wave propagation in three-dimensional NaCl crystals along the (100) direction [1], for example, and discretized bi-material rods [116, 117]. The corresponding unit cell contains alternating masses (m_a and m_b) coupled with linear (k_1), quadratic (k_2), and cubic (k_3) stiffness.

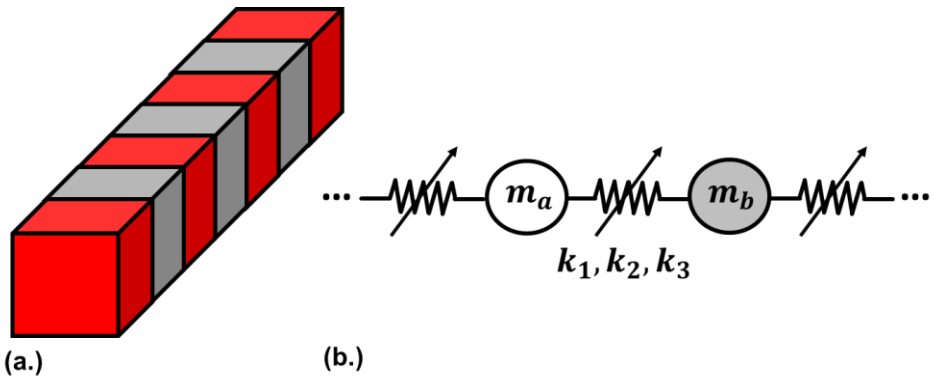

Figure 4-1. Nonlinear diatomic chain considered in this work. Bi-material rod that this system may model (a.) and its mass-spring representation (b.)

A locally-resonant lattice is also considered in which a network of primary masses contain embedded resonators, as illustrated in Figure 4-2. Coupling between the primary mass and its internal resonator, as well as between different primary masses, contains linear,

quadratic, and cubic stiffness terms. Such a system is used for the analysis of elastic metamaterials with negative effective properties and enhanced attenuation capabilities [6, 118, 119].

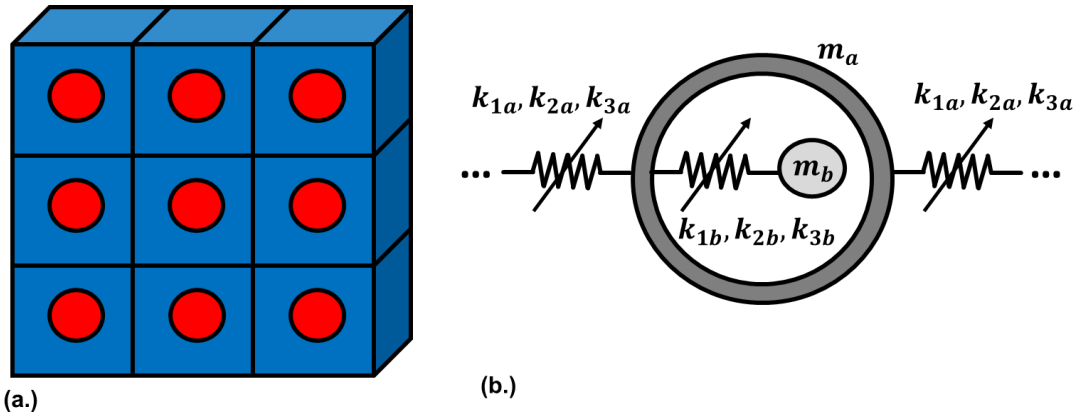

Figure 4-2. Nonlinear locally-resonant lattice. Plane wave propagation may occur perpendicular to the faces of the box-shaped unit cells containing spherical inclusions (a.). Spring-mass representation for plane wave propagation along a single direction (b.).

For both lattices, the equation of motion governing the j^{th} unit cell can be compactly represented in matrix form

$$\mathbf{M}\ddot{\mathbf{x}}_j + \sum_{p=-1}^{+1}\left[\mathbf{K}^{(p)}\mathbf{x}_{j+p}\right] + \varepsilon\mathbf{f}_{\mathbf{NL}}\left(\mathbf{x}_j, \mathbf{x}_{j-1}, \mathbf{x}_{j+1}\right) = \mathbf{0}, \quad j = -\infty \ldots \infty \tag{4.1}$$

where $\mathbf{x}_j = \begin{bmatrix} x_a(j,t) \\ x_b(j,t) \end{bmatrix}$ represents the displacement from equilibrium of each degree of freedom and $\dot{(\,)}$ denotes time differentiation. For Figure 4-1 and Figure 4-2, the mass matrices simplify to

$$\mathbf{M} = \begin{bmatrix} m_a & 0 \\ 0 & m_b \end{bmatrix} \tag{4.2}$$

Stiffness matrices for the lattice in Figure 4-1 are given by

$$\mathbf{K}^{(0)} = \begin{bmatrix} 2k_1 & -k_1 \\ -k_1 & 2k_1 \end{bmatrix} \tag{4.3}$$

$$\mathbf{K}^{(-1)} = \begin{bmatrix} 0 & -k_1 \\ 0 & 0 \end{bmatrix} \tag{4.4}$$

$$\mathbf{K}^{(1)} = \begin{bmatrix} 0 & 0 \\ -k_1 & 0 \end{bmatrix} \tag{4.5}$$

The associated stiffness matrices for the lattices with resonators in Figure 4-2 are given by

$$\mathbf{K}^{(0)} = \begin{bmatrix} 2k_{1\mathrm{a}} & -k_{1\mathrm{b}} \\ -k_{1\mathrm{b}} & k_{1\mathrm{b}} \end{bmatrix} \tag{4.6}$$

$$\mathbf{K}^{(-1)} = \mathbf{K}^{(1)} = \begin{bmatrix} 0 & -k_{1a} \\ 0 & 0 \end{bmatrix} \tag{4.7}$$

All interactions from nonlinear stiffness terms combine in the $\mathbf{f_{NL}}$ vector, which is ordered to be small with the book-keeping device ε. For the diatomic lattice, the nonlinear terms are

$$\begin{aligned} \mathbf{f_{NL}}(1) = &-k_2\big(x_b(j) - x_a(j)\big)^2 + k_2\big(x_b(j-1) - x_a(j)\big)^2 \\ &-k_3\big(x_b(j) - x_a(j)\big)^3 - k_3(x_b(j-1) - x_a(j))^3 \end{aligned} \tag{4.8}$$

$$\begin{aligned} \mathbf{f_{NL}}(2) = &-k_2\big(x_a(j+1) - x_b(j)\big)^2 + k_2\big(x_a(j) - x_b(j)\big)^2 \\ &-k_3\big(x_a(j+1) - x_b(j)\big)^3 - k_3(x_a(j) - x_b(j))^3 \end{aligned} \tag{4.9}$$

The locally-resonant lattice possesses the following nonlinear terms

$$\begin{aligned} \mathbf{f_{NL}}(1) = &-k_{2\mathrm{a}}\big(x_a(j+1) - x_a(j)\big)^2 + k_{2\mathrm{a}}\big(x_a(j-1) - x_a(j)\big)^2 \\ &-k_{3\mathrm{a}}\big(x_a(j+1) - x_a(j)\big)^3 - k_{3\mathrm{a}}\big(x_a(j-1) - x_a(j)\big)^3 \\ &-k_{2b}\big(x_b(j) - x_a(j)\big)^2 - k_{3b}(x_b(j) - x_a(j))^3 \end{aligned} \tag{4.10}$$

$$\mathbf{f_{NL}}(2) = k_{2b}\big(x_b(j) - x_a(j)\big)^2 + k_{3b}(x_b(j) - x_a(j))^3 \tag{4.11}$$

In general, quadratic (*i.e.*, k_2 or k_{2a}, k_{2b}) and cubic (*i.e.*, k_3 or k_{3a}, k_{3b}) stiffness may arise from a Taylor series expansion of an arbitrary nonlinear interaction.

4.3 Multiple Scales Analysis of Internally-Resonant Waves

A Multiple Scales technique is next proposed for investigating internal resonances appearing in Eq. (4.1). Time scales of successively slower progression are introduced

$$t = T_0 + \varepsilon T_1 + \cdots \varepsilon^n T_n \tag{4.12}$$

with their associated time derivatives

$$\left(\dot{\ }\right) = \mathrm{D}_0(\ \ ) + \varepsilon \mathrm{D}_1(\ \ ) + \cdots + \varepsilon^n \mathrm{D}_n(\ \ ) \tag{4.13}$$

where $\mathrm{D}_n(\ \ )$ denotes differentiation with respect to T_n. Additionally, the solution is expanded in a power series

$$\mathbf{x}_j = \mathbf{x}_j^{(0)} + \varepsilon \mathbf{x}_j^{(1)} + \cdots + \varepsilon^n \mathbf{x}_j^{(n)} \tag{4.14}$$

Using the expansions in Eqs. (4.13) and (4.14), Eq. (4.1) can be separated into a series of cascading differential equations by collecting matching orders of ε. The first two equations are

$$\varepsilon^0 \colon \mathbf{M}\ddot{\mathbf{x}}_j^{(0)} + \textstyle\sum_{p=-1}^{+1}\left[\mathbf{K}^{(p)}\mathbf{x}_{j+p}^{(0)}\right] = \mathbf{0} \tag{4.15}$$

$$\varepsilon^1 \colon \mathbf{M}\ddot{\mathbf{x}}_j^{(1)} + \textstyle\sum_{p=-1}^{+1}\left[\mathbf{K}^{(p)}\mathbf{x}_{j+p}^{(1)}\right] = -2\mathrm{D}_0\mathrm{D}_1\mathbf{M}\mathbf{x}_j^{(0)} - \mathbf{f}_{\mathbf{NL}}\left(\mathbf{x}_j^{(0)}, \mathbf{x}_{j-1}^{(0)}, \mathbf{x}_{j+1}^{(0)}\right) \tag{4.16}$$

In general, Eq. (4.15) admits a linear combination of Bloch waves, each of the form

$$\mathbf{x}_j^{(0)} = \tfrac{1}{2}\boldsymbol{\phi}(\omega_0) A \mathrm{e}^{\mathrm{i}\omega_0 T_0}\mathrm{e}^{-\mathrm{i}\mu j} + \mathrm{c.\,c.} \tag{4.17}$$

where A denotes the complex amplitude and c. c. denotes the complex conjugate of all preceding terms. The temporal frequency (ω_0) and non-dimensional wavenumber (μ) are related by the lattice's dispersion curve, which is found by substituting Eq. (4.17) into (4.15) and then solving the resulting eigenvalue problem.

$$\omega_0 = \sqrt{\frac{k_1(m_b+m_a)}{m_a m_b} \mp \frac{k_1}{2}\sqrt{\frac{4m_b^2+4m_a^2+8m_a m_b\cos\mu}{m_a^2 m_b^2}}} \tag{4.18}$$

$$\omega_0 = \tfrac{1}{2}\Big[\frac{2}{m_a m_b}\big((-2k_{1a}m_b\cos\mu + 2k_{1a}m_b + k_{1b}m_a + k_{1b}m_b) \mp (4k_{1a}^2 m_b^2\cos^2\mu - 8k_{1a}^2 m_b^2\cos\mu + 4m_a m_b k_{1a}k_{1b}\cos\mu - 4m_b^2 k_{1a}k_{1b}\cos\mu + 4k_{1a}^2 m_b^2 - 4k_{1a}k_{1b}m_a m_b + 4k_{1a}k_{1b}m_b^2 + k_{1b}^2 m_a^2 + 2k_{1b}^2 m_a m_b + k_{1b}^2 m_b^2)^{\frac{1}{2}}\big)\Big]^{\frac{1}{2}} \tag{4.19}$$

Eqs. (4.18) and (4.19) provide the 0^{th}-order dispersion relationships for the diatomic and locally-resonant chains, respectively. Additionally, displacements within each unit cell take on synchronous motion associated with the wave propagation mode shape $\boldsymbol{\phi}$

$$\boldsymbol{\phi} = \begin{bmatrix} 1 \\ \frac{-\omega_0^2 m_a + 2k_1}{k_1(1+e^{i\mu})} \end{bmatrix} \tag{4.20}$$

$$\boldsymbol{\phi} = \begin{bmatrix} 1 \\ \frac{-m_a\omega_0^2 + 2k_{1a}(1-\cos\mu) + k_{1b}}{k_{1b}} \end{bmatrix} \tag{4.21}$$

which correspond to Eqs. (4.18) and (4.19), respectively. Figure 4-3 displays the 0^{th}-order dispersion relationships for the example systems. Since two degrees of freedom exist per unit cell, two distinct branches form their band structures: a lower, or acoustic branch and an upper, or optical branch, separated by a bandgap.

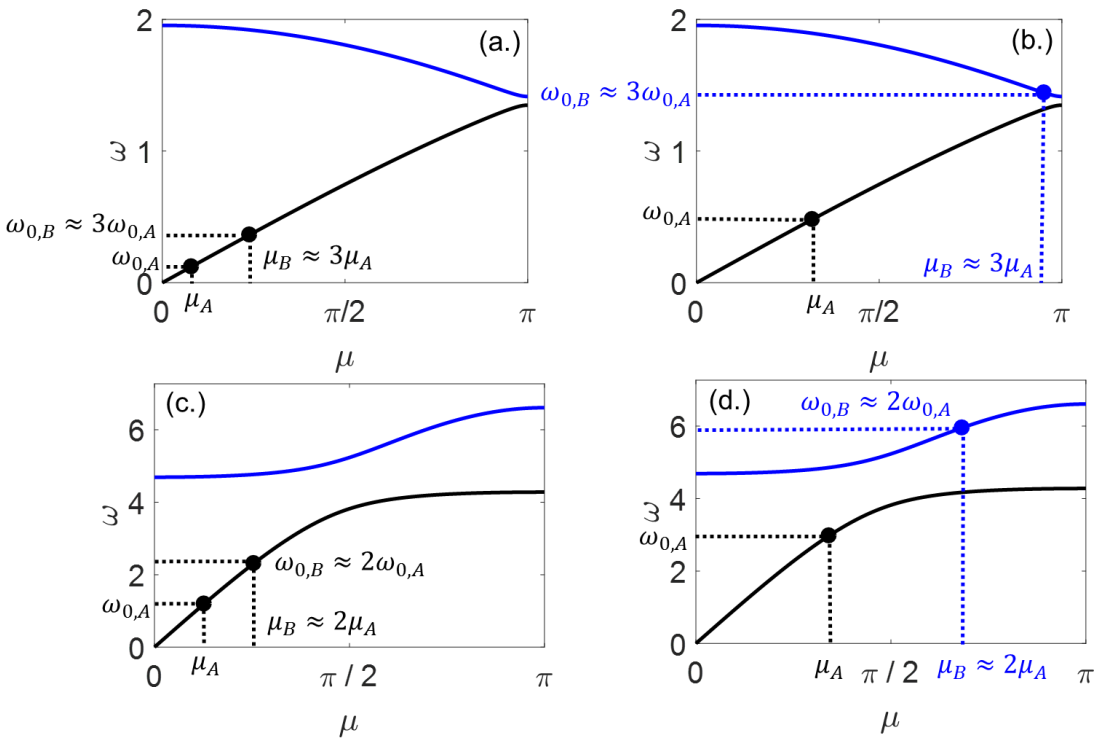

Figure 4-3. 0th-order dispersion curves for the diatomic (a,b) and locally-resonant (c,d) lattices. Internal resonance can occur within the same branch or between different branches and commonly takes the form of 2:1 or 3:1.

Recall from Sections 2.3, 2.4, and 3.3 that higher-order analysis of single-frequency nonlinear plane waves break down for frequencies associated with internal resonance. This phenomenon occurs when the considered wave, represented by *A*, is in a nearly-commensurate relationship with another wave, represented by *B*. This may occur whenever $\mu_B \approx \frac{n_2}{n_1}\mu_A$ and $\omega_{0,B} \approx \frac{n_2}{n_1}\omega_{0,A}$, where n_1 and n_2 are integers. As established herein, it can occur within the same branch or between different branches. Common forms of internal resonance are 2:1 and 3:1, which are enabled by quadratic and cubic stiffness interactions, respectively, and such forms are principally studied in this work. Figure 4-3 depicts these internal resonances as they appear in relation to band structure.

In the long wavelength limit, the near-linear slope of the dispersion curve technically produces many internal resonances. However, higher-order internal resonances, *e.g.* 5:3:1, can be expected to exhibit weaker interactions amongst the multiple wave propagation modes. Spectral content from weak stiffness nonlinearities naturally decreases at increasingly higher-harmonics. Thus, the interaction exclusively between two waves will be considered herein as their amplitudes will be dominant.

Anticipating internal resonance amongst two waves, an *A* and *B* wave are introduced at the 0^{th}-order

$$\mathbf{x}_j^{(0)} = \frac{1}{2}\boldsymbol{\phi}\left(\omega_{0,\mathrm{A}}\right)A\mathrm{e}^{\mathrm{i}\omega_{0,\mathrm{A}}T_0}\mathrm{e}^{-\mathrm{i}\mu_A j} + \frac{1}{2}\boldsymbol{\phi}\left(\omega_{0,\mathrm{B}}\right)B\mathrm{e}^{\mathrm{i}\omega_{0,\mathrm{B}}T_0}\mathrm{e}^{-\mathrm{i}\mu_B j} + \mathrm{c.c.} \quad (4.22)$$

For $n\colon 1$ internal resonance, the frequencies of the *A*-wave and *B*-wave are related by

$$\omega_{0,\mathrm{B}} = n\omega_{0,\mathrm{A}} + \varepsilon\sigma_\omega \quad (4.23)$$

$$\mu_{\mathrm{B}} = n\mu_{\mathrm{A}} + \varepsilon\sigma_\mu \quad (4.24)$$

where small detuning parameters σ_ω and σ_μ are introduced to also capture wave interactions in close proximity to the $n\colon 1$ relationship. Since both $\left(\mu_{\mathrm{A}}, \omega_{0,\mathrm{A}}\right)$ and $\left(\mu_{\mathrm{B}}, \omega_{0,\mathrm{B}}\right)$ must satisfy the lattice's linear dispersion relationship, the detuning parameters cannot be set independently of each other. For example, if the *A* wave frequency and wavenumber are known and σ_μ is prescribed, then μ_B can be determined from Eq. (4.24). The *B* wave frequency $\omega_{0,\mathrm{B}}$ can then be readily identified such that Eq. (4.18) or (4.19) is satisfied and the associated σ_ω can be found from Eq. (4.23).

The complex wave amplitudes A and B can be decomposed into polar form

$$A = \alpha_A \mathrm{e}^{\mathrm{i}\beta_A} \quad (4.25)$$

$$B = \alpha_B \mathrm{e}^{\mathrm{i}\beta_B} \quad (4.26)$$

By virtue of satisfying Eq. (4.15), the real quantities $\alpha_A, \alpha_B, \beta_A$, and β_B are functions of only the slower time scales: T_1, T_2, *etc.* Once $\mathbf{x}_j^{(0)}$ is defined, the right-hand side of Eq. (4.16) can be updated

$$\mathrm{D}_0^2\mathbf{M}\mathbf{x}_j^{(1)} + \sum_{p=-1}^{+1}\left[\mathbf{K}^{(p)}\mathbf{x}_j^{(1)}\right] = -\mathbf{M}\mathrm{D}_1\left(\mathrm{i}\omega_{0,\mathrm{A}}\boldsymbol{\phi}\left(\omega_{0,\mathrm{A}}\right)A\mathrm{e}^{\mathrm{i}\omega_{0,\mathrm{A}}T_0}\mathrm{e}^{-\mathrm{i}\mu_A j} + \mathrm{i}\omega_{0,\mathrm{B}}\boldsymbol{\phi}\left(\omega_{0,\mathrm{B}}\right)B\mathrm{e}^{\mathrm{i}\omega_{0,\mathrm{B}}T_0}\mathrm{e}^{-\mathrm{i}\mu_B j}\right) + \sum_{u=0}^{3}\sum_{w=-3}^{3}\mathbf{a}_{\mathbf{u},\mathbf{w}}\mathrm{e}^{\mathrm{ui}\left(\omega_{0,A}T_0-\mu_A j\right)}\mathrm{e}^{\mathrm{wi}\left(\omega_{0,B}T_0-\mu_B j\right)} + \mathrm{c.c.} \tag{4.27}$$

where $\mathbf{a}_{\mathbf{u},\mathbf{w}}$ denotes the amplitude at each of the multi-harmonic inhomogeneities and can be expected to be functions of the lattice parameters in addition to the A and B wave frequencies and amplitudes. All possible 1st-order frequency combinations that occur after inserting Eq. (4.18) into $\mathbf{f}_{\mathbf{NL}}$ are included in the double-summation. Quadratic nonlinearities result in even-integer higher harmonics whereas those from cubic nonlinearities result in odd-integer higher harmonics. Additionally, cubic nonlinearities produce secular terms at $\mathrm{e}^{\mathrm{i}\omega_{0,\mathrm{A}}T_0}\mathrm{e}^{-\mathrm{i}\mu_A j}$ and $\mathrm{e}^{\mathrm{i}\omega_{0,\mathrm{B}}T_0}\mathrm{e}^{-\mathrm{i}\mu_B j}$.

Due to the n: 1 internal resonance, terms at $\mathrm{e}^{n\mathrm{i}\omega_{0,A}T_0}\mathrm{e}^{-n\mathrm{i}\mu_A j}$ can be expressed in terms of $\mathrm{e}^{\mathrm{i}\omega_{0,\mathrm{B}}T_0}\mathrm{e}^{-\mathrm{i}\mu_B j}$ (and vice versa). This result is clear after manipulation of the relationships in Eqs. (4.23) and (4.24)

$$n\left(\omega_{0,A}T_0 - \mu_A j\right) = \omega_{0,B}T_0 - \mu_B j - \varepsilon\sigma_\omega T_0 + \varepsilon\sigma_\mu j \equiv \omega_{0,B}T_0 - \mu_B j - \sigma_\omega T_1 + \sigma_\mu J_1 \tag{4.28}$$

Note that a slow spatial scale, $J_1 \equiv \varepsilon j$, has been introduced analogous to the first slow time scale $T_1 \equiv \varepsilon t$, both of which appear with detuning parameters as phase shifts at a slower spatio-temporal scale.

Next, secular terms are removed from Eq. (4.23) in order to assure convergence of the imposed ordering approach. First, terms containing $e^{i\omega_{0,A}T_0}e^{-i\mu_A j}$ (as well as their complex conjugates) are addressed. To identify all of these terms, the relationships in Eq. (4.28) must be invoked since, for example, $\omega_{0,B} - \omega_{0,A} \approx \omega_{0,A}$ when $n = 2$. After pre-multiplying all terms with $e^{i\omega_{0,A}T_0}e^{-i\mu_A j}$ dependence by $\boldsymbol{\phi}^{\mathbf{H}}(\omega_{0,A})$ and separating real and imaginary parts, expressions for the slow-time amplitude and phase evolution for the *A* wave, $D_1(\alpha_A)$ and $D_1(\beta_A)$, result. Considering 2:1 internal resonance from solely quadratic stiffness, these evolution equations can be written as

$$D_1(\alpha_A) = \alpha_A \alpha_B \mathrm{Re}\left(\overline{G}e^{i\gamma}\right) \tag{4.29}$$

$$D_1(\beta_A) = \alpha_B \mathrm{Im}\left(\overline{G}e^{i\gamma}\right) \tag{4.30}$$

where $\overline{G}$ is a function of frequency and lattice parameters provided in Appendix B for both material systems. Additionally, a variable representing the relative phase between the *A* and *B* waves has been introduced

$$\gamma \equiv \beta_B + \sigma_\omega T_1 - \sigma_\mu J_1 - n\beta_A \tag{4.31}$$

which results in a set of autonomous evolution equations. The autonomous evolution equations associated with 3:1 internal resonance and solely cubic stiffness are similar to Eqs. (4.25)-(4.26)

$$D_1(\alpha_A) = \mathrm{Re}\left(\alpha_B \alpha_A^2 \bar{I} e^{i\gamma} + \alpha_B^2 \alpha_A \overline{L} + \alpha_A^3 \overline{N}\right) \tag{4.32}$$

$$D_1(\beta_A) = \mathrm{Im}\left(\alpha_B \alpha_A \bar{I} e^{i\gamma} + \alpha_B^2 \overline{L} + \alpha_A^2 \overline{N}\right) \tag{4.33}$$

where Appendix B provides expressions for $\bar{I}, \overline{L}$, and $\overline{N}$ for both material systems. Note that the presence of cubic stiffness will result in the appearance of additional terms in the

evolution equations for 2:1 internal resonance, while the presence of quadratic stiffness will *not* result in additional terms in the evolution equations governing 3:1 internal resonance. The additional terms in the 2:1 evolution equations complicate the procedure (introduced next) for reducing the state space from $(\alpha_A, \beta_A, \alpha_B, \beta_B)$ to (α_B, γ). However, numerical integration of the four-dimensional state space illustrates that cubic stiffness has a negligible effect on 2:1 energy exchange.

Likewise, terms appearing with $\mathrm{e}^{\mathrm{i}\omega_{0,\mathrm{B}}T_0}\mathrm{e}^{-\mathrm{i}\mu_B j}$ are also secular. To collect all terms at these frequencies requires application of Eq. (4.28) followed by premultiplying with $\boldsymbol{\phi}^{\mathbf{H}}(\omega_{0,\mathrm{B}})$. Expressions for the slow-time amplitude and phase evolution for the *B* wave, $\mathrm{D}_1(\alpha_B)$ and $\mathrm{D}_1(\beta_B)$, result. For a 2:1 internal resonance, the evolution equations are given by

$$\mathrm{D}_1(\alpha_B) = \alpha_A^2 \mathrm{Re}\left(\overline{H}\mathrm{e}^{-\mathrm{i}\gamma}\right) \tag{4.34}$$

$$\mathrm{D}_1(\beta_B) = \frac{\alpha_A^2}{\alpha_B} \mathrm{Im}\left(\overline{H}\mathrm{e}^{-\mathrm{i}\gamma}\right) \tag{4.35}$$

and for the 3:1 internal resonance by

$$\mathrm{D}_1(\alpha_B) = \mathrm{Re}\left(\alpha_A^2 \alpha_B \bar{P} + \alpha_B^3 \bar{Q} + \alpha_A^3 \bar{R}\mathrm{e}^{-\mathrm{i}\gamma}\right) \tag{4.36}$$

$$\mathrm{D}_1(\beta_B) = \mathrm{Im}\left(\alpha_A^2 \bar{P} + \alpha_B^2 \bar{Q} + \frac{\alpha_A^3}{\alpha_B} \bar{R}\mathrm{e}^{-\mathrm{i}\gamma}\right) \tag{4.37}$$

where Appendix B provides expressions for $\overline{H}$, $\bar{P}, \overline{Q}$, and $\bar{R}$ for each material system. At this point in the development, the state space of response quantities is either governed by Eqs. (4.29)-(4.30) and (4.34)-(4.35) in the case of a 2:1 internal resonance, or Eqs. (4.32)-(4.33) and (4.36)-(4.37) in the case of a 3:1 internal resonance.

The dimension of the state space can be reduced from four quantities $(\alpha_A, \alpha_B, \beta_A, \beta_B)$ to three $(\alpha_A, \alpha_B, \gamma)$ by differentiating Eq. (4.31) with respect to T_1 and substituting-in the known expressions for $\mathrm{D}_1(\beta_A)$ and $\mathrm{D}_1(\beta_B)$

$$\mathrm{D}_1(\gamma) = \mathrm{D}_1(\beta_B) + \sigma_\omega - n\mathrm{D}_1(\beta_A) \tag{4.38}$$

Applying this procedure to the case of 2:1 internal resonance yields the following reduced set of evolution equations quadratic in the wave amplitudes

$$\mathrm{D}_1(\alpha_A) = \alpha_A \alpha_B G \cos(\psi_G + \gamma) \tag{4.39}$$

$$\mathrm{D}_1(\alpha_B) = \alpha_A^2 H \cos(\psi_H + \gamma) \tag{4.40}$$

$$\mathrm{D}_1(\gamma) = \sigma_\omega - 2\alpha_B G \sin(\psi_G + \gamma) - \frac{\alpha_A^2}{\alpha_B} H \sin(\psi_H + \gamma) \tag{4.41}$$

where $\overline{G} = G\mathrm{e}^{\mathrm{i}\psi_G}$ and $\overline{H} = He^{-\mathrm{i}\psi_H}$. The case of 3:1 internal resonance gives rise to a reduced set evolution equations cubic in the wave amplitudes

$$\mathrm{D}_1(\alpha_A) = \alpha_B \alpha_A^2 I \cos(\psi_I + \gamma) \tag{4.42}$$

$$\mathrm{D}_1(\alpha_B) = \alpha_A^3 R \cos(\psi_R + \gamma) \tag{4.43}$$

$$\mathrm{D}_1(\gamma) = \alpha_A^2 P + \alpha_B^2 Q - \frac{\alpha_A^3}{\alpha_B} \mathrm{R} \sin(\psi_R + \gamma) + \sigma_\omega$$
$$-3(\alpha_B \alpha_A I \sin(\psi_I + \gamma) + \alpha_B^2 L + \alpha_A^2 N) \tag{4.44}$$

where $\overline{I} = I\mathrm{e}^{\mathrm{i}\psi_I}, \overline{L} = L\mathrm{e}^{\mathrm{i}\psi_L}, \overline{N} = N\mathrm{e}^{\mathrm{i}\psi_N}, \overline{P} = P\mathrm{e}^{\mathrm{i}\psi_P}, \overline{Q} = Q\mathrm{e}^{\mathrm{i}\psi_Q}$ and $\overline{R} = R\mathrm{e}^{-\mathrm{i}\psi_R}$.

Using the approach outlined in [115], solutions are sought on a hyperplane, reducing the phase space from $(\alpha_A, \alpha_B, \gamma)$ to (α_B, γ). Key to this step is to seek out-of-phase evolution of the *A* and *B* wave amplitudes. For energy exchange which conserves total mechanical energy, it can be expected that the $\mathrm{D}_1(\alpha_A)$ and $\mathrm{D}_1(\alpha_B)$ are out of phase. The first step is to recognize a relationship between the phase terms from the secular term removal

$$\psi_G - \psi_H = \pi \tag{4.45}$$

$$\psi_I - \psi_R = \pi \tag{4.46}$$

Although difficult to prove analytically due to the complexity of the expressions, numerical evaluation using multiple parameter sets has confirmed Eqs. (4.45)-(4.46) to machine

precision. The relationships in Eqs. (4.45) and (4.46) do not define out-of-phase amplitude evolution but instead enable a reduction of the dimension of the state space. Accordingly,

$$\frac{\mathrm{D}_1\alpha_A}{\mathrm{D}_1\alpha_B} = -\frac{1}{r}\frac{\alpha_B}{\alpha_A} \tag{4.47}$$

Eq. (4.47) simplifies to

$$r\alpha_A^2 + \alpha_B^2 = E \tag{4.48}$$

where $r = \frac{H}{G}$ for 2:1 internal resonance and $r = \frac{R}{I}$ for 3:1 internal resonance. While Eq. (4.48) is not a statement of conservation of energy, the solutions on such a hyperplane must conserve the energy-like integration constant E. Thus, since the *A* and *B* waves are the only wave propagation modes present, each mode grows and decays at the expense of exchanging energy with the other when considering solutions on the ellipse in Eq. (4.48). Substituting Eq. (4.48) into the 2:1 expressions in Eqs. (4.39)-(4.41) gives

$$\mathrm{D}_1(\alpha_B) = (E - \alpha_B^2)G\cos(\psi_H + \gamma) \tag{4.49}$$

$$\mathrm{D}_1(\gamma) = \sigma_\omega + 2\alpha_B G\sin(\psi_H + \gamma) - \frac{(E-\alpha_B^2)}{\alpha_B}G\sin(\psi_H + \gamma) \tag{4.50}$$

For 3:1 internal resonance, the energy-reduced phase space in Eqs. (4.42)-(4.44) simplifies to

$$\mathrm{D}_1\alpha_B = \left(\frac{1}{r}(E - \alpha_B^2)\right)^{\frac{3}{2}} R\cos(\psi_R + \gamma) \tag{4.51}$$

$$\mathrm{D}_1(\gamma) = \left(\frac{1}{r}(E - \alpha_B^2)\right)P + \alpha_B^2 Q - \frac{1}{\alpha_B}\left(\frac{1}{r}(E - \alpha_B^2)\right)^{\frac{3}{2}} R\sin(\psi_R + \gamma) + \sigma_\omega$$
$$-3\left(\alpha_B\left(\frac{1}{r}(E - \alpha_B^2)\right)^{\frac{1}{2}} I\sin(\psi_I + \gamma) + \alpha_B^2 L + \left(\frac{1}{r}(E - \alpha_B^2)\right)N\right) \tag{4.52}$$

4.4 Local Stability Analysis

The evolution of the amplitudes and phases of the *A* and *B* waves defines the interaction of the internally-resonant plane waves. The stability of their evolution must be assessed to predict if a given distribution of initial amplitudes and phases will persist for long spatial and temporal measures. To investigate stability, the temporal evolution of the two-dimensional reduced phase space is reconstituted to the original time scale

$$\dot{\alpha}_B = \varepsilon \mathrm{D}_1(\alpha_B) \tag{4.53}$$

$$\dot{\gamma} = \varepsilon \mathrm{D}_1(\gamma) \tag{4.54}$$

The associated fixed points (α_B^*, γ^*) satisfy $\dot{\alpha}_B|_{(\alpha_B^*,\gamma^*)} = 0$ and $\dot{\gamma}|_{(\alpha_B^*,\gamma^*)} = 0$. Stability can then be determined local to each fixed point by examining their associated λ value

$$\lambda = \det J \tag{4.55}$$

where

$$J = \begin{bmatrix} \frac{\partial}{\partial \alpha_B}\left(\mathrm{D}_1(\alpha_B)\right) & \frac{\partial}{\partial \gamma}\left(\mathrm{D}_1(\alpha_B)\right) \\ \frac{\partial}{\partial \alpha_B}\left(\mathrm{D}_1(\gamma)\right) & \frac{\partial}{\partial \gamma}\left(\mathrm{D}_1(\gamma)\right) \end{bmatrix}_{(\alpha_B^*,\gamma^*)} \tag{4.56}$$

When λ is purely real, $\lambda > 0$ denotes instability, $\lambda < 0$ stability, and $\lambda = 0$ denotes neutral stability. When λ is purely imaginary (*i.e.*, $\lambda = \pm \mathrm{i}\omega_J$), the evolution of $\alpha_A, \alpha_B,$ and γ are oscillatory with frequency ω_J. The fixed point equations arising from 2:1 resonance are quadratic with respect to α_B and consequently the fixed point solutions can readily be determined in closed form. Table 4-1 summarizes the results. Note the existence of two fixed points associated with periodic orbits and two unstable fixed points.

Table 4-1. Fixed Points for 2:1 internal resonance valid for both lattices considered. The *A*-wave fixed point is not a direct component of the two-dimensional phase space of (α_B, γ) but rather determined by the energy ellipse relationship.

Fixed Point	α_B^*	α_A^*	γ^*	λ
FP 1 & 2	$\frac{-\sigma_\omega \mp \sqrt{\sigma_\omega^2 + 12EG^2}}{6G\sin(\psi_H + \gamma^*)}$	$\sqrt{\frac{1}{r}\left[E - \left(\frac{-\sigma_\omega \mp \sqrt{\sigma_\omega^2 + 12EG^2}}{6G\sin(\psi_H + \gamma^*)}\right)^2\right]}$	$\cos(\gamma^* + \psi_H) = 0$	$\lambda = \pm i\omega_J$ (Periodic orbit)
FP 3 & 4	$\sqrt{E}$	0	$\sin(\gamma^* + \psi_H) = -\frac{\sigma_\omega}{2\sqrt{E}G}$	$\lambda > 0$ (Unstable)

Thus, Fixed Points 1 and 2 are centers, and initial amplitudes and phases in their vicinity should evolve periodically over time with frequency ω_J. Applying Eq. (4.55), an expression can be derived that gives the frequency of the energy exchange for waves undergoing stable 2:1 internal resonance

$$\omega_J = \frac{G}{\alpha_B^*}\sqrt{\left(E^2 + 2E{\alpha_B^*}^2 - 3{\alpha_B^*}^4\right)} \tag{4.57}$$

where α_B^* must be associated with Fixed Points 1 and 2 in Table 4-1. For 3:1 internal resonance, no closed form solutions were found for the fixed points and their associated λ values based on the cubic-dependence of their fixed point equations. However, for a given parameter set, numerical root-finding techniques can be employed to compute the fixed point solutions and their associated stability. It is important to note that periodic orbits similar to those observed for 2:1 internal resonance also arise for the case of 3:1 internal resonance.

4.5 Energy Exchange Results

To numerically validate the periodic energy exchange predicted by the presented multiple scales approach, direct numerical simulation of the equations of motion in Eq. (4.1) is carried-out. Plane waves of the form in Eq. (4.22) with internally-resonant frequency/wavenumber combinations are injected into the lattice as initial conditions. Initial amplitudes and phases of the *A* and *B* waves are selected to be sufficiently near centers. To replicate plane waves in infinite media, long chains are simulated (*e.g.*, approximately 800-1000 wavelengths of the *A*-wave). Viscous dampers are added near the chain's boundaries with coefficients increasing towards the ends of the structure to absorb reflections during the simulation. Such damping profile also dissipates initial displacements and velocities near the lattice's boundaries at the start of the simulation. Analysis is then restricted to the central region of the chain (*e.g.*, the middle 100-200 wavelengths of the *A*-wave). To track the energy exchange of the injected waves, spatial Fast Fourier Transforms (FFT's) are taken of the m_b masses in this central region. Thus, the magnitudes of the frequency content at μ_A and μ_B can be interpreted as α_A and α_B, respectively, which can in-turn be compared to the predictions of the multiple scales evolution equations in Eqs. (4.49)-(4.50) or (4.51)-(4.52) for 2:1 and 3:1 internal resonances, respectively. For a given value of E, fixed points associated with periodic orbits can be determined, either analytically, for the case of 2:1 internal resonance, or computationally, for the case of 3:1 internal resonance. The initial amplitudes and phases of the simulated *A* and *B* waves can then be selected to be sufficiently close to these fixed point predictions such that the simulated waves will expected to exchange energy over time. Values of E are sufficiently small so as to eliminate or minimize the generation of still higher-harmonics out of the *A* and *B* waves. Lastly, it is important to note that this

study focuses-on validating the orbits around lower fixed values as they are more likely to satisfy the weak nonlinearity criterion required for multiple scales validity.

4.5.1 Diatomic System

Figure 4-4 depicts the relationships between the frequency of the energy exchange, ω_J, and energy level, E, for an example diatomic lattice (parameters provided in the caption), considering 2:1 internal resonance within the acoustic branch and between the acoustic and optical branches. For both cases, a higher energy level produces a higher frequency energy exchange. Additionally, the strength of the quadratic nonlinearity at each fixed point, as measured by the dimensionless parameter $\Pi_2 \equiv \frac{k_2\alpha^*}{k_1}$, is evaluated as a function of E. To satisfy a conservative weak nonlinearity criterion, Π_2 should be roughly ≤ 0.1. Note that as E transitions beyond 0.1 for interactions within the acoustic branch, a bifurcation occurs in Fixed Point 2 such that α_B^* becomes real and nonzero. This result can be physically understood to be the minimum energy barrier needed to activate a periodic energy exchange for 2:1 internal resonance within the acoustic branch.

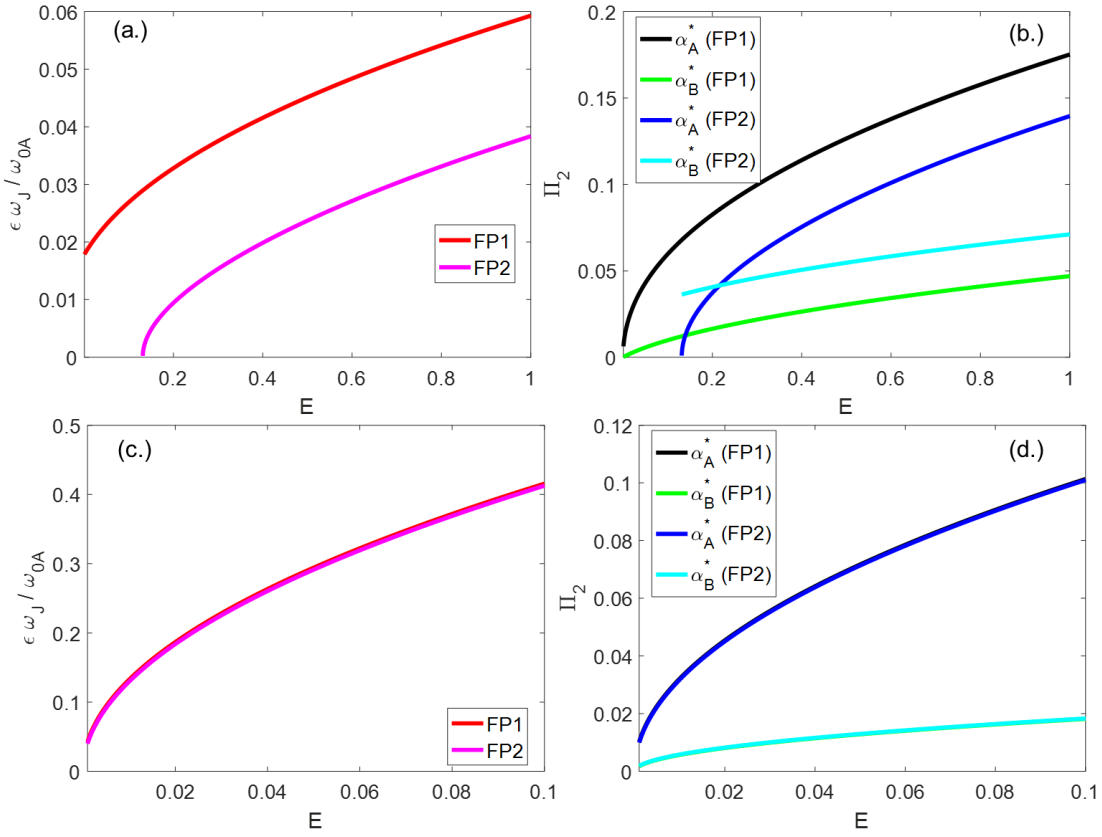

Figure 4-4. Frequency of energy exchange and strength of the nonlinearity associated with the centers Fixed Points 1 and 2 for 2:1 internal resonance within the acoustic branch (a,b) and between the acoustic and optical branches (c,d) of the diatomic lattice: (a,b) $m_a = 1, m_b = 1.5, k_1 = 1, k_2 = 1, k_3 = 0, \varepsilon = 0.1, \mu_A = 0.5,\ \sigma_\mu = 0, J_1 = 0$; (c,d) $m_a = 1, m_b = 1.5, k_1 = 1, k_2 = 1, k_3 = 0, \varepsilon = 0.1, \mu_A = \frac{\pi}{1.91},\ \sigma_\mu = 0, J_1 = 0$

Long wavelengths are considered for investigating internal resonance within the acoustic branch of the diatomic lattice. Figure 4-5 displays a sample phase portrait for 2:1 internal resonance within the acoustic branch. As documented in Table 4-1, there are two centers and two unstable fixed points. Validation of the lower amplitude center is of primary importance as it satisfies the weak nonlinearity criterion.

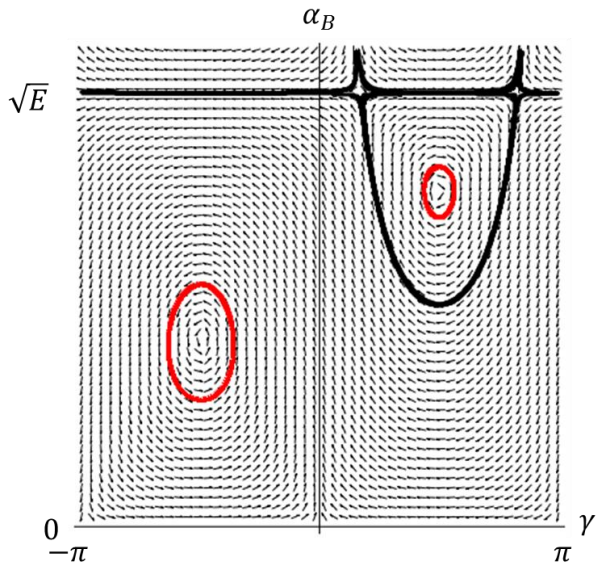

Figure 4-5. Phase portrait for 2:1 internal resonance within the acoustic branch of the diatomic lattice. Centers are plotted in red. $\boldsymbol{m_a = 1, m_b = 1.5, k_1 = 1, k_2 = 1, k_3 = 0, \varepsilon = 0.1, \mu_A = 0.5,\ \sigma_\mu = 0, J_1 = 0, E = 0.5}$

Figure 4-6 presents the results of simulating waves with 2:1 internally-resonant frequency combinations within the acoustic branch of the diatomic lattice. Note the close agreement between the multiple scales predictions and results from direct numerical simulation when viewing the energy exchange in the time domain. As expected, the *A* and *B* wave amplitudes oscillate out of phase. This energy exchange occurs at a single frequency and amplitude that matches well with the multiple scales prediction. Their agreement is especially evident after taking an FFT of the time histories of the energy exchange signals and filtering-out each of their zero frequency (DC) terms. The DC terms can be expected to be similar in magnitude to the fixed points, especially for the nearly-circular trajectories close to the centers in the phase plane.

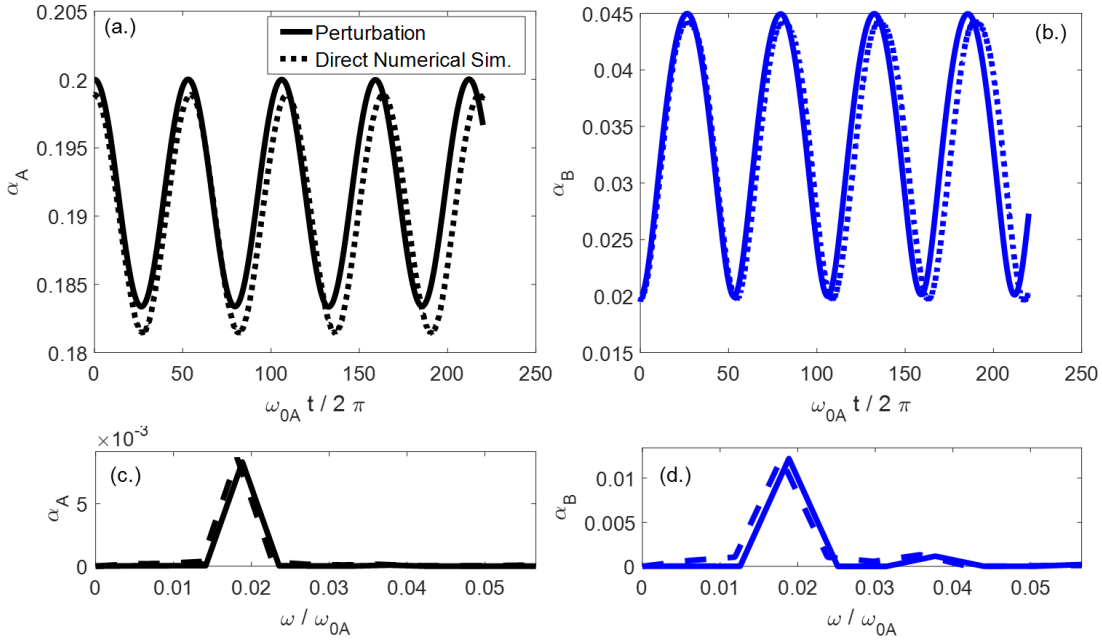

Figure 4-6. Direct numerical simulation of the lattice equations of motion compared to the multiple scales predictions of the periodic energy exchange in the diatomic lattice. 2:1 internal resonance within the acoustic branch is considered. (a,b) Time histories of the amplitude modulation. (c,d) Dominant, slow scale frequency content of the energy exchange, filtering-out the DC component $m_a = 1, m_b = 1.5, k_1 = 1, k_2 = 1, k_3 = 0, \varepsilon = 0.1, \mu_A = 0.5, \sigma_\mu = 0, J_1 = 0, E = 0.0106$

Next, wave interactions associated with internal resonance between the acoustic and optical branches are simulated. Figure 4-7 presents a sample phase portrait for 3:1 interactions between the two branches. Note that there are three fixed points: two associated with periodic orbits and one associated with instability. It is desired to validate periodic orbits about sufficiently low amplitude fixed points.

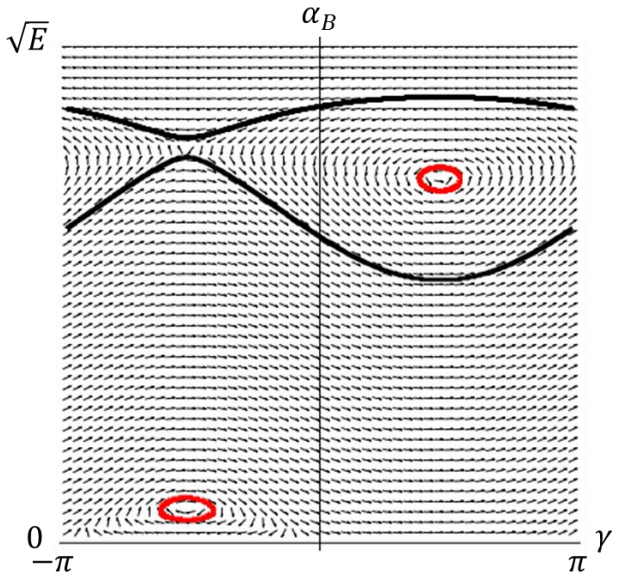

Figure 4-7. Phase portrait for 3:1 internal resonance between the acoustic and optical branches of the diatomic lattice. Centers are plotted in red. $m_a = 1, m_b = 1.1, k_1 = 1, k_2 = 0, k_3 = 1, \varepsilon = 0.1, \mu_A = \frac{\pi}{3.16}, \sigma_\mu = 0, J_1 = 0, E = 1$

Figure 4-8 compares the results from direct numerical simulation of the diatomic lattice to the multiple scales predictions for 3:1 interactions between the acoustic and optical branches. An FFT of the time histories of α_A and α_B reveal that multiple scales again accurately predicts the dominant frequency of the energy exchange. Their mean values are subtracted so as to determine the frequency content of the oscillations. High frequencies in the results from direct numerical simulation suggest that there is at least one additional wave with which the *A* and *B* waves may be exchanging energy. Clearly, the slow time scales introduced in Eq. (4.12) cannot be expected to predict amplitude modulation faster than the *A* wave's fundamental frequency. Re-formulating the multiple scales analysis to include both fast and slow time scales poses challenges that are left for future work. However, as evidenced in the figures, the dominant frequency of exchange

and the exchange amplitudes are accurately predicted by the presented multiple scales approach.

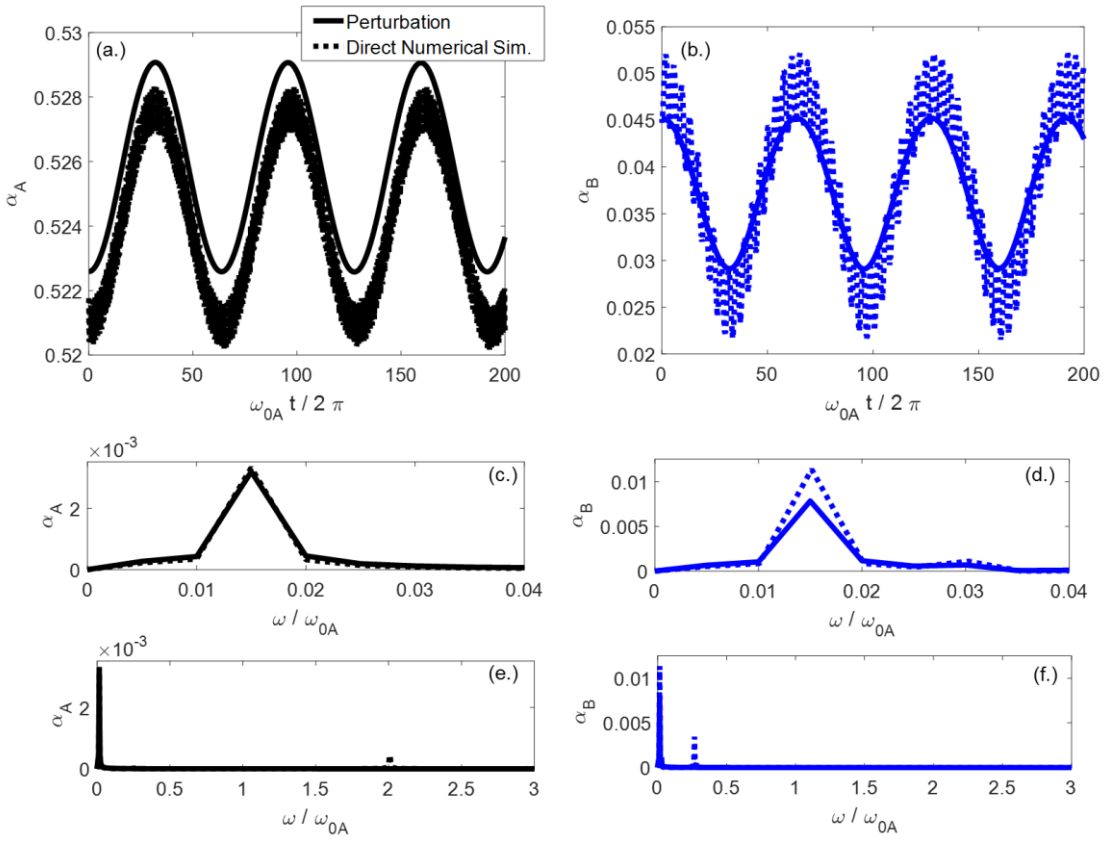

Figure 4-8. Direct numerical simulation of the lattice equations of motion compared to the multiple scales predictions of the periodic energy exchange in the diatomic lattice. 3:1 internal resonance between the acoustic and optical branches is considered. (a,b) Time histories of the amplitude modulation. (c,d) Dominant, slow scale frequency content of the energy exchange, filtering-out the DC component (e,f) Frequency content of the energy exchange, presenting the small high frequency components identified in numerical simulations $m_a = 1, m_b = 1.1, k_1 = 1, k_2 = 0, k_3 = 1, \varepsilon = 0.1, \mu_A = \frac{\pi}{3.16}, \sigma_\mu = 0, J_1 = 0, E = 0.05$

4.5.2 Locally-Resonant Metamaterial System

The expressions governing internal resonance in the locally-resonant metamaterial-type lattice are considered next. Figure 9 documents the frequency of energy exchange and strength of the quadratic nonlinearity for 2:1 internal resonance within the acoustic branch, and between the acoustic and optical branches. For Π_2, the primary chain's quadratic stiffness is referenced: $\Pi_{2a} \equiv \frac{k_{2a}\alpha^*}{k_1}$. Informed by the relationships in Figure 9, lattice parameters and initial conditions are selected such that a slow energy exchange (*i.e.*, ${}^{\varepsilon\omega_J}/_{\omega_{0A}} \leq 0.1$) with weak nonlinearities (*i.e.*, $\Pi_{2a} \leq 0.1$) are numerically simulated.

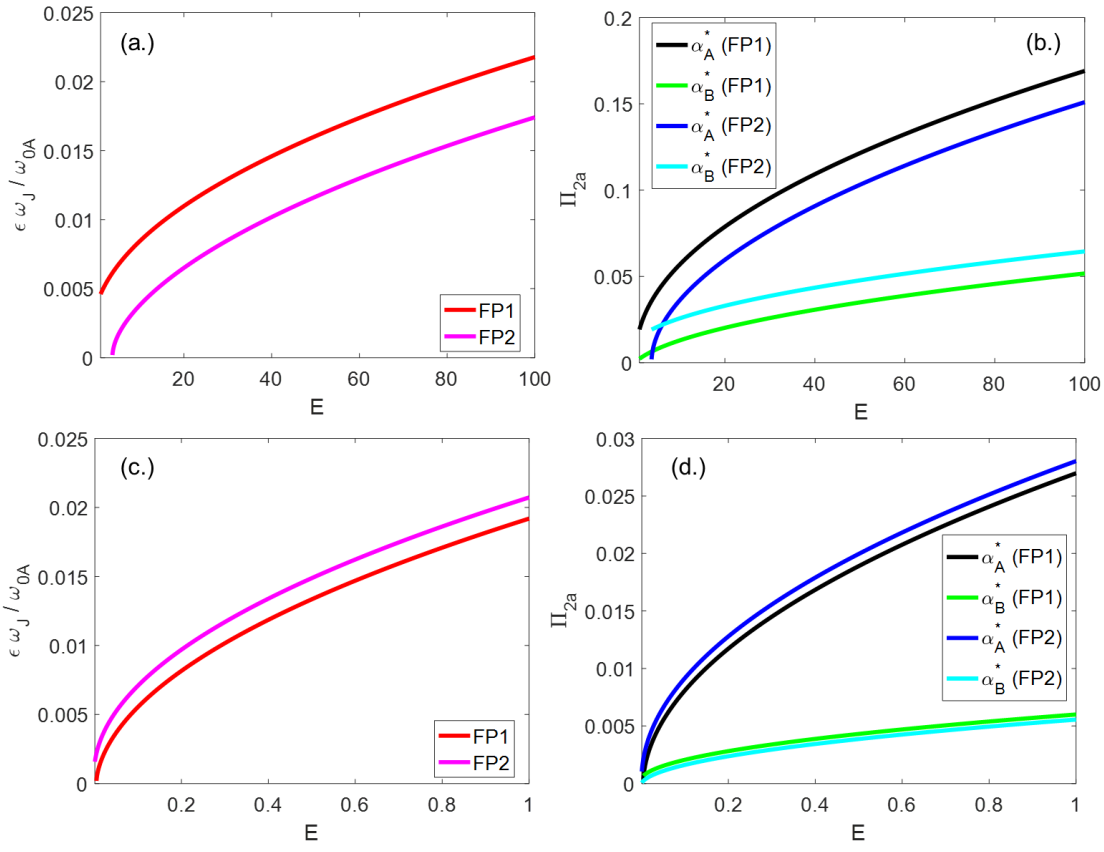

Figure 4-9. Frequency of energy exchange and strength of the nonlinearity associated with the centers Fixed Points 1 and 2 for 2:1 internal resonance within the acoustic branch (a,b) and between the acoustic and optical branches (c,d) of the locally-resonant lattice: (a,b) $m_a = 1, m_b = 0.1, k_{1a} = 10, k_{1b} = 2, k_{2a} = 1, k_{2b} =$

$\mathbf{1}, \boldsymbol{k_{3a}} = \mathbf{0}, \boldsymbol{k_{3b}} = \mathbf{0},\ \boldsymbol{\varepsilon} = \mathbf{0.1}, \boldsymbol{\mu_A} = \mathbf{0.1}, \boldsymbol{\sigma_\mu} = \mathbf{0}$; (c,d) $\boldsymbol{m_a} = \mathbf{1}, \boldsymbol{m_b} = \mathbf{0.1}, \boldsymbol{k_{1a}} = \mathbf{10}, \boldsymbol{k_{1b}} = \mathbf{2}, \boldsymbol{k_{2a}} = \mathbf{1}, \boldsymbol{k_{2b}} = \mathbf{1}, \boldsymbol{k_{3a}} = \mathbf{0}, \boldsymbol{k_{3b}} = \mathbf{0},\ \boldsymbol{\varepsilon} = \mathbf{0.1}, \boldsymbol{\mu_A} = \frac{\boldsymbol{\pi}}{\mathbf{2.93}}, \boldsymbol{\sigma_\mu} = \mathbf{0}$

Considering large wavelengths, Figure 4-10 illustrates a sample phase portrait for 3:1 internal resonance between two waves within the acoustic branch. Both periodic orbits and unstable trajectories can be observed as well as a high degree of symmetry between positive and negative γ values.

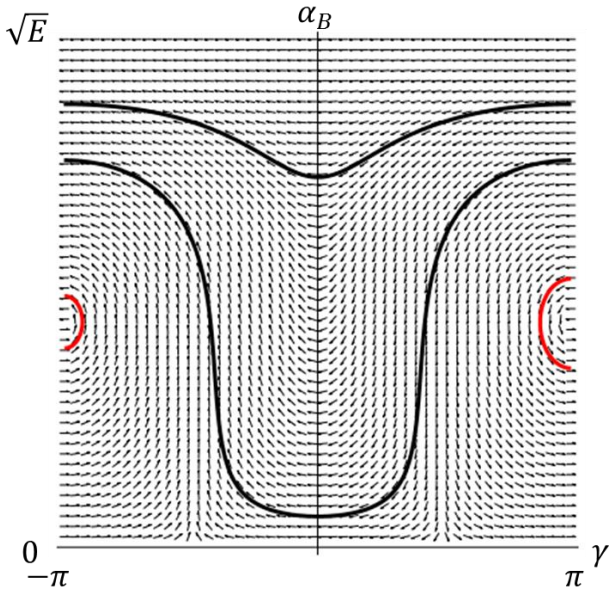

Figure 4-10. Phase portrait for 3:1 internal resonance within the acoustic branch of the locally-resonant lattice. Centers are plotted in red. $\boldsymbol{m_a} = \mathbf{1}, \boldsymbol{m_b} = \mathbf{0.4}, \boldsymbol{k_{1a}} = \mathbf{1}, \boldsymbol{k_{1b}} = \mathbf{1}, \boldsymbol{k_{2a}} = \mathbf{0}, \boldsymbol{k_{2b}} = \mathbf{0}, \boldsymbol{k_{3a}} = \mathbf{1}, \boldsymbol{k_{3b}} = \mathbf{1},\ \boldsymbol{\varepsilon} = \mathbf{0.1}, \boldsymbol{\mu_A} = \frac{\boldsymbol{\pi}}{\mathbf{12}}, \boldsymbol{\sigma_\mu} = \mathbf{0}, \boldsymbol{E} = \mathbf{5}$

Comparing the results from direct numerical simulation to the perturbation-based evolution equations for a locally-resonant lattice with 3:1 internal resonance within the acoustic branch, Figure 4-11 illustrates close agreement between theory and simulation for the dominant frequency and amplitude of the energy exchange. Additionally, the energy exchange of the waves consists of high frequency components, which can be expected to take place with waves not considered in the 0^{th}-order solution of the perturbation

framework. Nonetheless, as with the diatomic system, multiple scales accurately predicts the dominant frequency of the energy exchange, and overall exchange behavior, between the *A* and *B* waves.

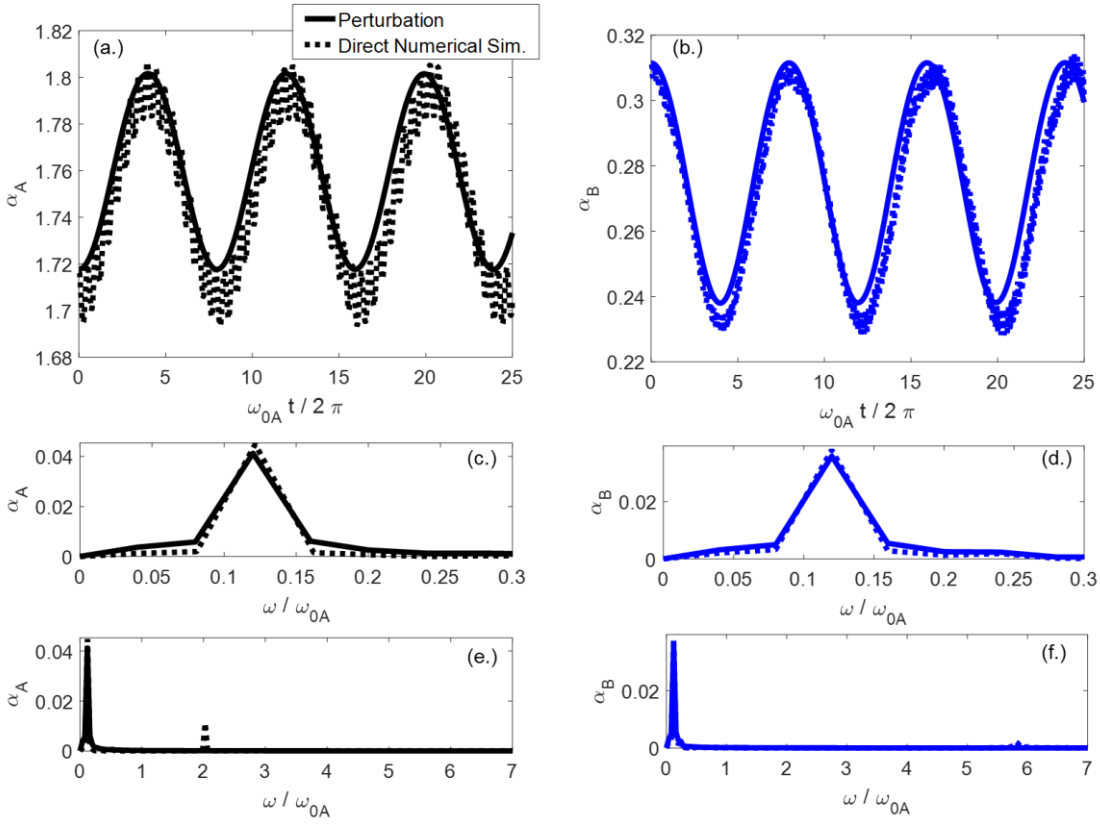

Figure 4-11. Direct numerical simulation of the lattice equations of motion compared to the multiple scales predictions of the periodic energy exchange in the locally-resonant lattice. 3:1 internal resonance within the acoustic branch is considered. (a,b) Time histories of the amplitude modulation. (c,d) Dominant, slow scale frequency content of the energy exchange, filtering-out the DC component (e,f) Frequency content of the energy exchange, presenting the small high frequency components identified in numerical simulations $m_a = 1, m_b = 0.4, k_{1a} = 1, k_{1b} = 1, k_{2a} = 0, k_{2b} = 0, k_{3a} = 1, k_{3b} = 1,\ \varepsilon = 0.1, \mu_A = \frac{\pi}{12}, \sigma_\mu = 0, E = 0.5$

Lastly, internal resonance between the acoustic and optical branches in the locally-resonant lattice is investigated. Figure 4-12 displays a sample phase portrait and Figure 4-13 summarizes the results comparing simulations to analytical predictions for 2:1 internal

resonance, again showing good agreement in the primary exchange frequency and amplitudes.

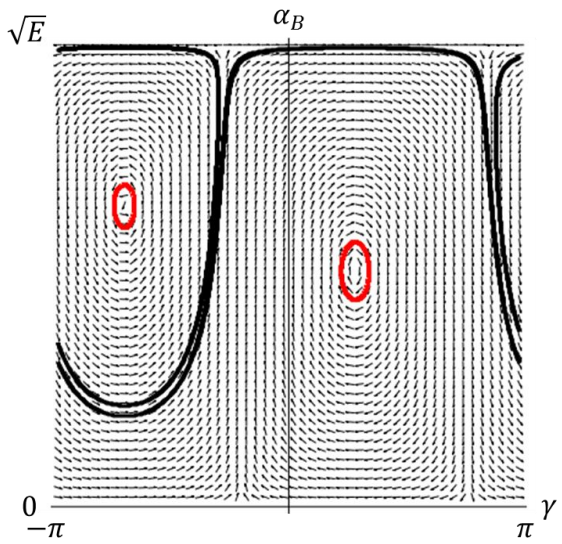

Figure 4-12. Phase portrait for 2:1 internal resonance between the acoustic and optical branches of the locally-resonant lattice. Centers are plotted in red. $\boldsymbol{m_a = 1, m_b = 0.1, k_{1a} = 10, k_{1b} = 2, k_{2a} = 1, k_{2b} = 1, k_{3a} = 0, k_{3b} = 0, c = 0, \varepsilon = 0.1, \mu_A = \frac{\pi}{2.93}, \sigma_\mu = 0, E = 0.1}$

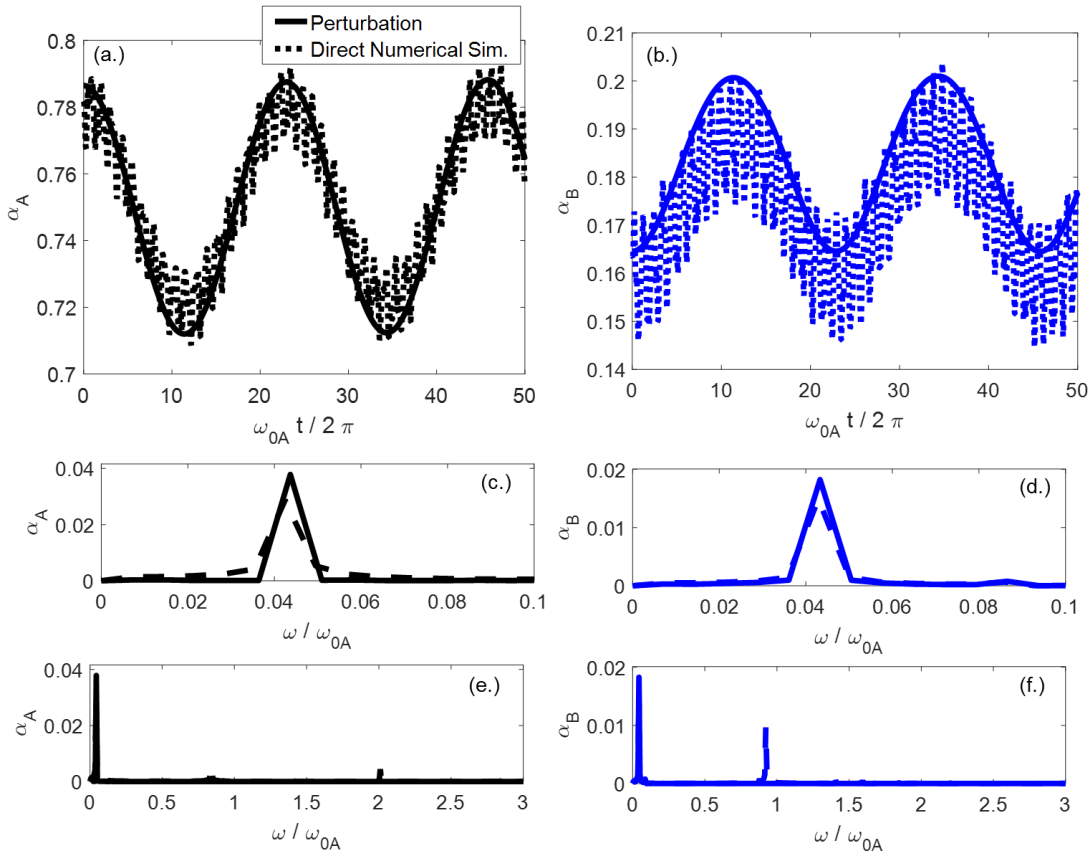

Figure 4-13. Direct numerical simulation of the lattice equations of motion compared to the multiple scales predictions of the periodic energy exchange in the locally-resonant lattice. 2:1 internal resonance between the acoustic and optical branches is considered. (a,b) Time histories of the amplitude modulation. (c,d) Dominant, slow scale frequency content of the energy exchange, filtering-out the DC component (e,f) Frequency content of the energy exchange, presenting the small high frequency components identified in numerical simulations. $\boldsymbol{m_a = 1, m_b = 0.4, k_{1a} = 1, k_{1b} = 1, k_{2a} = 1, k_{2b} = 1, k_{3a} = 0, k_{3b} = 0, \varepsilon = 0.1, \sigma_\mu = 0, J_1 = 0, \mu_A = \frac{\pi}{1.68}, E = 0.1.}$

4.6 Dispersion Analysis

As documented in Sections 2.3, 2.4, and 3.3, higher-order multiple scales analysis of a single-frequency plane wave does not provide valid dispersion shifts for frequencies near internal resonances. This stems from unaccounted-for secular terms arising from $\left(n\mu, n\omega_0(\mu)\right)$, that are instead treated as non-secular with associated particular solutions.

These 1st-order particular solutions become unbounded at frequencies associated with internal resonance, and consequently violate the asymptotic series expansion. Thus, singularities in dispersion corrections due to internal resonance for self-interacting cannot be seen until advancing to the 2nd-order. Note that first-order dispersion corrections do not exhibit singularities, and the natural question arises as to whether these lower-order approximations can be satisfactorily used near internal resonance.

Since quadratic stiffness interactions do not cause dispersion shifting until higher-orders (*i.e.,* $O(\varepsilon^2)$), cubic stiffness interactions are considered for this dispersion study. Additionally, internal resonance between the acoustic and optical branches is explored since there are negligible dispersion shifts at the long wavelengths at which internal resonance takes place solely within the acoustic branch. Recalling from [112] that evolution equations for phases directly provide the amplitude-dependent corrections to the band structure, Eqs. (4.33) and (4.37) are evaluated at the fixed points

$$\omega_{1,A} = I\alpha_A^*\alpha_B^* \sin(\psi_I + \gamma^*) + L{\alpha_B^*}^2 + N{\alpha_A^*}^2 \tag{4.58}$$

$$\omega_{1,B} = P{\alpha_A^*}^2 + Q{\alpha_B^*}^2 - R\frac{{\alpha_A^*}^3}{\alpha_B^*}\sin(\psi_R + \gamma^*) \tag{4.59}$$

where $\omega_{1,A}$ and $\omega_{1,B}$ denote the amplitude-dependent dispersion shifts for the *A* and *B* waves, respectively, for 3:1 internal resonance. The corrections in Eqs. (4.58) and (4.59) can be evaluated at any fixed point $(\alpha_A^*, \alpha_B^*, \gamma)$. To determine whether these expressions from internally-resonant interactions are comparable to the 1st-order predictions from a single plane wave analysis, Eq. (4.58) is evaluated with $E = r\alpha^2$, where α is the amplitude of the single-frequency plane wave to which results are compared.

Figure 4-14 compares the results for the internally-resonant dispersion predictions to those from the 1st-order perturbation predictions for a single plane wave in the diatomic chain. The frequency ω and wavenumber μ correspond to those of the single frequency plane wave. The *A*-wave frequency and wavenumber are used for the comparison. When evaluated at Fixed Point 6, the internally-resonant analysis gives results that would arise should the single-plane wave analysis be interpolated through its singularities. Fixed Point 5 converges to the single plane wave corrections as the wavenumber increases to values well above the frequency at which the singularity occurs. Fixed Point 7 exists for a narrow range of frequencies about the singularity and slowly approaches the single plane wave results. The results evaluated at Fixed Point 6 gives confidence that higher-order singularities can be avoided when studying a single plane wave by instead employing the first-order expressions.

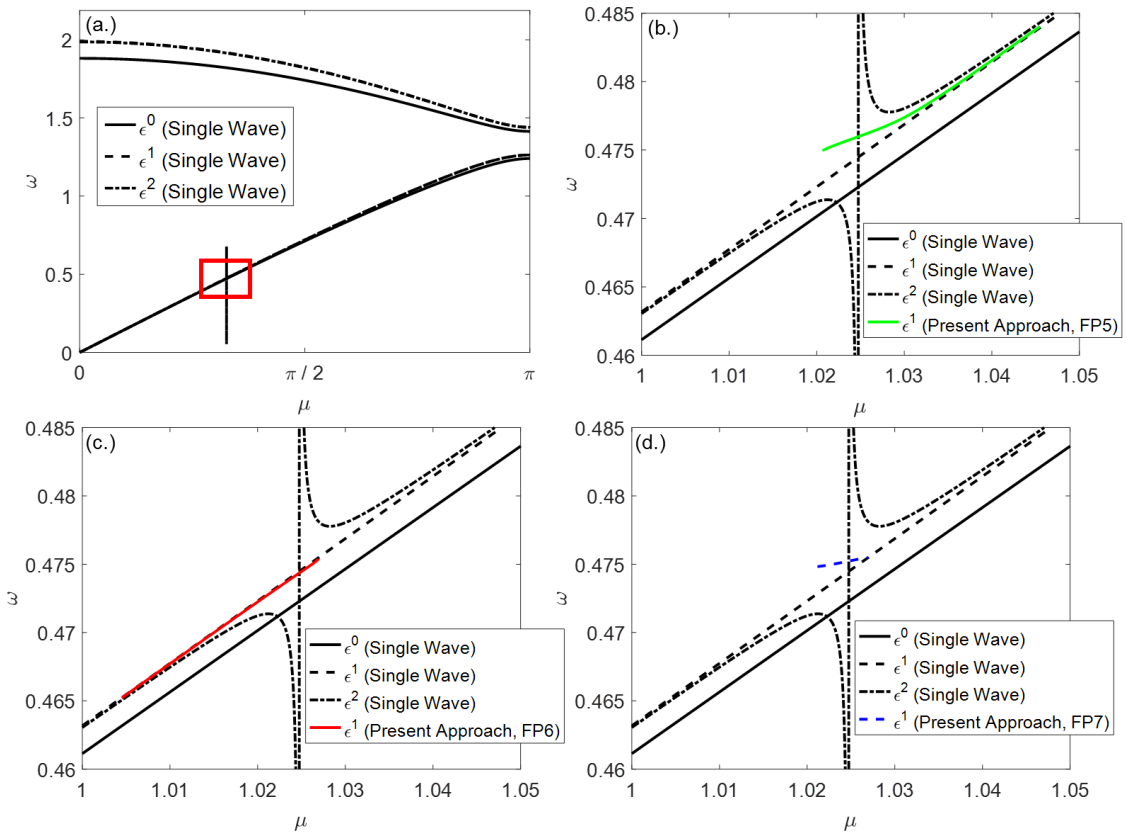

Figure 4-14. Comparison of multiple scales expressions for dispersion shifts in the diatomic chain. A single plane wave has singularities in its higher-order dispersion corrections at frequencies associated with internal resonance between branches (a.). Dispersion corrections based on 3:1 energy exchange (b-d) exist at specific ranges of frequencies and the results evaluated at Fixed Point 6 passes through the singularity found in the single plane wave results. $\boldsymbol{m_a = 1, m_b = 1.3, k_1 = 1, k_2 = 0, k_3 = 1, \varepsilon = 0.1, \sigma_\mu = 0, J_1 = 0, \alpha = 0.7}$

Using the framework detailed in Section 4.4, the stability of Fixed Points 5-7 in Figure 4-14 is analyzed as the wavenumber μ is varied to ensure the stability of the solutions. Figure 4-15 presents the results. Since Fixed Point 6 is a center, it provides justification for employing its value to interpolate through single plane wave singularities. Fixed Point 5 is also a center, which also can be used to approximate the dispersion shifts of a single plane wave at frequencies beyond the 3:1 singularity. Note that α_B^* for Fixed Points 6 and 7

coalesce and subsequently vanish as the control parameter μ is varied just above the value giving a singularity. This behavior is indicative of a saddle-node bifurcation.

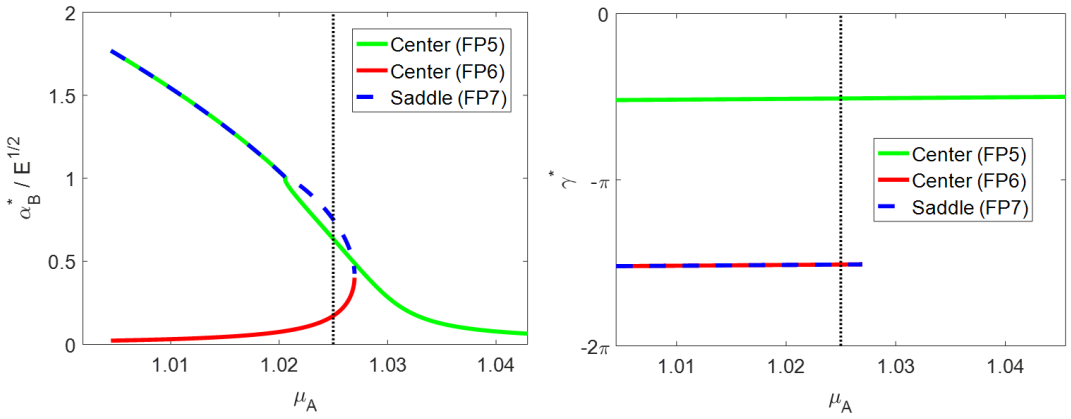

Figure 4-15. Bifurcation analysis of the multiple scales fixed point expressions in the vicinity of the singularity due to 3:1 internal resonance in the diatomic chain. The wavenumber of the A wave μ_A serves as the control parameter and the fixed points α_B^* (a.) and γ^* (b.) are evaluated. Fixed Points 5 and 6 are both centers giving confidence they can be used to interpolate through or approximate the singularity in the higher-order single plane wave dispersion correction. The vertical line represents the location of the singularity in the single plane wave dispersion correction.

4.7 Concluding Remarks

A multiple scales approach has been presented to analyze internally-resonant energy exchange in weakly nonlinear lattices with multiple degrees of freedom per unit cell. Both 2:1 and 3:1 internal resonances within the same branch, and between different branches, is considered for diatomic and locally-resonant example systems. A local stability analysis reveals distributions of amplitudes and phases associated with a slow periodic exchange of energy between the internally-resonant plane waves. These predictions are validated by direct numerical simulation of the lattices' equations of motion. A dispersion study reveals that 1st-order corrections from perturbation analysis of internally-resonant interactions

accurately characterizes regions of the band structure at which dispersion corrections of a single-frequency plane wave break down. The results presented herein may inform technology capable of long-range coherent signal transmission and detection in nonlinear periodic media.

CHAPTER 5. ISOLATED FREQUENCIES AT WHICH NONLINEAR MATERIALS BEHAVE LINEARLY

5.1 Overview

This chapter demonstrates that specific frequencies in weakly nonlinear lattices avoid generation of higher-harmonics, and thus the lattices behave almost linearly. A multiple scales analysis identifies plane wave solutions that persist at only a single frequency and wavenumber—*i.e.*, whose spatiotemporal production of higher-harmonics is remarkably small. This behavior is a specialization of the invariance phenomenon reported for 1-D lattices in Chapter 2. Monatomic and diatomic chains with quadratic and cubic stiffness nonlinearities are selected as example systems. Direct numerical integration of their equations of motion confirms that finite amplitude plane waves assigned to these special frequencies produce negligible higher harmonics when injected into the lattices. Such findings provide new considerations for the operating frequency of nonlinear communications devices, sensors, and transducers for enhanced signal-to-noise ratios.

Extensive research has explored the generation of extra-harmonics in nonlinear media, such as those resulting from normal and Umklapp phonon scattering processes in anharmonic lattices [120]. Other examples include finite amplitude bulk waves in elastic solids [107, 121, 122] and Lamb waves [123-128], which can support second-harmonic synchronization (internally-resonant energy exchanges). Similarly, higher-harmonic production has been studied in optical waves for media with nonlinear dielectric coefficients [129], piezoelectric crystals [130], and systems with interfaces [131]. Such

problems are posed in a finite, or semi-finite, setting by introducing an input boundary condition, commonly harmonic forcing. The growth of higher-harmonics in forced nonlinear periodic media has also been investigated, with notable recent discoveries of a periodic energy exchange between the forcing frequency and higher-harmonics [108], modal-mixing between dispersion branches [132], and the formation of subharmonic attenuation zones [133]. By contrast, other studies consider free-wave solutions for infinite nonlinear media. Solution forms include breathers [134-138], solitons [14, 26, 28, 29, 139-141], and cnoidal waves [89, 142, 143], which have been observed in water, fiber optic cables, granular media, and periodic structures.

In this chapter, special frequencies are identified at which higher-harmonic generation ceases in weakly nonlinear lattices. Such solutions are unique for each lattice design and tunable through wave amplitude, as identified by the multiple scales analysis. Section 5.2 reviews the example systems (*i.e.,* weakly nonlinear monatomic and diatomic chains) and summarizes the higher-order multiple scales analysis that reveals this peculiar behavior. Section 5.3 presents results from numerical simulations that verify the minimal growth of higher-harmonics at these special frequencies. Concluding remarks are made in Section 5.4.

5.2 Analysis Approach

Considered herein is 1-D wave propagation in lattices with physically-appropriate, small quadratic and cubic stiffness nonlinearities. This arises in anharmonic 3-D crystals when plane waves propagate in the [100], [110], and [111] directions. Analogously, these equations can govern electromagnetic wave propagation in discretized photonic crystals or

optical media whereby cubic "stiffness" appears as the Kerr nonlinearity [144-146]. Figure 5-1(a-b) presents example systems considered herein: nonlinear monatomic and diatomic lattices. The monatomic lattice comprises a single mass m that repeats in each unit cell whereas the diatomic lattice consists of alternating masses m_a and m_b. Both lattices possess linear stiffness denoted by k_1 as well as quadratic and cubic stiffness denoted by k_2 and k_3, respectively. In general, the equations of motion for the j^{th} unit cell of a weakly nonlinear lattice are

$$\mathbf{M}\ddot{\mathbf{x}}_j + \sum_{p=-1}^{+1}\left[\mathbf{K}^{(p)}\mathbf{x}_{j+p}\right] + \varepsilon\mathbf{f}_{\mathbf{NL}}\left(\mathbf{x}_j, \mathbf{x}_{j-1}, \mathbf{x}_{j+1}\right) = \mathbf{0}, \quad j = -\infty \ldots \infty \tag{5.1}$$

where $\mathbf{x}_j$ and $\ddot{\mathbf{x}}_j$ are vectors containing the displacements and accelerations of all masses in the unit cell, respectively, **M** and **K** denotes the mass and stiffness matrices, respectively, and $\mathbf{f}_{\mathbf{NL}}$ consists of the nonlinear restoring forces. The small parameter ε functions as a bookkeeping device in the multiple scales framework. Recall that the multiple scales procedure begins by introducing slow time scales and a series solution

$$t = T_0 + \varepsilon T_1 + \cdots \varepsilon^n T_n \tag{5.2}$$

$$\mathbf{x}_j = \mathbf{x}_j^{(0)} + \varepsilon\mathbf{x}_j^{(1)} + \cdots + \varepsilon^n\mathbf{x}_j^{(n)}. \tag{5.3}$$

In accordance with Eq. (5.2), an operator is defined $D_n(\ \ ) \equiv \frac{\partial}{\partial T_n}$. Collecting terms at matching powers of ε produces a series of cascading differential equations. The first two equations are

$$\varepsilon^0\text{:}\quad \mathbf{M}\ddot{\mathbf{x}}_j^{(0)} + \sum_{p=-1}^{+1}\left[\mathbf{K}^{(p)}\mathbf{x}_{j+p}^{(0)}\right] = \mathbf{0} \tag{5.4}$$

$$\varepsilon^1\text{:}\quad \mathbf{M}\ddot{\mathbf{x}}_j^{(1)} + \sum_{p=-1}^{+1}\left[\mathbf{K}^{(p)}\mathbf{x}_{j+p}^{(1)}\right] = -2D_0D_1\mathbf{M}\mathbf{x}_j^{(0)} - \mathbf{f}_{\mathbf{NL}}\left(\mathbf{x}_j^{(0)}, \mathbf{x}_{j-1}^{(0)}, \mathbf{x}_{j+1}^{(0)}\right). \tag{5.5}$$

At the 0^{th}-order, a Bloch wave is admitted, which in its simplest form comprises a single frequency and wavenumber

$$\mathbf{x}_j^{(0)} = \frac{1}{2}\boldsymbol{\phi}(\omega_0)Ae^{i\omega_0 T_0}e^{-i\mu j} + \text{c. c.}, \tag{5.6}$$

where A denotes the wave amplitude, ω_0 the frequency, μ the dimensionless wavenumber (or propagation constant), $\boldsymbol{\phi}(\omega_0)$ the wave propagation mode shape, and c. c. denotes the complex conjugate of all preceding terms. As depicted in Figure 5-1(c), the monatomic lattice possesses a single dispersion branch, whose maximum frequency supporting propagating waves (vis-à-vis evanescent waves) is termed the cut-off frequency. The diatomic lattice in Figure 5-1(d), on the other hand, consists of a lower acoustic branch and upper optical branch separated by a bandgap.

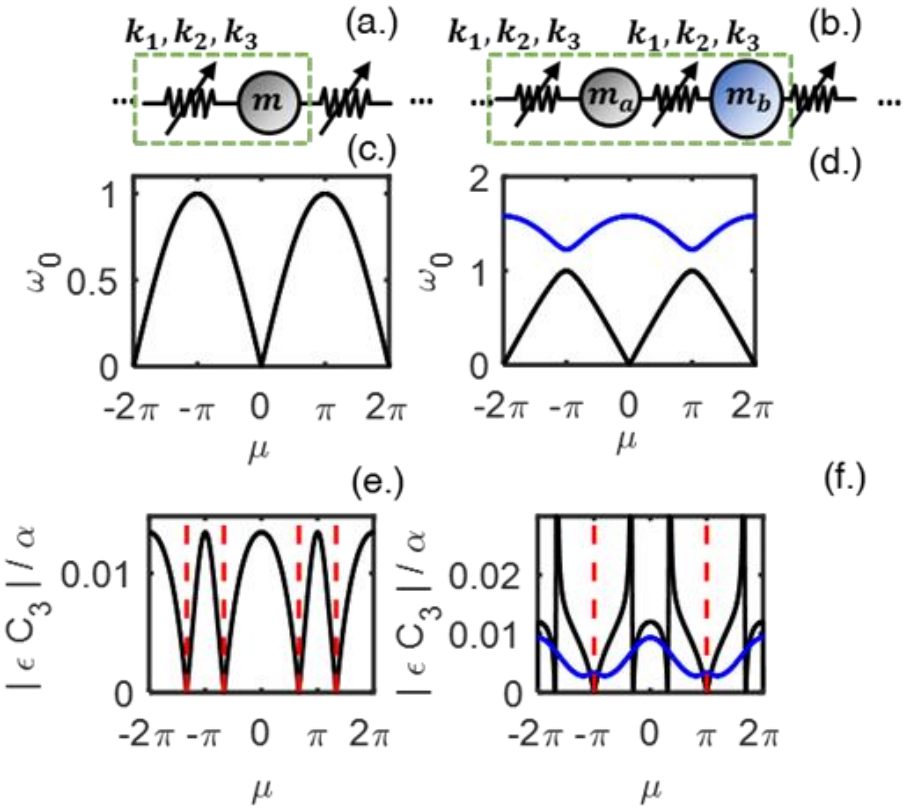

Figure 5-1. Schematics of nonlinear monatomic (a.) and diatomic (b.) chains with corresponding 0th-order dispersion relationships in (c.) and (d.) chains and multiple-scales derived 3rd-harmonic solution coefficients in (e.) and (f.) chains. Specific wavenumbers, μ_{null}, (vertical dashed lines) exist in which the solution coefficients vanish.

Updating Eq. (5.5) with the 0th-order solution in Eq. (5.6) gives

$$D_0^2\mathbf{M}\mathbf{x}_j^{(1)} + \sum_{p=-1}^{+1}\left[\mathbf{K}^{(p)}\mathbf{x}_j^{(1)}\right] = -\mathbf{M}D_1\left(i\omega_0\boldsymbol{\phi}(\omega_0)Ae^{i\omega_0 T_0}e^{-i\mu j}\right) + \sum_{u=0}^{3}\mathbf{a}_\mathbf{h}^{(1)}e^{ih(\omega_0 T_0-\mu j)} + \text{c. c.}, \quad (5.7)$$

where the $\mathbf{a}_\mathbf{h}^{(1)}$ coefficient represents the 1st-order contribution of each harmonic produced by the nonlinear stiffness interactions. The $\mathbf{a}_\mathbf{h}^{(1)}$ coefficients can therefore be expected to depend on the nonlinear stiffness, wave amplitude, and lattice parameters.

Secular terms on the right hand side of Eq. (5.7) at $e^{i\omega_0 T_0} e^{-i\mu j}$ (and its complex conjugate) must be eliminated, which yields 1st-order evolution equations

$$D_1(\alpha) = 0 \tag{5.8}$$

$$D_1(\beta) = \delta\alpha^2, \tag{5.9}$$

where α and β are the magnitude and phase, respectively, of the complex amplitude A, and δ is a function of μ, k_3, k_1, and m (if monatomic) or m_a and m_b (if diatomic). As previously studied in [22, 112], $D_1(\beta)$ provides closed-form amplitude-dependent corrections to the lattice's 0th-order band structure. As found in Section 2.6, quadratic stiffness does not shift the dispersion curve until higher-orders. With secular terms eliminated, particular solutions are determined for each of the inhomogeneities at $e^{ih(\omega_0 T_0 - \mu j)}$ (h ≠ 1)

$$\mathbf{x}_j^{(1)} = \sum_{h=0}^{3} \hat{\mathbf{a}}_{\mathrm{h}}^{(1)} e^{ih(\omega_0 T_0 - \mu j)} + \text{c. c.}, \tag{5.10}$$

where $\hat{\mathbf{a}}_{\mathrm{h}}^{(1)}$ can be obtained through the method of undetermined coefficients. The procedure repeats at each order: removal of secular terms followed by solving for a particular solution. Lattices with quadratic and cubic stiffness possess 1st-order particular solutions at twice and three times the fundamental frequency and wavenumber,

$$\mathbf{x}_j^{(1)} = \frac{1}{2}\mathbf{B_2} e^{2i(\omega_0 T_0 - \mu j)} + \frac{1}{2}\mathbf{C_3} e^{3i(\omega_0 T_0 - \mu j)} + \text{c. c.} \tag{5.11}$$

For the monatomic chain, the coefficients simplify to scalars

$$B_2 = \frac{ik_2 A^2(\sin 2\mu - 2\sin\mu)}{4m\omega_0^2 + 2k_1\cos 2\mu - 2k_1} = b_2 A^2 \tag{5.12}$$

$$C_3 = \frac{k_3 A^3(3\cos 2\mu - \cos 3\mu - 3\cos\mu + 1)}{18m\omega_0^2 + 4k_1\cos 3\mu - 4k_1} = c_3 A^3. \tag{5.13}$$

The vector expressions for the diatomic chain involve multiple terms, but can be represented symbolically in a similar manner; *i.e.*, $\mathbf{B_2} = \mathbf{b_2}A^2$ and $\mathbf{C_3} = \mathbf{c_3}A^3$. Note that such waves do not satisfy the 0^{th}-order dispersion relationship for the lattice; however, they both possess the same *phase velocity* as the 0^{th}-order solution in Eq. (5.6). Consequently, the particular solutions summed across all orders compose an invariant plane wave composed of specific magnitudes and phases of higher-harmonic frequencies and wavenumbers, valid for all space and time. The inclusion of these very specific higher-order particular solutions results in plane wave propagation with less spatiotemporal variation of its spectral content. This "shape-preserving" property makes these invariant waves similar to solitons except they are *not* spatially-localized solutions.

Figure 5-1(e-f) display the magnitude of the 3^{rd}-harmonic solution coefficient $|\mathbf{C_3}|$ as a function of the propagation constant μ for the nonlinear monatomic and diatomic lattices. As expected for these lattice systems, the solution coefficients repeat periodically across the Brillouin Zone. For the diatomic lattice, there are propagation constants in which the 3^{rd}-harmonic solution coefficient become unbounded. At these frequencies, an internally-resonant energy exchange occurs, and the multiple scales analysis requires the inclusion of two plane waves at the 0^{th}-order to capture such energy exchange, which is the subject of Chapter 4 The aspect focused-on herein are the wavenumbers, $\mu = \mu_{null}$, at which the 3^{rd}-harmonic solution coefficient becomes zero. By extension of the invariance phenomenon, the *absence* of such harmonics leads to a waveform that the nonlinear lattice admits for all space and time, and as such, this higher harmonic can be expected to not develop during propagation. This behavior is quite different from the conventionally-studied growth of harmonics in nonlinear waves. Such a finding has implications for the

design of sensors, transducers, and communications systems such that they exhibit *linear-like* responses at high-amplitude operation. In applications such as MEMS resonators, for example, one might increase input amplitude/power in an attempt improve the signal-to-noise ratio, but this is often accompanied by nonlinear behavior and loss of information at the sending frequency [147-150]. Operation at $(\mu_{null}, \omega(\mu_{null}))$ would avoid this compromise. Additionally, it may be possible to observe ballistic transport of heat-carrying phonons at these special frequencies. From here forward in this chapter, the analysis is restricted to cubic stiffness as quadratic stiffness does not exhibit this phenomenon at propagating wavenumbers (those with non-zero group velocity).

5.3 Numerical Results

As validation of this finding, direct numerical integration of the lattice equations of motion is conducted. Long chains were simulated (*e.g.*, 300 wavelengths for a given value of μ) with viscous dampers whose coefficients increase towards the edge of the structure to absorb reflections. As initial conditions, Eq. (5.6) (and its corresponding velocity) were assigned to all unit cells at a specific amplitude and frequency and wavenumber combination satisfying the 0^{th}-order dispersion relationship. The spatial and temporal spectral content of the lattice is then tracked throughout the simulation across time and space. Figure 5-2 compares the spatiotemporal spectral evolution for two separate simulations of the diatomic lattice: in Figure 5-2(a-b), the lattice is assigned a plane wave away from $(\mu_{null}, \omega(\mu_{null}))$, in Figure 5-2(c-d), the lattice is assigned a plane wave at $(\mu_{null}, \omega(\mu_{null}))$. In the first case, higher harmonics develop in the temporal and spatial frequency content of the wave, as expected. However, in the latter case, negligible higher-harmonic content develops. Note that the temporal frequency content at approximately

$2.67\omega_0$ and $3.46\omega_0$ correspond to $\omega_0(3\mu)$ for the acoustic and optical branches, respectively.

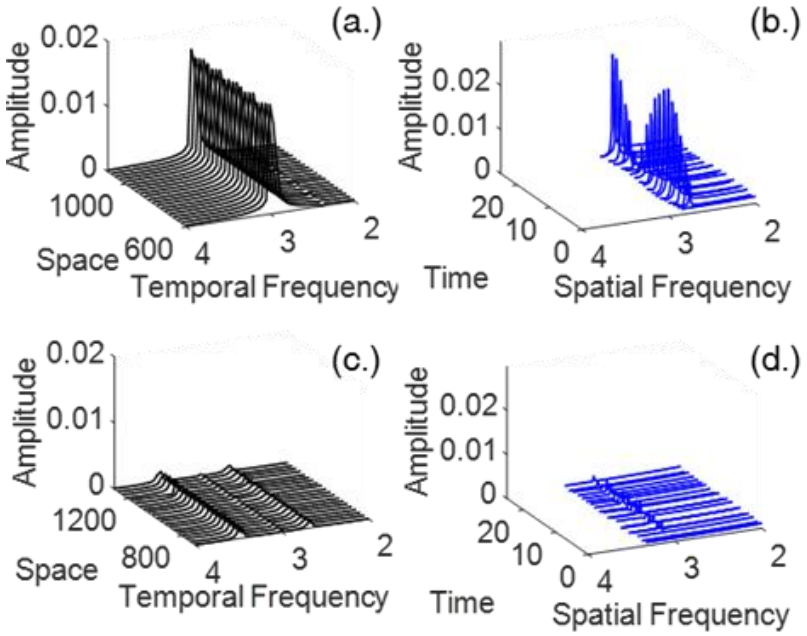

Figure 5-2. Spatiotemporal evolution of the spectral content for plane waves in the acoustic branch of the nonlinear diatomic lattice measured in numerical simulations. For lattices given wavenumbers away from μ_{null}, higher-harmonic amplitudes develop across space (a.) and time (b.). By contrast, for lattices assigned plane waves at μ_{null} (predicted by multiple scales), nearly-zero higher-harmonic amplitudes develop across space (c.) and time (d.). Amplitudes and frequencies are normalized with respect to their values at the fundamental frequency.

The procedure is formally repeated over several combinations of initial amplitude and frequency, and the higher-harmonic magnitudes are averaged over many unit cells (for temporal FFT's) and time steps (for spatial FFT's). Figure 5-3 summarizes the results over a range of signal amplitude α. For the monatomic lattice, the measured response of simulated waveforms at $(\mu_{null}, \omega(\mu_{null}))$ in Figure 5-3(a.) is vastly different than those at other frequencies: the magnitudes of higher harmonics are nearly zero regardless of the initial amplitude assigned to the plane wave. This small production of harmonics aligns

with the multiple scales prediction of μ_{null} as identified for the monatomic lattice in Figure 5-3(b.). Since higher-order particular solutions are functions of lower-order particular solutions, still higher-harmonic solution coefficients produced by the cubic stiffness (such as $\left(5\mu, 5\omega_0(\mu)\right)$ tend to also evaluate to zero at $(\mu_{null}, \omega(\mu_{null}))$.

Additionally, Figure 5-3(c-h) reveals that, for the nonlinear diatomic chain, higher-harmonic generation for a given degree-of-freedom within each unit cell can be blocked. Multiple scales identifies frequencies at which $\hat{\mathbf{a}}_{\mathbf{3}}^{(\mathbf{1})} = \begin{bmatrix} \hat{a}_{3,a}^{(1)} \\ 0 \end{bmatrix}$ or $\hat{\mathbf{a}}_{\mathbf{3}}^{(\mathbf{1})} = \begin{bmatrix} 0 \\ \hat{a}_{3,b}^{(1)} \end{bmatrix}$. Thus, there are multiple layers of tunability offered by the diatomic model, as μ_{null} differs based on the degree of freedom in addition to whether the acoustical or optical branch is excited. This trend is confirmed by the numerical simulations in Figure 5-3(c-f), agreeing with perturbation predictions of μ_{null} in Figure 5-3(g-h).

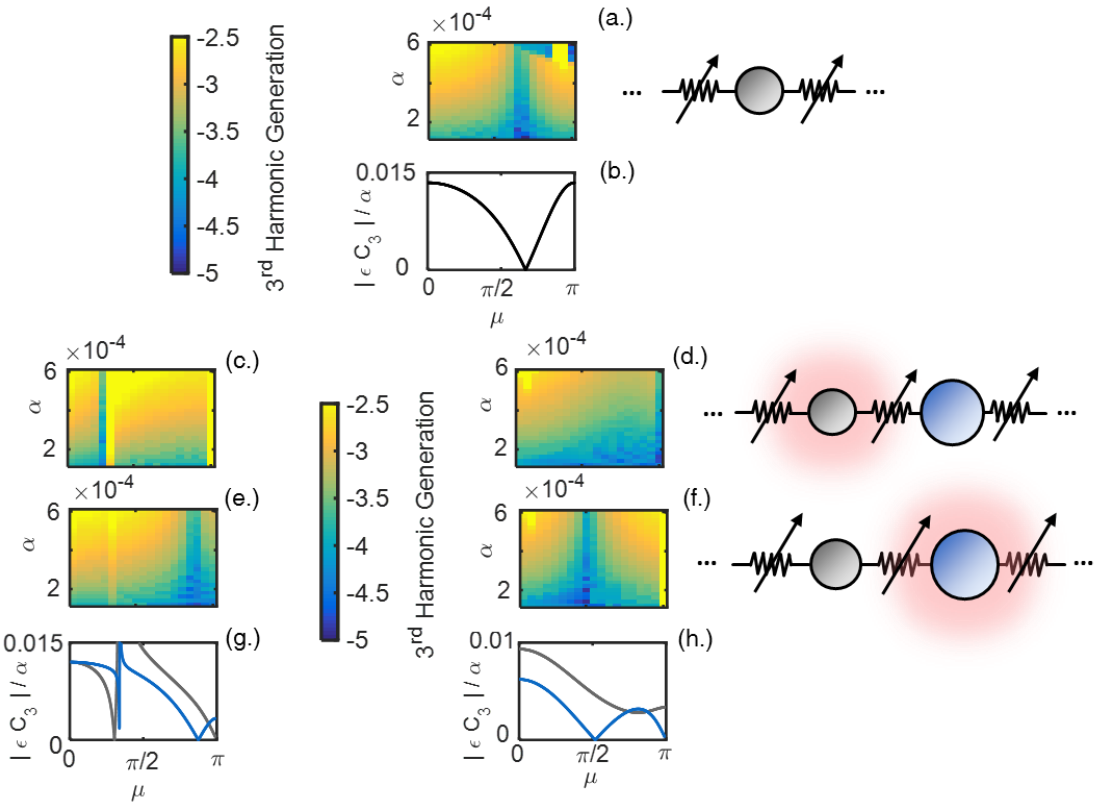

Figure 5-3. 3rd-harmonic generation relative to amplitude α at the fundamental frequency (log-scale) captured by numerical simulations of the nonlinear monatomic lattice (a.) compared to the multiple-scales predictions of the 3rd-harmonic solution coefficient as a function of the propagation constant (b.). Similarly, the 3rd-harmonic production measured in numerical simulations of the diatomic chain is presented for initial conditions at the acoustic branch (c, e) and optical branch (d, f) compared to the perturbation predictions at the acoustic branch (g.) and optical branch (h.). In (c.) and (d.) simulations, the light mass is tracked whereas in (e.) and (f.), the heavy mass is tracked.

A noteworthy feature of μ_{null} values is that they are independent of the wave's amplitude α. However, due to the amplitude-dependent band structure shifting from the cubic nonlinearity, the temporal frequency $\omega(\mu_{null})$ grows/shrinks as a function of amplitude, thereby enabling a means to tune the frequency at which the near-zero higher-harmonic generation occurs. Using the closed-form expressions for the amplitude-dependent band structures summarized in Eq. (5.9), Figure 5-4 displays the relationship between $\omega(\mu_{null})$,

the frequency of propagation relative to the first cut-off frequency, and $\Pi_3 \equiv \frac{k_3}{k_1}|A|^2$, the dimensionless strength of the nonlinearity in the system. For these dispersion corrections to remain valid, weak nonlinearities are conservatively enforced by $|\Pi_3| \leq 0.1$. These plots provide a design strategy for achieving a desired frequency at which higher-harmonics should not appear.

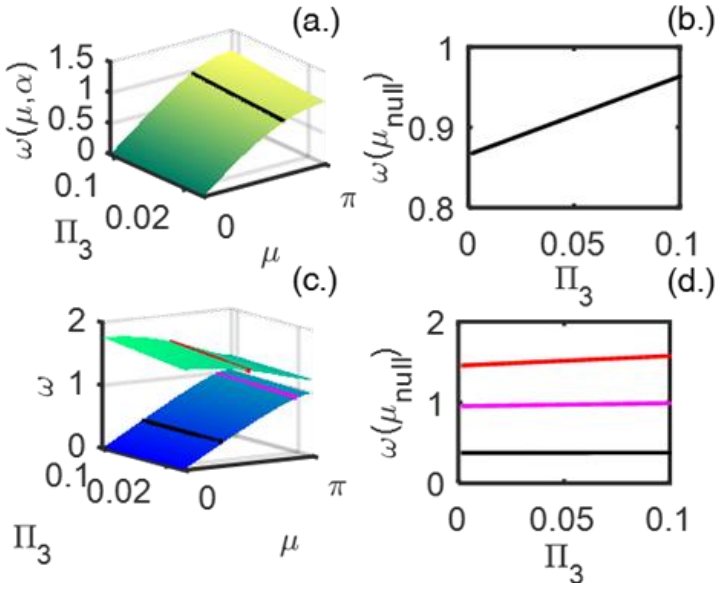

Figure 5-4. Analytical, amplitude-dependent dispersion shifting in the monatomic (a.) and diatomic (c.) lattices. The analytical predictions of dispersion shifting at μ_{null} are evaluated for the monatomic (b.) and diatomic (d.) lattices to illustrate the tunability of the negligible higher-harmonic generation.

Physical insight into the cause of near-zero higher harmonic generation is difficult to assess. Inspection of Eq. (5.13) identifies that $\mu_{null} = \frac{2\pi}{3}$ for the monatomic lattice. Thus, $\omega_0(3\mu_{null}) = 0$, yielding a zero phase velocity and indeterminate group velocity, which may explain the absence of the 3rd spatial harmonic, 3μ, for the monatomic chain but cannot justify the absence of the 3rd temporal harmonic, $3\omega_0(\mu_{null})$. For the diatomic chain, $\omega_0(3\mu_{null}) \neq 0$. More rich behavior may exist for μ_{null} in 2-D periodic structures as there

may be *directions* in which higher-harmonic generation ceases motivated by the direction-dependent stability and invariance in 2-D symmetric shear lattices [151].

5.4 Concluding Remarks

In summary, it was found that nonlinear lattices can admit plane waves at specific frequencies which avoid higher harmonics. Such behavior is a dramatic departure from the well-studied phenomenon of higher-harmonic generation of waves in nonlinear media. While the wavenumber at which this phenomena occurs remains fixed, the frequency varies with wave amplitude as predicted by a multiple scales analysis. Furthermore, lattices with many degrees-of-freedom per unit cell avoid higher harmonics at different wavelengths, which depend on the degree-of-freedom considered in each unit cell. This finding may pave the way for inducing linear behavior in nonlinear devices operating at high amplitudes, or achieving near-ballistic thermal transport of phonons at select frequencies.

CHAPTER 6. EXPERIMENTAL DEMONSTRATION OF AMPLITUDE-DEPENDENT BAND STRUCTURE AND PLANE WAVE STABILITY IN NONLINEAR LATTICES

6.1 Overview

This chapter experimentally investigates wave propagation in nonlinear lattices, extracting amplitude-dependent band structures from direct measurements of travelling waves and observing amplitude-dependent plane wave stability. Such findings provide experimental validation for analytical predictions from the multiple scales formulation. Both one-dimensional (1-D) and two-dimensional (2-D) monatomic shear lattices are explored. For the 1-D chain, tracking the phase difference of a plane wave's fundamental frequency component between neighboring unit cells provides direct measurements that populate the lattice's band structure. Re-measuring the band structure for successively higher wave amplitudes exhibits the expected lifting of the passband as is known to occur for media with hardening nonlinearity. Furthermore, time-windowed measurements of wave packets confirm the amplitude-dependent stability of plane waves in the 1-D chain. Low amplitude wave packets retain signal information almost exclusively at the fundamental frequency and higher harmonics. By contrast, the instabilities that develop for high amplitude wave packets are characterized by a significant broadening of frequency content across incommensurate frequencies. Stability exhibits its expected direction dependence in the 2-D lattice for symmetric (*i.e.* uniform) stiffness distributions. The experimental findings in this chapter demonstrate the viability of fabricating wave-based devices that exploit the amplitude-dependent filtering and stability characteristics of nonlinear plane waves.

Prior experimental studies of nonlinear periodic media revealed and validated various phenomena, such as higher-harmonic generation and modal coupling. In [152], high-amplitude, harmonic excitation of a perforated sheet reveals wave beaming at select frequencies that couple to other wave propagation modes. The use of a band-pass filter visualizes the wave energy distribution for each mode that is nonlinearly excited. Additionally, in [153] wave propagation in a long, flexible structure with heavy inclusions was experimentally investigated whereby excitation at flexural mode nonlinearly coupled to an axial mode at a higher harmonic. Other nonlinear experimental studies have considered chains of magnets that feature higher harmonic generation [113, 154] as well as mechanical soliton propagation [155-157]. The stability of plane waves in nonlinear periodic media has not yet been experimentally demonstrated. By contrast, experimental considerations of stability in nonlinear lattices have centered around bi-stable elements that support uni-directional transition waves [65] and enable bandgap penetration [158].

For experimental observation of amplitude-dependent band structures, prior studies have considered standing wave patterns formed by the steady-state combination of forward and reverse travelling waves, *i.e.,* observation of amplitude-dependent shifts in natural frequencies of a finite chain. In [159], amplitude-dependent shifting of the resonant frequencies associated with the band edges of a diatomic chain were measured. Nonlinear frequency response functions of a harmonically-driven granular chain were observed in [160]. Such chains also experimentally exhibited bifurcation behavior [161]. Experimental validation of multiple scales predictions of nonlinear band structure shifting was documented in [162] for a 1-D string of beads. The backbone of a Duffing-type curve was

mapped to the amplitude-dependent dispersion curve for the wave-wave interaction of a forward and reverse travelling wave. The experimental evidence of band structure shifting reported herein differs from the studies in [159, 160, 162] through its direct measurement of travelling waves propagating in a single direction. Boundary effects are safely avoided through the design and testing of a sufficiently large lattice.

This chapter is organized as follows. In Section 6.2, a higher-order multiple scales analysis of nonlinear lattices is reviewed, emphasizing the amplitude-dependent band structure and plane wave stability that it reveals. Section 6.3 describes the design of the experiment, detailing the apparatus and instrumentation employed as well as the lattice model used to guide the testing. Experimental evidence of amplitude-dependent band structure shifting is reported in Section 6.4 for the 1-D chain. Section 6.5 documents the experimental findings of plane wave stability for the 1-D and 2-D systems. The expected amplitude and direction-dependency are observed. Concluding remarks are provided in Section 6.6.

6.2 Theoretical Background

This section briefly introduces the underlying theory motivating the experimental studies. A higher-order multiple scales analysis is developed whose predictions of amplitude-dependent band structure and plane wave stability are experimentally validated. While results for a 1-D lattice are discussed, the manners in which the 2-D lattice possesses key differences are highlighted. Consider a generic 1-D lattice as depicted in Figure 6-1.

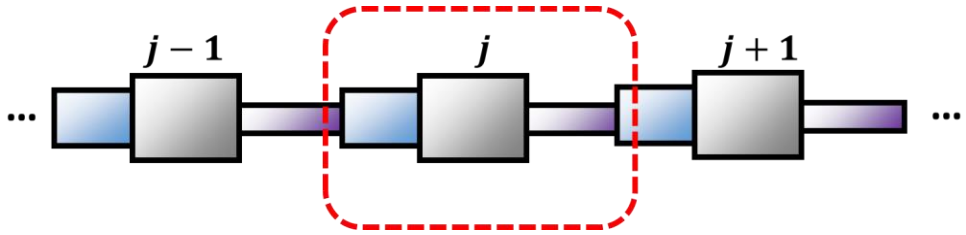

Figure 6-1. Generic 1-D lattice system

Representing the equations of motion of the j^{th} unit cell in matrix form yields

$$\mathbf{M}\ddot{\mathbf{z}}_j + \sum_{p=-1}^{+1}\left[\varepsilon\mathbf{C}^{(p)}\dot{\mathbf{z}}_{j+p} + \mathbf{K}^{(p)}\mathbf{z}_{j+p} + \varepsilon\mathbf{f}_{\mathbf{NL}}\left(\mathbf{z}_{j+p}\right)\right] = \mathbf{0}, \quad \mathrm{j} = -\infty \ldots \infty \tag{6.1}$$

where $\mathbf{z}_j$ denotes the out-of-plane displacement, $\mathbf{M}$, $\mathbf{K}$, and $\mathbf{C}$ denote the mass, stiffness, and damping matrices, respectively, and $\mathbf{f}_{\mathbf{NL}}$ contains the weakly nonlinear restoring forces from quadratic and cubic stiffness. A small parameter ε functions as a book-keeping device. Such general system is capable of specializing to monatomic and diatomic lattices. Proceeding with the multiple scales formulation, various time scales are introduced

$$T_0 = t, T_1 = \varepsilon t, \ldots, T_n = \varepsilon^n t \tag{6.2}$$

where each time scale progresses more slowly than its predecessor. Differentiation with respect to each time scale will be denoted with $D_n(\quad) \equiv \frac{\partial}{\partial T_n}(\quad)$. Additionally, a series solution is introduced

$$\mathbf{z}_j = \mathbf{z}_j^{(0)} + \varepsilon\mathbf{z}_j^{(1)} + \cdots + \varepsilon^n\mathbf{z}_j^{(n)} \tag{6.3}$$

A series of cascading differential equations can now be formed by collecting terms at matching orders of ε. The first three equations appear as

$$\varepsilon^0\text{: } \mathrm{D}_0^2\mathbf{M}\mathbf{z}_j^{(0)} + \sum_{p=-1}^{+1}\left[\mathbf{K}^{(p)}\mathbf{z}_{j+p}^{(0)}\right] = \mathbf{0} \tag{6.4}$$

$$\varepsilon^1\colon\ \mathrm{D}_0^2\mathbf{M}\mathbf{z}_j^{(1)}\sum_{p=-1}^{+1}\left[\mathbf{K}^{(p)}\mathbf{z}_{j+p}^{(1)}\right] = -2\mathrm{D}_0\mathrm{D}_1\mathbf{M}\mathbf{z}_j^{(0)} - \sum_{p=-1}^{+1}\left[\mathrm{D}_0\mathbf{C}^{(p)}\mathbf{z}_{j+p}^{(0)} + \mathbf{f}_{\mathbf{NL}}\left(\mathbf{z}_{j+p}^{(0)}\right)\right] + \mathrm{c.\,c.} \tag{6.5}$$

$$\varepsilon^2\colon\ \mathrm{D}_0^2\mathbf{M}\mathbf{z}_j^{(2)}\sum_{p=-1}^{+1}\left[\mathbf{K}^{(p)}\mathbf{z}_{j+p}^{(2)}\right] = -(2\mathrm{D}_0\mathrm{D}_2 + \mathrm{D}_1^2)\mathbf{M}\mathbf{z}_j^{(0)} - \sum_{p=-1}^{+1}\left[\mathrm{D}_0\mathbf{C}^{(p)}\mathbf{z}_{j+p}^{(1)} + \mathrm{D}_1\mathbf{C}^{(p)}\mathbf{z}_{j+p}^{(0)} + \mathbf{f}_{\mathbf{NL}}^{(2)}\left(\mathbf{z}_{j+p}^{(0)}, \mathbf{z}_{j+p}^{(1)}\right)\right] + \mathrm{c.\,c.} \tag{6.6}$$

where $\mathbf{f}_{\mathbf{NL}}^{(2)}\left(\mathbf{z}_{j+p}^{(0)}, \mathbf{z}_{j+p}^{(1)}\right)$ contains all the $\mathrm{O}(\varepsilon^2)$ terms from the nonlinear force vector and c. c. denotes the complex conjugate of all preceding terms.

Examination of Eq. (6.4) identifies the 0th-order solution as a Bloch Wave

$$\mathbf{z}_j^{(0)} = \frac{1}{2}\boldsymbol{\phi}A\mathrm{e}^{\mathrm{i}\omega_0 T_0}\mathrm{e}^{-\mathrm{i}\mu j} + \mathrm{c.\,c.} \tag{6.7}$$

where A denotes the wave's complex amplitude and the frequency/wavenumber pair (ω_0, μ) in conjunction with the wave propagation mode shape $\boldsymbol{\phi}$ satisfy the linear dispersion relationship of the lattice. In 2-D, a lattice possesses two wavenumber components that satisfy a 0th-order dispersion surface. For analytical convenience, the wave amplitude is decomposed into polar form $A = \alpha\mathrm{e}^{\mathrm{i}\beta}$ where the magnitude α and phase β must be functions of only slower time scales $(T_1, T_2, \ldots, T_n)$ by virtue of satisfying Eq. (6.4).

With the 0th-order solution defined by Eq. (6.7), the 1st-order equation in Eq. (6.5) is updated, giving rise to inhomogeneous terms on its right hand side. Secular terms, which must be removed, appear at $\mathrm{e}^{\mathrm{i}(\omega_0 T_0 - \mu j)} + \mathrm{c.\,c.}$ whereas non-secular terms appear at $\mathrm{e}^{\mathrm{i}h(\omega_0 T_0 - \mu j)} + \mathrm{c.\,c.}, h \neq 1$. Removal of secular terms is facilitated by expanding the damping and nonlinear vectors on the right hand side into their Fourier components $\sum_{l=0}^{\infty}\mathbf{f}_l^{(1)}\mathrm{e}^{\mathrm{i}l(\omega_0 T_0 - \mu j)}$ as well as re-writing the solution in modal coordinates $\mathbf{z}_j^{(n)} = \boldsymbol{\Phi}\boldsymbol{u}_j^{(n)}$ where $\boldsymbol{\Phi}$ is a matrix whose columns are the 0th-order wave propagation mode shapes of the lattice. Pre-multiplying Eq. (6.5) with $\boldsymbol{\phi}_\sigma^{\mathbf{H}}$, the Hermitian transpose of mode σ gives

$$m_\sigma\mathrm{D}_0^2 u_j^{(1)} + k_\sigma u_j^{(1)} = -2\mathrm{i}m_\sigma\omega_0\mathrm{D}_1\left(\alpha e^{\mathrm{i}\beta}\right)e^{\mathrm{i}(\omega_0 T_0 - \mu j)} + \boldsymbol{\phi}_\sigma^{\mathbf{H}}\sum_{l=0}^{\infty}\mathbf{f}_l^{(1)}e^{\mathrm{i}l(\omega_0 T_0 - \mu j)} + \mathrm{c.\,c.} \tag{6.8}$$

where m_σ and k_σ denote the modal mass and wavenumber-reduced stiffness values for mode σ and u_j is the modal coordinate governing mode σ. Eq. (6.8) is in a form amenable to removing secular terms by imposing

$$-2\mathrm{i}m_\sigma\omega_0(\mathrm{D}_1\alpha + \mathrm{i}\alpha\mathrm{D}_1\beta)e^{\mathrm{i}\beta} = \boldsymbol{\phi}_\sigma^{\mathrm{H}}\mathbf{f}_1^{(1)} \tag{6.9}$$

Further decomposition of Eq. (6.9) into its real and imaginary parts provides closed-form solutions for the evolution equation for phase, $\mathrm{D}_1\beta$, and amplitude, $\mathrm{D}_1\alpha$. Such results provide crucial information about the lattice. The evolution equation for phase represents an amplitude-dependent correction to the 0th-order band structure whereas the evolution equation for amplitude contains information about plane wave stability.

Non-secular terms remain and demand a particular solution that propagates at the corresponding multi-harmonic content

$$u_j^{(1)} = \sum_{h=0}^{\infty} a_h^{(1)}\mathrm{e}^{\mathrm{i}h(\omega_0 T_0 - \mu j)} + \mathrm{c.\,c.} \tag{6.10}$$

where $h \neq 1$. The complex amplitude $a_h^{(1)}$ is found using the method of undetermined coefficients

$$a_h^{(1)} = \frac{\boldsymbol{\phi}_\sigma^{\mathrm{T}}\mathbf{f}_h^{(1)}}{-(h\omega_0)^2 m_\sigma + k_\sigma} \tag{6.11}$$

These solutions compose an invariant plane wave solution that propagates at a single constant phase velocity without dispersing.

Now that the 1st-order solution is defined, analysis at the 2nd order follows a similar procedure. The updated Eq. (6.6) appears as

$$\begin{aligned} m_\sigma\mathrm{D}_0^2 u_j^{(2)} + k_\sigma u_j^{(2)} = {} & -m_\sigma(\mathrm{D}_1^2 + 2\mathrm{i}\omega_0\mathrm{D}_2)\left(\alpha\mathrm{e}^{\mathrm{i}\beta}\right)\mathrm{e}^{\mathrm{i}(\omega_0 T_0 - \mu j)} \\ & + \boldsymbol{\phi}_\sigma^{\mathrm{H}}\sum_{l=0}^{\infty}\mathbf{f}_l^{(2)}\mathrm{e}^{\mathrm{i}l(\omega_0 T_0 - \mu j)} + \mathrm{c.\,c.} \end{aligned} \tag{6.12}$$

where $\mathbf{f}_l^{(2)}$ is the l^{th} Fourier coefficient for the 2nd-order damping and nonlinear inhomogeneous terms. The secular terms at $\mathrm{e}^{\mathrm{i}(\omega_0 T_0 - \mu j)} + \mathrm{c.\,c.}$ can be removed by satisfying

$$-m_\sigma(\mathrm{D}_1^2 + 2\mathrm{i}\omega_0\mathrm{D}_2)\left(\alpha\mathrm{e}^{\mathrm{i}\beta}\right) = \boldsymbol{\phi}_\sigma^{\mathrm{H}}\mathbf{f}_1^{(2)} \tag{6.13}$$

which identifies the 2nd-order evolution equations $\mathrm{D}_2(\beta)$ and $\mathrm{D}_2(\alpha)$. Note that also, a particular solution arises from the non-secular terms of the form

$$u_j^{(2)} = \sum_{h=0}^{\infty} a_h^{(2)}\mathrm{e}^{\mathrm{i}h(\omega_0 T_0 - \mu j)} + \mathrm{c.\,c.} \tag{6.14}$$

whose complex amplitude is found through the method of undetermined coefficients

$$a_h^{(2)} = \frac{\boldsymbol{\phi}_\sigma^{\mathrm{H}} \mathbf{f}_h^{(2)}}{-(h\omega_0)^2 m_\sigma + k_\sigma} \tag{6.15}$$

A standard reconstitution process presents the total evolution of phase and amplitude

$$\dot{\beta} = \varepsilon \mathrm{D}_1(\beta) + \varepsilon^2 \mathrm{D}_2(\beta) \tag{6.16}$$

$$\dot{\alpha} = \varepsilon \mathrm{D}_1(\alpha) + \varepsilon^2 \mathrm{D}_2(\alpha) \tag{6.17}$$

In an un-damped chain, $\mathrm{D}_1(\alpha) = \mathrm{D}_2(\alpha) = 0$ and it becomes increasingly evident that evolution equations for phase β represent shifts in band structure since $\mathrm{D}_1(\beta)$ and $\mathrm{D}_2(\beta)$ are constant and thus the solution to Eq. (6.16) is

$$\beta = \beta_0 + \varepsilon \mathrm{D}_1(\beta) T_0 + \varepsilon^2 \mathrm{D}_2(\beta) T_0 \tag{6.18}$$

where the initial phase β_0 can be set to zero without loss of generality. Updating the 0^{th}-order solution in Eq. (6.7)

$$\mathbf{z}_j^{(0)} = \frac{1}{2} \boldsymbol{\phi} \alpha \mathrm{e}^{\mathrm{i}\omega T_0} \mathrm{e}^{-\mathrm{i}\mu j} + \mathrm{c.\,c.} \tag{6.19}$$

where the total amplitude-dependent frequency ω is

$$\omega = \omega_0 + \overbrace{\varepsilon \mathrm{D}_1(\beta)}^{\omega_1} + \overbrace{\varepsilon^2 \mathrm{D}_2(\beta)}^{\omega_2} \tag{6.20}$$

In the case of light damping, Eq. (6.20) holds yet the correction terms ω_1 and ω_2 decay slowly over time.

Additionally, a local stability analysis can be carried-out on Eq. (6.17) to extract fixed points α^* governing wave amplitude.

$$\dot{\alpha}|_{\alpha^*} = 0 \tag{6.21}$$

See Sections 2.7 and 3.6 for further details. In general, the procedure identifies two fixed points

$$\alpha^* = 0, \sqrt{\frac{\omega_0}{\varepsilon \delta}} \tag{6.22}$$

where $\alpha^* = 0$ is stable and $\alpha^* = \sqrt{\frac{\omega_0}{\varepsilon \delta}}$ is unstable. Such result establishes the amplitude-dependent stability of plane waves: low amplitude plane waves are attracted to the stable fixed point in the presence of light viscous damping whereas sufficiently high amplitudes undergo a loss of stability. While the non-zero fixed point is large enough to violate the weak nonlinearity assumption, the multiple scales analysis qualitatively defines the amplitude-dependent stability characteristics of the lattice system which was validated by

numerical simulation (see Section 2.7.2). In 2-D lattices, the fixed point $\alpha^* = \sqrt{\frac{\omega_0}{\varepsilon\delta}}$ varies based on the plane wave's orientation θ (measured relative to the lattice direction). Inclined directions are inherently more stable than lattice directions as indicated by the lowest amplitude fixed point existing at $\theta = 0$.

6.3 Experimental Design

6.3.1 Apparatus and Instrumentation

To physically realize nonlinear monatomic lattices in 1-D and 2-D, the apparatus in Figure 6-2 was constructed. Nylon string is tensioned along an aluminum frame to provide elastic restoring forces. Periodically-spaced magnetic inclusions form the discrete mass elements of the lattices. For the 1-D configuration, a single column of magnets forms a chain coupled via a longitudinal string. Each unit cell is additionally grounded with transverse string clamped between the aluminum frame and a rigid member affixed to the structure. Since two magnets snap together at locations where strings intersect, a thin foam material is added between the magnets to ensure their contact remains level across their attracting faces. Pretension is set by pulling each string with a force gauge (Mark-10 Series 2 Model M2-10) to a desired tension and then tightening a bolt and nut combination to lock the string in place. Excitation is introduced to the system via an electrodynamic shaker attached to a single mass.

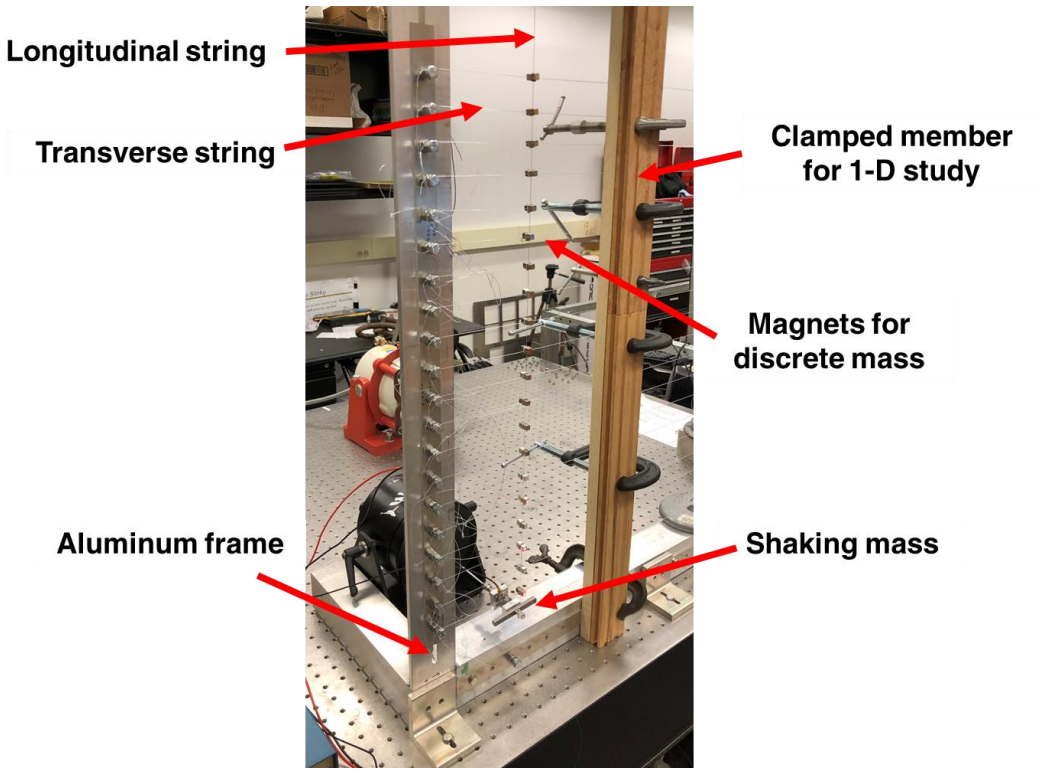

Figure 6-2. Experimental design of a 1-D monatomic shear lattice

For the testing of amplitude-dependent band structure, Figure 6-3a depicts the physical set-up whereas Figure 6-3 b represents the flow of signal information through a block diagram. Since weak nonlinear behavior is desired, a moderate stroke shaker (B&K Type 4809, 8 mm peak-to-peak max stroke) is incorporated. Velocity is measured by two neighboring single point scanning laser Doppler vibrometers (Polytec PDV 100) to capture the propagation of a travelling wave. This dual laser configuration makes this set-up robust to small differences in propagation delay that may arise if instead combining the results from separate tests.

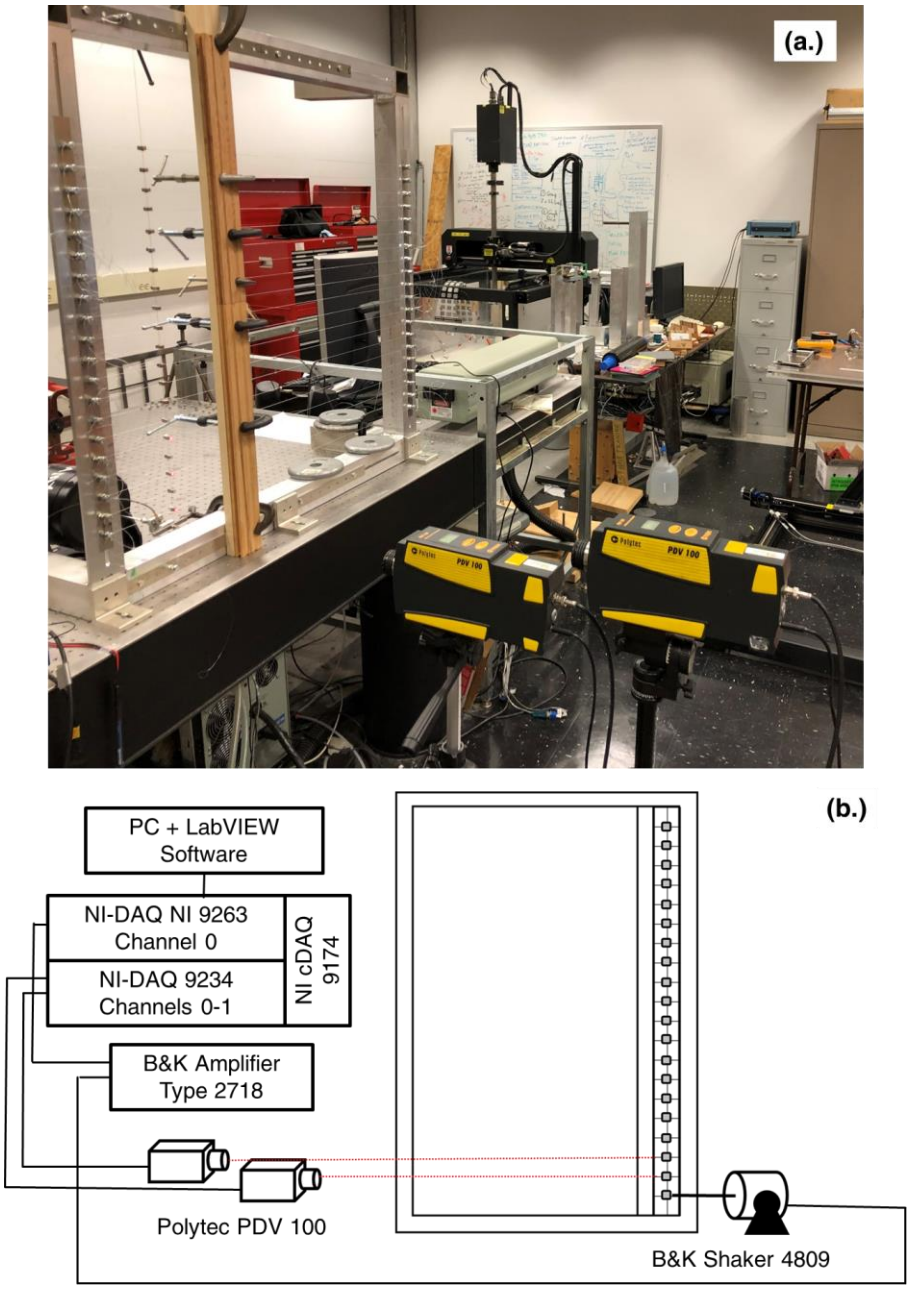

Figure 6-3. Experimental set-up for testing amplitude-dependent band structure incorporating two single point lasers and a moderate stroke shaker . (a.) Physical apparatus (b.) Block diagram

Figure 6-4 illustrates the configuration for exploring waveform stability with the physical apparatus pictured in Figure 6-4a and the block diagram represented in Figure 6-4b. Large amplitude motion beyond the weakly nonlinear limit must be introduced to the lattice and

thus a large stroke shaker (LDS V408, 14 mm peak-to-peak max stroke) is used. Velocity measurements are obtained through a single scanning laser Doppler vibrometer (Polytec PSV 400). The scanning laser facilitates the recording of several masses without requiring to re-position the laser's tripod. Thus, such equipment is more amenable to imaging the stability of a plane wave through a spatiotemporal spectral analysis. Furthermore, the scanning laser possesses a higher limit to its maximum velocity measurement compared to the single point laser (*i.e.*, 10 m/s compared to 0.5 m/s) thus giving it a better advantage to capture wave propagation beyond the weakly nonlinear limit.

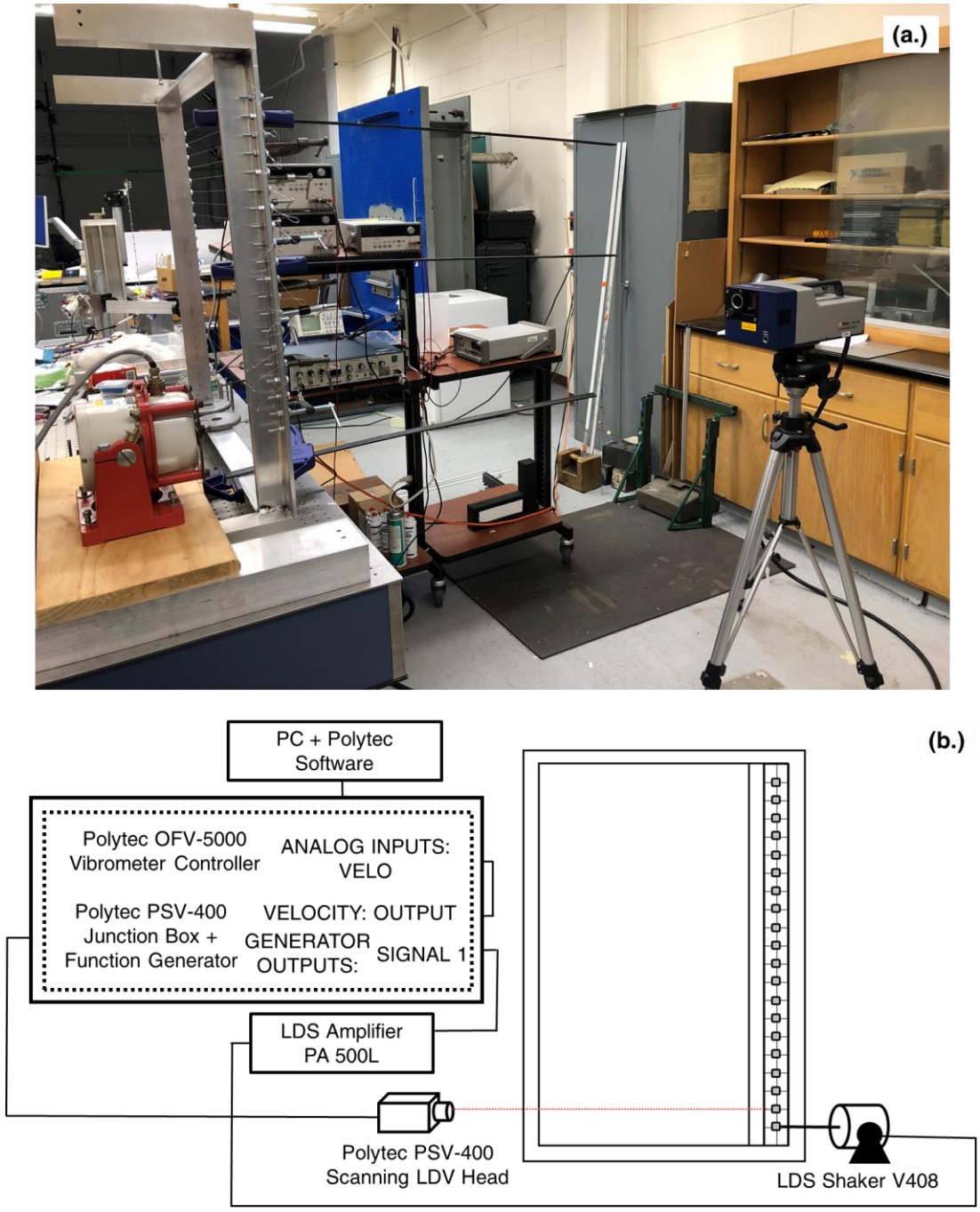

Figure 6-4. Experimental set-up for testing plane wave stability incorporating a scanning point laser and a high stroke shaker. (a.) Physical apparatus (b.) Block diagram

The scanning LDV and high stroke shaker were also implemented when investigating the stability of plane waves in the 2-D shear lattice, pictured in Figure 6-5. Consequently, the

same block diagram in Figure 6-4b applies to this experimental configuration. Note that the shaker is affixed to the center-most mass in the 19x19 unit cell lattice such that the source is farthest from all boundaries.

Figure 6-5. Experimental configuration for stability analysis of the 2-D lattice. The high stroke shaker excites the lattice in its center and the scanning LDV (not shown) records the resultant velocities.

6.3.2 Model Development

To guide the design of the experiment, the lumped wire model developed in [162] was referenced. The model analytically describes the geometric nonlinearity arising in a pre-

tensioned chain of beads undergoing transverse oscillations. An adaptation of the model as it relates to the lattice explored this work is summarized in this section. The model is developed for the 1-D chain pictured in Figure 6-2 and then extended analogously to a 2-D system.

The governing equation for transverse vibration of a wire $w(x,t)$ stretched by a pre-tension T_0 along its length, which is aligned with the x-direction, is

$$(\rho S + \delta(x-na)m)\ddot{w} - T_0\frac{\partial^2 w}{\partial x^2} = (ES - T_0)\frac{\partial}{\partial x}\left[\frac{1}{2}\frac{\partial w}{\partial x}\left(\frac{\partial w}{\partial x}\right)^2\right] - F_g(w)\delta(x-na) \tag{6.23}$$

where ρ, E and S denote the density, Young's modulus, and cross sectional area of the wire, respectively. The effect of the periodic placement of inclusions of mass m at a lattice spacing a, is captured by the Dirac function $\delta(x-na)$, where n is an integer. Furthermore, restoring forces due to the transverse "grounding" springs $F_g(w)$ are also periodically spaced by the lattice constant a and take the form [163]

$$F_g(w) = \frac{2T_{0,g}}{L}w + \frac{ES}{L^3}w^3 \tag{6.24}$$

where $T_{0,g}$ and $2L$ are the pre-tension and length of the transverse wire, respectively. As discussed in Section 6.3.1, the transverse wire possesses identical material properties to the longitudinal wire. Note that Eq. (6.24) was derived assuming transverse displacements are large enough to strain the transverse wire yet small enough to neglect geometric nonlinearity due to "large angles", which is a nonlinear softening effect that initiates when $w \approx L$.

Letting the inclusions be heavy relative to the mass of the wire, *i.e.*, $m \gg \rho Sa$, the dynamics of the system concentrates to the discrete lattice sites located at $x = na$. Consequently, spatial derivatives become finite difference approximations, and the equation governing the oscillation of the j^{th} mass, w_j, becomes

$$m\ddot{w}_j + \frac{T_0}{a}\left(2w_j - w_{j-1} - w_{j+1}\right) + \frac{ES}{2a^3}\left(w_j - w_{j-1}\right)^3 + \frac{ES}{2a^3}\left(w_j - w_{j+1}\right)^3 + \frac{2T_{0,g}}{L}w_j + \frac{ES}{L^3}{w_j}^3 = 0 \tag{6.25}$$

\where it is assumed $ES \gg T_0$ consistent with the development in [162]. The result in Eq. (6.25) now resembles the equation governing a nonlinear grounded monatomic chain as pictured in Figure 6-6a. By comparing terms, $k_1 = \frac{T_0}{a}, k_3 = \frac{ES}{2a^3}, k_{1,g} = \frac{2T_{0,g}}{L}$ and $k_{3,g} = \frac{ES}{L^3}$. The corresponding linear band structure is plotted in Figure 6-6c. Note that there is a non-zero cut-on frequency due to the grounding stiffness. Since all coefficients in Eq. (6.25) must necessarily be positive to remain physically valid, this system possesses hardening stiffness nonlinearity. Thus, it is expected that the 0^{th}-order dispersion curve in Figure 6-6c will rise in the presence of high-amplitude plane waves. Furthermore, due to the generality of the framework presented in Section 6.2, the matrix equations of motion in Eq. (6.1) apply to Eq. (6.25).

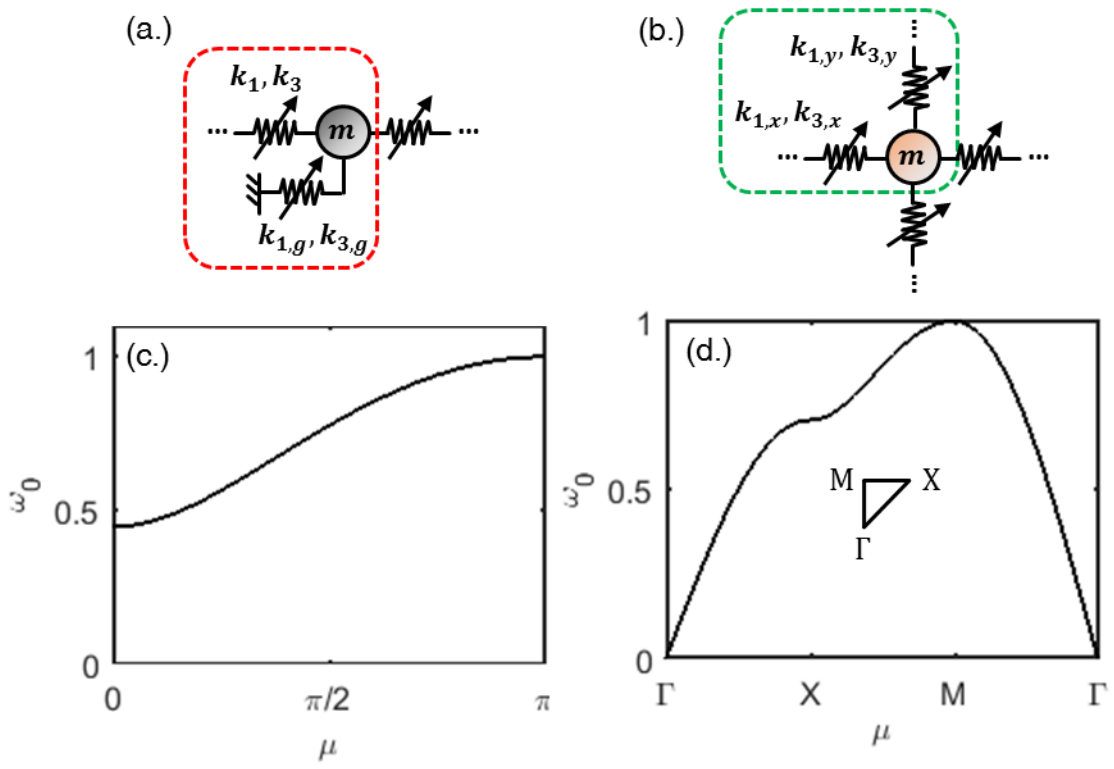

Figure 6-6. Discrete lattice models investigated in this work. (a.) 1-D grounded monatomic chain and (b.) 2-D monatomic shear lattice. The corresponding linear band structures are presented for the 1-D chain (c.) and 2-D lattice (d.).

Using the expressions for the nonlinear coefficients, the non-dimensional strength of the cubic nonlinearity is

$$\Pi_3 = \frac{ES}{2T_{max}L_{max}^2}\alpha^2 \tag{6.26}$$

where α is the 0[th]-order plane wave amplitude as described in Section 6.2 and T_{max} is the maximum tension in the lattice, which is either T_0 or $T_{0,g}$ for the 1-D chain and L_{max} is the maximum length between a and L.

For the 2-D configuration, the grounding term vanishes since each mass is coupled to its four nearest neighbors as opposed to being coupled to two neighbors and two fixed

columns as in the 1-D chain. Furthermore, symmetric restoring forces arise from the identical tensioning of all strings, resulting-in the model in Figure 6-6b. The associated equation of motion is

$$m\ddot{w}_{j,k} + \frac{T_0}{a}\left(2w_{j,k} - w_{j-1,k} - w_{j+1,k}\right) + \frac{T_0}{a}\left(2w_{j,k} - w_{j,k-1} - w_{j,k+1}\right) + \frac{ES}{2a^3}\left(w_{j,k} - w_{j-1,k}\right)^3 + \frac{ES}{2a^3}\left(w_{j,k} - w_{j+1,k}\right)^3 + \frac{ES}{2a^3}\left(w_{j,k} - w_{j,k-1}\right)^3 + \frac{ES}{2a^3}\left(w_{j,k} - w_{j,k+1}\right)^3 = 0 \quad (6.27)$$

where $w_{j,k}$ is the displacement of the mass at unit cell (j,k). Comparing terms and noting the lattice's symmetry gives the following relationships: $k_{1,x} = k_{1,y} = \frac{T_0}{a}$ and $k_{3,x} = k_{3,y} = \frac{ES}{2a^3}$. Since there are no grounding springs in this model, the strength of the cubic nonlinearity is $\Pi_3 = \frac{ES}{2T_0a^2}\alpha^2$. As depicted in Figure 6-6d, the band structure for a 2-D lattice can be represented as a curve if evaluated along the special lattice directions.

6.4 Amplitude-Dependent Band Structure

In this section, experimental results are detailed that demonstrate amplitude-dependent shifting of band structure in nonlinear 1-D lattices. Unlike prior work that experimentally extracted nonlinear band structures from standing waves (*i.e.* vibration modes) on a periodic string [162], these experiments capture a travelling wave as it propagates through the medium, recording time histories at two unit cells which are subsequently used to compute the plane wave's wavenumber. Such approach more directly observes the self-interacting plane wave solutions revealed by multiple scales analysis of the lattice equations of motion.

For these tests, the configuration in Figure 6-3 is considered. Using the procedure described in Section 6.3.1, all transverse strings were tensioned to the same level and the tension in the single longitudinal string was set. To identify the linear natural frequencies of the finite 19-unit cell system, low-amplitude white noise was sent to the shaker and the resultant velocity was recorded at the bottom-most unit cell in the chain over a long period of time. Processing the velocity time history using the Fast Fourier Transform (FFT) revealed the natural frequencies of the system. To experimentally obtain the lattice's band structure, the shaker was programmed to vibrate at narrowband frequencies in a 2 Hz spaced interval between 20 and 44 Hz, limits identified by the white noise test. To gradually introduce harmonic loading to the lattice, the signal was given a 1st-order exponential envelope, such that the total voltage signal sent to the shaker was

$$V(t) = \left(1 - \mathrm{e}^{-t/\tau}\right) V_0 \sin(2\pi f t) \tag{6.28}$$

where V_0 and f denote the amplitude and frequency of the voltage signal, respectively, and the time constant τ was selected to be $\tau = \frac{1}{2f}$. For a given series of tests, the voltage amplitude V_0 was held constant as the frequency was varied. The ramped harmonic signal injected a plane wave into the lattice which propagated up the chain until reaching the upper-most unit cell, whereupon the plane wave experienced a reflection due to an impedance change. The two LDV's recorded velocity signals of the unit cells directly above the shaker, $v_1(t)$ and $v_2(t)$, as the initial travelling wave propagated. Figure 6-7 displays the two sample time-windowed velocities obtained from $f = 28$ Hz and $V_0 = 0.3$ V. The signals are uncorrupted by wave reflections as indicated by their time delay and

nearly constant amplitudes. Indeed, monitoring both components—time delay and amplitude—indicated whether the considered signal contained reflected wave information.

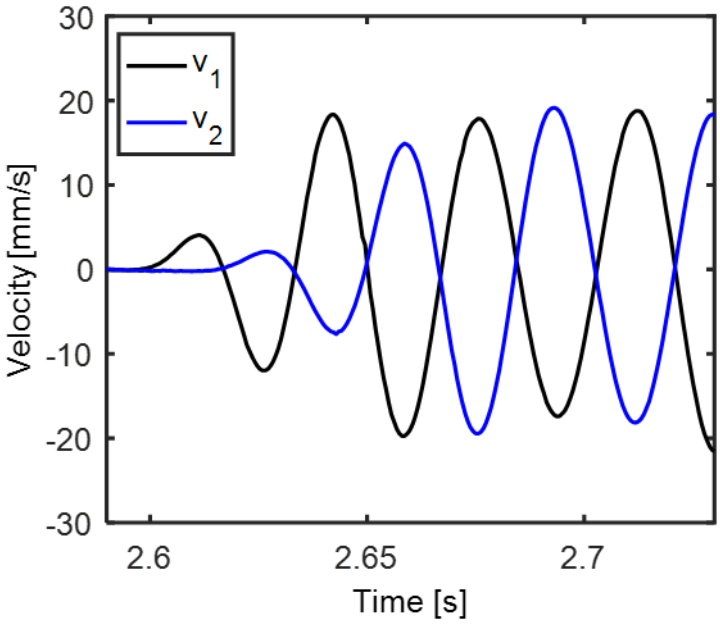

Figure 6-7. Velocity time histories at two neighboring unit cells above the shaker in the 1-D chain. The time delay and constant amplitude indicate that a travelling wave is captured.

Removing the initial rising portion of the signals and processing the time-windowed velocities with an FFT algorithm yielded their frequency content

$$v_1(t) \rightarrow \left(V_1(\hat{f}), \phi_1(\hat{f})\right) \tag{6.29}$$

$$v_2(t) \rightarrow \left(V_2(\hat{f}), \phi_2(\hat{f})\right) \tag{6.30}$$

where $V_1(\hat{f})$ and $\phi_1(\hat{f})$ denote the magnitude and phase, respectively, at the discrete Fourier frequency $\hat{f}$ for $v_1(t)$, and the same naming convention applies for $V_2(\hat{f})$ and $\phi_2(\hat{f})$. Recalling the analysis in [22], the difference between phases at the forcing frequency can be used to determine the fundamental wavenumber μ

$$\mu = \phi_2(f) - \phi_1(f) \tag{6.31}$$

Thus, a frequency paired with a wavenumber populates the lattice's band structure. Figure 6-8 displays band structures measured for the 1-D lattice at different input voltage amplitudes. Higher voltage amplitudes correspond to longer strokes on the shaker and thus higher plane wave amplitudes. The wavenumber decreases as the plane wave amplitude increases confirming the nonlinear hardening behavior predicted by multiple scales. Horizontal error bars quantify the variation of the wavenumber from three repeated tests, which are relatively small and thus demonstrate the repeatability of the experiment. The group velocity, or slope, of the dispersion curve does not tend to zero at the edge of the Irreducible Brillouin Zone since this is a forced lattice system with viscous damping. Such characteristic was also observed experimentally in [113].

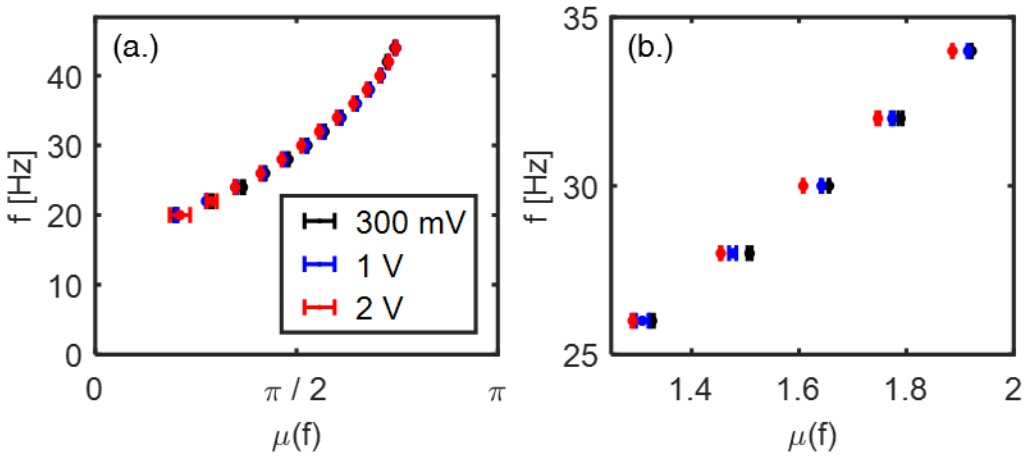

Figure 6-8. Amplitude-dependent band structure measured from travelling waves (a.) Irreducible Brillouin Zone (b.) Zoomed-in region illustrating the wavenumber shifts due to hardening nonlinearity

To observe still larger shifts, the longitudinal pretension T_0 is lowered to enhance the effect of nonlinearity according to Eq. (6.26). A 0.5 Hz sampling of frequencies are tested in the range 20 to 27 Hz at two input voltages: $V_0 = 1$ V and $V_0 = 2$ V. The closeness of this

sampling enables one to clearly observe a nearly 6% increase in the pass band around μ =1.8 as highlighted in Figure 6-9.

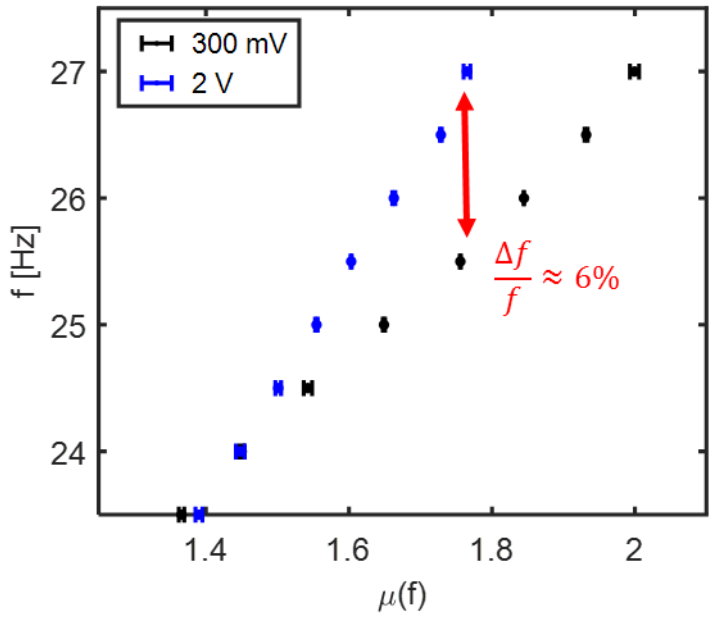

Figure 6-9. A nearly 6% shift in band structure can be experimentally achieved by lowering the pretension in the longitudinal string.

Typically, nonlinear band structures are reported for a fixed displacement amplitude [21, 22]. At constant voltage amplitude, displacement generally decreases as the frequency increases to conserve the shaker's power. Experimentally ensuring constant amplitude would add a layer of complexity to the instrumentation and apparatus: a controller would need to be devised that operates on the fundamental frequency component of the shaking mass' velocity and settles quickly enough to minimize error before wave reflections return. Nonetheless, higher amplitudes raise the passband in the experimental results, consistent with the multiple scales analysis. Indeed, prior experimental studies that extracted

dispersion curves from travelling waves did not report experimental evidence of amplitude-dependent shifting [113, 153].

6.5 Plane Wave Stability

This section details an experimental demonstration of plane wave stability in nonlinear lattices. Both the 1-D configuration in Figure 6-2 and 2-D configuration in Figure 6-5 are explored, and the block diagram in Figure 6-4b applies to each case. The test results are consistent with the multiple scales predictions.

6.5.1 Amplitude-Dependent Stability in 1-D Chains

For studying stability, a low-frequency modulated wave packet is injected into the bottom-most mass of the chain. The functional form of the voltage sent to the shaker is

$$V(t) = \begin{cases} V_p \sin(2\pi f t)\sin(\Omega t), & 0 \le t \le \frac{\pi}{\Omega} \\ 0, & t \ge \frac{\pi}{\Omega} \end{cases} \tag{6.32}$$

where V_p and f denote the amplitude and frequency of the shaker's input signal. To serve as a low frequency envelope, the parameter Ω is set to $\frac{2\pi f}{10}$. Such signal enables a finite burst of energy to enter the lattice and tracked as it propagates. Thus, wave reflections can be monitored by observing when the packet returns to the considered unit cell, which is typically salient for these weakly dispersive media. Use of the long-stroke shaker (LDS V408) enables high voltage amplitudes to actuate into large displacements.

The scanning LDV facilitates the tracking of the wave packet as it propagates. After pre-defining the unit cells to measure, separate tests are run with the scanning laser positioned

at the different locations. Each result can then be combined to image the wave packet's propagation. Additionally, the scanning LDV has a larger limit for the velocities it can measure without clipping (10 m/s) compared to that of the single point laser Doppler vibrometer (0.5 m/s).

Figure 6-10 displays an experimental demonstration of amplitude-dependent stability for plane waves in nonlinear chains. Pictured is the spectral content revealed by an FFT of a wave packet's arrival four unit cells from the shaker, which is forced at $f = 17$ Hz. Note that the frequency spectrum is normalized with respect to the amplitude and frequency hosting the peak spectral component (*i.e.*, the spectral content approximately at the forcing frequency f). Also note that the signal is Hanning-windowed and zero-padded to avoid spectral leakage and interpolate frequency content, respectively. Low amplitude plane waves produced by $V_p = 0.5$ V (solid line), retain its spectral content at the fundamental frequency and are thus considered stable. High amplitude plane waves produced by $V_p = 2$ V (dashed line), experience a high degree of spreading of its frequency content across incommensurate frequencies. Such waveform is considered unstable as it drastically deviates from the multi-harmonic plane wave solutions in the multiple scales analysis. This amplitude-dependent stability is precisely predicted by the local stability analysis of the multiple scales evolution equations.

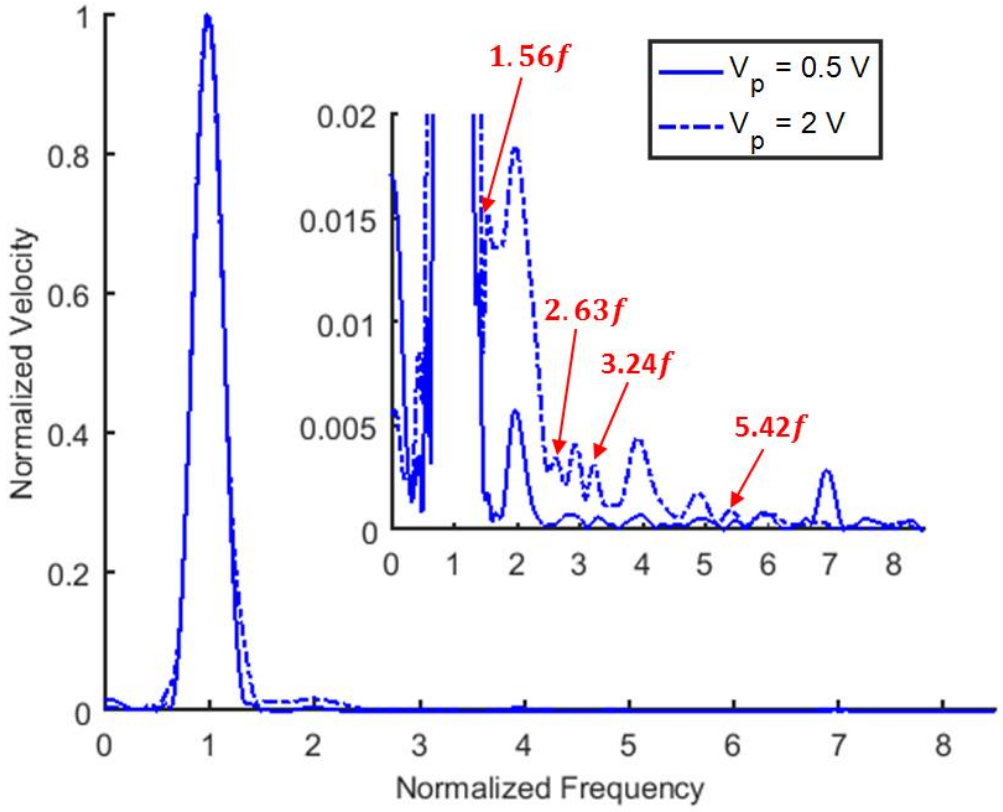

Figure 6-10. Amplitude-dependent plane wave stability is experimentally observed in the 1-D chain. A low amplitude plane wave (solid line) retains its spectral content almost exclusively at the fundamental frequency and higher harmonics whereas a high amplitude plane wave (dashed line) undergoes spreading of its spectral content across incommensurate frequencies.

While the nonlinearity in the model in Eq. (6.25) arises from only cubic-stiffness, higher-harmonic generation of stable plane waves does not manifest exclusively in odd-harmonics, *i.e.* $3f, 5f, 7f$, *etc.* The production of zero frequency and even-harmonics may be explained by magnetic interactions between unit cells which were not included in the model but have been shown in other studies to undergo such effects [113].

The amplitude-dependent stability trend is observed at other measurement sites in the 1-D lattice. Thus, as the plane wave propagates, stability characteristics are not altered. Figure

6-11 displays the frequency content of wave packet arrivals at different distances from the shaker, each exhibiting either the stable harmonic generation or unstable spectral spreading from low and high amplitude plane waves, respectively.

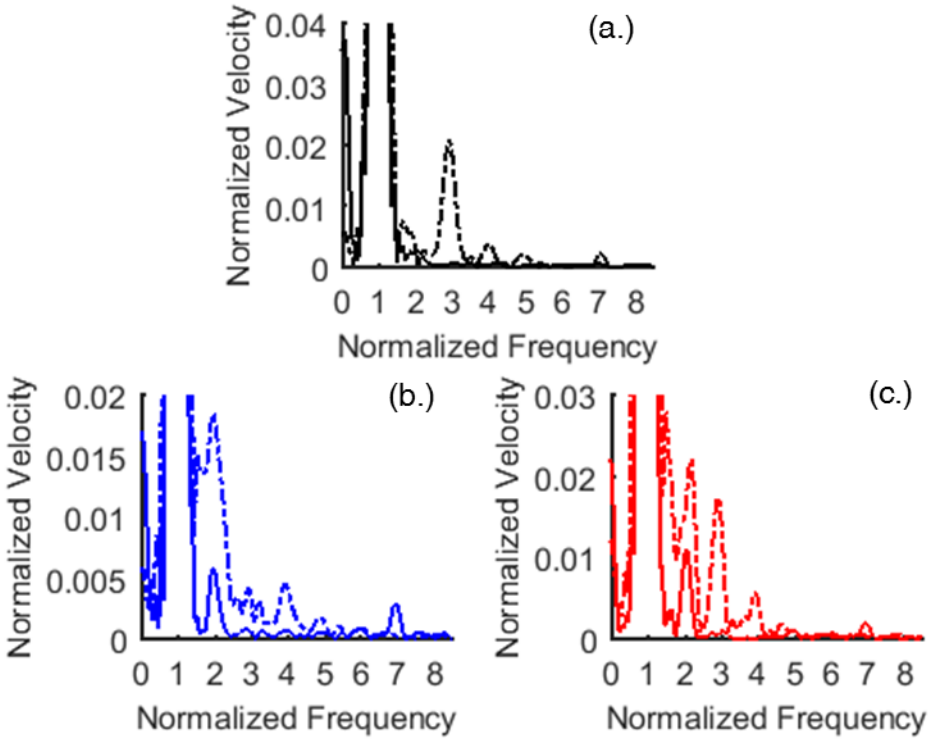

Figure 6-11. Waveforms experimentally recorded at different locations in the 1-D chain when different amplitudes are sent to the shaker. Low amplitude plane waves (solid line) retain their spectral content almost exclusively in the fundamental frequency and higher-harmonics whereas high amplitude plane waves (dashed line) undergo a spreading of their frequency content across incommensurate frequencies. Distances from the shaker are (a.) $j = 2$, (b.) $j = 4$, and (c.) $j = 6$.

As further demonstration of the amplitude-dependent stability in the 1-D chain, a constant harmonic load is sent to the shaker of the form $V(t) = V_h \sin(2\pi f t)$. The steady state result can be interpreted as the nonlinear wave-wave interaction of a forward-oriented travelling wave sent by the shaker and a backward-oriented reflected wave from the chain's termination [162]. In Figure 6-12, it is evident by comparing the spectral content of the plane waves at various lattice sites that plane wave stability (or instability) irreversibly

persists when stable (or unstable) plane waves interact with a harmonic load, sent at $f = 17\ Hz$.

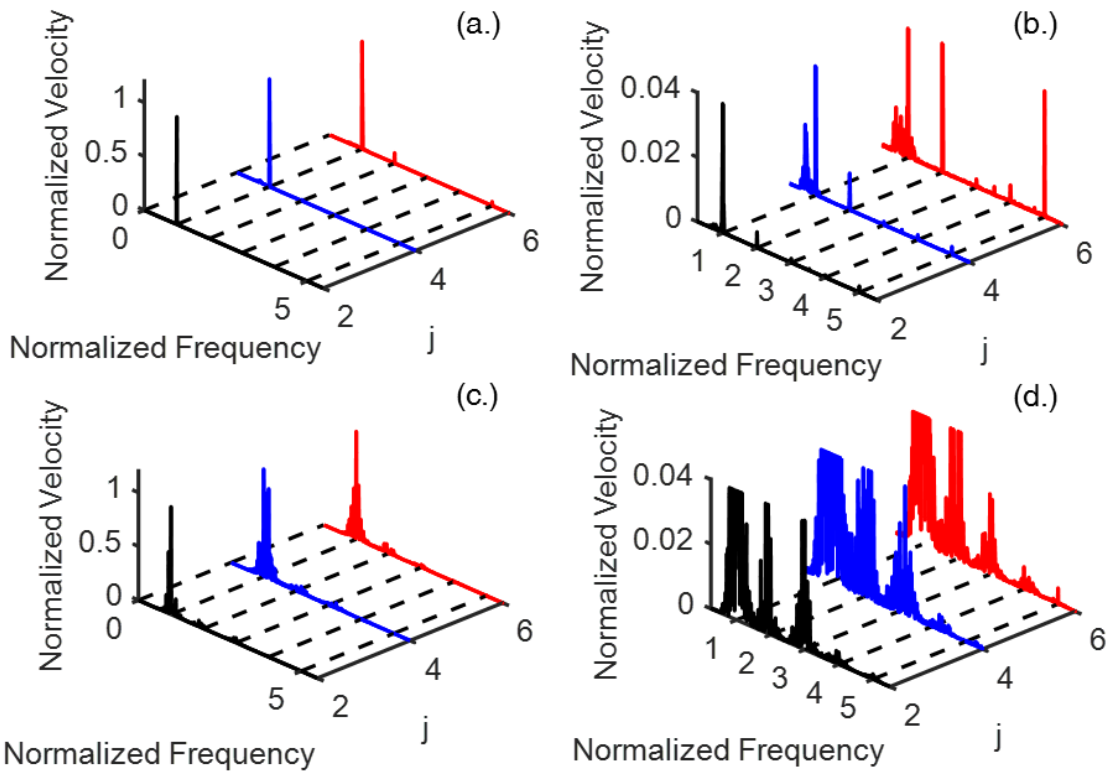

Figure 6-12. A constant harmonic load to the 1-D chain originates as a plane wave and transitions into a nonlinear standing wave over time. In (a.), low amplitude ($V_h = 0.3$ V) plane waves produce stable standing. In (c.), high amplitude ($V_h = 2$ V) plane waves produce unstable standing waves. To further distinguish the two results, zoomed-in views of the stable (b.) and unstable (d.) spectral content are also displayed.

6.5.2 Amplitude and Direction-Dependent Stability in 2-D Lattices

According to the multiple scales fixed point analysis, plane wave stability should vary along different directions with greater stability associated with propagation along inclined directions relative to that along the lattice direction. The 2-D shear lattice assembly in Figure 6-5 was experimentally tested to confirm this behavior. Using the techniques

outlined in Section 6.5.1, wave packet arrivals along various directions were captured by the scanning LDV, and the spectral content of the velocity signals were probed with the same FFT algorithm. Using the digital force gauge, all strings were tensioned to the same force level such that the linear and nonlinear stiffness terms were identical as proposed by Eq. (6.27).

Figure 6-13 displays experimental results for a high amplitude wave packet arrival three unit cells from the shaker yet along different orientations. Referencing the functional form in Eq. (6.32), the shaker was programmed to oscillate at $f = 17$ Hz and $V_p = 1.5$ V. Defining θ to be the angle relative to the lattice direction, wave propagation is seen to be less stable for propagation along $\theta = 0^o$ as compared to $\theta = 45^o$. This is evident by observing the incommensurate frequencies (*e.g.*, $3.39f$ and $4.29f$) that arise along the lattice direction yet the spectral content along the inclined direction is preserved in the fundamental and higher harmonics.

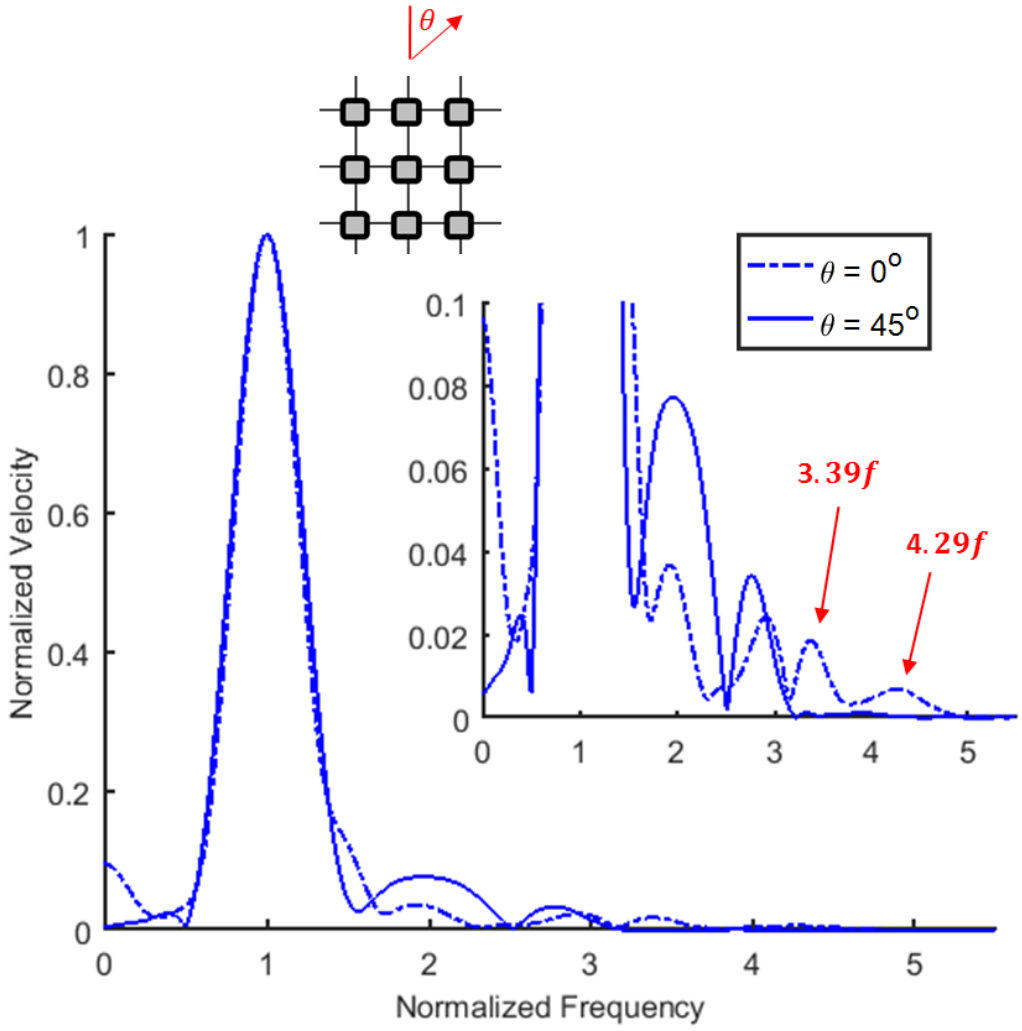

Figure 6-13. Direction-dependent stability experimentally observed in the 2-D lattice. High amplitude plane waves propagate unstably along the lattice direction (dashed line) yet stably along an inclined direction (solid line), consistent with the multiple scales prediction. Velocities are captured three unit cells from the shaker, which was parameterized by $V_p = 1.5$ V and $f = 17$ Hz.

The directional stability trend continues along different unit cells in the 2-D shear lattice as documented by Figure 6-14. For the velocity signal captured at both one and five unit cells away from the shaker, there is significant incommensurate spectral content found between a normalized frequency of 1 and 2 relative to the stable plane wave signal. While the presence of side lobes inevitably arises from applying a Hanning window to a signal,

such effect is expected to be small compared to be unstable frequency content considered in these results. A vibration-based study similar to that in Figure 6-12 cannot be conducted for the 2-D lattice since the boundaries and corners cause wave reflections to occur along many directions and thus the steady state standing wave is a nonlinear combination of travelling waves from various paths.

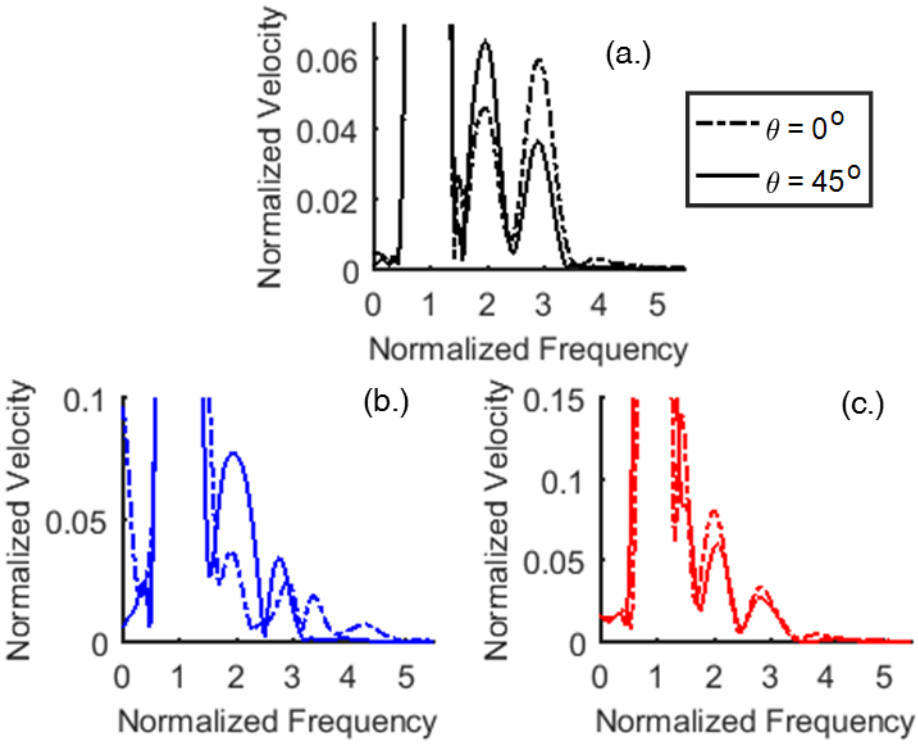

Figure 6-14. Directional stability experimentally observed in the lattice along different distances from the source. The distances from the shaker are (a.) $j = 1$, (b.) $j = 3$, and (c.) $j = 5$.

While beaming is known to occur in symmetric shear lattices at high frequencies [23, 92, 93], this effect is not present in this system at 17 Hz. Such conclusion can be drawn by comparing the magnitude of the plane wave velocities recorded along the two orientations. For example, the peak velocity measured by the scanning LDV positioned five unit cells from the source is 0.083 m/s and 0.078 m/s for propagation oriented along 0^o and 45^o,

respectively. By contrast, the presence of beaming would result in a drastically larger velocity along the 45^o direction as compared to the 0^o direction.

6.6 Concluding Remarks

This chapter reported experimental evidence of amplitude-dependent band structure and plane wave stability in nonlinear lattices. For the first time, the amplitude-dependent "lifting" of a monatomic passband is documented based on experimental measurements of travelling waves in a 1-D chain. Multiple scales predictions of plane wave stability are validated for both 1-D and 2-D systems. Amplitude-dependent stability of plane waves occurs in 1-D chains in which low amplitude wave packets retain their spectral content at the fundamental frequency and higher harmonics whereas unstable wave packets spread their spectral content across incommensurate frequencies. Stability exhibits its expected direction-dependence in 2-D lattices whereby a notable difference arises in wave packet arrivals along the lattice direction as compared to an inclined direction. The former direction is inherently less stable than the latter, as proposed by the multiple scales fixed point analysis.

CHAPTER 7. NON-RECIPROCITY IN LATTICES WITH NONLINEARITY, INTERNAL HIERARCHY, AND ASYMMETRY

7.1 Overview

Reciprocity is a property of linear, time-invariant systems whereby the energy transmission from a source to a receiver is unchanged after exchanging the locations of the source and receiver. Non-reciprocity violates this property and can be introduced to systems if time-reversal symmetry and/or parity symmetry is lost. This study presents a lattice structure with strong stiffness nonlinearities, internal scale hierarchy and asymmetry that breaks reciprocity. Under broadband (*i.e.*, impulsive) excitation, numerical simulations demonstrate that the structure supports highly asymmetrical wave propagation, and hence globally nonreciprocal behavior.

Many studies have induced non-reciprocity by *active* means. One such approach is to induce an odd-symmetric external bias such as a magnetic field [68] or circulating fluid flow [69, 70]. Another approach that has received increased attention over recent years is the spatiotemporal modulation of a medium's material [72-74] or geometrical [75] properties. Considerably less attention has been given to elastic and acoustic structures that *passively* break reciprocity. Some realizations include phononic systems with linear/nonlinear interfaces [79-81] or the strategic placement of a nonlinear defect [82].

The passive strategy of achieving non-reciprocity reported herein is inspired by prior studies of targeted energy transfer in systems with light, highly nonlinear attachments [164-

166]. In these studies, impulsive energy preferentially transmits from the large to small scale where it is then dissipated, and transient resonance capture is identified as the primary mechanism governing this phenomenon. Recently, such systems were generalized to contain any number of nested scales [167]. When each successively smaller scale is coupled with a proportional amount of nonlinear stiffness, the system exhibits highly non-reciprocal behavior. This work builds-upon the concept in [167] by designing a lattice whose unit cells feature the nonlinearity and hierarchy of the isolated system. Additionally, asymmetry is imposed through a difference in the inter-cell coupling on the left and right sides. Numerical simulations of the lattice equations of motion confirm that reciprocity is broken globally. It is important to note that, in conjunction with the numerical studies presented herein, experimental observation of non-reciprocity in a lattice with two-scale unit cells is reported in [168].

This chapter is organized as follows. Section 7.2 presents and describes the key features of the lattice incorporating nonlinearity, asymmetry, and internal hierarchy. Section 7.3 reviews the local non-reciprocity as made possible by an isolated unit cell with nonlinearity and internal hierarchy. Following the review, Section 7.4 presents numerical simulations of the full lattice assembly subjected to broadband (*i.e.*, impulsive) loading. The results of varying impulse amplitude provide strong evidence that transient resonance capture drives this behavior. Lastly, concluding remarks are put forth in Section 7.5.

7.2 System Description

The proposed structure consists of a chain of unit cells containing an arbitrary number of nested springs, masses, and dampers. An isolated single unit cell of this periodic structure

is presented in Figure 7-1. In this particular example, the unit cell contains three scales: an outer mass (the large scale) is grounded via a linear spring and couples, via a purely cubic spring, to a smaller mass (the intermediate small scale) nested within it, which in turn couples by another purely cubic spring to a still smaller mass (the smallest scale). Linear dampers are included in parallel with all springs. The extension to multiple nested layers (and hence internal hierarchies of multiple, continuously decreasing small scales) is straightforward. While the spring-mass-damper configuration is shown at the right, a proposed concept for constructing the structure is shown at the left, in which the pyramids represent elastomeric bumpers that are known to provide near-cubic restoring forces in compression [169-171].

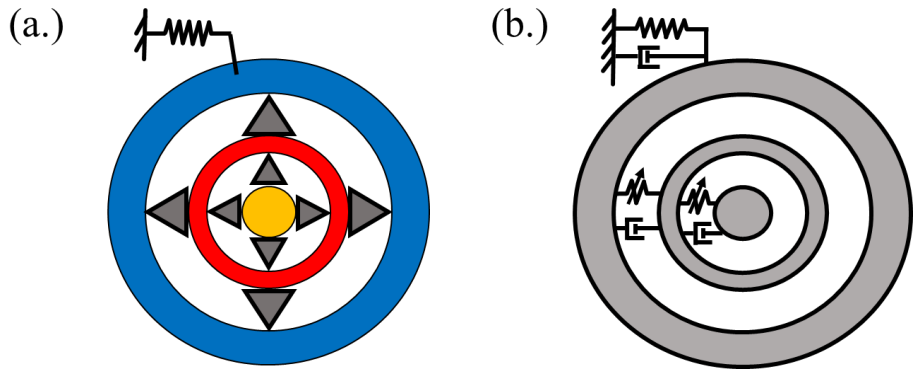

Figure 7-1. Isolated unit cell of the asymmetrical, hierarchical lattice structure. (a.) Proposed fabrication method in which nonlinear coupling is achieved by elastomeric bumpers (b.) The equivalent spring-mass-damper model of the unit cell

Normalized parameter values are chosen such that they scale down at each layer of the unit cell, thus producing internal hierarchy. A labeled schematic is presented in Figure 7-2 and sample set of parameter values given in Table 7-1. Note that physical parameters in an experimental configuration of a lattice were identified in [168].

Table 7-1. Sample normalized parameter values for the hierarchical unit cell

Parameter	Value
m_{outer}	1
m_{middle}	0.05
m_{inner}	0.005
k_1	1
$k_{3,middle}$	1
$k_{3,inner}$	0.1
c_{outer}	2E-03
c_{middle}	2E-03
c_{inner}	2E-03

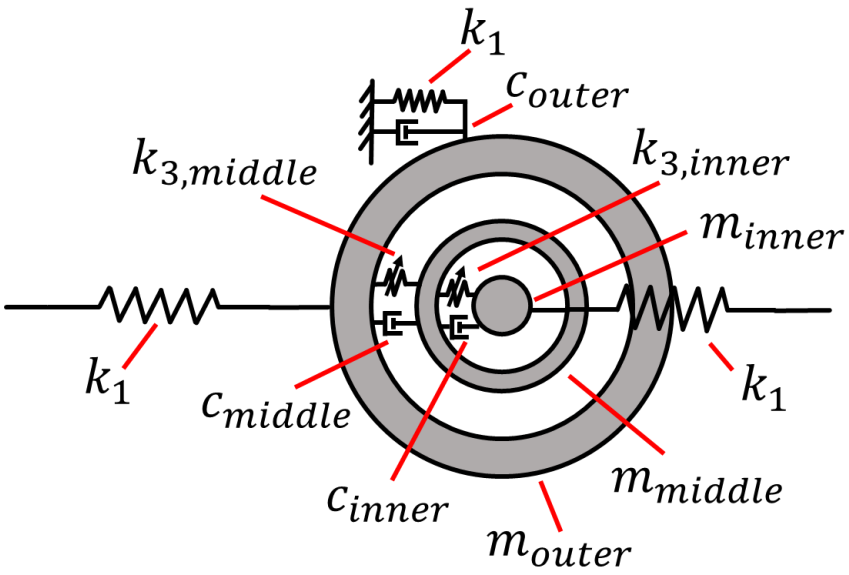

Figure 7-2. Hierarchical unit cell with labeled parameter notation

The hierarchical structure repeats periodically to form a lattice as shown in Figure 7-3. Note that the smallest mass in the unit cell is coupled to the largest mass of its right-neighboring unit cell via a linear spring. Thus, this periodic arrangement exhibits the requisite asymmetry.

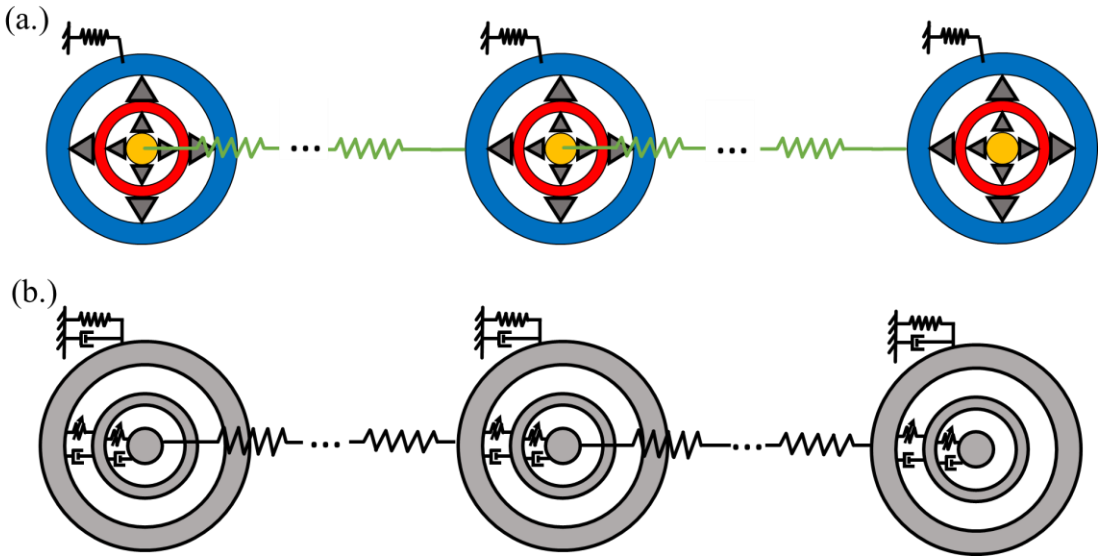

Figure 7-3. Lattice structure containing unit cells with internal hierarchy, nonlinearity, and asymmetry. (a.) The elastomeric bumper design is extended periodically (b.) Spring-mass-damper representation of the lattice

7.3 Local Non-Reciprocity Study

Analysis of a single unit cell consisting of only two scales is first reviewed in this section, detailing the findings in [167] as well as presenting new results on the effect of varying the normalized parameters on the local nonreciprocity. Two scales are considered to reduce the complexity of this isolated unit cell analysis and present the basic principles governing the global system. However, this analysis extends to any number of nested scales. Figure

7-4 presents a dynamical model of this isolated unit cell with labeled coordinates and parameter names.

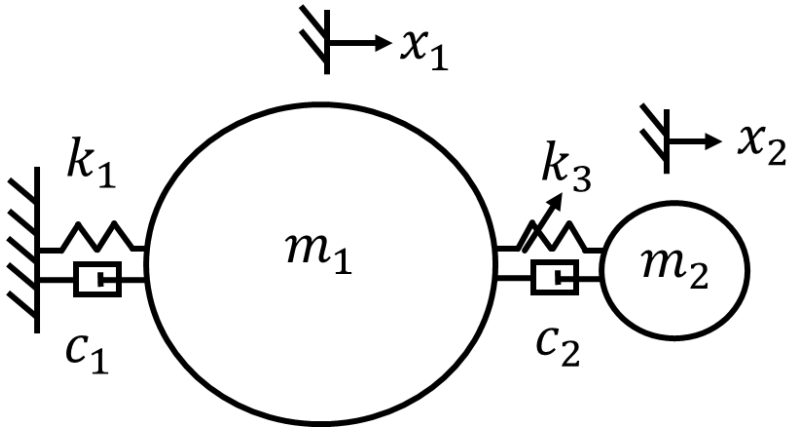

Figure 7-4. Hierarchical unit cell consisting of two scales

The equations of motion governing this system are

$$m_1\ddot{x}_1 = -k_1x_1 - k_3(x_1 - x_2)^3 - c_1\dot{x}_1 - c_2(\dot{x}_1 - \dot{x}_2) \tag{7.1}$$

$$m_2\ddot{x}_2 = k_3(x_1 - x_2)^3 + c_2(\dot{x}_1 - \dot{x}_2) \tag{7.2}$$

To investigate non-reciprocity, the response of this system to impulses at either the large scale (LS) or small scale (SS) is simulated by direct numerical integration of the equations of motion, with the aim of measuring the steady state distribution of energy when either scale is excited. To model the impulses, nonzero initial velocities are assigned to the desired scale of the form,

$$V_0 = \frac{I_0}{m_n} \tag{7.3}$$

where V_0 denotes the initial velocity, m_n the desired scale to excite ($n = 1$ or 2 for LS or SS excitation, respectively) and I_0 is the total momentum, or impulse magnitude, imparted

into the system. For a fair comparison of the system's response when either scale is excited, I_0 remains constant.

To track the energy distribution in the system, a dimensionless parameter $E_{D,SS}$ is defined

$$E_{D,SS} = \lim_{T\to\infty} \frac{\int_0^T c_2(\dot{x}_2(t)-\dot{x}_1(t))^2 dt}{\frac{1}{2}m_n V_0^2} \tag{7.4}$$

where again $n = 1$ or 2 for LS or SS excitation, respectively. This dimensionless parameter is the steady state fraction of system energy that is dissipated by the damper coupling the two scales. The limit imposes that T should be large enough for the system energy to dissipate and $E_{D,SS}$ to converge. By examining $E_{D,SS}$, the distribution of impulse energy over the course of the simulation can be assessed for both LS and SS excitation.

Impulse magnitudes I_0 are varied and $E_{D,SS}$ computed for both LS and SS excitations and the results are presented in Figure 7-5. When $0.1 < I_0 < 0.7$, the system energy transfers from the LS to the SS when the LS is excited; however, energy remains confined at the SS for all the impulse magnitudes shown. *Thus, reciprocity is broken locally.*

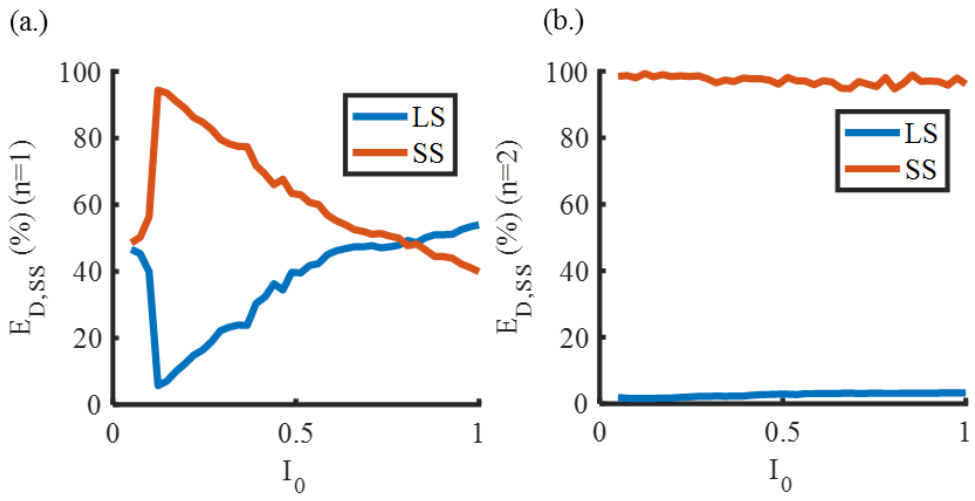

Figure 7-5. Response of the two-scale system to different impulse magnitudes. (a.) LS excitation (b.) SS excitation

The underlying mechanism behind this local breaking of reciprocity is elucidated by analyzing the dynamics of the two-scale system in the frequency domain. For LS excitation, the SS quickly "tunes" its frequency via 1:1 transient resonance capture (TRC) to oscillate near the LS natural frequency [164-166]. The innermost mass and essentially nonlinear spring have no predefined natural frequency, but rather can match the instantaneous natural frequency of the LS assuming it has enough energy. Thus, the impedance mismatch of the two oscillators rapidly minimizes and energy efficiently transmits, or "pumps" from the LS to the SS where it is then dissipated by the damper coupling the two scales. TRC is activated only at certain energy levels: when the initial momentum delivered to the system is too low, TRC is not activated and the response is considerably more reciprocal. When the SS is excited, it does not immediately oscillate at the LS natural frequency. Rather, the essentially nonlinear spring produces various frequencies at which the SS vibrates until the SS finally settles upon the LS natural frequency. By the time the SS reaches this frequency for efficient energy transfer, most of

the system energy has been dissipated by the damper coupling the two scales. Thus, energy remains *localized* at the SS instead of transferring to the LS as would be expected in a linear, time invariant system. Additional analysis of the TRC phenomenon in this system can be found in [167].

7.4 Global Non-Reciprocity Study

The global periodic configuration of the hierarchical structure is now considered for broadband excitation. Considering now the three scale system depicted in Figure 7-2, the j^{th} unit cell is governed by

$$m_{outer}\ddot{x}_{outer}(j) + c_{outer}\dot{x}_{outer}(j) + c_{middle}(\dot{x}_{outer}(j) - \dot{x}_{middle}(j)) + k_1(2x_{outer}(j) - x_{inner}(j-1)) + k_{3,middle}(x_{outer}(j) - x_{middle}(j))^3 = 0 \quad (7.5)$$

$$m_{middle}\ddot{x}_{middle}(j) + c_{middle}(\dot{x}_{middle}(j) - \dot{x}_{outer}(j)) + c_{inner}(\dot{x}_{middle}(j) - \dot{x}_{inner}(j)) + k_{3,middle}(x_{middle}(j) - x_{outer}(j))^3 + k_{3,inner}(x_{middle}(j) - x_{inner}(j))^3 = 0 \quad (7.6)$$

$$m_{inner}\ddot{x}_{inner}(j) + c_{inner}(\dot{x}_{inner}(j) - \dot{x}_{middle}(j)) + k_1(x_{inner}(j) - x_{outer}(j+1)) + k_{3,inner}(x_{inner}(j) - x_{middle}(j))^3 = 0 \quad (7.7)$$

Informed by the 1:1 TRC that governs the non-reciprocity in an isolated unit cell, results from direct numerical simulation of the lattice equations of motion strongly suggest that TRC governs the global breaking of reciprocity for wave propagation in the lattice structure. Systems with both two and three scales will be discussed to demonstrate the generality of the hierarchical structure design and the effect of nesting varying number of scales will be presented for impulsive excitation.

These numerical studies simulate broadband (impulsive) excitations applied either at the free boundaries or the middle of the nonlinear lattice. When assigning impulses to the 1-D

chain, it is convenient to express their magnitude relative to I_{norm}, the maximum momentum associated with a plane wave in a linear monatomic chain

$$I_{norm} = m_{outer} v_{g,max} \tag{7.8}$$

where $v_{g,max}$ is the maximum group velocity of the monatomic chain formed by m_{outer} and coupling and grounding springs of stiffness k_1:

$$v_{g,max} = \max\left(\frac{k_1 \sin\mu}{m_{outer}\omega_0}\right) \tag{7.9}$$

where $\omega_0 = \sqrt{\frac{k_1}{m}(3 - 2\cos\mu)}$ and μ is the dimensionless wavenumber/propagation constant. Figure 7-6 presents results for impulsively exciting the largest mass of the three scale unit cell with $I_0 = 7.36\, I_{norm}$ at the center of a chain composed of 50 unit cells. Lattices are terminated with the convention depicted in Figure 7-3, in which the first and last unit cells are linearly grounded. As with the local study of the previous section, nonzero initial velocity V_0 applied to a single unit cell of the system model impulses. In all cases considered the impulses are applied to the corresponding large scales of the unit cells. The quantity E_{frac} is the fraction of energy at the unit cell relative to the energy delivered to the system by the impulse, $\frac{1}{2} m_{outer} V_0^2$. As a reference, essentially nonlinear springs are replaced by linear springs with the same spring constants in Figure 7-6b. For the nonlinear case, note the considerably different behavior of energy propagation to the left of the center as compared to the right: *energy preferentially travels from left-to-right, thus indicating a global breaking of reciprocity*. Energy radiates symmetrically outwards in Figure 7-6b highlighting the crucial role that nonlinearity plays for breaking reciprocity in this lattice structure.

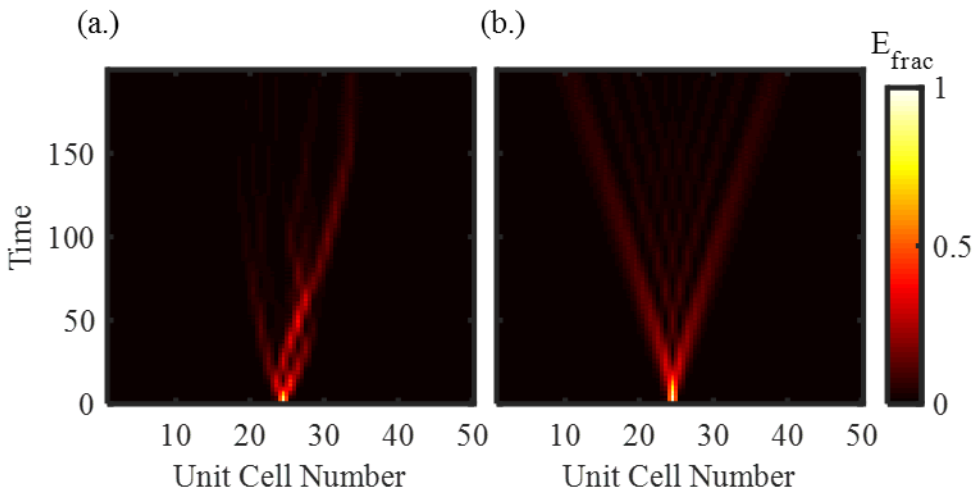

Figure 7-6. Impulsive excitation of the large scale of the unit cell at the chain's center in a nonlinear (a.) and linear (b.) lattice. Note the preferential propagation of energy from left-to-right for the case with nonlinear interactions: $m_{outer} = 1, m_{middle} = 0.05, m_{inner} = 0.005, k_1 = 1, k_{1,middle} = 0, k_{1,inner} = 0, k_{3,middle} = 1, k_{3,inner} = 0.1, c_{outer} = 0.002, c_{middle} = 0.002, c_{inner} = 0.0002,\ I_0/I_{norm} = 7.36$. For (b.) , $k_{3,middle}$ and $k_{3,inner}$ govern linear restoring forces.

To quantify the amount of transmission in the lattice, a transmission ratio TR is defined to be

$$TR = \frac{\max(PE+KE)}{\frac{1}{2}m_{outer}V_0^2} \tag{7.10}$$

where $\max(PE + KE)$ is the maximum sum of potential and kinetic energy that occurs for each unit cell across all time in a simulation.

Figure 7-7 depicts the results of applying various impulse values to the large scale of the unit cell at the center of a chain with 50 unit cells, with TR computed at each impulse value. Note that non-reciprocity activates when $6 < I_0/I_{norm} < 8$, as indicated by the preference for left-to-right over right-to-left propagation. The highest degree of nonreciprocity occurs near $I_0/I_{norm} = 7.5$; however, this effect weakens for larger impulse amplitudes as the response becomes more symmetrical. Such result is reminiscent of the response of the two-

scale isolated unit cell in Figure 7-5 in which TRC takes effect when the impulse magnitude falls within a well-defined range of values for breaking reciprocity.

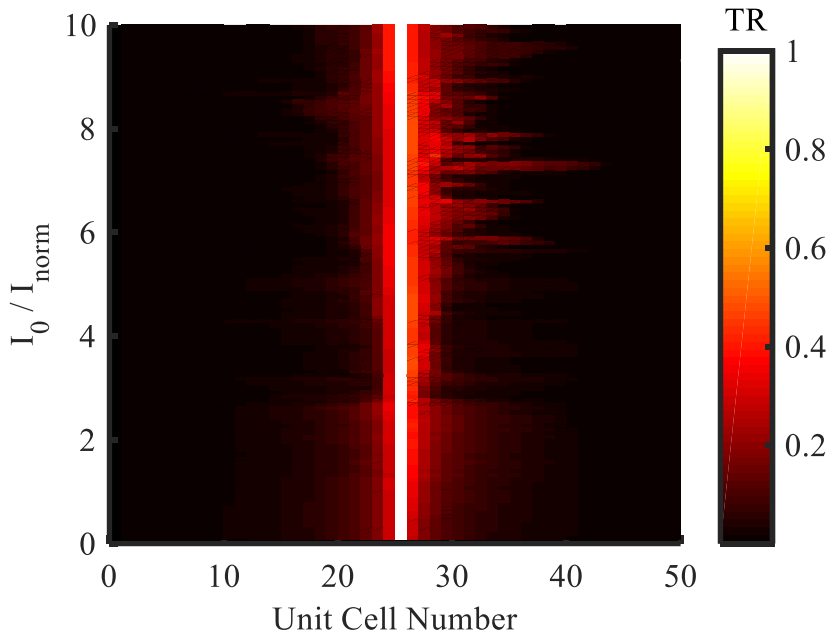

Figure 7-7. Response of a 1-D lattice to various impulse amplitudes applied to the large scale of the unit cell at its center. Non-reciprocal behavior occurs at specific impulse magnitudes: $\boldsymbol{m_{outer} = 1, m_{middle} = 0.05, m_{inner} = 0.005, k_1 = 1, k_{1,middle} = 0.05, k_{1,inner} = 0.05, k_{3,middle} = 1, k_{3,inner} = 0.1, c_{outer} = 0.002, c_{middle} = 0.002, c_{inner} = 0.0002.}$

Figure 7-8 presents the results of applying an impulse of $I_0 = 0.1\ I_{norm}$ to the large scale at the left and right boundaries of the chain (in separate simulations). These results again demonstrate that energy propagates from left-to-right but not right-to-left. Note that weak linear springs of stiffness $k_{1,middle}, k_{1,inner}$ are added in parallel to the nonlinear stiffnesses $k_{3,middle}, k_{3,inner}$ respectively to increase the wave's range, though they are not necessary for inducing non-reciprocity. The minimal effect of weak linear terms in parallel

with strongly nonlinear forces on the global nonreciprocity in this lattice was experimentally confirmed in [168].

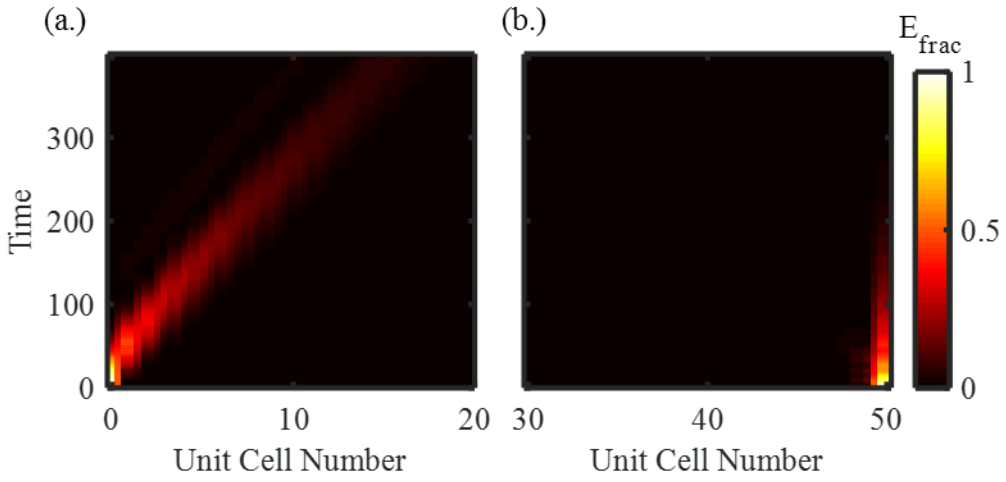

Figure 7-8. Impulsive excitation of the large scale of the unit cells at the chain's boundaries. Energy propagates rightward when initiated at the left boundary (a.) but localizes when initiated at the right boundary (b.): $m_{outer} = 1, m_{middle} = 0.05, m_{inner} = 0.005, k_1 = 1, k_{1,middle} = 0.05, k_{1,inner} = 0.05, k_{3,middle} = 1, k_{3,inner} = 0.1, c_{outer} = 0.002, c_{middle} = 0.002, c_{inner} = 0.0002,\ I_0/I_{norm} = 0.1$.

Figure 7-9 displays results from exciting the large scales of the unit cells at the chain's left and right boundaries with various impulse values. As with center excitation, non-reciprocity occurs at a finite range of impulse amplitudes. It is important to note that the preferential transmission of energy from left-to-right and not right-to-left is unaffected by the direction of the impulse delivered to the outer mass, *i.e.*, leftward directed initial momentum ($I_0 < 0$) produces nearly identical results. It is also interesting to note that exciting the chain's boundaries requires smaller impulse magnitudes to break reciprocity as compared to exciting the chain's center.

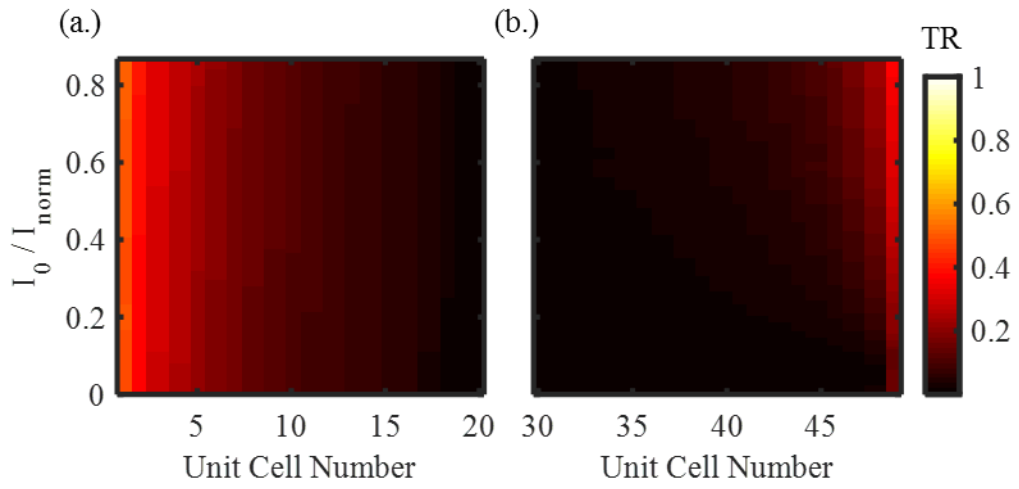

Figure 7-9. Response of a 1-D lattice to various impulse amplitudes applied to the large scale of the unit cells at the left (a.) and right (b.) boundaries. The preferential energy propagation occurs at various impulse amplitudes: $\boldsymbol{m_{outer} = 1, m_{middle} = 0.05, m_{inner} = 0.005, k_1 = 1, k_{1,middle} = 0.05, k_{1,inner} = 0.05, k_{3,middle} = 1, k_{3,inner} = 0.1, c_{outer} = 0.002, c_{middle} = 0.002, c_{inner} = 0.0002.}$

The following explanation proposes the sequence of events that determine the global breaking of reciprocity in the lattice with nonlinearity, asymmetry and internal scale hierarchy excited at its boundaries:

Left-to-Right: The directly excited large scale of the left-most unit cell oscillates at a predefined natural frequency due to the linear grounding spring. Assuming enough energy is in the system from the impulse, energy transfers from the large scale to the next smallest scale via 1:1 transient resonance capture associated with the cubically nonlinear spring, and it continues to transmit down to each successively smaller scale. When the energy arrives at the smallest scale, it can then readily flow to the largest scale of its neighboring unit cell on the right because of the linear coupling spring. The process then repeats and a wave propagates from left-to-right.

Right-to-Left: Energy transfers from the directly excited large scale of the right-most unit cell to the smallest scale of its neighboring unit cell on the left because of the linear coupling spring. However, energy cannot transmit from the small scale to the large scale and is ultimately dissipated at the smallest scale due to the failure to initiate TRC, as evidenced by the results in the local study. Thus, energy is arrested and waves cannot propagate from right-to-left.

This design scheme could be added to systems to redirect mechanical shock and vibration. For example, adding this lattice to buildings, bridges, or aircraft could achieve a variety of purposes: to protect diagnostic sensors from being contaminated by unwanted mechanical disturbances, to focus energy towards structural health monitoring equipment, or to direct energy away from sensitive structural components. In the local study in Section 7.3, damping plays an important role in trapping energy at the small scale (see Figure 7-5). Consequently, it was considered in the lattice and, while it limited the wave's range, demonstrated that highly asymmetric wave propagation can be achieved in dissipative media. Since the proposed lattice would be fabricated and added to systems, the degree of damping is largely in control of the design engineer. Careful unit cell design can increase or decrease damping as desired.

7.5 Concluding Remarks

Nonlinear elastic non-reciprocity is reported for a lattice structure exhibiting asymmetry and purely cubic stiffness nonlinearity in its unit cell design. Studying the dynamics of an isolated unit cell reveals that transient resonance capture governs the breaking of reciprocity when the system energy lies within a critical range of values. Direct numerical

simulation of the lattice's equations of motion when subjected to impulsive excitation yields asymmetrical wave propagation. The global non-reciprocity activates at higher energy levels, providing strong evidence that transient resonance capture induces this behavior. Because this is a passive structure, these findings could be useful for shock and noise mitigation applications.

CHAPTER 8. CONCLUSIONS AND CONTRIBUTIONS

8.1 Summary

This thesis presents a variety of new phenomena associated with wave propagation in nonlinear periodic media. Findings of waveform invariance, plane wave stability, internal resonance, near-zero higher-harmonic generation, and non-reciprocity advance the current understanding of the nature and behavior of waves in nonlinear lattices. Analytical predictions, which can ultimately be used for the design of real engineering systems, are accompanied by numerical simulations and experimental demonstrations.

Considering plane wave propagation in weakly nonlinear lattices, a higher-order multiple scales analysis reveals the existence of multi-harmonic invariant waveforms. The summation of specific amplitudes and phases at each harmonic of the fundamental generates a plane wave that persists with theoretically no variation of its spectral composition, despite propagating through a dispersive medium. In 1-D systems, such solutions tune with lattice parameters and wave amplitude. An additional degree of tunability arises for 2-D shear lattices whereby invariant solutions vary with a wave's orientation. For both 1-D and 2-D problems, direct numerical simulations of lattice equations of motion confirm the addition of higher-order terms in a plane wave's initial conditions results-in measurably less variation of spectral amplitudes.

The stability of plane wave propagation is also assessed through a local stability analysis of multiple scales-based evolution equations. Results identify an inherent stability of low amplitude plane waves yet a loss of stability at high amplitudes. Numerical simulations

elucidate that low amplitude, stable waveforms retain their spectral information in the fundamental frequency and its higher harmonics (though not necessarily invariantly). Unstable waveforms, on the other hand, which are triggered by high amplitudes, undergo substantial spreading of spectral energy across incommensurate frequency bands. Counterintuitively, plane wave stability varies as a function of a wave's orientation in 2-D shear lattices. Waves travelling along the lattice direction are inherently less stable than waves oriented along inclined directions. Such findings are informed by a higher-order multiple scales framework and validated by direct numerical simulations of lattice equations of motion.

Internal resonance of plane waves with commensurate ratios of both frequency and wavenumber experience a slow-scale periodic energy exchange, as proposed by a multiple scales analysis. Such phenomena can occur within a single branch or between different branches of a lattice's band structure. A stability analysis of the two-wave evolution equations presents centers, *i.e.* initial amplitudes about which energy exchange occurs, in addition to unstable fixed points. Numerical simulations validate that internally-resonant plane waves with initial conditions sufficiently near the centers' exchange energy at the expected frequency and amplitude according to multiple scales.

At special frequencies, invariant waveforms comprise only their fundamental term, suggesting that higher-harmonic generation should cease. Plane waves at these specific frequencies propagate invariantly with only a fundamental frequency and wavenumber pair. Numerical simulations demonstrate that higher-harmonic production rapidly decreases at these special frequencies compared to plane waves assigned initial conditions throughout the irreducible Brillouin Zone. The frequencies at which this phenomenon

occurs varies with wave amplitude and, for diatomic systems, the degree-of-freedom and dispersion branch.

An experimental demonstration of amplitude-dependent band structure and plane wave stability is presented. Unlike prior studies which consider standing wave vibration in finite lattices [162], this work captures the propagation of travelling waves. Large dispersion shifts are reported as the addition of grounding springs prevent whirling behavior. Furthermore, the inherent stability of low amplitude, as opposed to high amplitude, wave propagation is experimentally observed. As documented in numerical simulations, unstable plane waves spread spectral energy across incommensurate frequency bands whereas stable plane waves retain signal information at the fundamental frequency and its higher harmonics.

Nonreciprocity was achieved by a lattice incorporating nonlinearity, asymmetry, and internal hierarchy. Prior work has shown that energy can preferentially transfer from large to small scales when coupled with essentially nonlinear stiffness. The mechanism is a 1:1 transient resonance capture in which strong nonlinearity enables small nonlinear attachments to tune their vibration frequency to match that of the linearly grounded large scale. Extending this concept to a lattice system results-in a global, giant breaking of reciprocity for both impulsive excitation as evidenced by numerical simulations.

8.2 Research Contributions

The key contributions of this research as summarized as follows:

- Multi-harmonic invariant plane wave solutions are presented for weakly nonlinear lattices informed by a higher-order multiple scales analysis.
- Amplitude and direction-dependent stability is reported for plane wave propagation in nonlinear lattices.
- Internal resonance of plane waves with commensurate frequencies and wavenumbers are shown to undergo slow scale energy exchange between the wave propagation modes, which can exist on the same or different branches of a lattice's band structure.
- Special frequencies are identified through a multiple scales analysis in which higher harmonic generation nearly vanishes for waves propagating in nonlinear periodic media
- Substantial nonlinearity-induced band structure shifting and amplitude-dependent stability was experimentally observed for travelling waves in a shear lattice.
- A novel, passive strategy of breaking reciprocity is revealed using lattices with internal hierarchy, asymmetry, and nonlinearity.

8.3 Recommendations for Future Work

8.3.1 Waveform Invariance and Stability in Continuous Nonlinear Periodic Media

Wave propagation in periodic continuous media can guide and filter waves much like their discrete lattice counterparts [79, 114, 172]. In many practical settings, it may be simpler to design, fabricate, and implement periodic structures that are not a network of discrete oscillators but rather alternating layers of continuous fluid/fluid, fluid/solid, or solid/solid interfaces. Figure 8-1a illustrates an example schematic of such a system in which there

are alternating layers with different density (ρ_a, ρ_b) and longitudinal sound speed (c_a, c_b). Finite amplitude wave propagation may induce material or geometric nonlinearities in such systems. An alternative setting is proposed in Figure 8-1b in which a continuous acoustic waveguide contains periodically-spaced elastic membranes. Such membranes have been shown to exhibit tunable geometric stiffness nonlinearity [173-175].

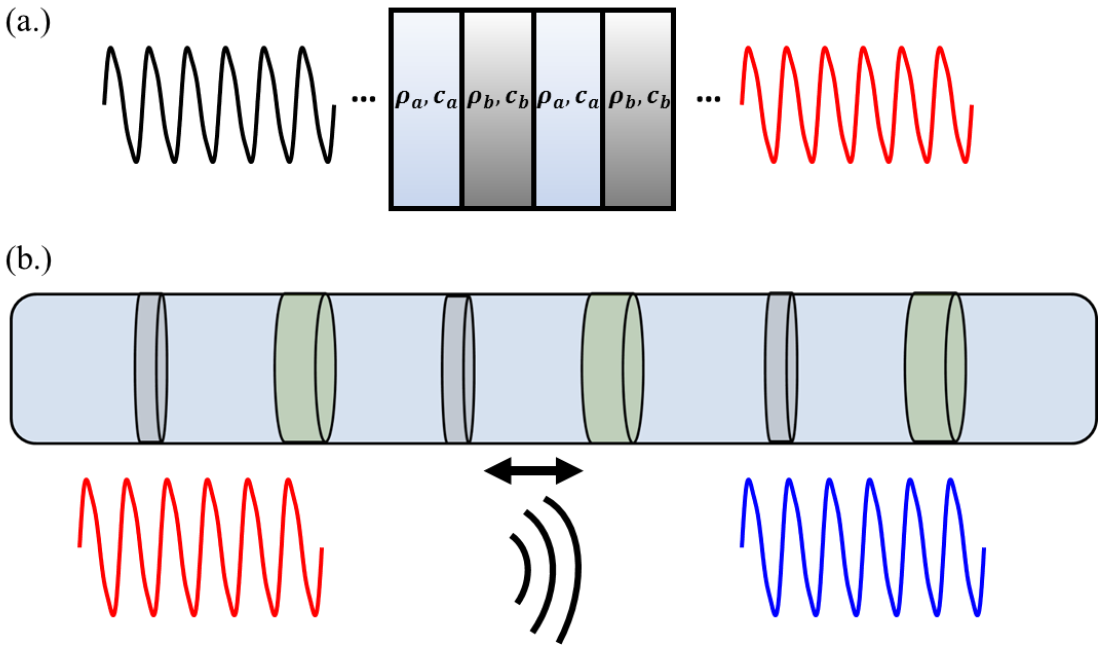

Figure 8-1. Examples of continuous nonlinear periodic media. (a.) Layered media (b.) Acoustic waveguide with periodically spaced membranes.

For either example system, the existence of invariant plane wave solutions could be studied using the higher-order multiple scales framework detailed in this work. Knowledge of these waveforms may impact the design of SONAR systems by preventing multi-harmonic acoustic bursts from dispersing. Furthermore, the stability of plane waves in these systems can be analyzed, discovering the conditions for stable (or unstable) wave propagation.

8.3.2 Wave Propagation in Media with Gradients in Nonlinear Stiffness

Another exciting avenue for the extension of this work is to explore the spatial modulation and grading of weak stiffness nonlinearities in periodic systems. By extending the multiple scales framework detailed in this work, various functions governing the modulation and grading of the nonlinear stiffness can be studied to observe local shifts in band structure and potentially new phenomena such as amplitude-dependent wave trapping and arbitrary waveform patterning. Figure 8-2 depicts an example scenario in which a monatomic lattice is formed by a single mass value m coupled by linear, quadratic, and cubic stiffness k_1, k_2, and k_3, respectively. For quadratic and cubic stiffness varying at each mass in a sinusoidal manner, the resultant wave propagation features would be examined.

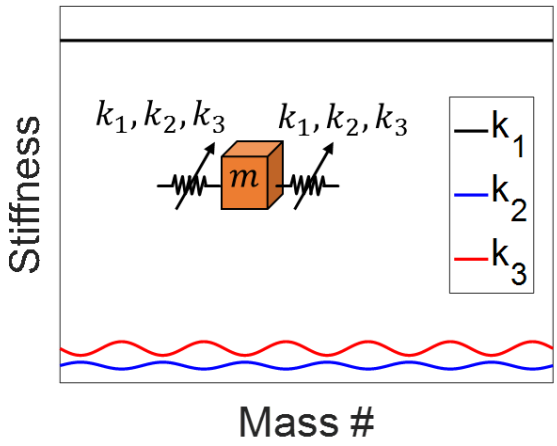

Figure 8-2. Lattice featuring a gradient in its stiffness nonlinearity

Previous studies have considered the modulation of *linear* mechanical properties in periodic structures [72, 74, 176], often with the goal of biasing the wave propagation direction. Little attention has been given to periodic systems with gradient nonlinear stiffness terms, especially in the weakly nonlinear regime. The modulation of weak stiffness nonlinearities enables greater preservation of signal integrity as compared to their strongly or essentially nonlinear counterparts and allows for previous methods of deriving

closed-form amplitude dependent dispersion corrections to apply [21, 22, 151, 177]. Depending on the function governing the grading of nonlinearity combined with the possibility for allowing negative stiffness, analysis of waveform stability will be critical to assess the conditions under which solutions persist for long spatiotemporal scales or rapidly degrade due to their inherent instability.

8.3.3 Wave Propagation in the Human Spine

The human spine is a complex structure. As can be observed in Figure 8-3, it exhibits near periodicity from its arrangement of vertebrae and slightly bent curvature. An approximation of its "lattice constant" can be determined by dividing the number of vertebrae by the length of the spinal column, yielding $a \sim 1.4$ cm. Despite such a structural composition, a treatment from a wave-based, phononic perspective has not been put forth by the research community. Rather, studies have considered vibration modes of the human spine, *i.e.,* its natural frequencies and mode shapes [27-31]. An analytical, experimental, and computational study of the human spine may reveal a fascinating, nontrivial band structure. Knowledge of this band structure could inform a variety of non-invasive spinal health evaluation techniques that could replace more invasive procedures such as spinal taps. Due to the spine's complex nature, a full consideration of linear wave propagation would precede any investigation of nonlinearities.

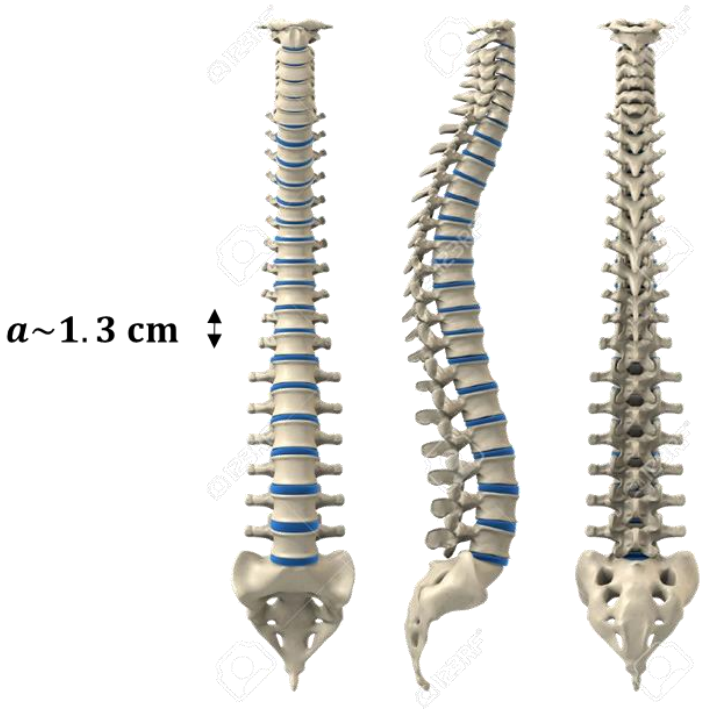

Figure 8-3. The human spine has a nearly-periodic distribution of vertebrae

8.3.4 Non-Reciprocity of Airborne and Waterborne Acoustic Signals through Internal Hierarchy, Nonlinearity, and Asymmetry

Non-reciprocity has received increasing attention by the physics and engineering communities. When breaking reciprocity for acoustic waves in fluids (*e.g.*, air or water), prior work has been limited to active methods such as through circulating fluid flow [69, 70] and modulation of geometry properties [75]. Minimal attention has been given to methods of breaking reciprocity *passively* for airborne or waterborne acoustic waves. Such findings may inspire acoustic-shielding devices for submarines or aircraft that receive—but cannot emit—acoustic signals. Figure 8-4 displays one proposed idea. By extension of the nonlinearity, internal hierarchy, and asymmetry design presented in Chapter 7, cascading networks of Helmholtz resonators and membranes may achieve nonreciprocal

behavior passively. Nonlinearity (from the membranes) and hierarchy (from the nested Helmholtz resonators) enable an acoustic signal to transmit from the large to small scale but not vice versa, thus breaking reciprocity locally. An asymmetrical coupling between unit cells containing nested resonators would extend this design into a periodic structure that breaks reciprocity globally.

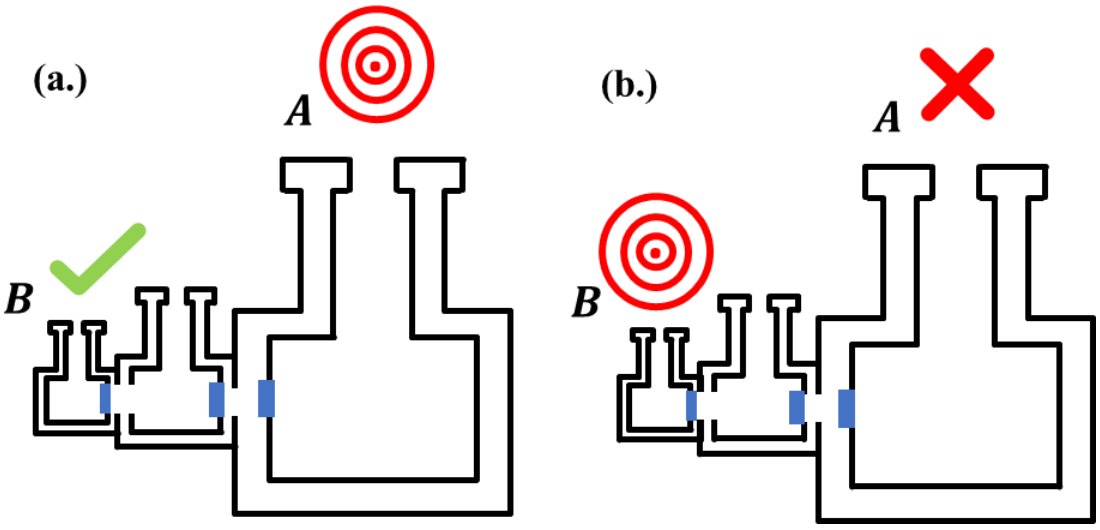

Figure 8-4. Structure with nonlinearity and internal hierarchy to break reciprocity for airborne and waterborne acoustic waves. An acoustic source travels through an array of Helmholtz resonators coupled by elastic membranes (in blue). In (a.), the source, sent from the large scale, is identified by the receiver at the small scale. However, in (b.), the source, sent from the small scale, cannot be identified by the receiver at the larger scale.

APPENDIX A. ADDITIONAL STABILITY AND WAVEFORM INVARIANCE STUDIES

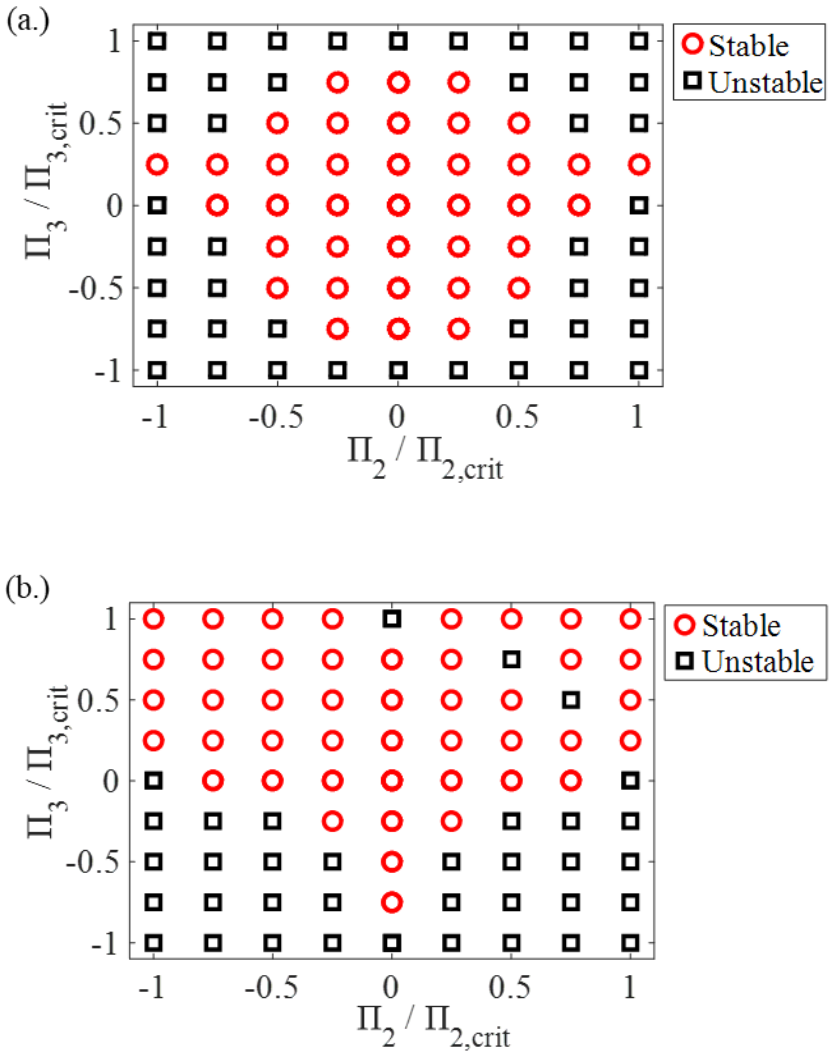

Figure A. 1. Diatomic numerical chain stability study: x_b, 2nd-order IC's, $\Pi_1 = 0.01, \Pi_4 = 1.5, \mu = \frac{\pi}{4}$, Acoustic (a.), Optical (b.).

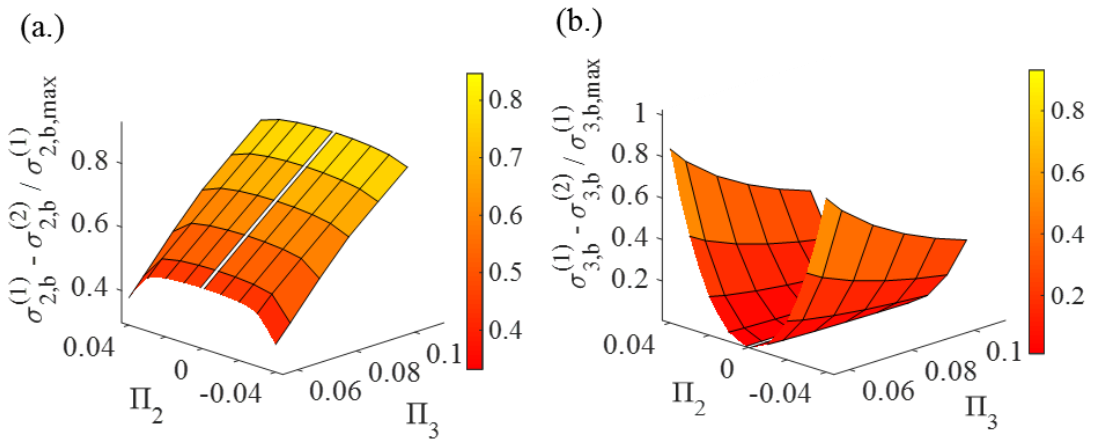

Figure A. 2. Reduction of variance in the 2nd (a.) and 3rd (b) harmonics numerically measured in simulations of the 1-D diatomic chain: x_b, Acoustic Branch, $\Pi_4 = 2$, $\mu = \frac{\pi}{4}, \Pi_1 = 0$.

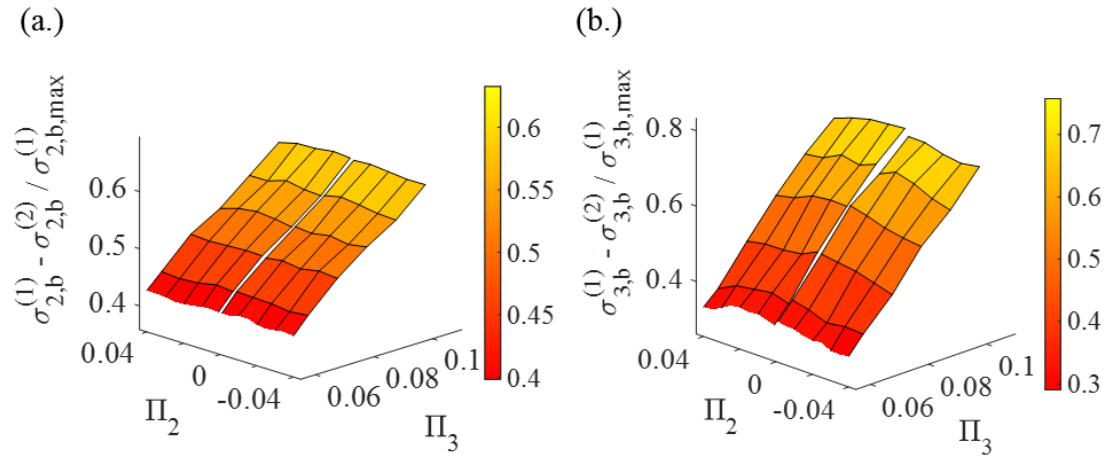

Figure A. 3. Reduction of variance in the 2nd (a.) and 3rd (b.) harmonics numerically measured n simulations of the 1-D diatomic chain: in x_b, Optical Branch, $\Pi_4 = 2$, $\mu = \frac{\pi}{4}, \Pi_1 = 0$.

APPENDIX B. SYMBOLIC EXPRESSIONS FOR INTERNAL RESONANCE IN EXAMPLE LATTICE SYSTEMS

B.1 2:1 internal resonance in the diatomic lattice

$$\bar{G} = -\frac{k_2}{\omega_{0,A}(|\phi_{a1}|^2 m_a + |\phi_{b1}|^2 m_b)}\left(\frac{1}{2}\mathrm{i}\left(\mathrm{e}^{2\mathrm{i}\mu_A}\bar{\phi}_{a1}^2\phi_{b2} - \overline{\phi}_{b1}^2\phi_{a2}\mathrm{e}^{-2\mathrm{i}\mu_A} + 2\,\bar{\phi}_{a1}\overline{\phi}_{b1}\phi_{a2}\mathrm{e}^{-\mathrm{i}\mu_A} - 2\bar{\phi}_{a1}\,\overline{\phi}_{b1}\phi_{b2}\mathrm{e}^{\mathrm{i}\mu_A} - \overline{\phi}_{a1}^2\,\phi_{b2} - 2\bar{\phi}_{a1}\overline{\phi}_{b1}\phi_{a2} + 2\,\overline{\phi}_{b1}\bar{\phi}_{a1}\phi_{b2} + \overline{\phi}_{b1}^2\,\phi_{a2}\right)\right) \tag{B1}$$

$$\bar{H} = \frac{1}{8}\,\frac{k_2}{\omega_{0,A}(|\phi_{a2}|^2 m_a + |\phi_{b2}|^2 m_b)}\left(-\mathrm{i}\overline{\phi}_{b2}\phi_{a1}^2\mathrm{e}^{-2\mathrm{i}\mu_A} + 2\mathrm{i}\overline{\phi}_{b2}\phi_{a1}\phi_{b1}\mathrm{e}^{-\mathrm{i}\mu_A} + \mathrm{i}\bar{\phi}_{a2}\phi_{b1}^2\mathrm{e}^{2\mathrm{i}\mu_A} - 2\mathrm{i}\,\overline{\phi}_{a2}\phi_{a1}\phi_{b1}\mathrm{e}^{\mathrm{i}\mu_A} + 2\mathrm{i}\phi_{b1}\left(\phi_{a1} - \frac{1}{2}\phi_{b1}\right)\overline{\phi}_{a2} + \mathrm{i}\overline{\phi}_{b2}(\phi_{a1} - 2\phi_{b1})\phi_{a1}\right) \tag{B2}$$

where $\boldsymbol{\phi}(\omega_{0,A}) = \begin{bmatrix}\phi_{a1}\\ \phi_{b1}\end{bmatrix}$ and $\boldsymbol{\phi}(\omega_{0,B}) = \begin{bmatrix}\phi_{a2}\\ \phi_{b2}\end{bmatrix}$.

B.2 3:1 internal resonance in the diatomic lattice

$$\overline{I} = \frac{1}{8}\frac{k_3}{\omega_{0,A}(|\phi_{a1}|^2 m_a + |\phi_{b1}|^2 m_b)}\left(3\mathrm{i}\overline{\phi}_{b1}^3\phi_{a3}\mathrm{e}^{-3\mathrm{i}\mu_A} - 9\mathrm{i}\bar{\phi}_{a1}\,\overline{\phi}_{b1}^2\phi_{a3}\mathrm{e}^{-2\mathrm{i}\mu_A} + 9\mathrm{i}\,\bar{\phi}_{a1}^2\overline{\phi}_{b1}\phi_{a3}\mathrm{e}^{-\mathrm{i}\mu_A} - 9\mathrm{i}\bar{\phi}_{a1}^2\overline{\phi}_{b1}\phi_{b3}\mathrm{e}^{2\mathrm{i}\mu_A} + 3\mathrm{i}\,\bar{\phi}_{a1}^3\phi_{b3}\mathrm{e}^{3\mathrm{i}\mu_A} + 9\mathrm{i}\bar{\phi}_{a1}\,\overline{\phi}_{b1}^2\phi_{b3}\mathrm{e}^{\mathrm{i}\mu_A} - 6\mathrm{i}\left(\bar{\phi}_{a1}^2 - \bar{\phi}_{a1}\overline{\phi}_{b1} + \overline{\phi}_{b1}^2\right)\left(\left(\phi_{a3} - \frac{1}{2}\phi_{b3}\right)\bar{\phi}_{a1} - \frac{1}{2}\overline{\phi}_{b1}(\phi_{a3} - 2\phi_{b3})\right)\right) \tag{B3}$$

$$\overline{L} = \frac{1}{4}\frac{k_3}{\omega_{0,A}(|\phi_{a1}|^2 m_a + |\phi_{b1}|^2 m_b)}\left(3\mathrm{i}\left(\overline{\phi}_{b3}\phi_{a3}(|\phi_{a1}|^2 + |\phi_{b1}|^2)\right)\mathrm{e}^{-3\mathrm{i}\mu_A} + 3\mathrm{i}\phi_{a1}\,(|\phi_{a3}|^2 + |\phi_{b3}|^2)\overline{\phi}_{b1}\mathrm{e}^{-\mathrm{i}\mu_A} + 3\mathrm{i}\phi_{b3}(|\phi_{a1}|^2 + |\phi_{b1}|^2)\overline{\phi}_{a3}\mathrm{e}^{3\mathrm{i}\mu_A} - 3\mathrm{i}\phi_{a1}\overline{\phi}_{b1}\phi_{a3}\,\overline{\phi}_{b3}\mathrm{e}^{-4\mathrm{i}\mu_A} - 3\mathrm{i}\phi_{b1}\,\bar{\phi}_{a1}\phi_{a3}\overline{\phi}_{b3}\mathrm{e}^{-2\mathrm{i}\mu_A} - 3\mathrm{i}\phi_{a1}\overline{\phi}_{b1}\phi_{b3}\overline{\phi}_{a3}\mathrm{e}^{2\mathrm{i}\mu_A} - 3\mathrm{i}\phi_{b1}\bar{\phi}_{a1}\phi_{b3}\overline{\phi}_{a3}\mathrm{e}^{4\mathrm{i}\mu_A} + 3\mathrm{i}(|\phi_{a3}|^2 + |\phi_{b3}|^2)\phi_{b1}\bar{\phi}_{a1}\mathrm{e}^{\mathrm{i}\mu_A} + 3\mathrm{i}\phi_{b1}\left(|\phi_{a3}|^2 + |\phi_{b3}|^2 - \phi_{b3}\overline{\phi}_{a3} - \phi_{a3}\,\overline{\phi}_{b3}\right)\bar{\phi}_{a1} + 3\mathrm{i}\phi_{b3}\left(|\phi_{a1}|^2 + |\phi_{b1}|^2 - \phi_{a1}\,\overline{\phi}_{b1}\right)\overline{\phi}_{a3} + 3\mathrm{i}\phi_{a1}\left(|\phi_{a3}|^2 + |\phi_{b3}|^2 - \phi_{a3}\overline{\phi}_{b3}\right)\overline{\phi}_{b1} -$$

$$6\mathrm{i}\left(|\phi_{a3}|^2+|\phi_{b3}|^2-\frac{1}{2}\phi_{a3}\overline{\phi}_{b3}\right)(|\phi_{a1}|^2+|\phi_{b1}|^2)\Big)$$

(B4)

$$\overline{N}=-\frac{k_3}{\omega_{0,A}(|\phi_{a1}|^2m_a+|\phi_{b1}|^2m_b)}\Bigg(\frac{3}{8}\mathrm{i}\Big(-2\mathrm{e}^{-\mathrm{i}\mu_A}\overline{\phi}_{b1}|\phi_{a1}|^2\phi_{a1}-2\mathrm{e}^{-\mathrm{i}\mu_A}\overline{\phi}_{b1}|\phi_{b1}|^2\phi_{a1}+$$

$$\bar{\phi}_{a1}^2\phi_{b1}^2\mathrm{e}^{2\mathrm{i}\mu_A}+\overline{\phi}_{b1}^2\phi_{a1}^2\mathrm{e}^{-2\mathrm{i}\mu_A}-2\bar{\phi}_{a1}|\phi_{a1}|^2\mathrm{e}^{\mathrm{i}\mu_A}\phi_{b1}-2\bar{\phi}_{a1}|\phi_{b1}|^2\mathrm{e}^{\mathrm{i}\mu_A}\phi_{b1}+$$

$$\phi_{a1}^2\overline{\phi}_{b1}^2-2\phi_{a1}\overline{\phi}_{b1}^2\phi_{b1}-2\bar{\phi}_{a1}\overline{\phi}_{b1}\phi_{a1}^2-2\bar{\phi}_{a1}\overline{\phi}_{b1}\phi_{b1}^2-2\phi_{b1}\bar{\phi}_{a1}^2\phi_{a1}+\phi_{b1}^2\bar{\phi}_{a1}^2+$$

$$2|\phi_{a1}|^4+2|\phi_{b1}|^4+8|\phi_{a1}^2\phi_{b1}^2|\Big)\Bigg) \qquad \text{(B5)}$$

$$\overline{P}=\frac{1}{4}\frac{k_3}{\omega_{0,A}(|\phi_{a3}|^2m_a+|\phi_{b3}|^2m_b)}\Bigg(\mathrm{i}\overline{\phi}_{b3}\phi_{a3}(|\phi_{a1}|^2+|\phi_{b1}|^2)\mathrm{e}^{-3\mathrm{i}\mu_A}+\mathrm{i}\phi_{a1}(|\phi_{a3}|^2+$$

$$|\phi_{b3}|^2)\,\overline{\phi}_{b1}\mathrm{e}^{-\mathrm{i}\mu_A}+\mathrm{i}\phi_{b3}(|\phi_{a1}|^2+|\phi_{b1}|^2)\,\overline{\phi}_{a3}\mathrm{e}^{3\mathrm{i}\mu_A}-\mathrm{i}\phi_{a1}\,\overline{\phi}_{b1}\phi_{a3}\overline{\phi}_{b3}\mathrm{e}^{-4\mathrm{i}\mu_A}-$$

$$\mathrm{i}\phi_{b1}\bar{\phi}_{a1}\phi_{a3}\overline{\phi}_{b3}\mathrm{e}^{-2\mathrm{i}\mu_A}-\mathrm{i}\phi_{a1}\overline{\phi}_{b1}\phi_{b3}\overline{\phi}_{a3}\mathrm{e}^{2\mathrm{i}\mu_A}-\mathrm{i}\phi_{b1}\,\bar{\phi}_{a1}\phi_{b3}\overline{\phi}_{a3}e^{4\mathrm{i}\mu_A}+\mathrm{i}(|\phi_{a3}|^2+$$

$$|\phi_{b3}|^2)\phi_{b1}\bar{\phi}_{a1}\mathrm{e}^{\mathrm{i}\mu_A}+\mathrm{i}\phi_{b1}\big(|\phi_{a3}|^2+|\phi_{b3}|^2-\phi_{b3}\overline{\phi}_{a3}-\phi_{a3}\overline{\phi}_{b3}\big)\overline{\phi}_{a1}+\mathrm{i}\phi_{b3}\big(|\phi_{b1}|^2-$$

$$\phi_{a1}\overline{\phi}_{b1}+|\phi_{a1}|^2\big)\overline{\phi}_{a3}+\mathrm{i}\phi_{a1}\big(|\phi_{a3}|^2+|\,\phi_{b3}|^2-\phi_{a3}\overline{\phi}_{b3}\overline{\phi}_{b1}\big)-2\mathrm{i}\Big(|\phi_{a3}|^2+|\phi_{b3}|^2-$$

$$\frac{1}{2}\phi_{a3}\,\overline{\phi}_{b3}\Big)(|\phi_{a1}|^2+|\phi_{b1}|^2)\Big) \qquad \text{(B6)}$$

$$\overline{Q}=-\frac{k_3}{\omega_{0,A}(|\phi_{a3}|^2m_a+|\phi_{b3}|^2m_b)}\frac{1}{8}\mathrm{i}\Big(-2\mathrm{e}^{3\mathrm{i}\mu_A}\,\overline{\phi}_{a3}|\phi_{a3}|^2\phi_{b3}-2\mathrm{e}^{3\mathrm{i}\mu_A}\overline{\phi}_{a3}|\phi_{b3}|^2\phi_{b3}-$$

$$2\mathrm{e}^{-3\mathrm{i}\mu_A}\overline{\phi}_{b3}|\phi_{b3}|^2\phi_{a3}+\overline{\phi}_{b3}^2\phi_{a3}^2\mathrm{e}^{-6\mathrm{i}\mu_A}+\overline{\phi}_{a3}^2\,\phi_{b3}^2\mathrm{e}^{6\mathrm{i}\mu_A}+\overline{\phi}_{b3}^2\phi_{a3}^2-2\,\overline{\phi}_{b3}^2\phi_{a3}\phi_{b3}-$$

$$2\overline{\phi}_{b3}^2\phi_{a3}\phi_{b3}-2\,\overline{\phi}_{b3}^2\phi_{a3}\phi_{b3}-2\overline{\phi}_{b3}\,\overline{\phi}_{a3}\phi_{a3}^2-2\overline{\phi}_{b3}\overline{\phi}_{a3}\phi_{b3}^2\Big)$$

(B7)

$$\overline{R}=\frac{1}{24}\frac{k_3}{\omega_{0,A}(|\phi_{a3}|^2m_a+|\phi_{b3}|^2m_b)}\Bigg(\mathrm{i}\overline{\phi}_{b3}\phi_{a3}^3\mathrm{e}^{-3\mathrm{i}\mu_A}-3\mathrm{i}\overline{\phi}_{b3}\phi_{b1}\phi_{a1}^2\mathrm{e}^{-2\mathrm{i}\mu_A}+$$

$$3\mathrm{i}\overline{\phi}_{b3}\phi_{b1}^2\phi_{a1}\mathrm{e}^{-\mathrm{i}\mu_A}-3\mathrm{i}\overline{\phi}_{a3}\phi_{b1}^2\phi_{a1}\mathrm{e}^{2\mathrm{i}\mu_A}+\mathrm{i}\overline{\phi}_{a3}\phi_{b1}^3\mathrm{e}^{3\mathrm{i}\mu_A}+3\mathrm{i}\overline{\phi}_{a3}\phi_{b1}\phi_{a1}^2\mathrm{e}^{\mathrm{i}\mu_A}-$$

$$2\mathrm{i}(\phi_{a1}^2-\phi_{a1}\phi_{b1}+\phi_{b1}^2)\left(\left(-\frac{1}{2}\phi_{b1}+\phi_{a1}\right)\overline{\phi}_{a3}-\frac{1}{2}\,\overline{\phi}_{b3}(-2\phi_{b1}+\phi_{a1})\right)\Bigg)$$

(B8)

where $\boldsymbol{\phi}(\omega_{0,A})=\begin{bmatrix}\phi_{a1}\\ \phi_{b1}\end{bmatrix}$ and $\boldsymbol{\phi}(\omega_{0,B})=\begin{bmatrix}\phi_{a3}\\ \phi_{b3}\end{bmatrix}$.

B.3 2:1 internal resonance in the locally-resonant lattice

$$\bar{G} = \frac{1}{2}\frac{1}{\omega_{0,A}(|\phi_{a1}|^2 m_a + |\phi_{b1}|^2 m_b)}\left(2\bar{\phi}_{a1}^2 k_{2a}\phi_{a2}\sin(2\mu_A) + (-4k_{2a}\phi_{a2}\sin(\mu_A) - \mathrm{i}(\phi_{a2} - \phi_{b2})k_{2b})\bar{\phi}_{a1}^2 + 2\mathrm{i}(\phi_{a2} - \phi_{b2})\bar{\phi}_{b1}k_{2b}\overline{\phi}_{a1} - \mathrm{i}(\phi_{a2} - \phi_{b2})\bar{\phi}_{b1}^2 k_{2b}\right) \tag{B9}$$

$$\overline{H} = \frac{1}{8}\frac{-2\bar{\phi}_{a2}k_{2a}\phi_{a1}^2\sin(2\mu_A) + \left(4k_{2a}\phi_{a1}^2\sin\mu_A - \mathrm{i}(\phi_{a1} - \phi_{b1})^2 k_{2b}\right)\bar{\phi}_{a2} + \mathrm{i}(\phi_{a1} - \phi_{b1})^2\overline{\phi}_{b2}k_{2b}}{\omega_{0,A}(|\phi_{a2}|^2 m_a + |\phi_{b2}|^2 m_b)} \tag{B10}$$

where $\boldsymbol{\phi}(\omega_{0,A}) = \begin{bmatrix}\phi_{a1}\\ \phi_{b1}\end{bmatrix}$ and $\boldsymbol{\phi}(\omega_{0,B}) = \begin{bmatrix}\phi_{a2}\\ \phi_{b2}\end{bmatrix}$.

B.4 3:1 internal resonance in the locally-resonant lattice

$$\overline{I} = \frac{1}{8}\frac{1}{\omega_{0,A}(|\phi_{b1}|^2 m_b + |\phi_{a1}|^2 m_a)}\left(-18\mathrm{i}\bar{\phi}_{a1}^3 k_{3a}\phi_{a3}\cos 2\mu_A + 6\mathrm{i}\overline{\phi}_{a1}^3 k_{3a}\phi_{a3}\cos 3\mu_A + (18\mathrm{i}k_{3a}\phi_{a3}\cos\mu_A + 3\mathrm{i}(-2k_{3a} - k_{3b})\phi_{a3} + 3\mathrm{i}k_{3b}\phi_{b3})\overline{\phi}_{a1}^3 + 9\mathrm{i}k_{3b}\overline{\phi}_{b1}(\phi_{a3} - \phi_{b3})\overline{\phi}_{a1}^2 - 9\mathrm{i}k_{3b}\bar{\phi}_{b1}^2(\phi_{a3} - \phi_{b3})\overline{\phi}_{a1} + 3\mathrm{i}k_{3b}\overline{\phi}_{b1}^3(\phi_{a3} - \phi_{b3})\right) \tag{B11}$$

$$\overline{L} = \frac{1}{4}\frac{1}{\omega_{0,A}(|\phi_{b1}|^2 m_b + |\phi_{a1}|^2 m_a)}\left(-6\mathrm{i}k_{3a}(\cos 2\mu_A - 2\cos 3\mu_A + \cos 4\mu_A)|\phi_{a1}^2\phi_{a3}^2| + \left(3\mathrm{i}(4k_{3a}\cos\mu_A - 4k_{3a} - k_{3b})|\phi_{a3}|^2 - 3\mathrm{i}k_{3b}\left(|\phi_{b3}|^2 - \phi_{b3}\overline{\phi}_{a3} - \phi_{a3}\overline{\phi}_{b3}\right)\right)|\phi_{a1}|^2 - 3\mathrm{i}k_{3b}\left(|\phi_{a3}|^2 + |\phi_{b3}|^2 - \phi_{b3}\overline{\phi}_{a3} - \phi_{a3}\overline{\phi}_{b3}\right)\left(|\phi_{b1}|^2 - \overline{\phi}_{a1}\phi_{b1} - \overline{\phi}_{b1}\phi_{a1}\right)\right) \tag{B12}$$

$$\overline{N} = \frac{1}{8}\frac{1}{\omega_{0,A}(|\phi_{b1}|^2 m_b + |\phi_{a1}|^2 m_a)}\left(-12\mathrm{i}k_{3b}|\phi_{a1}^2\phi_{b1}^2| - 6\mathrm{i}|\phi_{a1}|^4 k_{3a}\cos 2\mu_A - 3\mathrm{i}(-8k_{3a}\cos\mu_A + 6k_{3a} + k_{3b})|\phi_{a1}|^4 - 3\mathrm{i}k_{3b}\left((-2\phi_{a1}\phi_{b1} + \phi_{b1}^2)\overline{\phi}_{a1}^2 - 2\overline{\phi}_{b1}(\phi_{a1}^2 + \phi_{b1}^2)\overline{\phi}_{a1} + \phi_{a1}(\phi_{a1} - 2\phi_{b1})\overline{\phi}_{b1}^2 + |\phi_{b1}|^4\right)\right) \tag{B13}$$

$$\overline{P} = \frac{1}{4}\frac{1}{\omega_{0,A}(|\phi_{b3}|^2 m_b + |\phi_{a3}|^2 m_a)}\left(-2\mathrm{i}|\phi_{a3}|^2|\phi_{a1}|^2 k_{3a}\cos 2\mu_A + 4\mathrm{i}|\phi_{a3}|^2|\phi_{a1}|^2 k_{3a}\cos 3\mu_A - 2\mathrm{i}|\phi_{a3}|^2|\phi_{a1}|^2 k_{3a}\cos 4\mu_A + \left(\mathrm{i}(4k_{3a}\cos\mu_A - 4k_{3a} -\right.\right.$$

$k_{3b})|\phi_{a1}|^2 - \mathrm{i}k_{3b}\left(|\phi_{b1}|^2 - \overline{\phi}_{a1}\phi_{b1} - \overline{\phi}_{b1}\phi_{a1}\right)\Big)|\phi_{a3}|^2 - \mathrm{i}k_{3b}\left(|\phi_{a1}|^2 + |\phi_{b1}|^2 - \overline{\phi}_{a1}\phi_{b1} - \overline{\phi}_{b1}\phi_{a1}\right)\left(|\phi_{b3}|^2 - \phi_{b3}\overline{\phi}_{a3} - \phi_{a3}\overline{\phi}_{b3}\right)\Big)$ (B14)

$$\overline{Q} = \frac{1}{8}\frac{1}{(|\phi_{b3}|^2 m_b + |\phi_{a3}|^2 m_a)\omega_{0A}}\Bigg(-4\mathrm{i}k_{3b}|\phi_{a3}^2\phi_{b3}^2| + 8\mathrm{i}|\phi_{a3}|^4 k_{3a}\cos 3\mu_A - 2\mathrm{i}|\phi_{a3}|^4 k_{3a}\cos 6\mu_A + \mathrm{i}(-6k_{3a} - k_{3b})|\phi_{a3}|^4 - \mathrm{i}k_{3b}\Big((-2\phi_{a3}\phi_{b3} + \phi_{b3}^2)\overline{\phi}_{a3}^2 - 2\overline{\phi}_{b3}(\phi_{a3}^2 + \phi_{b3}^2)\overline{\phi}_{a3} + \phi_{a3}(\phi_{a3} - 2\phi_{b3})\overline{\phi}_{b3}^2 + |\phi_{b3}|^4\Big)\Bigg)$$

(B15)

$$\overline{R} = \frac{1}{24}\frac{1}{\omega_{0,A}(|\phi_{b3}|^2 m_b + |\phi_{a3}|^2 m_a)}\left(-6\mathrm{i}\overline{\phi}_{a3}k_{3a}\phi_{a1}^3\cos(2\mu_A) + 2\mathrm{i}\phi_{a3}k_{3a}\phi_{a1}^3\cos 3\mu_A + \mathrm{i}(6\cos\mu_A\, k_{3a}\phi_{a1}^3 - k_{3b}\phi_{a1}^3 + 3k_{3b}\phi_{a1}^2\phi_{b1} - 3k_{3b}\phi_{a1}\phi_{b1}^2 + k_{3b}\phi_{b1}^3 - 2k_{3a}\phi_{a1}^3)\overline{\phi}_{a3} + \mathrm{i}k_{3b}\overline{\phi}_{b3}(-\phi_{b1} + \phi_{a1})^3\right)$$ (B16)

where $\boldsymbol{\phi}(\omega_{0,A}) = \begin{bmatrix}\phi_{a1}\\ \phi_{b1}\end{bmatrix}$ and $\boldsymbol{\phi}(\omega_{0,B}) = \begin{bmatrix}\phi_{a3}\\ \phi_{b3}\end{bmatrix}$.

REFERENCES

[1] Brillouin, L. *Wave Propagation in Periodic Structures: Electric Filters and Crystal Lattices.* Courier Corporation (2003).

[2] Ruppel, C. C., 2017, "Acoustic Wave Filter Technology–a Review," IEEE transactions on ultrasonics, ferroelectrics, and frequency control, 64, pp. 1390-1400.

[3] Fleuret, C., Andreani, A.-S., Lainé, É., Grandidier, J.-C., L'héritier, S., and Gorge, A.-L., 2016, "Complex Wing Spar Design in Carbon Fiber Reinforced Composite for a Light Aerobatic Aircraft," Mechanics & Industry, 17, pp. 614.

[4] Roebling Bridge, March 12, 2019, https://historicbridges.org/bridges/browser/?bridgebrowser=ohio/roebling/

[5] Saw Filters, February 25, 2019, http://www.itf.co.kr/product/technology/technology.php

[6] Liu, Z., Zhang, X., Mao, Y., Zhu, Y., Yang, Z., Chan, C. T., and Sheng, P., 2000, "Locally Resonant Sonic Materials," science, 289, pp. 1734-1736.

[7] Yilmaz, C., Hulbert, G. M., and Kikuchi, N., 2007, "Phononic Band Gaps Induced by Inertial Amplification in Periodic Media," Physical Review B, 76, pp. 054309.

[8] Farzbod, F. "Analysis of Bloch Formalism in Undamped and Damped Periodic Structures." PhD Thesis Georgia Institute of Technology, 2010.

[9] Halkjær, S., Sigmund, O., and Jensen, J. S., 2006, "Maximizing Band Gaps in Plate Structures," Structural and Multidisciplinary Optimization, 32, pp. 263-275.

[10] Fermi, E., Pasta, P., Ulam, S., and Tsingou, M., 1955, "Studies of the Nonlinear Problems," Technical Report No. Los Alamos Scientific Lab., N. Mex.,

[11] Kolmogorov, A., 1954, "The General Theory of Dynamical Systems and Classical Mechanics," Proceedings of the Proc. Intl. Congress of Math., Amsterdam,

[12] Arnold, V., 1963, "A Proof of the an Kolmogorov's Theorem on the Conservation of Conditional-Periodic Motions in a Small Change of the Hamiltonian Function," Usp. Mat. Nauk, 18, pp. 13.

[13] Moser, J. *Stable and Random Motions in Dynamical Systems: With Special Emphasis on Celestial Mechanics.* Princeton university press (2001).

[14] Zabusky, N. J., and Kruskal, M. D., 1965, "Interaction of" Solitons" in a Collisionless Plasma and the Recurrence of Initial States," Physical review letters, 15, pp. 240.

[15] Israiljev, F., and Chirikov, B. V., 1965, "The Statistical Properties of a Non-Linear String," Technical Report No. SCAN-9908053,

[16] Vakakis, A. F., and King, M. E., 1995, "Nonlinear Wave Transmission in a Monocoupled Elastic Periodic System," The Journal of the Acoustical Society of America, 98, pp. 1534-1546.

[17] Chakraborty, G., and Mallik, A. K., 2001, "Dynamics of a Weakly Non-Linear Periodic Chain," International Journal of Non-Linear Mechanics, 36, pp. 375-389.

[18] Ganesh, R., and Gonella, S., 2015, "From Modal Mixing to Tunable Functional Switches in Nonlinear Phononic Crystals," Physical review letters, 114, pp. 054302.

[19] Jiao, W., and Gonella, S., 2019, "Doubly Nonlinear Waveguides with Self-Switching Functionality Selection Capabilities," Physical Review E, 99, pp. 042206.

[20] Dubus, B., Swinteck, N., Muralidharan, K., Vasseur, J., and Deymier, P., 2016, "Nonlinear Phonon Modes in Second-Order Anharmonic Coupled Monoatomic Chains," Journal of Vibration and Acoustics, 138, pp. 041016.

[21] Manktelow, K. L., Leamy, M. J., and Ruzzene, M., 2014, "Weakly Nonlinear Wave Interactions in Multi-Degree of Freedom Periodic Structures," Wave Motion, 51, pp. 886-904.

[22] Narisetti, R. K., Leamy, M. J., and Ruzzene, M., 2010, "A Perturbation Approach for Predicting Wave Propagation in One-Dimensional Nonlinear Periodic Structures," Journal of Vibration and Acoustics, 132, pp. 031001.

[23] Narisetti, R. K., Ruzzene, M., and Leamy, M. J., 2011, "A Perturbation Approach for Analyzing Dispersion and Group Velocities in Two-Dimensional Nonlinear Periodic Lattices," Journal of Vibration and Acoustics, 133, pp. 061020-061020-12.

[24] Aluko, O. "Implementation and Application of Dispersion-Based Waveguide Models for Shallow-Water Sonar Processing." PhD Thesis University of Pittsburgh, 2004.

[25] Scott-Russell, J., 1844, "Report on Waves," Proceedings of the Proc. Roy. Soc. Edinburgh,

[26] Hasegawa, A., and Tappert, F., 1973, "Transmission of Stationary Nonlinear Optical Pulses in Dispersive Dielectric Fibers. I. Anomalous Dispersion," Applied Physics Letters, 23, pp. 142-144.

[27] Hasegawa, A., and Tappert, F., 1973, "Transmission of Stationary Nonlinear Optical Pulses in Dispersive Dielectric Fibers. Ii. Normal Dispersion," Applied Physics Letters, 23, pp. 171-172.

[28] Nesterenko, V., 1983, "Propagation of Nonlinear Compression Pulses in Granular Media," Journal of Applied Mechanics and Technical Physics, 24, pp. 733-743.

[29] Daraio, C., Nesterenko, V., Herbold, E., and Jin, S., 2005, "Strongly Nonlinear Waves in a Chain of Teflon Beads," Physical Review E, 72, pp. 016603.

[30] Pnevmatikos, S., Flytzanis, N., and Remoissenet, M., 1986, "Soliton Dynamics of Nonlinear Diatomic Lattices," Physical Review B, 33, pp. 2308-2321.

[31] Iooss, G., and James, G., 2005, "Localized Waves in Nonlinear Oscillator Chains," Chaos: An Interdisciplinary Journal of Nonlinear Science, 15, pp. 015113.

[32] Peregrine, D. H., 2009, "Water Waves, Nonlinear Schrödinger Equations and Their Solutions," The Journal of the Australian Mathematical Society. Series B. Applied Mathematics, 25, pp. 16-43.

[33] Remoissenet, M. *Waves Called Solitons: Concepts and Experiments.* Springer Science & Business Media (2013).

[34] Lamb Jr, G. L., 1980, "Elements of Soliton Theory," New York, Wiley-Interscience, 1980. 300 p. $29.95., pp.

[35] Biship, A., 1981, "Nonlinear Mode Phenomenology for Sine-Gordon Breather Excitations," Journal of Physics A: Mathematical and General, 14, pp. 1417.

[36] Remoissenet, M., 1986, "Low-Amplitude Breather and Envelope Solitons in Quasi-One-Dimensional Physical Models," Physical Review B, 33, pp. 2386.

[37] Yu, M., Jang, J. K., Okawachi, Y., Griffith, A. G., Luke, K., Miller, S. A., Ji, X., Lipson, M., and Gaeta, A. L., 2017, "Breather Soliton Dynamics in Microresonators," Nature Communications, 8, pp. 14569.

[38] Peyrard, M., and Kruskal, M. D., 1984, "Kink Dynamics in the Highly Discrete Sine-Gordon System," Physica D: Nonlinear Phenomena, 14, pp. 88-102.

[39] Campbell, D. K., Peyrard, M., and Sodano, P., 1986, "Kink-Antikink Interactions in the Double Sine-Gordon Equation," Physica D: Nonlinear Phenomena, 19, pp. 165-205.

[40] Chen, W., Hu, B., and Zhang, H., 2002, "Interactions between Impurities and Nonlinear Waves in a Driven Nonlinear Pendulum Chain," Physical Review B, 65, pp. 134302.

[41] Faber, M., 2014, "Spin and Charge from Space and Time," Proceedings of the Journal of Physics: Conference Series,

[42] Zakharov, V., and Shabat, A., 1973, "Interaction between Solitons in a Stable Medium," Sov. Phys. JETP, 37, pp. 823-828.

[43] Zhang, W., Walls, D. F., and Sanders, B. C., 1994, "Atomic Soliton in a Traveling Wave Laser Beam," Physical Review Letters, 72, pp. 60-63.

[44] Burger, S., Bongs, K., Dettmer, S., Ertmer, W., Sengstock, K., Sanpera, A., Shlyapnikov, G. V., and Lewenstein, M., 1999, "Dark Solitons in Bose-Einstein Condensates," Physical Review Letters, 83, pp. 5198-5201.

[45] Zaera, R., Vila, J., Fernandez-Saez, J., and Ruzzene, M., 2018, "Propagation of Solitons in a Two-Dimensional Nonlinear Square Lattice," International Journal of Non-Linear Mechanics, 106, pp. 188-204.

[46] Grosvenor, G., 1933,

[47] Fenton, J. D., 1999, Developments in Offshore Engineering, Elsevier, The Cnoidal Theory of Water Waves.

[48] Zakharov, V. E. E., and Faddeev, L. D., 1971, "Korteweg–De Vries Equation: A Completely Integrable Hamiltonian System," Funktsional'nyi Analiz i ego Prilozheniya, 5, pp. 18-27.

[49] Newton, P. K., and Keller, J. B., 1987, "Stability of Periodic Plane Waves," SIAM Journal on Applied Mathematics, 47, pp. 959-964.

[50] Benjamin, T. B., 1967, "Instability of Periodic Wavetrains in Nonlinear Dispersive Systems," Proceedings of the Royal Society of London. Series A. Mathematical and Physical Sciences, 299, pp. 59-76.

[51] Benjamin, T. B., and Feir, J. E., 1967, "The Disintegration of Wave Trains on Deep Water Part 1. Theory," Journal of Fluid Mechanics, 27, pp. 417-430.

[52] Lighthill, M., 1965, "Contributions to the Theory of Waves in Non-Linear Dispersive Systems," IMA Journal of Applied Mathematics, 1, pp. 269-306.

[53] Whitham, G., 1965, "A General Approach to Linear and Non-Linear Dispersive Waves Using a Lagrangian," Journal of Fluid Mechanics, 22, pp. 273-283.

[54] Zakharov, V. E., and Ostrovsky, L., 2009, "Modulation Instability: The Beginning," Physica D: Nonlinear Phenomena, 238, pp. 540-548.

[55] Bickham, S. R., Kiselev, S. A., and Sievers, A. J., 1993, "Stationary and Moving Intrinsic Localized Modes in One-Dimensional Monatomic Lattices with Cubic and Quartic Anharmonicity," Physical Review B, 47, pp. 14206-14211.

[56] Friesecke, G., and Pego, R. L., 2004, "Solitary Waves on Fermi–Pasta–Ulam Lattices: Iii. Howland-Type Floquet Theory," Nonlinearity, 17, pp. 207.

[57] Flach, S., and Gorbach, A. V., 2008, "Discrete Breathers — Advances in Theory and Applications," Physics Reports, 467, pp. 1-116.

[58] Huang, G., and Hu, B., 1998, "Asymmetric Gap Soliton Modes in Diatomic Lattices with Cubic and Quartic Nonlinearity," Physical Review B, 57, pp. 5746-5757.

[59] Gorbach, A. V., and Johansson, M., 2003, "Discrete Gap Breathers in a Diatomic Klein-Gordon Chain: Stability and Mobility," Physical Review E, 67, pp. 066608.

[60] Kochmann, D. M., and Bertoldi, K., 2017, "Exploiting Microstructural Instabilities in Solids and Structures: From Metamaterials to Structural Transitions," Applied mechanics reviews, 69, pp.

[61] Bilal, O. R., Foehr, A., and Daraio, C., 2017, "Bistable Metamaterial for Switching and Cascading Elastic Vibrations," Proceedings of the National Academy of Sciences, 114, pp. 4603-4606.

[62] Kamrava, S., Mousanezhad, D., Ebrahimi, H., Ghosh, R., and Vaziri, A., 2017, "Origami-Based Cellular Metamaterial with Auxetic, Bistable, and Self-Locking Properties," Scientific reports, 7, pp. 1-9.

[63] Katz, S., and Givli, S., 2018, "Solitary Waves in a Bistable Lattice," Extreme Mechanics Letters, 22, pp. 106-111.

[64] Xia, Y., Ruzzene, M., and Erturk, A., 2019, "Dramatic Bandwidth Enhancement in Nonlinear Metastructures Via Bistable Attachments," Applied Physics Letters, 114, pp. 093501.

[65] Nadkarni, N., Arrieta, A. F., Chong, C., Kochmann, D. M., and Daraio, C., 2016, "Unidirectional Transition Waves in Bistable Lattices," Physical Review Letters, 116, pp. 244501.

[66] Hwang, M., and Arrieta, A. F., 2018, "Input-Independent Energy Harvesting in Bistable Lattices from Transition Waves," Scientific reports, 8, pp. 1-9.

[67] Zhen Wu, K.-W. W., 2017, "On the Wave Propagation Analysis and Supratransmission Prediction of a Metastable Modular Metastructure for Non-Reciprocal Energy Transmission (in Review)," Physical Review E, pp.

[68] Kittel, C., 1958, "Interaction of Spin Waves and Ultrasonic Waves in Ferromagnetic Crystals," Physical Review, 110, pp. 836-841.

[69] Fleury, R., Sounas, D. L., Sieck, C. F., Haberman, M. R., and Alù, A., 2014, "Sound Isolation and Giant Linear Nonreciprocity in a Compact Acoustic Circulator," Science, 343, pp. 516-519.

[70] Naghdi, M., and Farzbod, F., 2018, "Acoustic Nonreciprocity in Coriolis Mean Flow Systems," The Journal of the Acoustical Society of America, 143, pp. 230-236.

[71] Quan, L., Sounas, D., and Alu, A., 2017, "Non-Reciprocal Sound Propagation in Zero-Index Metamaterials," The Journal of the Acoustical Society of America, 141, pp. 3698-3698.

[72] Trainiti, G., and Ruzzene, M., 2016, "Non-Reciprocal Elastic Wave Propagation in Spatiotemporal Periodic Structures," New Journal of Physics, 18, pp. 083047.

[73] Nassar, H., Xu, X. C., Norris, A. N., and Huang, G. L., 2017, "Modulated Phononic Crystals: Non-Reciprocal Wave Propagation and Willis Materials," Journal of the Mechanics and Physics of Solids, 101, pp. 10-29.

[74] Attarzadeh, M. A., and Nouh, M., 2018, "Non-Reciprocal Elastic Wave Propagation in 2d Phononic Membranes with Spatiotemporally Varying Material Properties," Journal of Sound and Vibration, 422, pp. 264-277.

[75] Shen, C., Zhu, X., Li, J., and Cummer, S. A., 2019, "Nonreciprocal Acoustic Transmission in Space-Time Modulated Coupled Resonators," Physical Review B, 100, pp. 054302.

[76] Seif, A., Degottardi, W., Esfarjani, K., and Hafezi, M., 2018, "Thermal Management and Non-Reciprocal Control of Phonon Flow Via Optomechanics," Nature Communications, 9, pp. 1207.

[77] Croënne, C., Vasseur, J. O., Matar, O. B., Ponge, M.-F., Deymier, P. A., Hladky-Hennion, A.-C., and Dubus, B., 2017, "Brillouin Scattering-Like Effect and Non-Reciprocal Propagation of Elastic Waves Due to Spatio-Temporal Modulation of Electrical Boundary Conditions in Piezoelectric Media," Applied Physics Letters, 110, pp. 061901.

[78] Ansari, M. H., Attarzadeh, M. A., Nouh, M., and Karami, M. A., 2018, "Application of Magnetoelastic Materials in Spatiotemporally Modulated Phononic Crystals for Nonreciprocal Wave Propagation," Smart Materials and Structures, 27, pp. 015030.

[79] Liang, B., Guo, X. S., Tu, J., Zhang, D., and Cheng, J. C., 2010, "An Acoustic Rectifier," Nature Materials, 9, pp. 989-992.

[80] Liang, B., Yuan, B., and Cheng, J.-C., 2009, "Acoustic Diode: Rectification of Acoustic Energy Flux in One-Dimensional Systems," Physical Review Letters, 103, pp. 104301.

[81] Luo, B., Gao, S., Liu, J., Mao, Y., Li, Y., and Liu, X., 2018, "Non-Reciprocal Wave Propagation in One-Dimensional Nonlinear Periodic Structures," AIP Advances, 8, pp. 015113.

[82] Boechler, N., Theocharis, G., and Daraio, C., 2011, "Bifurcation-Based Acoustic Switching and Rectification," Nature Materials, 10, pp. 665-668.

[83] Kartashov, Y. V., Malomed, B. A., Vysloukh, V. A., and Torner, L., 2009, "Two-Dimensional Solitons in Nonlinear Lattices," Optics letters, 34, pp. 770-772.

[84] Borovkova, O. V., Kartashov, Y. V., and Torner, L., 2010, "Stabilization of Two-Dimensional Solitons in Cubic-Saturable Nonlinear Lattices," Physical Review A, 81, pp. 063806.

[85] Kastner, M., 2004, "Dimension Dependent Energy Thresholds for Discrete Breathers," Nonlinearity, 17, pp. 1923.

[86] Butt, I. A., and Wattis, J. A., 2006, "Discrete Breathers in a Two-Dimensional Fermi–Pasta–Ulam Lattice," Journal of Physics A: Mathematical and General, 39, pp. 4955.

[87] Friesecke, G., and Pego, R. L., 1999, "Solitary Waves on Fpu Lattices: I. Qualitative Properties, Renormalization and Continuum Limit," Nonlinearity, 12, pp. 1601.

[88] Gaison, J., Moskow, S., Wright, J. D., and Zhang, Q., 2014, "Approximation of Polyatomic Fpu Lattices by Kdv Equations," Multiscale Modeling & Simulation, 12, pp. 953-995.

[89] Friesecke, G., and Mikikits-Leitner, A., 2015, "Cnoidal Waves on Fermi–Pasta–Ulam Lattices," Journal of Dynamics and Differential Equations, 27, pp. 627-652.

[90] Mark F. Hamilton, D. T. B. *Nonlinear Acoustics.* Academic Press San Diego, California (1998).

[91] Swinteck, N. Z., Muralidharan, K., and Deymier, P. A., 2013, "Phonon Scattering in One-Dimensional Anharmonic Crystals and Superlattices: Analytical and Numerical Study," Journal of Vibration and Acoustics, 135, pp. 041016-041016.

[92] Langley, R. S., 1996, "The Response of Two-Dimensional Periodic Structures to Point Harmonic Forcing," Journal of Sound and Vibration, 197, pp. 447-469.

[93] Langley, R. S., Bardell, N. S., and Ruivo, H. M., 1997, "The Response of Two-Dimensional Periodic Structures to Harmonic Point Loading: A Theoretical and Experimental Study of a Beam Grillage," Journal of Sound and Vibration, 207, pp. 521-535.

[94] Laude, V., Moiseyenko, R. P., Benchabane, S., and Declercq, N. F., 2011, "Bloch Wave Deafness and Modal Conversion at a Phononic Crystal Boundary," AIP Advances, 1, pp. 041402.

[95] Kulpe, J. A., Sabra, K. G., and Leamy, M. J., 2014, "Bloch-Wave Expansion Technique for Predicting Wave Reflection and Transmission in Two-Dimensional Phononic Crystals," The Journal of the Acoustical Society of America, 135, pp. 1808-1819.

[96] Kulpe, J. A., Sabra, K. G., and Leamy, M. J., 2015, "A Three-Dimensional Bloch Wave Expansion to Determine External Scattering from Finite Phononic Crystals," The Journal of the Acoustical Society of America, 137, pp. 3299-3313.

[97] Phani, A. S., Woodhouse, J., and Fleck, N. A., 2006, "Wave Propagation in Two-Dimensional Periodic Lattices," The Journal of the Acoustical Society of America, 119, pp. 1995-2005.

[98] Ruzzene, M., and Scarpa, F., 2005, "Directional and Band-Gap Behavior of Periodic Auxetic Lattices," physica status solidi (b), 242, pp. 665-680.

[99] Spadoni, A., Ruzzene, M., Gonella, S., and Scarpa, F., 2009, "Phononic Properties of Hexagonal Chiral Lattices," Wave Motion, 46, pp. 435-450.

[100] Kohrs, T., and Petersson, B. a. T., 2009, "Wave Beaming and Wave Propagation in Light Weight Plates with Truss-Like Cores," Journal of Sound and Vibration, 321, pp. 137-165.

[101] Picó, R., Pérez-Arjona, I., Sánchez-Morcillo, V. J., and Staliunas, K., 2013, "Evidences of Spatial (Angular) Filtering of Sound Beams by Sonic Crystals," Applied Acoustics, 74, pp. 945-948.

[102] Kushwaha, M. S., Halevi, P., Martinez, G., Dobrzynski, L., and Djafari-Rouhani, B., 1994, "Theory of Acoustic Band Structure of Periodic Elastic Composites," Physical Review B, 49, pp. 2313.

[103] Zhou, X.-Z., Wang, Y.-S., and Zhang, C., 2009, "Effects of Material Parameters on Elastic Band Gaps of Two-Dimensional Solid Phononic Crystals," Journal of Applied Physics, 106, pp. 014903.

[104] Khelif, A., Aoubiza, B., Mohammadi, S., Adibi, A., and Laude, V., 2006, "Complete Band Gaps in Two-Dimensional Phononic Crystal Slabs," Physical Review E, 74, pp. 046610.

[105] Goffaux, C., and Vigneron, J., 2001, "Theoretical Study of a Tunable Phononic Band Gap System," Physical Review B, 64, pp. 075118.

[106] Kuang, W., Hou, Z., and Liu, Y., 2004, "The Effects of Shapes and Symmetries of Scatterers on the Phononic Band Gap in 2d Phononic Crystals," Physics Letters A, 332, pp. 481-490.

[107] Zarembo, L., and Krasil'nikov, V., 1971, "Nonlinear Phenomena in the Propagation of Elastic Waves in Solids," Soviet Physics Uspekhi, 13, pp. 778.

[108] Sánchez-Morcillo, V. J., Pérez-Arjona, I., Romero-García, V., Tournat, V., and Gusev, V., 2013, "Second-Harmonic Generation for Dispersive Elastic Waves in a Discrete Granular Chain," Physical Review E, 88, pp. 043203.

[109] Rosenberg, R. M., 1966, Advances in Applied Mechanics, Elsevier, On Nonlinear Vibrations of Systems with Many Degrees of Freedom.

[110] Rushchitsky, J., and Cattani, C., 2004, "Evolution Equations for Plane Cubically Nonlinear Elastic Waves," International Applied Mechanics, 40, pp. 70-76.

[111] Rushchitsky, J., and Savel'eva, E., 2006, "On the Interaction of Cubically Nonlinear Transverse Plane Waves in an Elastic Material," International Applied Mechanics, 42, pp. 661-668.

[112] Manktelow, K., Leamy, M. J., and Ruzzene, M., 2011, "Multiple Scales Analysis of Wave–Wave Interactions In a cubically Nonlinear Monoatomic Chain," Nonlinear Dynamics, 63, pp. 193-203.

[113] Mehrem, A., Jiménez, N., Salmerón-Contreras, L. J., García-Andrés, X., García-Raffi, L. M., Picó, R., and Sánchez-Morcillo, V. J., 2017, "Nonlinear Dispersive Waves in Repulsive Lattices," Physical Review E, 96, pp. 012208.

[114] Jiménez, N., Mehrem, A., Picó, R., García-Raffi, L. M., and Sánchez-Morcillo, V. J., 2016, "Nonlinear Propagation and Control of Acoustic Waves in Phononic Superlattices," Comptes Rendus Physique, 17, pp. 543-554.

[115] Panigrahi, S. R., Feeny, B. F., and Diaz, A. R., 2017, "Wave–Wave Interactions in a Periodic Chain with Quadratic Nonlinearity," Wave Motion, 69, pp. 65-80.

[116] Spadoni, A., and Daraio, C., 2009, "Vibration Isolation Via Linear and Nonlinear Periodic Devices," Proceedings of the ASME 2009 International Design Engineering Technical Conferences and Computers and Information in Engineering Conference, San Diego, CA.

[117] Frandsen, N. M. M. "Design of Advanced Materials for Linear and Nonlinear Dynamics." PhD Thesis S201. Technical University of Denmark, Lyngby, Denmark. 2016.

[118] Huang, H., and Sun, C., 2009, "Wave Attenuation Mechanism in an Acoustic Metamaterial with Negative Effective Mass Density," New Journal of Physics, 11, pp. 013003.

[119] Tan, K. T., Huang, H., and Sun, C., 2014, "Blast-Wave Impact Mitigation Using Negative Effective Mass Density Concept of Elastic Metamaterials," International Journal of Impact Engineering, 64, pp. 20-29.

[120] Kittel, C. *Introduction to Solid State Physics.* Wiley New York (1976).

[121] Zhou, S., Jiang, W., and Shui, Y., 1995, "Nonlinear Bulk Acoustic Waves in Anisotropic Solids: Propagation, Generation, and Reflection," Journal of applied physics, 78, pp. 39-46.

[122] Rushchitskii, Y. Y., and Cattani, C., 2002, "Generation of the Third Harmonics by Plane Waves in Murnaghan Materials," International Applied Mechanics, 38, pp. 1482-1487.

[123] Müller, M. F., Kim, J.-Y., Qu, J., and Jacobs, L. J., 2010, "Characteristics of Second Harmonic Generation of Lamb Waves in Nonlinear Elastic Plates," The Journal of the Acoustical Society of America, 127, pp. 2141-2152.

[124] Matlack, K. H., Kim, J.-Y., Jacobs, L. J., and Qu, J., 2011, "Experimental Characterization of Efficient Second Harmonic Generation of Lamb Wave Modes in a Nonlinear Elastic Isotropic Plate," Journal of Applied Physics, 109, pp. 014905.

[125] Matsuda, N., and Biwa, S., 2011, "Phase and Group Velocity Matching for Cumulative Harmonic Generation in Lamb Waves," Journal of Applied Physics, 109, pp. 094903.

[126] Xiang, Y., Deng, M., Xuan, F.-Z., and Liu, C.-J., 2011, "Cumulative Second-Harmonic Analysis of Ultrasonic Lamb Waves for Ageing Behavior Study of Modified-Hp Austenite Steel," Ultrasonics, 51, pp. 974-981.

[127] Liu, Y., Chillara, V. K., and Lissenden, C. J., 2013, "On Selection of Primary Modes for Generation of Strong Internally Resonant Second Harmonics in Plate," Journal of sound and vibration, 332, pp. 4517-4528.

[128] Matlack, K., Kim, J.-Y., Jacobs, L., and Qu, J., 2015, "Review of Second Harmonic Generation Measurement Techniques for Material State Determination in Metals," Journal of Nondestructive Evaluation, 34, pp. 273.

[129] Franken, E. P., Hill, A. E., Peters, C., and Weinreich, G., 1961, "Generation of Optical Harmonics," Physical Review Letters, 7, pp. 118.

[130] Miller, R. C., 1964, "Optical Second Harmonic Generation in Piezoelectric Crystals," Applied Physics Letters, 5, pp. 17-19.

[131] Shen, Y.-R., 1984, "The Principles of Nonlinear Optics," New York, Wiley-Interscience, 1984, 575 p., pp.

[132] Ganesh, R., and Gonella, S., 2017, "Nonlinear Waves in Lattice Materials: Adaptively Augmented Directivity and Functionality Enhancement by Modal Mixing," Journal of the Mechanics and Physics of Solids, 99, pp. 272-288.

[133] Silva, P., Leamy, M., Geers, M., and Kouznetsova, V., 2019, "Emergent Subharmonic Band Gaps in Nonlinear Locally Resonant Metamaterials Induced by Autoparametric Resonance," Physical Review E, 99, pp. 063003.

[134] Sievers, A., and Takeno, S., 1988, "Intrinsic Localized Modes in Anharmonic Crystals," Physical Review Letters, 61, pp. 970.

[135] Takeno, S., and Hori, K., 1991, "Self-Localized Modes in a Pure One-Dimensional Lattice with Cubic and Quartic Lattice Anharmonicity," Journal of the Physical Society of Japan, 60, pp. 947-959.

[136] Sandusky, K., Page, J., and Schmidt, K., 1992, "Stability and Motion of Intrinsic Localized Modes in Nonlinear Periodic Lattices," Physical Review B, 46, pp. 6161.

[137] Chen, D., Aubry, S., and Tsironis, G., 1996, "Breather Mobility in Discrete Φ 4 Nonlinear Lattices," Physical review letters, 77, pp. 4776.

[138] Chabchoub, A., Hoffmann, N., Onorato, M., and Akhmediev, N., 2012, "Super Rogue Waves: Observation of a Higher-Order Breather in Water Waves," Physical Review X, 2, pp. 011015.

[139] Menyuk, C., 1987, "Nonlinear Pulse Propagation in Birefringent Optical Fibers," IEEE Journal of Quantum Electronics, 23, pp. 174-176.

[140] Weiner, A., Heritage, J., Hawkins, R., Thurston, R., Kirschner, E., Leaird, D., and Tomlinson, W., 1988, "Experimental Observation of the Fundamental Dark Soliton in Optical Fibers," Physical review letters, 61, pp. 2445.

[141] Coste, C., Falcon, E., and Fauve, S., 1997, "Solitary Waves in a Chain of Beads under Hertz Contact," Physical review E, 56, pp. 6104.

[142] Wiegel, R., 1960, "A Presentation of Cnoidal Wave Theory for Practical Application," Journal of Fluid Mechanics, 7, pp. 273-286.

[143] Shin, H., 2001, "Soliton Scattering from a Finite Cnoidal Wave Train in a Fiber," Physical Review E, 63, pp. 026606.

[144] Teixeira, F. L., 2008, "Time-Domain Finite-Difference and Finite-Element Methods for Maxwell Equations in Complex Media," IEEE Transactions on Antennas and Propagation, 56, pp. 2150-2166.

[145] Dissanayake, C. M., Premaratne, M., Rukhlenko, I. D., and Agrawal, G. P., 2010, "Fdtd Modeling of Anisotropic Nonlinear Optical Phenomena in Silicon Waveguides," Optics Express, 18, pp. 21427-21448.

[146] Manktelow, K., Leamy, M. J., and Ruzzene, M., 2013, "Comparison of Asymptotic and Transfer Matrix Approaches for Evaluating Intensity-Dependent Dispersion in Nonlinear Photonic and Phononic Crystals," Wave Motion, 50, pp. 494-508.

[147] Kaajakari, V., Mattila, T., Oja, A., and Seppa, H., 2004, "Nonlinear Limits for Single-Crystal Silicon Microresonators," Journal of Microelectromechanical systems, 13, pp. 715-724.

[148] Agarwal, M., Chandorkar, S. A., Candler, R. N., Kim, B., Hopcroft, M. A., Melamud, R., Jha, C. M., Kenny, T. W., and Murmann, B., 2006, "Optimal Drive Condition for Nonlinearity Reduction in Electrostatic Microresonators," Applied physics letters, 89, pp. 214105.

[149] Tocchio, A., Comi, C., Langfelder, G., Corigliano, A., and Longoni, A., 2011, "Enhancing the Linear Range of Mems Resonators for Sensing Applications," IEEE Sensors Journal, 11, pp. 3202-3210.

[150] Zhao, C., Sobreviela, G., Pandit, M., Du, S., Zou, X., and Seshia, A., 2017, "Experimental Observation of Noise Reduction in Weakly Coupled Nonlinear Mems Resonators," Journal of Microelectromechanical Systems, 26, pp. 1196-1203.

[151] Fronk, M. D., and Leamy, M. J., 2019, "Direction-Dependent Invariant Waveforms and Stability in Two-Dimensional, Weakly Nonlinear Lattices," Journal of Sound and Vibration, pp.

[152] Ganesh, R., and Gonella, S., 2017, "Experimental Evidence of Directivity-Enhancing Mechanisms in Nonlinear Lattices," Applied Physics Letters, 110, pp. 084101.

[153] Jiao, W., and Gonella, S., 2018, "Intermodal and Subwavelength Energy Trapping in Nonlinear Metamaterial Waveguides," Physical Review Applied, 10, pp. 024006.

[154] Allein, F., Tournat, V., Gusev, V., and Theocharis, G., 2020, "Linear and Nonlinear Elastic Waves in Magnetogranular Chains," Physical Review Applied, 13, pp. 024023.

[155] Molerón, M., Leonard, A., and Daraio, C., 2014, "Solitary Waves in a Chain of Repelling Magnets," Journal of Applied Physics, 115, pp. 184901.

[156] Deng, B., Raney, J. R., Tournat, V., and Bertoldi, K., 2017, "Elastic Vector Solitons in Soft Architected Materials," Physical Review Letters, 118, pp. 204102.

[157] Deng, B., Tournat, V., Wang, P., and Bertoldi, K., 2019, "Anomalous Collisions of Elastic Vector Solitons in Mechanical Metamaterials," Physical review letters, 122, pp. 044101.

[158] Frazier, M. J., and Kochmann, D. M., 2017, "Band Gap Transmission in Periodic Bistable Mechanical Systems," Journal of Sound and Vibration, 388, pp. 315-326.

[159] Cabaret, J., Tournat, V., and Béquin, P., 2012, "Amplitude-Dependent Phononic Processes in a Diatomic Granular Chain in the Weakly Nonlinear Regime," Physical Review E, 86, pp. 041305.

[160] Lydon, J., Theocharis, G., and Daraio, C., 2015, "Nonlinear Resonances and Energy Transfer in Finite Granular Chains," Physical review E, 91, pp. 023208.

[161] Hoogeboom, C., Man, Y., Boechler, N., Theocharis, G., Kevrekidis, P., Kevrekidis, I., and Daraio, C., 2013, "Hysteresis Loops and Multi-Stability: From Periodic Orbits to Chaotic Dynamics (and Back) in Diatomic Granular Crystals," EPL (Europhysics Letters), 101, pp. 44003.

[162] Manktelow, K. L., Leamy, M. J., and Ruzzene, M., 2014, "Analysis and Experimental Estimation of Nonlinear Dispersion in a Periodic String," Journal of Vibration and Acoustics, 136, pp. 031016.

[163] Mcfarland, D. M., Bergman, L. A., and Vakakis, A. F., 2005, "Experimental Study of Non-Linear Energy Pumping Occurring at a Single Fast Frequency," International Journal of Non-Linear Mechanics, 40, pp. 891-899.

[164] Vakakis, A. F., and Gendelman, O., 2000, "Energy Pumping in Nonlinear Mechanical Oscillators: Part Ii—Resonance Capture," Journal of Applied Mechanics, 68, pp. 42-48.

[165] Gendelman, O., Manevitch, L., Vakakis, A. F., and M'closkey, R., 2001, "Energy Pumping in Nonlinear Mechanical Oscillators: Part I—Dynamics of the Underlying Hamiltonian Systems," J. Appl. Mech., 68, pp. 34-41.

[166] Vakakis, A. F., Gendelman, O. V., Bergman, L. A., Mcfarland, D. M., Kerschen, G., and Lee, Y. S., 2008,

[167] Moore, K. J., Bunyan, J., Tawfick, S., Gendelman, O. V., Li, S., Leamy, M., and Vakakis, A. F., 2018, "Nonreciprocity in the Dynamics of Coupled Oscillators with Nonlinearity, Asymmetry, and Scale Hierarchy," Physical Review E, 97, pp. 012219.

[168] Bunyan, J., Moore, K. J., Mojahed, A., Fronk, M. D., Leamy, M., Tawfick, S., and Vakakis, A. F., 2018, "Acoustic Nonreciprocity in a Lattice Incorporating Nonlinearity, Asymmetry, and Internal Scale Hierarchy: Experimental Study," Physical Review E, 97, pp. 052211.

[169] Luo, J., Wierschem, N. E., Fahnestock, L. A., Bergman, L. A., Spencer, B. F., Al-Shudeifat, M., Mcfarland, D. M., Quinn, D. D., and Vakakis, A. F., 2014, "Realization of a Strongly Nonlinear Vibration-Mitigation Device Using Elastomeric Bumpers," Journal of Engineering Mechanics, 140, pp.

[170] Luo, J., Wierschem, N. E., Fahnestock, L. A., Spencer, B. F., Quinn, D. D., Mcfarland, D. M., Vakakis, A. F., and Bergman, L. A., 2014, "Design, Simulation, and Large-Scale Testing of an Innovative Vibration Mitigation Device Employing Essentially Nonlinear Elastomeric Springs," Earthquake Engineering & Structural Dynamics, 43, pp. 1829-1851.

[171] Wierschem, N. E., Hubbard, S. A., Luo, J., Fahnestock, L. A., Spencer, B. F., Mcfarland, D. M., Quinn, D. D., Vakakis, A. F., and Bergman, L. A., 2017, "Response Attenuation in a Large-Scale Structure Subjected to Blast Excitation Utilizing a System of Essentially Nonlinear Vibration Absorbers," Journal of Sound and Vibration, 389, pp. 52-72.

[172] Fomenko, S., Golub, M., Zhang, C., Bui, T., and Wang, Y.-S., 2014, "In-Plane Elastic Wave Propagation and Band-Gaps in Layered Functionally Graded Phononic Crystals," International Journal of Solids and Structures, 51, pp. 2491-2503.

[173] Bellet, R., Cochelin, B., Herzog, P., and Mattei, P.-O., 2010, "Experimental Study of Targeted Energy Transfer from an Acoustic System to a Nonlinear Membrane Absorber," Journal of Sound and Vibration, 329, pp. 2768-2791.

[174] Bellet, R., Cochelin, B., Côte, R., and Mattei, P.-O., 2012, "Enhancing the Dynamic Range of Targeted Energy Transfer in Acoustics Using Several Nonlinear Membrane Absorbers," Journal of Sound and Vibration, 331, pp. 5657-5668.

[175] Zhang, J., Romero-García, V., Theocharis, G., Richoux, O., Achilleos, V., and Frantzeskakis, D. J., 2016, "Second-Harmonic Generation in Membrane-Type Nonlinear Acoustic Metamaterials," Crystals, 6, pp. 86.

[176] Trainiti, G., Rimoli, J., and Ruzzene, M., 2018, "Optical Evaluation of the Wave Filtering Properties of Graded Undulated Lattices," Journal of Applied Physics, 123, pp. 091706.

[177] Fronk, M. D., and Leamy, M. J., 2017, "Higher-Order Dispersion, Stability, and Waveform Invariance in Nonlinear Monoatomic and Diatomic Systems," Journal of Vibration and Acoustics, 139, pp. 051003.